AN ULTRASONICS BASED SYSTEM FOR THE EXTRACTION OF RANGE AND BEARING DATA FOR MULTIPLE TARGETS

by

Philip F. Webb B.Eng

Thesis submitted to the University of Nottingham

for the degree of Dbctor of Philosophy

January 1994

ABSTRACT:

With the increasing use of automatically guided vehicles and a requirement for greater flexibility from fixed robots there is a need for a system which can locate and map the position of objects within a defined workspace in real time. The purpose of this research is to design and evaluate a system which will provide a possible solution to this problem using ultrasonics and to investigate the applicability of different signal processing strategies to the enhancement of such data.

ACKNOWLEDGEMENTS

I would like to give particular thanks to my supervisor Dr. Catherine Wykes for the inspiration and guidance she has given me throughout this project.

I am also grateful to all the staff of the Department of Manufacturing and Operations Management for the facilities and support provided and without which this work would not have been possible. Particular thanks must also go to my former colleagues, within the Ultrasonics Research Group, Farrukh Nagi, Catherine Zhang and Nick Cope.

Finally I would like to thank my wife for her support and encouragement.

CONTENTS

Chapter 3 - Generation propagation and Reflection of ultrasound in air

CHAPTER 1

INTRODUCTION

1.1 Ultrasonics research at the University of Nottingham.

This work forms part of a large research project into the development and application of ultrasonic sensors for manufacturing applications. The project has been funded, since 1983, by the Science and Engineering Research Council, initially as part of the Applications of Computers in Manufacturing Engineering (ACME) project and latterly as part of the Link scheme in conjunction with Transfer Technology Ltd. Over the past 10 years technology has been developed enabling the manufacture of ultrasonic transducers with a wide range of geometries and operating frequencies[1,2,3,4]. Specialised techniques have been developed for the analysis of the performance of such transducers[5] as well as an analytical model to describe their behaviour[6]. The project has also resulted in the development of a sophisticated computer based system for the modelling of ultrasound propagation[7].

1.2 Aims and objectives.

Over the past decade there has been an increasing use of flexible manufacturing systems and autonomous mobile robots in industry. This increase in automation has led to a requirement for a rapid and accurate method of determining the precise

location of objects in space. This may be for the purposes of navigation and collision avoidance for mobile robots or work space monitoring and collision avoidance for fixed robots. The primary objective of the research described in this thesis was to use the technology described in section 1.1 to develop a practical solution to these requirements. The result was a system that could extract the locations of multiple objects present in a robot workspace in real time. To fulfil this objective both hardware and software had to be developed. To produce a successful system new signal processing strategies and data handling methods needed to be developed. Although data acquisition systems have been developed for the acquisition and processing of ultrasonic data[2], a new approach was used to enable the data to be acquired and processed in real time. Some of the design parameters were also influenced by the results of a feasibility study performed by Advanced Robotics Research Limited, this is discussed in more detail in chapter 5.

The system was to be based on an ultrasonic phased array operating at 100KHz. For the purpose of validation the system was used to guide a Unimation PUMA 560 robot, with a workspace measuring 700mm x 1000mm, in a pick and place operation.

It was also an objective of the work that the developed hardware would be as flexible as possible to allow the system to be expanded without the need for major hardware upgrades.

1.3 Thesis overview.

This section gives an overview of the contents of each of the chapters and appendices contained within this thesis.

Chapter 1: Introduction.

Chapter 2: This contains a detailed review of previous research that has been carried out into the use of airborne ultrasound. It covers the development of sensors and their application to different tasks. These tasks include measurement, imaging and object characterisation and identification.

Chapter 3: This chapter provides an in-depth study of the propagation and generation of ultrasound in air. It covers the alternative types of transducer available and how the sound field develops as the waves leave the transducer. The effect of environmental factors and the reflection characteristics of ultrasound are also studied. Many of the factors that must be compensated for to produce a reliable system are described.

Chapter 4: In this chapter, classical methods of object location using reflected radiation are explored. The most common methods are presented in detail whilst references are given for others. A new method is also described which removes a severe limitation imposed on resolution by the more traditional approaches.

Chapter 5: Here the design considerations considered in the development of the system hardware are described in detail. The limitations placed on the hardware by the transducer are also explored.

Chapter 6: This chapter covers the practical realisation of the system developed in chapter 5. It describes the construction and function of a real time data acquisition and processing system. An overview of the Digital Signal Processing system used is included.

Chapter 7: This describes the implementation of the location methods described in chapter 4 as being the most suitable for this particular application. The algorithms used are described in detail as well as their implementation.

Chapter 8: This chapter investigates the application of various signal processing algorithms to improve the system developed in chapters 5 to 7. The theory behind each algorithm is described as well as its implementation.

Chapter 9: This contains a presentation and analysis of the experiments used to verify the operation of the system as a measurement tool. These results are then compared with a theoretical analysis of system performance.

Chapter 10: This contains a presentation and analysis of the experiments used to verify the operation of the system as an imaging tool. The problems caused by the generation of ambiguous returns are discussed and resolution of the system is also

examined. The chapter also gives the speed of the different processing algorithms used.

Chapter 11: Here the results of a practical implementation of the system are described and the results are presented along with details of the hardware configuration used.

An analysis of the viability of such a system is also provided.

Chapter 12: Chapter 12 summarises the work done and suggests how the results could be improved. There is also a discussion of the possibilities for the fusion of ultrasonics with other technologies.

Appendix A: This covers the structure and operation of the system software written in support of this research.

Appendix B: Appendix B contains the beam former assembly language listings.

Appendix C: This appendix contains an analysis of the system hardware. Such factors as bandwidth, signal to noise ratio and data transfer rates are covered.

Appendix D: This describes the results obtained from a noise measurement experiment. The experiment was performed to assess the impact on the system of the noise generated by a welding robot.

1.4 References.

1. M. Wybrow, "An Ultrasonic Recognition System for Flexible Manufacturing", Ph. D. Thesis, University of Nottingham, 1988.

2. S. C. Pomeroy, "Ultrasonic Phased Arrays for Robotics Modelling and Experimental Implementation", Ph. D. Thesis, University of Nottingham, 1989.

3. W. S. H. Munro, "Ultrasonic Phased Arrays for Use in Imaging and Automatic Vehicle Guidance", Ph. D. Thesis, University of Nottingham, 1990.

4. F. Nagi, "Physical Beam Forming and Array Processing for Sources Location", Ph. D. Thesis, University of Nottingham, 1993.

5. H. J. Carr, M. Rafiq and C. Wykes, "The Use of Interferometry in the Investigation of Ultrasound Transducers", J. Phys. D: Appl. Phys., Vol. 22, 1989, pp495-499.

6. H. Carr, "Capacitive Transducers for Ultrasonic Sensing in Robotics", Ph. D. Thesis, University of Nottingham, 1989.

7. G. Zhang, "The Application of the Transmission Line Matrix Method to the Modelling of Airborne Ultrasound", Ph. D. Thesis, University of Nottingham, 1993.

CHAPTER 2

REVIEW OF PREVIOUS WORK IN AIRBORNE ULTRASONICS

2.1 Introduction.

A huge amount of research effort has been expended in the use of ultrasound in medical imaging, nondestructive testing and airborne imaging and ranging. Chapter 2 contains a summary of work concerned with airborne imaging and ranging, work from other areas will only be discussed if it is felt to be of particular relevance.

Section 2.2 describes the work done on the development of suitable ultrasonic transducers for use in air. Sections 2.3 and 2.4 give a summary of the work done so far in the use of airborne ultrasound for measurement and imaging. Section 2.5 provides a summary of the application of ultrasonic sensing specifically to robot control and guidance and section 2.6 covers the application of ultrasonics to the identification and classification of objects. Finally the conclusions which may be drawn from the work described in this chapter are discussed in section 2.7.

2.2 Ultrasonic sensors.

The development of ultrasonic transducers for use in air has been concentrated in two main areas, the development of capacitive transducers and the impedance matching of existing piezo electric transducers.

2.2.1 Electrostatic transducers.

The most commonly used electrostatic transducer is that manufactured by the Polaroid corporation since 1982[1]. This consists of a single circular transducer 1.5 inches in diameter with a textured backplane and a fixed operating frequency of 50khz. The fixed size and operating frequency gives the transducer a beamwidth of 30°; this makes the construction of any form of phased array impossible see chapter 3. The fixed frequency and size are the main limitations of this device, making it only really suitable for use as a simple rangefinder. The Polaroid transducer was originally designed for use as a camera range finder for auto focusing but its ease of availability has made it almost a 'standard transducer' for robot sensing.

Research at Nottingham university has developed fabrication methods whereby electrostatic transducers can be manufactured to operate at frequencies between 50kHz and 3MHz. A novel production method also allows arrays of any size and geometry to be produced[2,3,4,5,6,7,8].

An electrostatic transmitting array has been developed by Huissoon and Moziar using a series of transducers etched onto a printed circuit board[9]. Unlike most other electrostatic transducers, the backplane behind the membrane is untextured. Backplane texture is normally considered to be one of the most crucial factors in determining the sensitivity of this style of transducer. Texturing may not be so critical in this applications since the array is used as a transmitter only. The technique has been demonstrated by the manufacture of a 6 element array operating at 50kHz.

Kay[10] has developed an electrostatic transducer array made from grooved

metal blocks embedded in plastic. The only detailed documentation available on the construction of the transducer is given in a UK patent[11].

2.2.2 Piezo electric transducers.

Piezo electric transducers are widely used in both medical and non destructive testing applications. They are not widely used in airborne applications due to impedance matching problems. The commonest way of improving their performance in air by is the insertion of a matching layer between the transducer and the air.

A piezo electric transducer capable of matching with air has been produced by LaComb et al[12] using a multilayer ZnO structure to match the transducer. The resulting transducer is capable of operating in the GHz frequency range.

Fox et al[13] have demonstrated an acoustic microscope operating at 2Mhz using an epoxy matching layer.

Kleinschmidt and Mágori[14] have produced a transducer operating at 200kHz using a plastic matching material.

A different matching method has been used by Babič[15] in which a metal membrane is used to match the transducer. The ceramic transducer is used to drive the membrane and it is the membrane which transmits the ultrasound. This technique has been demonstrated by the production of a 12mm diameter transducer operating at 200kHz.

2.3 Ultrasonic measurement.

A good summary of the use of ultrasonics for measurement is provided in the paper by Hickling and Moran[16]. Some of the other work in this area is also mentioned below.

A commonly available commercial ultrasonic measurement system is the "Ultrasonic Tape Measure". These normally have a range of up to 12m and a quoted accuracy of ±1%. A typical example is that available from RS Components Ltd[17].

A measurement system has also been developed by Holmberg[18]. This is based on a Polaroid transducer with the addition of advanced signal processing to produce a much more robust and accurate system than the normal Polaroid system. The frequency modulated carrier wave method (FMCW) is used instead of the more common pulse echo method. The system is quoted as being able to measure distances with an accuracy of 0.25mm. A pulse echo measurement system has also been developed by Yano et al[19] which gives 0.1mm accuracy at an operating frequency of 1MHz.

Canali et al[20] have developed a simple system which automatically compensates for variation in temperature. The accuracy quoted is ±1% at ranges of up to 1m.

2.4 Ultrasonic imaging.

Whilst the use of ultrasound in medical and NDT applications is well established

there is relatively little documented work for airborne imaging.

A system has been demonstrated by Horiguchi[21] using an array of 16 microphones as receivers and a single Polaroid as a transmitter. The documented results of the system are very promising but the system does have two drawbacks. The microphones used are very expensive. Because of their relative bulkiness the spacing of the microphones is greater than the optimal $\lambda/2$, see chapter 4, this results in an angular view of 18° before the first set of grating lobes appear[1].

2.5 Applications of airborne ultrasound.

This section describes the applications of ultrasonics to the direct guidance and control of robots.

2.5.1 Mobile robots.

There is a very large amount of published material available on the use of ultrasonics, or airborne sonar as it is often called, for the guidance of mobile robots. Since the work described in this thesis is directed towards the application of ultrasonics to fixed robot guidance applications, only a brief summary of current work in this area will be presented.

Two very prolific writers on the use of ultrasonics for mobile robot guidance are Borenstein and Koren[22,23,24,25,26]. Their work initially used two Polaroids mounted on a robot and used for collision avoidance. This work later

---

[1] The formation of grating lobes and the $\lambda/2$ restriction for arrays is fully discussed in chapter 4.

progresses to the use of a ring of Polaroids mounted around the outside of the robot. These sensors provide a 360° angle of view and are used for navigation as well as collision avoidance.

Brady et al[27,28,29] have also published a number of papers on this subject again using the Polaroid as a basis for a robot navigation system. Crowley[30,31,32] describes the use of a rotating ultrasonic sensor but does not define what type is used. In ref 31 he has abandoned the use of a rotating sensor in favour of a ring of 24 fixed sensors. These sensors are used both for collision avoidance and navigation.

Some of the most interesting work in the use of ultrasonics in mobile robot guidance is that published by Peremans et al[33]. This is based on the use of three Polaroid transducers mounted side by side but with the outer sensors inclined slightly towards the centre. The centre transducer only is used as transmitter whilst all three act as receivers. A triangulation system is used to then find the position of any target that is within view of all three transducers. The system is also capable of deriving basic information about the type of object being viewed. The system can differentiate between edges, planes and curved surfaces. The system does suffer from a relatively small angle of view (~25°) and is not capable of operating in cluttered environments.

A phased array system operating at 50kHz has been demonstrated by Munro et al[34]. This was demonstrated as an experimental system and proved capable of locating a series of 4" diameter cylinders at ranges of up to 10m and with an angular resolution of 6°.

2.5.2 Fixed robots.

A common application of ultrasonics to fixed robot guidance has been in the use of sensors for gripper positioning.

Another common application is in seam tracking which is used in many robotic production processes. These include robotic welding, gluing, sealing grinding and cutting. Systems using single transducers for seam tracking have been demonstrated by Estochen et al[35] and Macqueria et al[36]. This application is a special case since it relies for its operation on the large echo produced by the discontinuity in a flat piece of material caused by the presence of the seam.

An ultrasonic performance measurement system has been developed by Ayogi et al[37]. This system is capable of accurately measuring the orientation and position of a robot gripper. It consists of a spark transmitter and three electrically rotatable receivers. The transmitter produces an isotropic radiation pattern and the three receivers, which have a very narrow beamwidth (6°), are used to track the reflections from the end of the robot arm. The system is reported to be of sufficient accuracy to be used as a calibration device for robots.

Kleinschmidt and Mágori[14] have used a single transmitter and receiver mounted on a robot gripper to provide both positional and shape information for robot manipulation of an unknown object.

2.6 Object characterisation and identification using ultrasound.

A system has been developed by Barsham and Kuc[38] which is capable of differentiating the reflections from corners and planes. The system uses multiple

transducers operating in a time of flight measurement mode -see chapter 4. By comparing the range and amplitude values obtained with different transmitter/receiver pairs, corners and planes can be differentiated. This system has been expanded to 3 dimensions by Hong and Kleeman[39] who have been able to differentiate corners, edges and planes using three transducers. A more comprehensive approach to object identification has been taken by Bull et al[40,41,42] who have concentrated on the use of neural networks both to improve the quality of the received signal and to identify the reflecting object. Initially they used the output of a mechanically rotated Polaroid to identify surface features but are now successfully using a multi element electrostatic array, of the type manufactured at Nottingham University, to identify complete objects. Three dimensional objects have also been identified by Watanabe and Yoneyama[43] using a 2D array and neural network processing. A different system has been developed by Wybrow[44] who used an ultrasonic ranger, held in a robot end effector, to generate range profiles of an object by scanning. By comparing the resulting range profiles with stored range profiles the object could be identified. A similar approach has been taken by Brown[45,46] who uses an ultrasonic transducer mounted on a robot gripper to scan an unknown object. The system then processes the received range data to extract the surface features of the object.

2.7 Summary.

It is obvious from the quantity of literature published that much work has been carried out on the application of airborne ultrasonics. The work on the investigation of ultrasonic imaging using phased arrays is, however, limited. This is probably due to the lack of a suitable sensor. There is therefore a need for work to take advantage of the expertise gained in the manufacture of ultrasonic arrays and develop accurate and robust ultrasonic imaging system for use in robotic guidance and control.

2.8 References.

1. Polaroid corporation, "Ultrasonic range finders", Polaroid corporation, 1982.

2. W.S.H. Munro,"Ultrasonic phased arrays for use in imaging and automatic vehicle guidance", PhD thesis, Nottingham university, 1990.

3. H.J. Carr, M. Rafiq and C. Wykes, "The use of interferometry in the Investigation of ultrasound transducers", J. Phys. D, 1989, **Vol 22**, pp495-499.

4. H. Carr, "Electro-static transducers for air-borne ultrasound", Ph.D. thesis, University of Nottingham, 1989.

5. M. Rafiq and C. Wykes, "The performance of capacitive ultrasonic transducers using V-grooved backplates", 1991, **Vol 2**, Meas. Sci. Technol. (formerly J. Phys. E.), pp. 168-174.

6. H. Carr, W.S.H. Munro, M. Rafiq and C. Wykes, "Developments in Capacitive Transducers", Nondestructive Test. 1992, Eval, **Vol 10**, pp3-13.

7. H. Carr and C. Wykes "Diagnostic Measurements in Capacitive Transducers", accepted for publication in Ultrasonics, 1992.

8. W.S.H. Munro and C. Wykes, "Arrays for air-borne ultrasound", submitted for publication to Ultrasonics, 1992.

9. J. P. Huissoon and D. M. Moziar, "Curved ultrasonic array transducer for AGV applications", Ultrasonics, Vol. 27, July, 1989, pp221-225.

10. L. Kay, "Airborne Ultrasonic Imaging of a Robot Work space", Sensor Review, Vol. 5, No. 1, Jan 1985, pp8-11.

11. L. Kay. UK Patent No. GB2151025 "Improvements relating to transducers".

12. L. J. LaComb, Jr., B. T. Khuri-Yakub, C. F. Quate and B. Hadimioglu, "Interface structure of multilayer ZnO acoustic transducers", IEEE Ultrasonics symposium, 1988, pp327-329.

13. J. D. Fox, B. T. Khuri-Yakub and G. S. Kino, "An Imaging microscope and a resonant rangefinder", IEEE Ultrasonics symposium, 1985, pp463-467.

14. P. Kleinschmidt and V. Mágori, "Ultrasonic robotic-sensors for exact short range distance measurement and object identification", IEEE Ultrasonics symposium, 1985, pp457-462.

15. M. Babič, "A 200kHz ultrasonic transducer coupled to the air with a radiating membrane", IEEE Transactions on ultrasonics, ferroelectrics and frequency control, Vol. 38, No. 3, May 1991, pp252-255.

16. R. Hichling and S. P. Marin, " The use of ultrasonics for gauging and proximity sensing in air", J. Acoust. Soc. America, Vol. 79, No. 4, April 1986, pp1151-1160.

17. Radio Spares Ltd. catalogue 1993.

18. P. Holmberg, "Robust Ultrasonic Range Finder", Meas. Sci. Technol., Vol. 3, 1992, pp1025-1037.

19. T. Yano, M. Tone, and A. Fukumoto, "Range finding and surface characterization using high-frequency transducers", IEEE Transactions on Ultrasonics, Ferroelectrics and Frequency Control, Vol. 34, No. 2, March 1987, pp232-236.

20. C. Canali, G. De Cicco, B. Moreton, M. Prudeenzati and A. Taroni, "A temperature compensated ultrasonic sensor operating in air for distance and proximity measurement", IEEE Transactions on Industrial Electronics, Vol. 29, No. 4, November 1992, pp336-340.

21. Horiguchi T, "A full digital delay compensation beam forming scheme for ultrasonic imaging using arrays", NEC Research and development, No. 88, Jan., 1988, pp47-55.

22. J. Borenstein, Y. Koran, Obstacle avoidance with ultrasonic sensors", IEEE Journal of Robotics and Automation, Vol. 4, No. 2, April 1988, pp213-218.

23. J. Borenstein and Y. Koren, "Real time obstacle avoidance for fast mobile robots", IEEE Transactions on Systems, Man and Cybernetics, Vol. 19, No 5, October 1979, pp1179-1187.

24. J. Borenstein and Y. Koren, "Real time object avoidance for fast mobile robots in cluttered environments", Proceedings IEEE International Conference on Robotics and Automation, 1990, pp572-577.

25. J. Borenstein and Y. Koren, "Histogramic in-motion mapping for mobile robot obstacle avoidance", IEEE Transactions on Robotics and Automation, Vol. 7, No. 4, August 1991, pp535-539.

26. J. Borenstein and Y. Koren, "Noise rejection for ultrasonic sensors in mobile robot applications", Proceedings of the 1992 IEEE International Conference on Robotics and Automation, Nice, France, May 1992, pp1727-1732.

27. M. Brady, H. Durrant-Whyte, P. Probert and H. Hu, "A sensing autonomous guided vehicle for advanced manufacturing", Proceedings IEEE International Conference on Robotics and Automation, Cincinnati, May 13-18, 1990, pp140-145.

28. M. Brady, H. Durrant-Whyte, H. Hu, J. Leonard, P. Probert and B. S. Y. Rao, "Sensor-based control of AGVs", IEE Computing and Control Engineering Journal, March 1990, pp64-69.

29. J. Leonard and H. F. Durrant-Whyte, "Mobile Robot Localization by Tracking Geometric Beacons", IEEE Transactions on Robotics and Automation, Vol. 7, No. 3, June 1991, pp376-382.

30. J. L. Crowley, "Navigation for an Intelligent Mobile Robot", IEEE Journal of robotics and automation, Vol. 1, No. 1, March 1985, pp31-41.

31. J. L. Crowley, "Dynamic World Modelling for an Intelligent Mobile Robot Using a Rotating Ultrasonic Ranging Device", IEEE Ultrasonics symposium, 1985, pp128-135.

32. J. L. Crowley, "World Modelling and Position Estimation for a Mobile Robot Using Ultrasonic Ranging", IEEE Ultrasonics symposium, 1989, pp674-680.

33. H. Peremans, K. Audenaert and J. M. Van Campenhout, "A High Resolution Sensor Based on Tri-aural Perception", IEEE Transactions on robotics and automation, Vol. 9, No. 1, February, 1993, pp36-48.

34. W. S. H. Munro, S. Pomeroy, M. Rafiq, H. R. Williams, M. D. Wybrow, C. Wykes, "An Ultrasonic Vehicle guidance System", Proceedings of IROS, IEEE International workshop , Tskuba, Japan, September, 1989.

35. E. L. Estochen, C. P. Neuman and F. B. Prinz, "Application of acoustic sensors to robotic seam tracking", IEEE Transactions on industrial

electronics, Vol. 31, No. 3, August 1984, pp219-224.

36. B. Macqueria, C. Umeagukwu and J. Jarzynski, "Robotic seam tracking of weld joints through the use of ultrasonic sensors",IEEE Ultrasonics symposium, 1987, pp291-296.

37. S. Ayogi, S. Okabe, K. Sasaki and M. Tackano, "Measurement of 3-D position and orientation of a robot using ultrasonic waves", Proc. of the 1991 IEEE International Conference on Industrial Electronics, Control and Instrumentation, Vol. 3, Kobe, 1991, pp2466-2471.

38. B. Barsham and R. Kuc, "Differentiating sonar reflections from corners and planes by employing an intelligent sensor", IEEE Transactions on Pattern Analysis and Machine Intelligence, Vol. 12, No. 6, June 1990, pp560-569.

39. M. L. Hong and L. Kleeman, "Analysis of ultrasonic differentiation of three dimensional corners, edges and planes", Proceedings of the 1992 IEEE International Conference on Robotics and Automation, Nice, France, May 1992, pp580-584.

40. S. M. Thomas and D. R. Bull, "Neural processing of airborne sonar for mobile robot applications", Proceedings of The IEE International Conference on Artificial Neural Networks, Bournmouth, U.K. Nov 1991, pp267-270.

41. P. D. Smith, D. R. Bull and C. Wykes, "Target classification with artificial neural networks using ultrasonic phased arrays",Proc eighth international conference on applications of artificial intelligence in engineering, Toulouse, 1993, pp788-800.

42. D. R. Bull and S. M. Thomas "Digital filtering solutions to ultrasonic specular reflection", Proceedings Institute of Physics Conference on Sensors and their Applications, Edinburgh, 1991, pp399-404.

43. S. Watanabe and M. Yoneyama, "An Ultrasonic Visual Sensor for Three-Dimensional Object Recognition Using Neural Networks", IEEE Transactions on robotics and automation, Vol. 8, No. 2, April 1992, pp240-249.

44. M. Wybrow and C. Wykes, "An Ultrasonic system for object recognition in a manufacturing environment", Journal of Intelligent Manufacturing, Vol. 3, 1992, pp163-172.

45. M. K. Brown, "Feature Extraction Techniques for Recognising Solid Objects with an Ultrasonic Range Sensor",IEEE journal of robotics and automation", Vol. 1, No. 4, December, 1985, pp191-205.

46. M. K. Brown, "On Ultrasonic Detection of Surface Features", Proceedings IEEE international conference on robotics and automation, 1986, pp1785-1790.

CHAPTER 3

GENERATION, PROPAGATION AND REFLECTION OF ULTRASOUND IN AIR

3.1 Introduction.

Chapter 3 provides a general introduction to the generation and propagation of ultrasound in air. Section 3.2 covers the principal methods employed in the generation of ultrasound. Section 3.3 examines the way in which energy is transmitted through an aperture. Section 3.4 gives an introduction to the propagation of ultrasound in air. Finally, section 3.5 examines the interaction of airborne ultrasound with solid objects.

3.2 Ultrasonic transducers.

Ultrasound can be generated in many different ways; some of these are listed below:

Mechanical vibration.

Escaping gas.

Electrical discharge.

These three methods are described in further detail in sections 3.2.1, 3.2.1.1 and 3.2.1.2. It is important to note that all these forms of ultrasound generation may be present, in an industrial environment, as noise sources.

3.2.1 Mechanical vibration.

This section describes the methods which use mechanical vibration to produce ultrasound.

3.2.1.1 Piezo-electric.

Piezo-electric transducers are manufactured from crystals that display the piezo-electric effect[1]. This effect occurs in crystals that have one or more polar axis or no centre of symmetry. If a section is cut from such a crystal with parallel faces lying normal to one of the polar axis and an electric field applied in the direction of the polar axis then the crystal will become strained. If a stress is applied to the crystal then equal and opposite electrical fields will be developed on the faces of the material. The most common of these crystals are Quartz or Zinc oxide. A diagram of a simple piezo-electric transducer is shown in Figure 1. The transducer consists of two differently polarised slabs of crystal. When a voltage is applied, the two sections of crystal deform in opposite directions according to the polarity of the supply. If an alternating current is applied the crystal will vibrate. When a sound wave hits the crystal, an alternating current will be generated by a reverse process. Unfortunately piezo-electric transducers couple badly with air because they have a high acoustic impedance relative to air. Acoustic impedance, Z_a, is defined as the product of the speed of sound in the material and the density of the material. With a piezo electric transducer only 0.05% of the transmission energy is coupled to air as compared to 70% in water[2]. This coupling can be improved by the introduction of a material with an intermediate impedance between the transducer and air. Kuri-Yakub et al[3] have

produced successful transducers, operating in the range 0.5-10MHz, by this method using an interface made from silica aerogel.

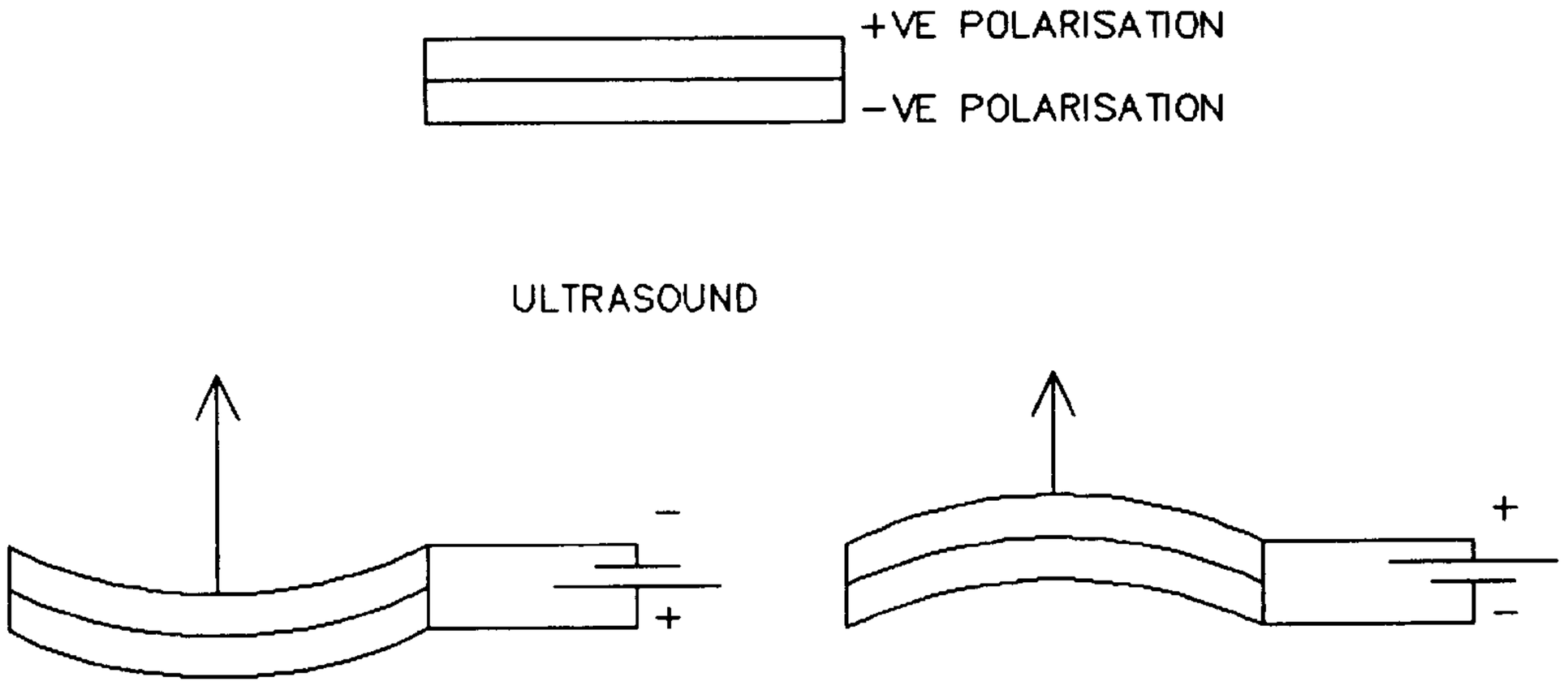

Figure 1: Operation of Piezo-electric transducer.

3.2.1.2 Electrostatic.

A diagram of an electrostatic or capacitive transducer is shown in Figure 2. It consists of a thin metallised dielectric membrane stretched across a textured backplane. A DC bias is applied between the membrane and the backplane. If either the bias is switched on and off or an additional alternating voltage superimposed the membrane will vibrate.

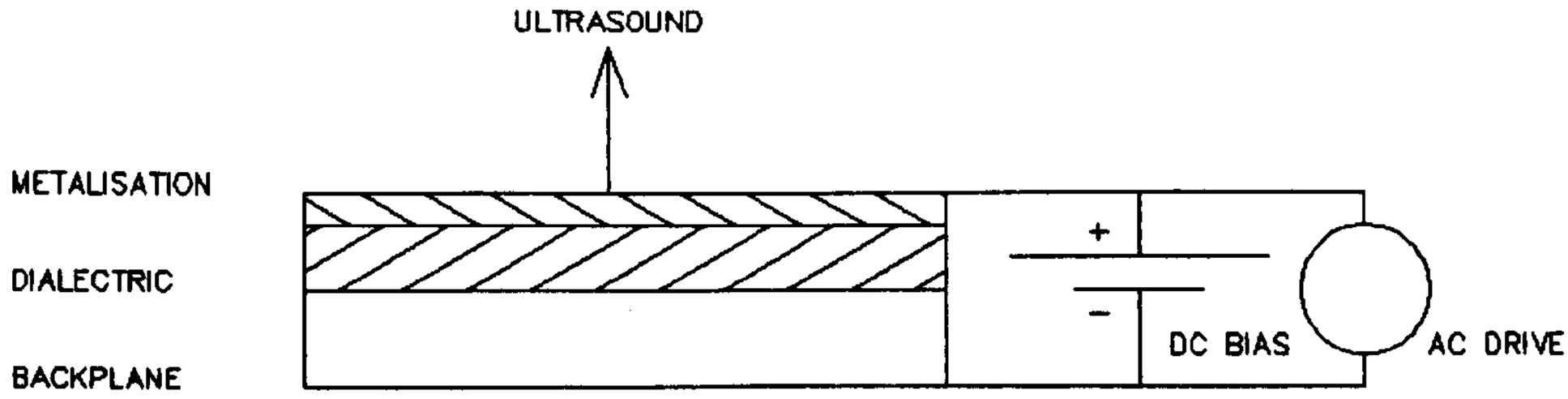

Figure 2: Construction of Electrostatic transducer.

On receive, the transducer behaves like a capacitor with moveable plates.

Due to the bias voltage, an electrical charge Q is developed between the membrane and the backplane. If a sound wave hits the membrane, it vibrates and the distance between it and the fixed backplane will vary.

From the equation for the charge, *Q*, on a capacitor:

$$Q = CV \tag{1}$$

where

C = capacitance.

V = Voltage between plates.

and from the equation for the capacitance C of a capacitor:

$$C = \frac{\epsilon_0 A}{d} \tag{2}$$

where:

A = area of a two plate capacitor.

d = distance between plates.

ϵ_0= permittivity of free space.

if the two equations are combined, an equation relating the voltage on the plates of a capacitor to the distance between the plates is obtained:

$$V = \frac{Qd}{\epsilon_0 A} \tag{3}$$

The voltage across the transducer is thus directly proportional to the distance between the membrane and the backplane, if all other variables remain constant. If the membrane is vibrated by a sound wave, then an alternating voltage will be produced. Since the membrane has a low acoustic impedance, the matching

between an electrostatic transducer and air is much better than for a piezo-electric transducer.

The resonant frequency, bandwidth and sensitivity of electrostatic transducers are governed by a complex interaction between factors such as membrane tension, thickness, and backplane surface finish. These have been investigated in detail by several workers[2,4,5,6,7,8,9,10].

3.2.1.3 Magnetostrictive.

Magnetostrictive transducers are frequently used in ultrasonic cleaning applications and also in ultrasonic drills. They are manufactured from materials such as nickel, cobalt and iron which display the so called magnetostrictive or joule effect. This means that when a bar or rod of one of these materials is placed in a magnetic field, the length will change. The reverse effect which allows magnetostrictive transducers to be used as receivers is known as the Villari effect. A change in the mechanical stress applied to a ferromagnetic rod placed in a magnetic field results in a change in flux density. A simplified diagram of such a transducer is shown in Figure 3

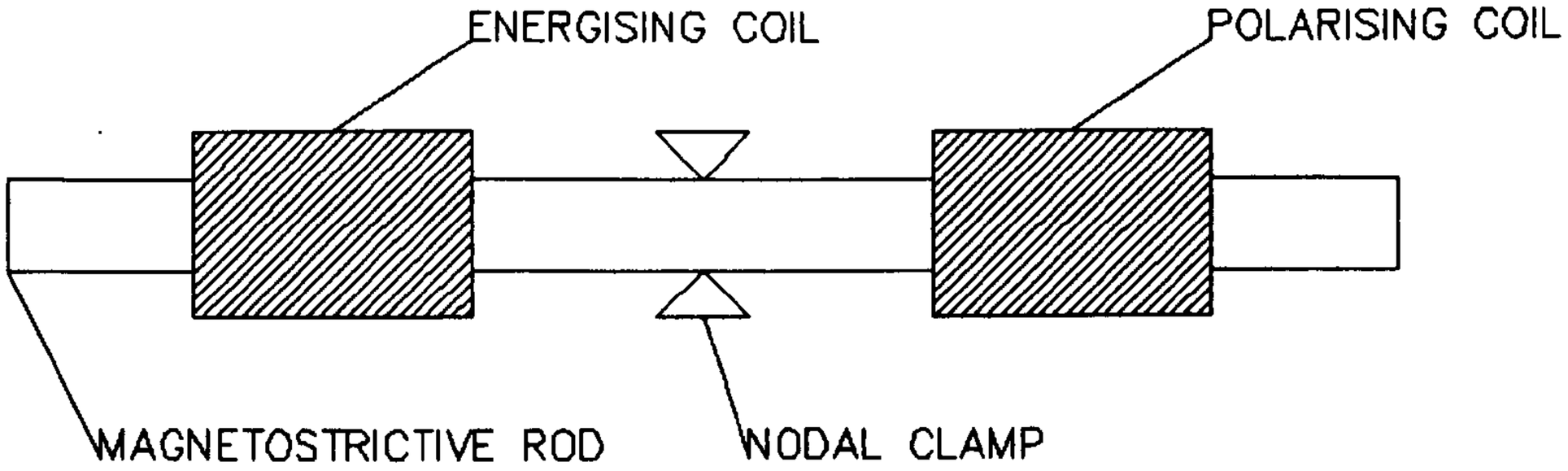

Figure 3: Simplified diagram of magnetostrictive transducer.

Since the value of the strain in the rod is dependent on only the magnitude of the applied magnetic field, and not its sense, a polarising field is required. Without this, the transducer would oscillate at twice the frequency of the applied signal. In the case of an AC signal, the output would have the appearance of an unsmoothed rectified sine wave. The resonant frequency of the device is an inverse function of the length of the bar. The bar is usually nodally clamped to minimise the generation of harmonics.

These devices, like piezo-electric transducers, couple poorly with air and are not used to transmit ultrasound into air.

3.2.2 Escaping gas.

The two most common types of generators using the principle of escaping gas are cavity resonators and wedge resonators. These are both ultrasonic whistles and can be used with both gases and liquids.

3.2.2.1 Cavity resonators.

The two most common cavity resonators are the Galton whistle and the Hartman generator. The Galton whistle consists (see Figure 4) of a cylinder terminated by a moveable piston which forms the end of resonant cavity. The frequency of the sound produced may be adjusted by altering the position of the piston. Gas or fluid is forced, at high speed, through an annular slit in front of the cavity. This causes vortices to be created when the gas strikes the rim of the tube. Where the vortices form sound is produced. The frequency of this sound is adjusted, by varying the gas velocity through the nozzle, until the air in the cavity resonates.

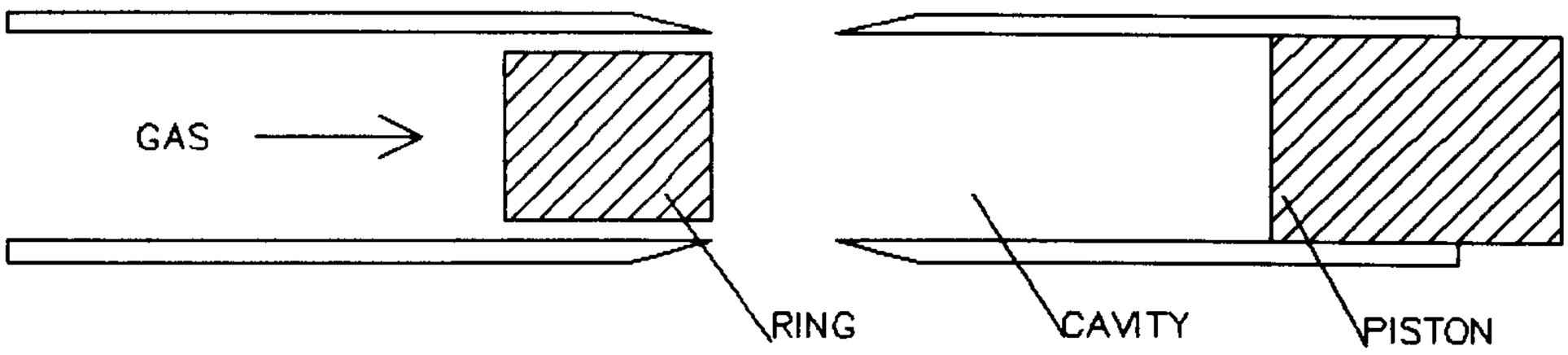

Figure 4: Galton whistle.

The other common type of cavity resonator is the Hartman generator (Figure 5). This is similar to the Galton whistle but a conical nozzle is used instead of an annular slit. The gas exits from the nozzle at supersonic velocity and produces a shock wave that stimulates the cavity.

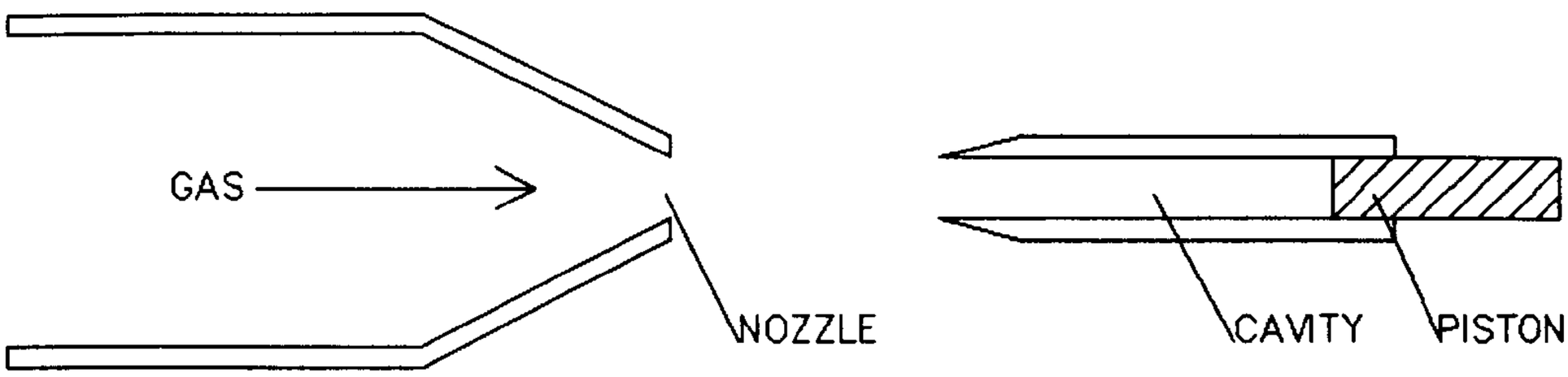

Figure 5: Hartman generator.

Both these types of resonator are capable of producing high power outputs, up to 50W in the case of the Hartman generator, but the maximum output frequency is limited to around 30-40kHz[11]. They do however have the advantage that they will couple well to both air and liquids. Neither the Hartman resonator or Galton's resonator can be used to detect ultrasound.

3.2.2.2 Wedge resonator.

The wedge resonator (Figure 6) consists of a plate with wedge shaped edges which is suspended in a jet of gas produced by a nozzle. The jet sets up vibrations within the plate to generate ultrasound.

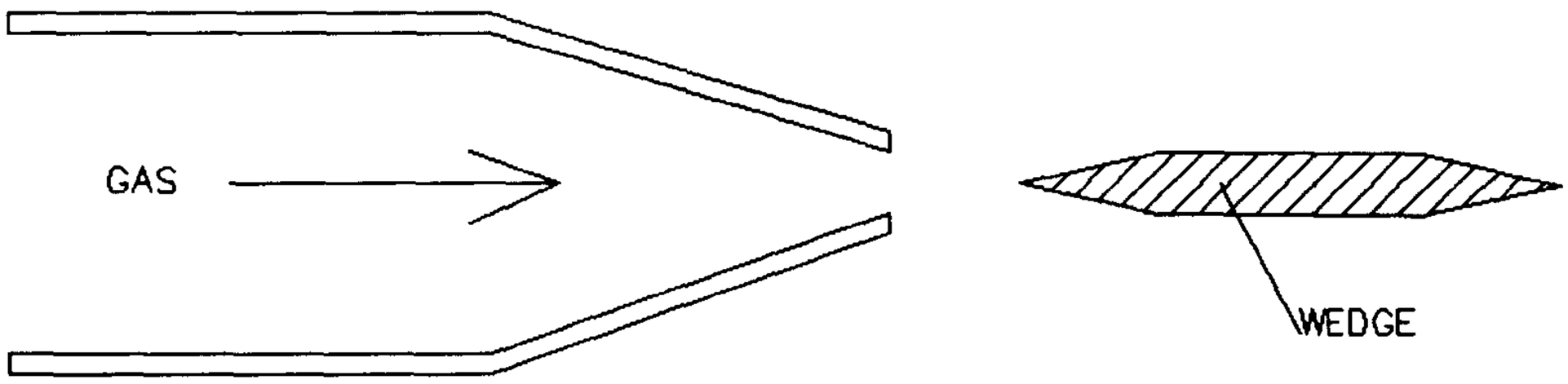

Figure 6: Wedge resonator.

The wedge resonator is capable of high power outputs but the maximum frequency is limited to about 20kHz. This transducer can be used with both liquids and gases but tends to be used with the former. The wedge resonator cannot be used as a detector.

3.2.2.3 Ultrasonic siren.

The ultrasonic siren generally consists of a perforated disk which is rotated over a gas jet (see Figure 7). The normal upper limit for sirens is again 30-40kHz.

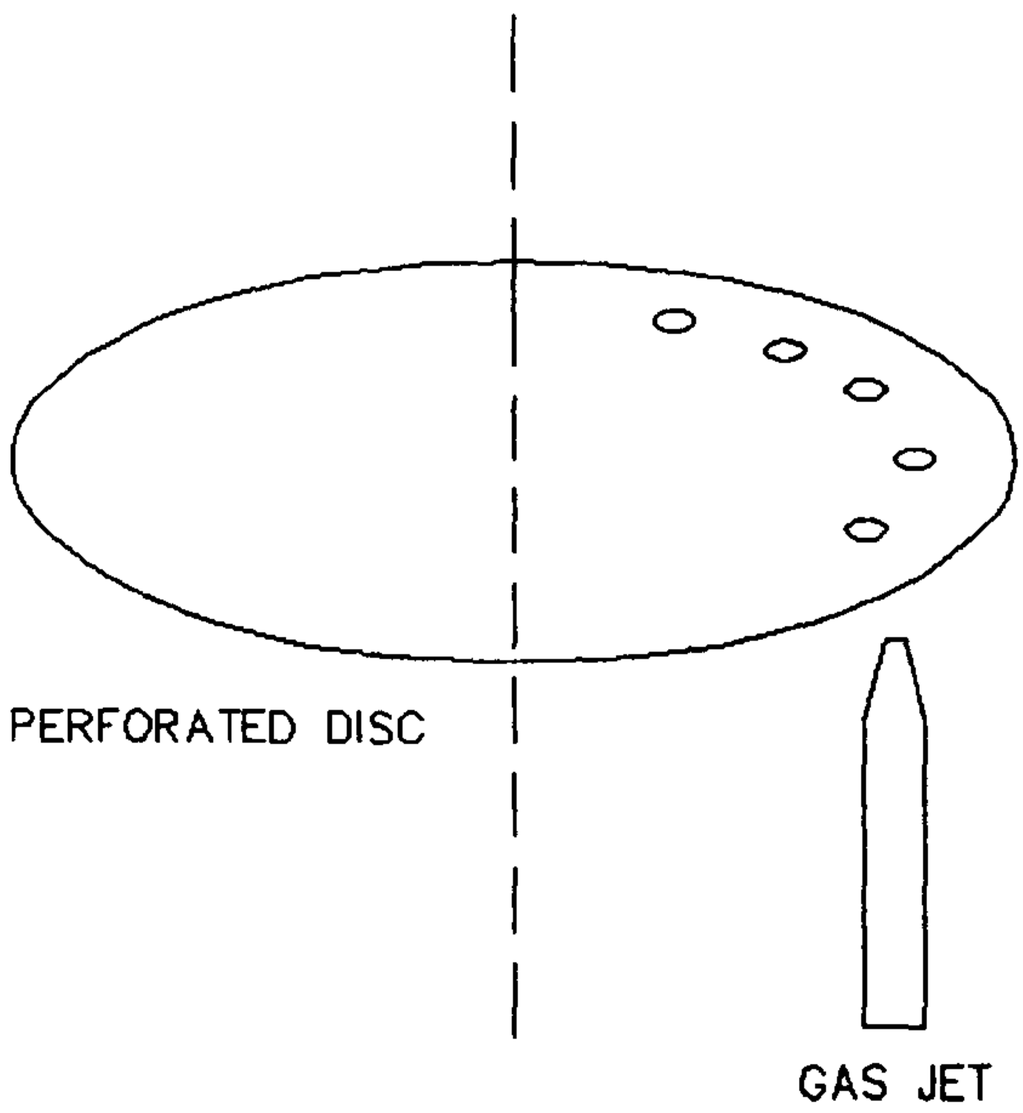

Figure 7: Ultrasonic siren.

3.2.3 Electrical discharge.

The only common type of electrical discharge generator is the spark gap generator.

3.2.3.1 Spark gap generator.

The spark gap generator produces broadband pulses of ultrasound due to periodic temperature changes that take place when a high voltage of a given frequency is discharged across a gap between two electrodes. The spark gap generator can not be used as a receiver but is capable of producing ultrasound at high intensities.

3.3 Transmission of ultrasound through an aperture.

This section provides the fundamental theory behind the transmission of energy through an aperture. Although the analysis given here concentrates on a rectangular aperture with equi-phase equi-amplitude illumination a similar analysis can be performed on any aperture configuration. This analysis is useful since any transducer may be treated as a radiating aperture.

From Huygens principle[12], it can be shown that for any radiating aperture the field intensity is a function of the amplitude and phase distribution across the aperture[13]. When attempts are made to evaluate the intensity at different ranges from the aperture it is found that there is no single approximation that is valid at all ranges. Broadly there are two types of solution, known as the Fresnel or near-field region and the Frauhoffer or far-field region. The two regions are illustrated in Figure 8. In the far field ray from the aperture to the point of observation, or target, are considered to be parallel whilst in the near field region

they are considered to be convergent. In reality far field conditions only exist at infinity.

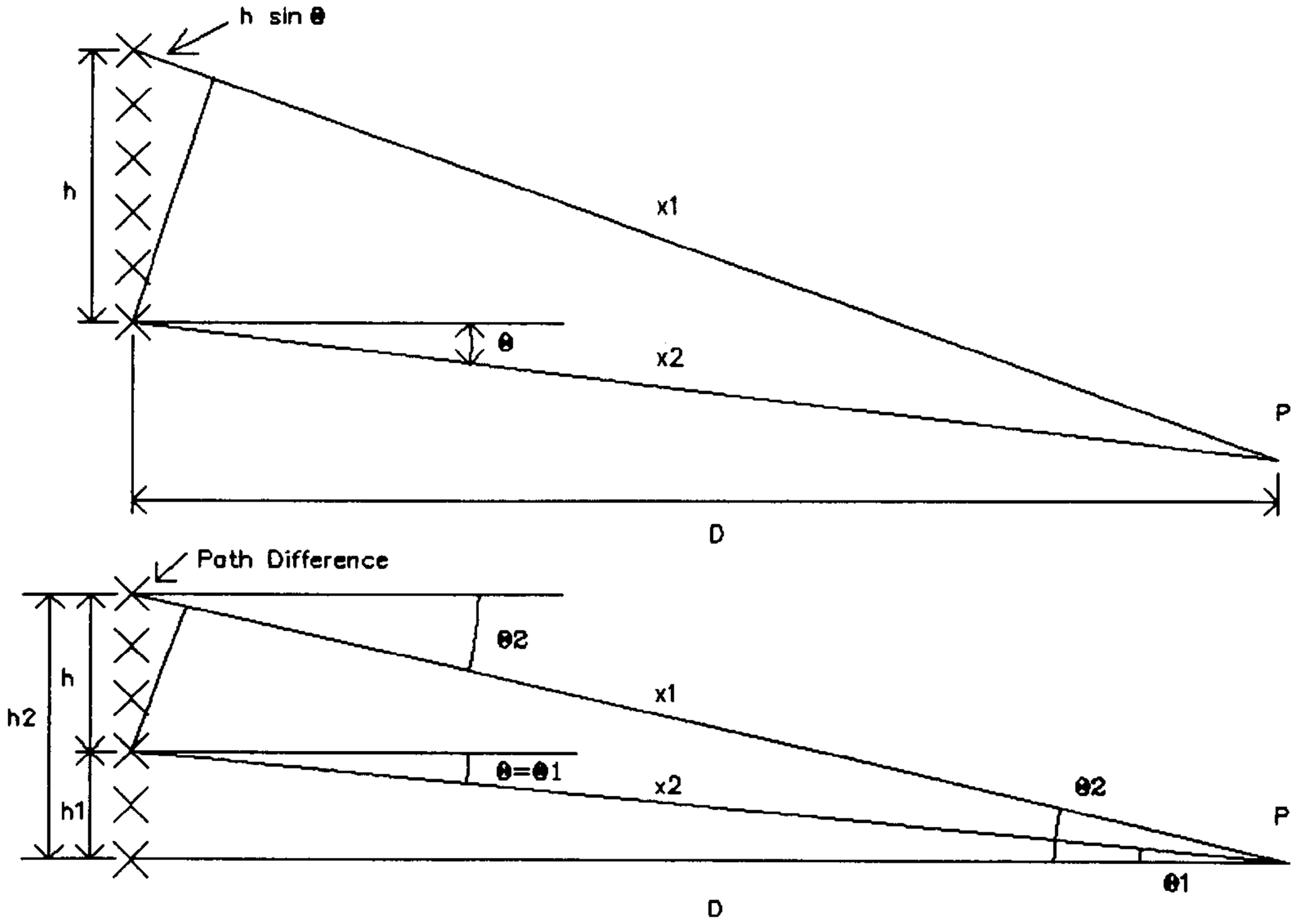

Figure 8: Diagram showing difference between near-field and far-field of an aperture.

The intensity $E(\phi)$ in any direction may be found by considering the aperture as a series of radiating elements and taking the summation of the signals from each of the elements. If the point P is very far away from the aperture then the path difference between the two rays x_1 and x_2 may be treated as being dependent only on $h\sin\theta$. If however P is close to the aperture then the difference between the two angles θ_1 and θ_2 is no longer negligible. It is the distance at which this difference is not negligible that is taken as being the boundary between the near-field and far-field regions. The distance R_f at which the regions intersect is

usually represented by the approximation[13]:

$$R_f = \frac{d^2}{\lambda} \tag{4}$$

A more conservative approximation is sometimes used:

$$R_f = \frac{2d^2}{\lambda} \tag{5}$$

where:

d = size of the aperture.

λ = wavelength.

Separate expressions can be obtained for the field intensity in the two regions.

3.3.1 Far field region.

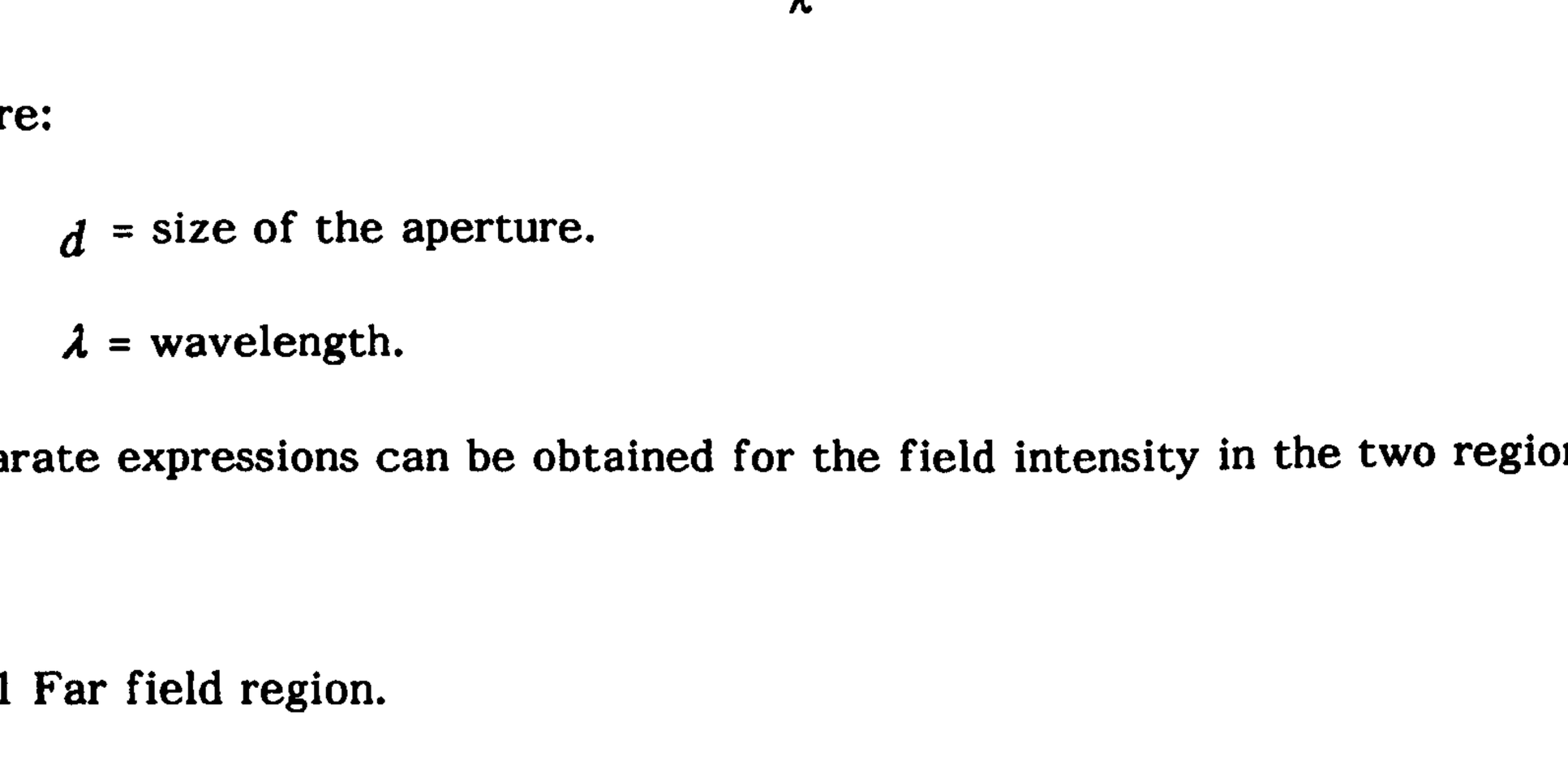

Figure 9: Diagram showing an aperture as a large number of array elements.

As mentioned in 3.3 an aperture may be treated as a series of radiating elements.

The equation for the radiation pattern of an N element array (this is derived in chapter 4) may therefore be used to evaluate the field intensity in the far field. In this case the evaluation is performed for an infinite slit. The variation of amplitude with angle or radiation pattern of an array is:

$$G_a(\theta) = \frac{\sin^2[N\pi(d/\lambda)\sin\theta]}{N^2\sin^2[\pi(d/\lambda)\sin\theta]} \qquad (6)$$

From Figure 9 then letting $d = \Delta x$ gives:

$$G_a(\theta) = \frac{\sin^2[N\Delta x(\pi/\lambda)\sin\theta]}{N^2\sin^2[\Delta x(\pi/\lambda)\sin\theta]} \qquad (7)$$

If N is very large then Δx is very small, and $N.\Delta x = a$ the following approximation can then be made:

$$\sin(\Delta x(\pi/\lambda)\sin\theta) \simeq \Delta x(\pi/\lambda)\sin\theta = \frac{1}{N}a(\pi/\lambda)\sin\theta \qquad (8)$$

The radiation pattern of the aperture thus becomes:

$$G_a(\theta) = \frac{\sin^2\alpha}{\alpha^2} \qquad (9)$$
$$\alpha = a(\pi/\lambda)\sin\theta$$

which is a sinc function. This is shown diagrammatically in Figure 10. This is not the most common method of evaluating the radiation pattern of an aperture but is given as it will be expanded later to demonstrate how the radiation pattern of

an array may be modified.

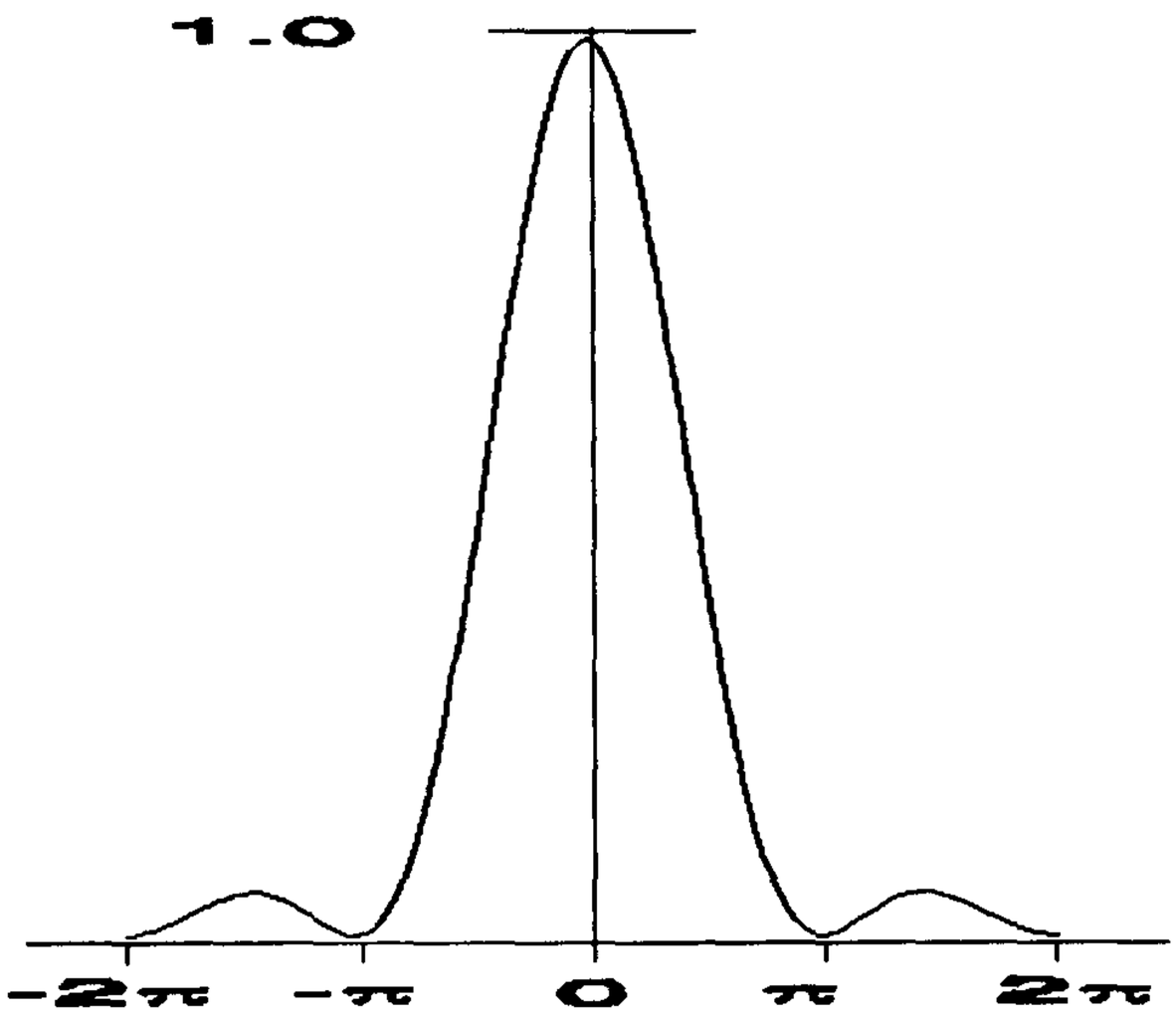

Figure 10: Radiation pattern for rectangular aperture.

The above analysis assumes a rectangular energy distribution across the aperture.

It can be shown that the far field radiation pattern is the Fourier transform of the aperture field distribution[13]. This allows the far-field radiation pattern to be calculated for any amplitude and phase distribution.

The energy distribution of a two dimensional aperture may be evaluated from the Frauhofer diffraction integral[14]. For the rectangular aperture shown in Figure 11 the Frauhofer diffraction integral may be written as:

$$\begin{aligned} E &= A_0 \int_{-a}^{a} \int_{-b}^{b} e^{-jk(px+qy)} dx dy \\ &= A_0 \int_{-a}^{a} e^{-jkpx} dx \int_{-b}^{b} e^{-jkqy} dy \end{aligned} \tag{10}$$

where

$k = 2\pi/\lambda$ (the wave number).

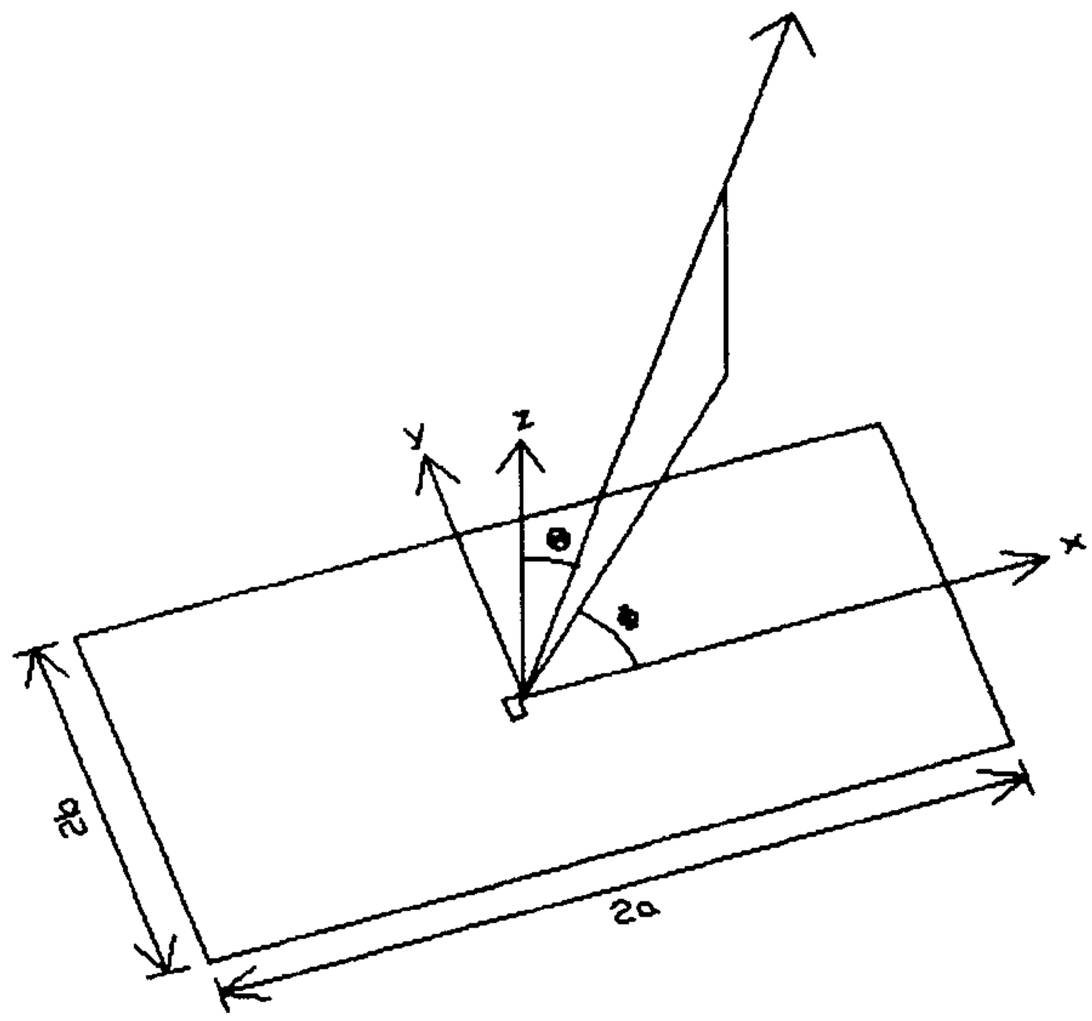

Figure 11: Two dimensional aperture.

If this integral is solved for the rectangular aperture shown then:

$$|E(\theta,\phi)|^2 = A_0 \left(\frac{\sin^2\alpha}{\alpha^2}\right)\left(\frac{\sin^2\beta}{\beta^2}\right) \qquad (11)$$

where

$$\alpha = \frac{\pi a}{\lambda}\sin\theta$$
$$\beta = \frac{\pi b}{\lambda}\sin\phi \qquad (12)$$

3.3.2 Near field region.

In the near-field the analysis is more complex. The near-field situation is shown in Figure 12. Point P is now very close to the array and D is very short.

To calculate the phase difference between two waves emitted at points A and B, the difference in the path lengths must be found;

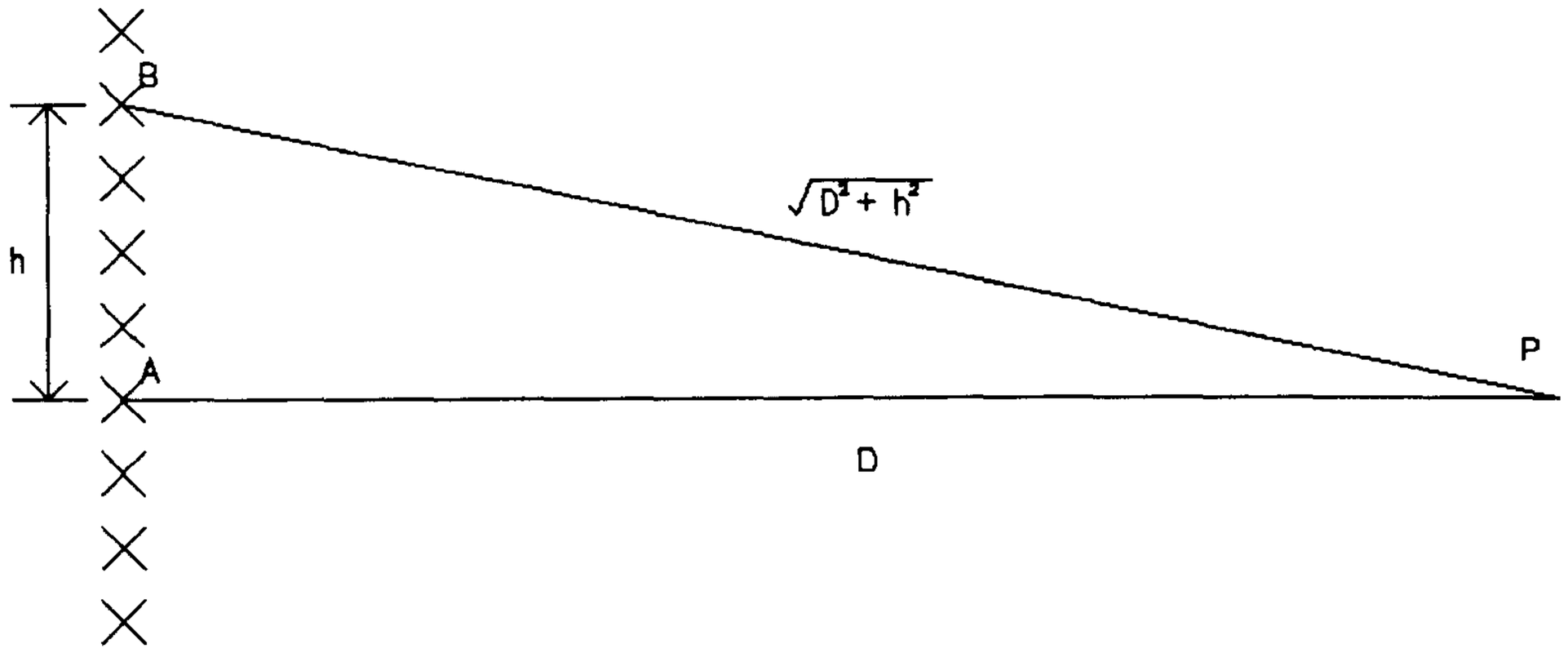

Figure 12: Near-field aperture.

this is:

$$\sqrt{D^2+h^2} \simeq D\left(1+\frac{h^2}{2D^2}\right)-D = \frac{h^2}{2D} \tag{13}$$

The phase difference is thus proportional to h^2, not h as in the far-field. The phase difference is thus:

$$\phi(h) = \frac{2\pi h^2}{\lambda 2D} = \frac{\pi h^2}{\lambda D} \tag{14}$$

To examine the way the intensity changes across the aperture we must examine the way in which the phase changes across the aperture. If this is plotted, it produces a spiral which is called a Cornu spiral (Figure 13). This can not be easily described mathematically but its shape may be examined by plotting two integrals known as the Fresnel integrals[18].

These are:

$$C(s) = \int_0^s \cos\left(\frac{\pi}{2}s^2\right)ds$$
$$S(s) = \int_0^s \sin\left(\frac{\pi}{2}s^2\right)ds \qquad (15)$$

This may then be used to calculate the intensity pattern across the aperture. Choosing the reference point $h = 0$ in Figure 8 to represent the point at which a reference electrical field E_R is emitted, then points below point A in Figure 12 will appear in the third quadrant of Figure 14 and those above appear in the first. The amplitude of the electric field is then calculated by moving the vector E_R around the spiral as shown in Figure 14. The resultant intensity pattern is shown in Figure 15.

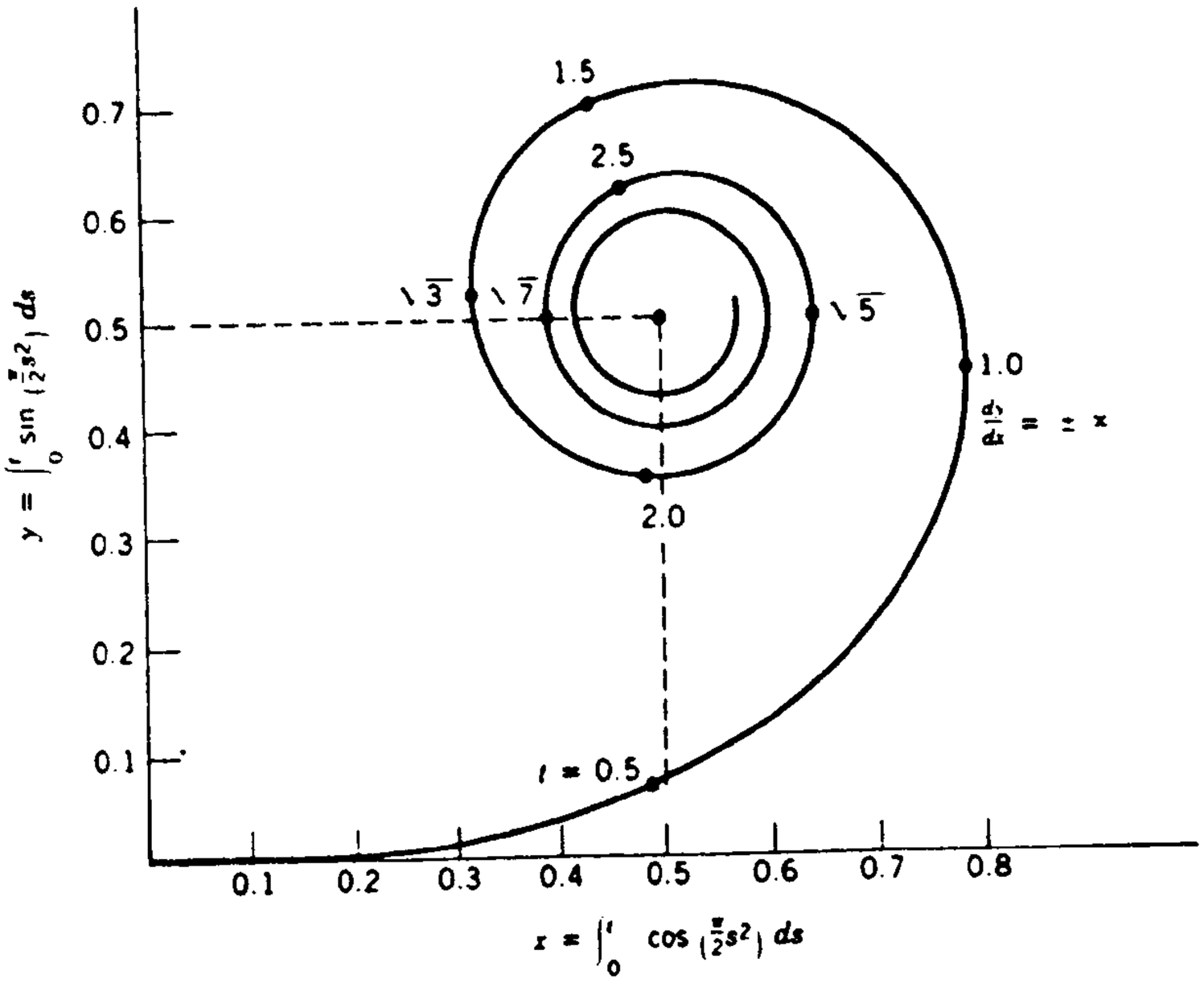

Figure 13: Cornu spiral. (After Hirose[18]).

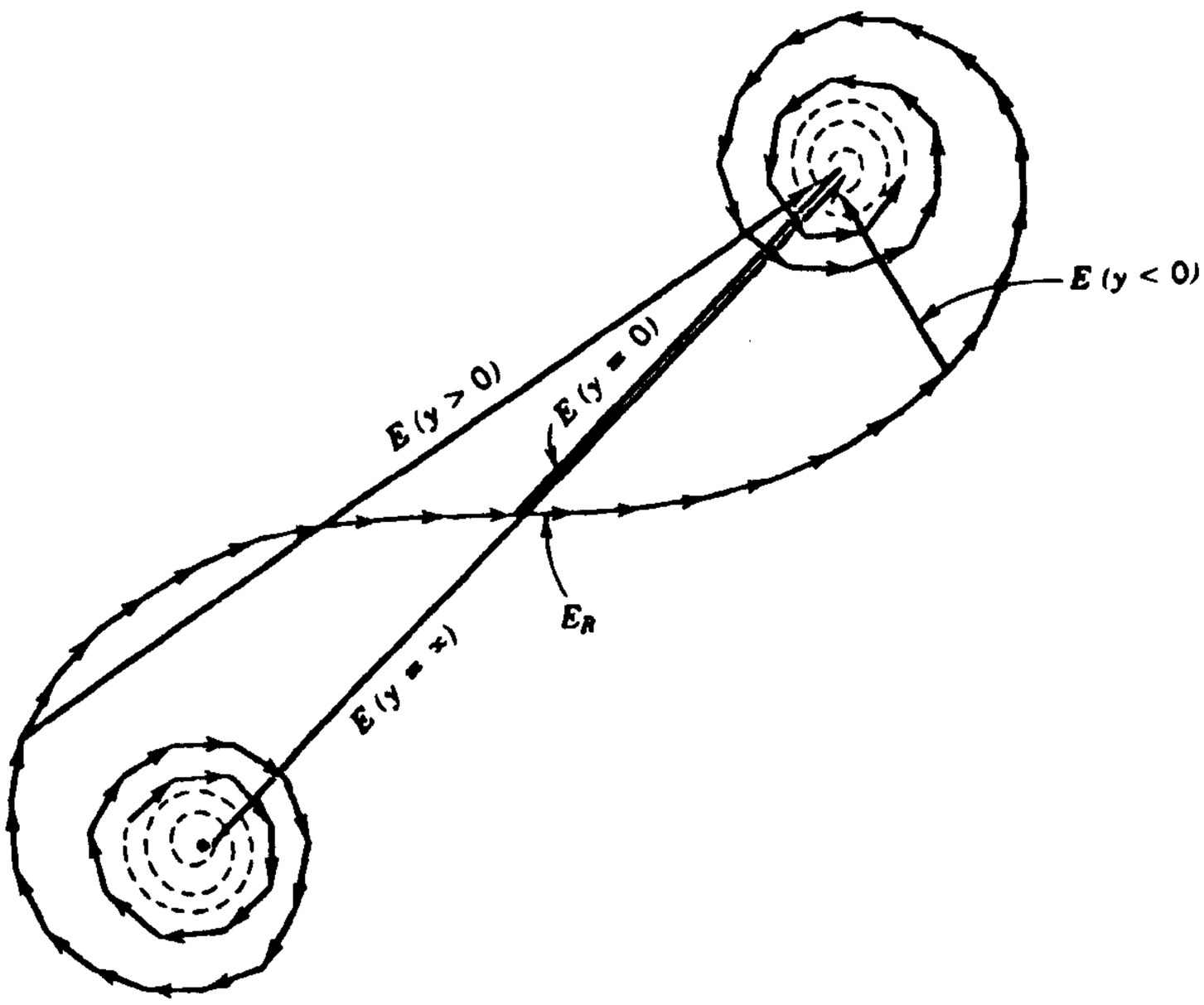

Figure 14: Method of field calculation using Cornu spiral (after Hirose[18]).

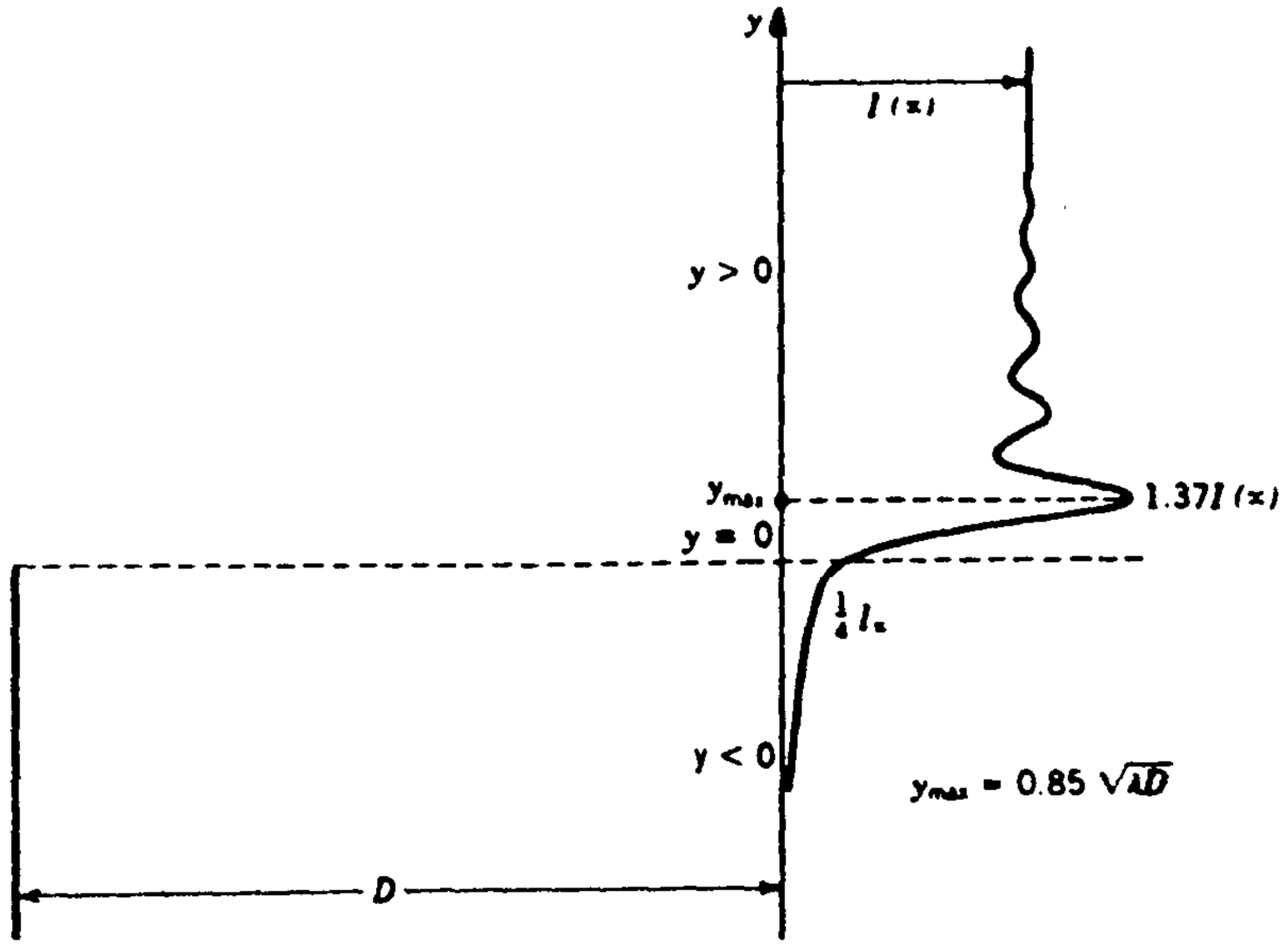

Figure 15: Fresnel intensity pattern constructed from the Cornu spiral. (After Hirose[19]).

3.4 Propagation in air.

3.4.1 Attenuation of ultrasound.

There are three principle mechanisms by which the intensity of a propagating ultrasound wave is reduced. These are absorption, diffraction and scattering.

3.4.1.1. Absorption.

Ultrasound propagating through any material is attenuated due to absorption. In air the level of absorption is governed by temperature and humidity. An expression for the attenuation of ultrasound in air has been defined by Kinsler[15] as:

$$P(x) = P_0 \exp^{-\alpha x} \qquad (16)$$

where:

P_0 = initial pressure amplitude at position x_0.

Px = attenuated pressure amplitude at distance x from x_0.

α = attenuation coefficient.

A classical expression for α in air is[15]:

$$\alpha = \frac{\omega^2}{2\rho c^3}\left[\frac{4\mu}{3} + \frac{(\gamma-1)k}{C_p}\right] \qquad (17)$$

where:

c = speed of sound.

C_p = specific heat at constant temp.

k = coeff of thermal conductivity.

μ = coeff of viscosity.

ρ = density.

ω = angular frequency.

From this it can be shown that attenuation is proportional to the square of frequency. It also increases proportionally with temperature[16]. The effect of humidity is more complex with α increasing in a nonlinear fashion, the change being most marked between 10% and 50% relative humidity[19].

A common measure of the attenuation in air due to absorption is the extinction distance. This is the distance over which the amplitude of a sound wave is reduced to *1/e* of its original value. This can be expressed by the simple relationship[17]

$$extinction\ distance = \frac{5\times10^{13}}{f_2}\ mm \qquad (18)$$

where f is the frequency and air pressure is assumed to be 1 atmosphere.

3.4.1.2. Diffraction.

As already described in 3.3, there are two distinct diffraction processes that occur when ultrasound is produced from a radiating aperture. In the near field, the beam produced by the aperture may be considered to be parallel. Within this region, the amplitude varies considerably across the aperture with a series of fluctuating maximums and minimums decaying towards the centre (see Figure 15). With a small aperture, the amplitude is often considered to be constant with range. In the far field range, the wave front appears divergent from a point at the centre of the aperture. Within this region, the wave amplitude varies in the same way as

radiation from a point source would. This relationship is shown in Figure 16 where θ_b is the beam width. The far field attenuation is a simple inverse square relationship given by:

$$P_d = \frac{P_t}{4\pi R^2} \tag{19}$$

where:

P_t = power transmitted.

P_d = power density at any range R from the source of transmission.

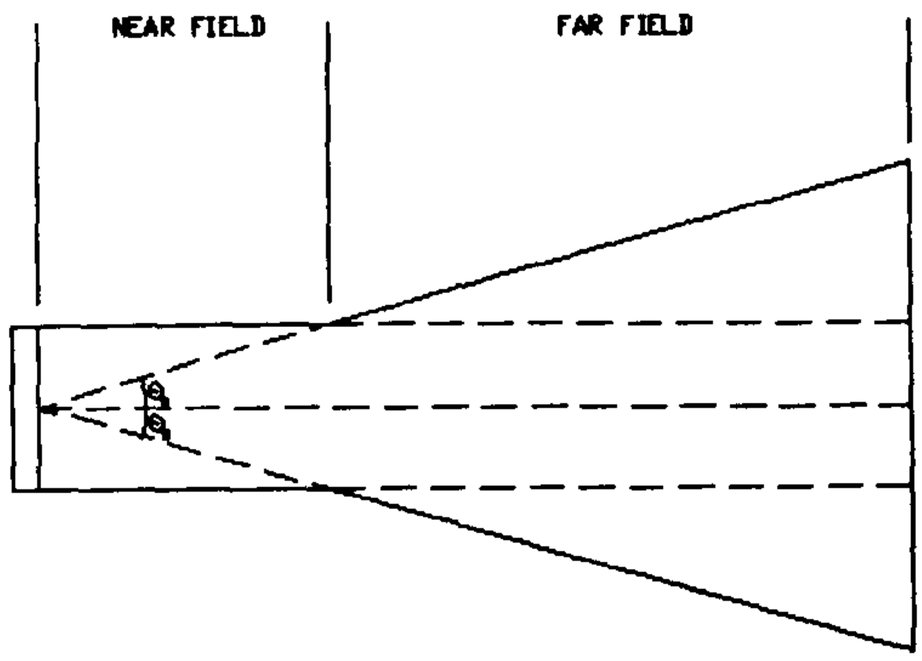

Figure 16: Diagram showing near field and far field beam shapes of simple piston transducer.

3.4.1.3. Scattering:

Scattering of ultrasound occurs when the propagating wave is reflected in all directions by either small particles suspended in liquid and gaseous mediums or structural flaws and discontinuities in solids. If the particles are small relative to the wavelength and reflection is random for each of the particles then this is

called Rayleigh scattering. The attenuation coefficient α for Rayleigh scattering is given by:

$$\alpha = Kf^4D^3 \tag{20}$$

where:

K is a constant for a particular material and is dependent on the relative acoustic impedances of the suspended particles and the propagating medium.

D = mean particle diameter.

f = frequency.

3.4.2 Environmental effects on the velocity of sound in air.

This section describes the effects of temperature, humidity and pressure on the velocity of sound in air.

3.4.2.1. Temperature.

The speed of sound in air is proportional to temperature and can be calculated from[18]:

$$C_w = \sqrt{\frac{\gamma RT}{M_{mol}}} \tag{21}$$

Where:

R = the gas constant (8.3 J/K mol for air).

γ = ratio of specific heats (7/5 for air).

M_{mol} = mass of one mole 0.029 Kg for air).

3.23

T = absolute temperature (°K).

This gives the speed of sound in dry air as 343 m/sec at 20°C.

3.4.2.2. Humidity.

The presence of moisture affects the density of air and thus from (21) it can be seen the velocity of sound is affected. The average molecular weight of damp air is less than that of dry air so M is reduced. The presence of moisture also causes the ratio of specific heats γ to decrease but the decrease in M dominates so the speed of sound increases with increasing humidity[19].

The value of γ for damp air can be calculated from19

$$\gamma = \frac{7+h}{5+h}$$

where

h is the fraction of molecules in the air that are water.

The average molecular wait M_w for damp air can be calculated from:

$$M_W = 29-11h \tag{23}$$

This may be calculated from:

$$h = \frac{0.01RH\ e(t)}{p} \tag{24}$$

where:

RH = Relative humidity (expressed as a percentage).

$e(t)$ = is the vapour pressure of water at temperature t.

p = equals ambient pressure.

By taking the ratio of wet and dry speeds for sound, an expression for the percentage increase in velocity with humidity can be obtained:

$$\%increase = 455.13\sqrt{\frac{\gamma_w}{M_w}} - 100 \qquad (25)$$

3.4.2.3. Pressure:

Except at very high or very low pressures the velocity of sound in a gas remains constant.

3.4.2.4. Turbulence

The presence of turbulence affects the speed of sound in air by introducing differing temperature gradients within the path of the ultrasound. Since such a variation is random, it is difficult to assess this effect quantitivley. Some investigation and measurement of this have been undertaken by Hickling and Marin[17] who found that for a 7.5 m/s air stream, the accuracy of a simple time of flight ranging system varied between ±0.1 mm at a range of between 100 and 220mm.

3.5 Reflection properties.

When a sound wave travelling in one medium meets a boundary with another medium three things may occur; the wave may be completely absorbed, completely reflected, or a mixture of the two may occur (see Figure 17).

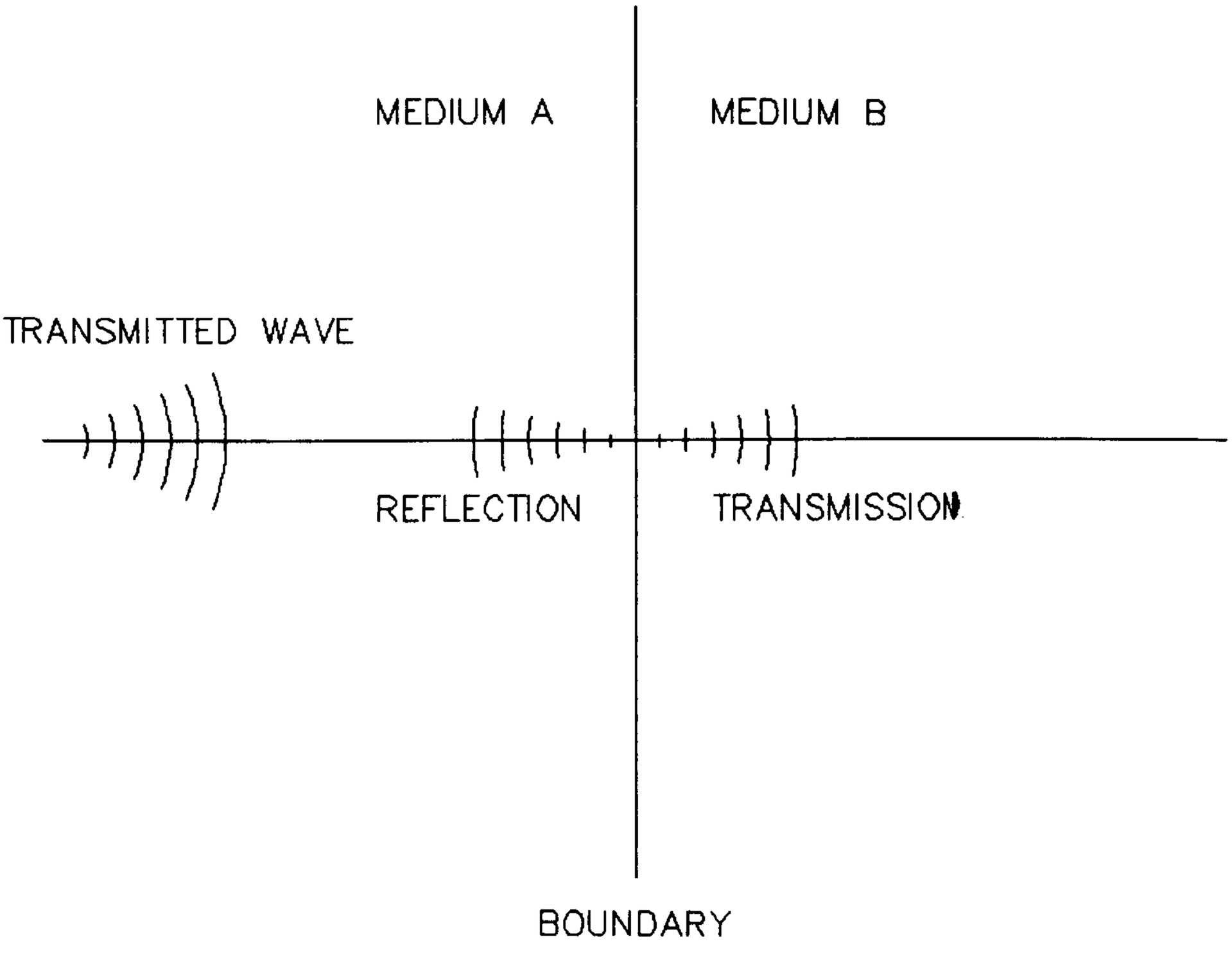

Figure 17: Reflection and absorbtion at the boundary between differing mediums.

The outcome of such an interaction depends on the acoustic impedance of the object relative to that of air. If the impedance of the object is much less or much greater then the sound will be completely reflected. If the impedances are equal then all the sound energy will be transmitted. The amount of absorption or reflection may be calculated by comparing the acoustic impedances of the two mediums. If the amplitude of the incident wave is ξ_1 and the amplitudes of the reflected and transmitted waves are ξ_r and ξ_2 respectively;

then:

$$\zeta_1 = \zeta_r + \zeta_2 \qquad (26)$$

It can be shown that[18]:

$$\zeta_r = \frac{Z_1/Z_2 - 1}{Z_1/Z_2 + 1}\zeta_1 \qquad (27)$$

and

$$\zeta_2 = \frac{2}{1 + Z_2/Z_1}\zeta_1 \qquad (28)$$

where:

Z_1 = Acoustic impedance of medium A.

Z_2 = Acoustic impedance of medium B.

For air Z_a = 430 $Kgm^{-2}s^{-1}$ and for steel $Z_a = 4.7 \times 10^7$ $Kgm^{-2}s^{-1}$

So if a sound wave travelling in air hits a steel object, we have

$\xi_r = 0.99998\xi_1$ and $\xi_2 = 0.00002\xi_1$.

and the sound wave is therefore almost totally reflected.

3.5.1 Types of reflection:

From the calculation in 3.5 it can be seen that the absorbtion of sound in air by a solid object is very small relative to the reflected sound and it will therefore be assumed, in all future analysis, that total reflection occurs. When sound hits a solid object the wave may either be scattered or reflected at an angle equal to the angle of incidence -Figure 18. The type of interaction which occurs is governed by the surface roughness of the object and the wavelength of the incident wave. Surface roughness may be quantified according to the Roughness Average (R_a) of the reflecting surface. The R_a height of the roughness irregularities on a surface is defined as the average value of the departures from its centre line throughout

a prescribed length the centre line being drawn such that the sum of the areas enclosed by the profile and the centre line are equal above and below the centre line[20]. Surfaces with $R_a \ll \lambda$ behave like mirrors and produce specular reflections, while if $R_a \gg \lambda$ the incident wave is scattered. For sound at 100kHz the wavelength is 3.43mm; therefore almost all surfaces behave as mirrors. This can either be an advantage or disadvantage according to the application.

A special case of occurs for an edge when diffraction rather than reflection occurs, see Figure 19, when a diverging cylindrical wavefront is produced.

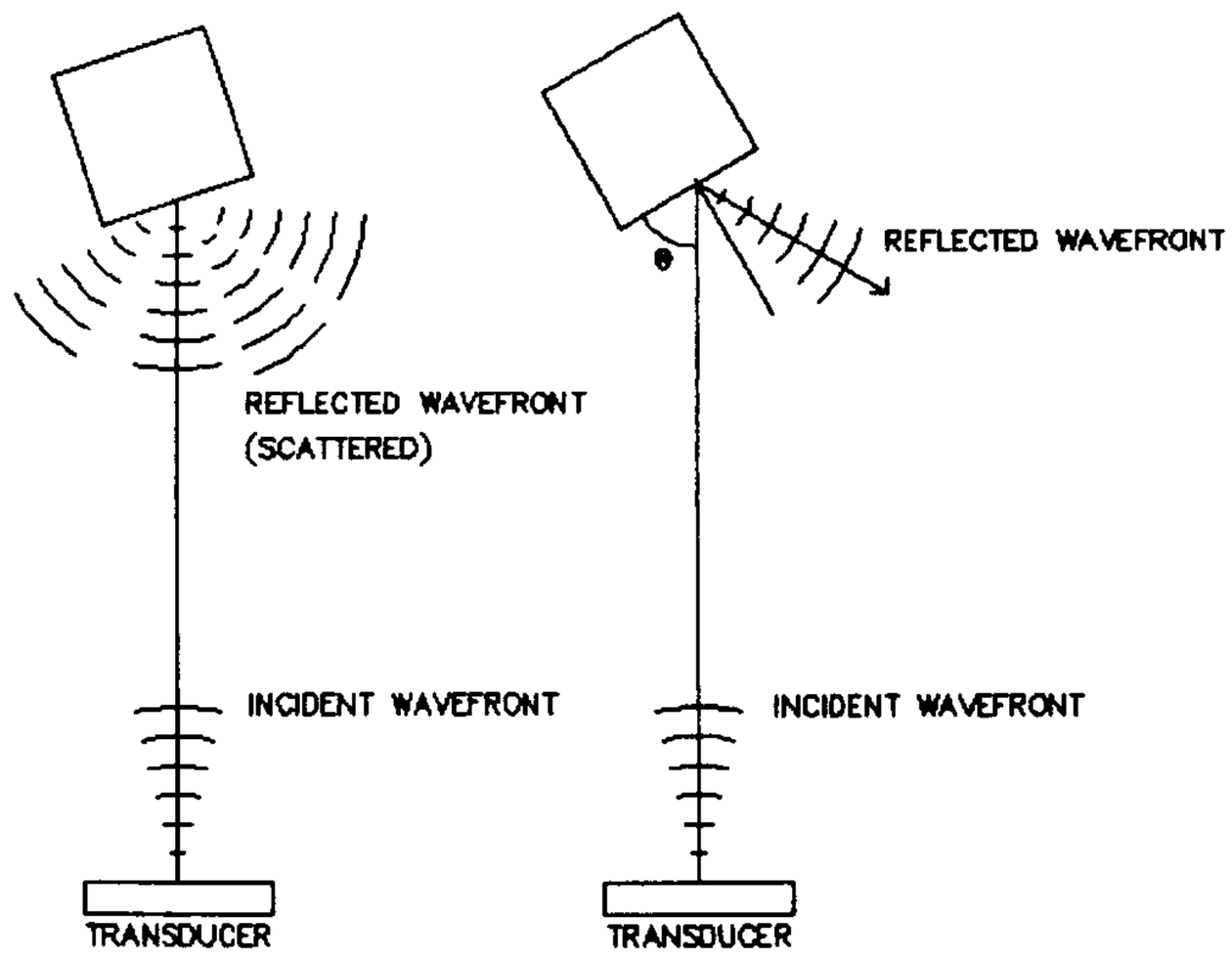

Figure 18: Direct reflection and scattering of sound.

It should also be noted that since a cylindrical (divergent) wavefront is produced the amplitude of the reflection received in any direction is much lower than that received from a specular reflection.

This section has only covered very simple reflection mechanisms. In airborne ultrasonics most of the reflections encountered from an object consist of a complex mixture of specular echoes and diffraction echoes from edges. To

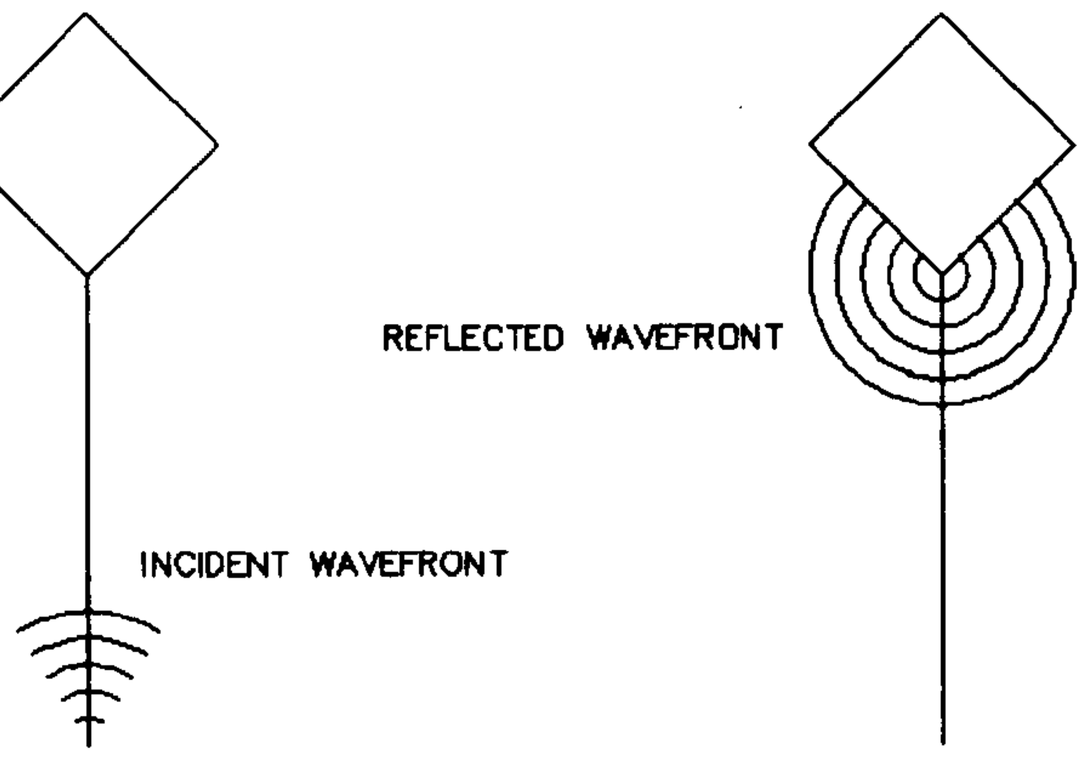

Figure 19: Diffraction effect of wave incident on an edge.

complicate matters further the specular echoes may have undergone multiple reflections. Multiple echoes from corners are not usually a problem since the amplitude is relatively so small that the echo is usually extinct by the time it reaches the sensor. The problem of ambiguous reflections is one of the major difficulties encountered in the use of airborne ultrasound for imaging.

3.6 References.

1. Blitz J. "Ultrasonics Methods and Applications", Butterworth group, 1971.

2. W.S.H. Munro, "Ultrasonic phased arrays for use in imaging and automatic vehicle guidance", Phd thesis, University of Nottingham, 1990.

3. Kuri-Yakub B. T., Kim J. H., Chou C., Parent P., Kino G. S. "A New Design For Air Transducers", Proceedings IEEE Ultrasonics Symposium, 1988 pp503-506.

4. H. Sell, "Eine neue methode zur umwandlung mechaniser schwingungenin electrische und umgekehrt", Z. techn. Phys. Vol. 18, No. 3, 1937.

5. W. Kuhl, G. R. Schrodder and F. K. Schrodder, "Condenser transmitters and microphones with solid dielectric for airborne ultrasonics", Acoustica, Vol. 4, No. 5, 1954, pp519-532.

6. K. Matsuzawa, "Condenser microphones with plastic diaphragms for airborne ultrasonics", J. Phys. Soc. Japan, Vol. 12, No. 12, 1958, pp1525-1543.

7. H. J. Carr, W.S.H. Munro, M. Rafiq and C. Wykes, "Developments in capacitive transducers", Nondestructive test, 1992, Vol. 10, pp3-13.

8. W.S.H. Munro and C. Wykes, "Arrays for airborne ultrasound", Accepted for publication Ultrasonics, 1992.

9. L. Kay, "Airborne ultrasonic imaging of a robot workspace", Sensor review, 1985, pp8-12.

10. J. P. Huissoon and D. M. Moziar, "Curved Ultrasonic Array Transducer for AGV Applications", Ultrasonics, Vol. 27, July, 1989, pp221-225.

11. A. P. Cracknell, "Ultrasonics", Wykeham publications, 1980.

12. B. D. Steinberg, "Principles of Aperture and Array System Design", J. Wiley & Sons, 1976.

13. M. I. Skolnik, "Introduction to Radar Systems", McGraw Hill International, 1981.

14. M. Born, E. Wolf, "Principles of Optics", Pergamon press, 1980.

15. L. E. Kinsler, A. R. Frey, A. B. Coppens and J. V. Sanders, "Fundamentals of Acoustics", John Wiley & Sons, 1982.

16. C. M. Harris, "Absorbtion of sound in air versus humidity and temperature",J. Acoust. Soc. of America, Vol. 40, No. 1, 1966, pp148-159.

17. R. Hickling and S. P. Marin, "The use of ultrasonics for gauging and proximity sensing in air", J. Acoust. Soc. Am. No. 79, April, 1986, pp1150-1160.

18. A. Hirose and K. Lonngren, "Introduction to wave phenomena", John Wiley and Sons, 1985.

19. D. A. Bohn, "Environmental Effects on the Speed of Sound", J. Audio Eng. Soc., Vol. 36, No. 4, April 1988, pp223-231.

20. Talysurf operating manual, Taylor Hobson, Leicester.

CHAPTER 4

TARGET LOCATION METHODS

4.1 Introduction

Chapter 4 provides an introduction to the most common methods of extracting positional information using the transmission and reflection of energy. Most of these methods are applicable both to sound waves and electromagnetic waves. Section 4.2 covers three basic methods of range measurement and section 4.3 covers the determination of bearing by both mechanical and electrical methods. Sections 4.3.2 and 4.3.4 cover the theory behind arrays and beam steering while section 4.3.5 describes a digital implementation of the beam steering process. The resolutions obtainable with arrays are analyzed in section 4.4. Section 4.5 introduces a new approach to digital beam forming. The chapter is summarised in section 4.6.

4.2 Range Measurement

The simplest method of range measurement is to measure the time it takes for energy to travel to an object and be reflected back to a receiver; this is called time of flight (TOF) ranging. The methods described in this chapter all rely on this basic principle of time measurement.

4.2.1 Pulse echo.

A single pulse, or a group of pulses, of energy is transmitted and the time taken for an echo to be returned by an object in the path of the pulse is measured. It can be seen from figure 1 that if the speed of propagation for the wave within the medium in which the object lies is known, then the range can be calculated

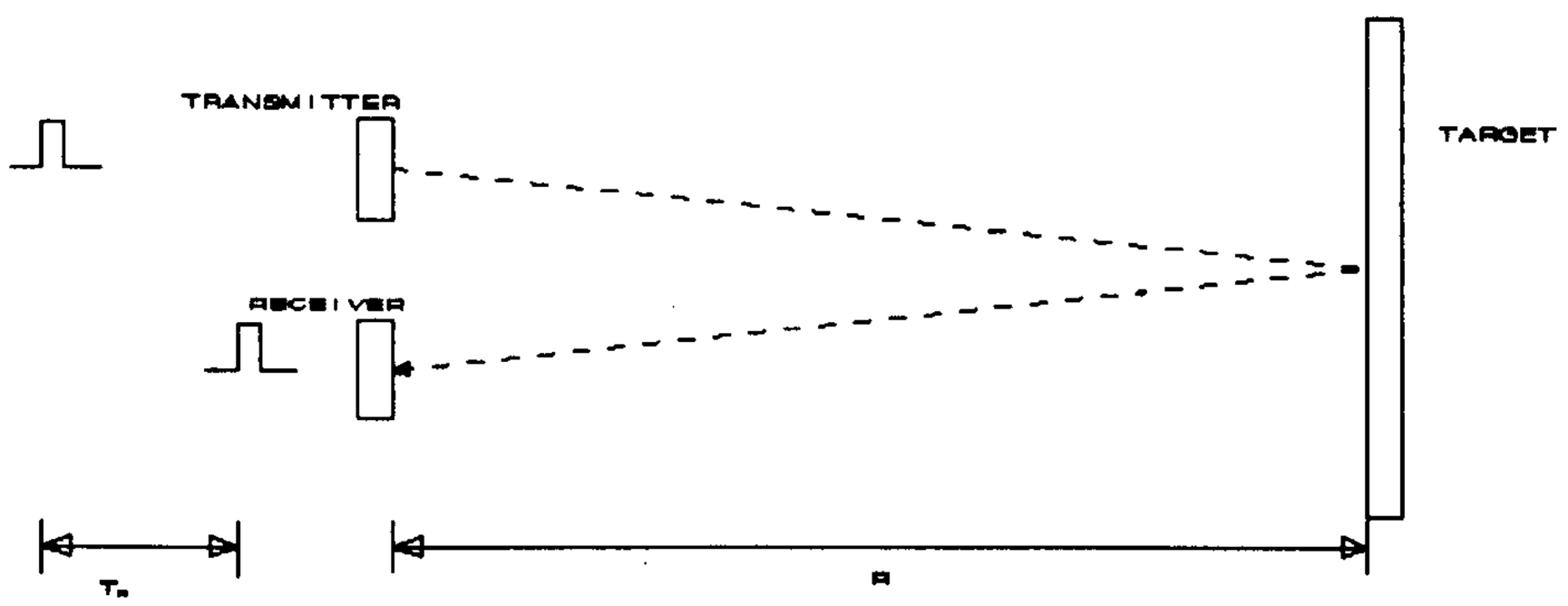

Figure 1 Pulse echo range measurement principle.

from:

$$R = \frac{CT_R}{2} \tag{1}$$

where:

R = Range.

C = speed of propagation.

T_R = time taken for pulse to travel to and return from target.

This method is used both in conventional radar and sonar systems. It is also the method used in the 'Polaroid Ultrasonic Ranging System'.

4.2.2 Frequency modulated continuous wave (FMCW)

Here energy is transmitted continuously but the frequency of the radiation is varied in a known way, usually in the form of a ramp or 'chirp'. The range of a

target can be obtained by comparing the frequency of the received signal with that of the signal being transmitted at the instant of reception, (see figure 2).

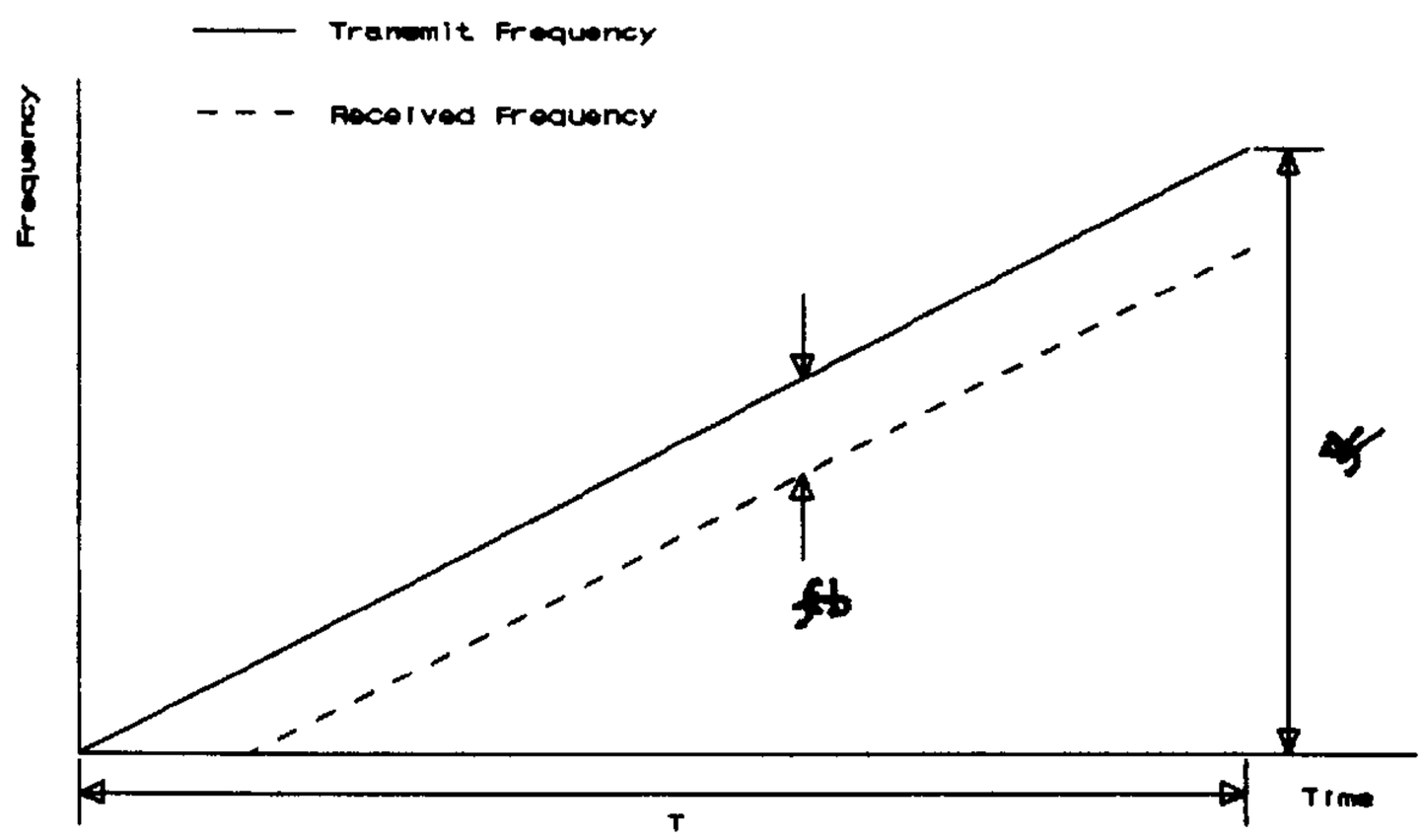

Figure 2 Frequency time relationship of transmitted and received signals in FMCW range measurement.

The range may be calculated from:

$$R = \frac{(f_b/f_0)C}{2} \tag{2}$$

$$f_o = \frac{\Delta f}{T} \tag{3}$$

where:

R = range.

C = velocity of propagation.

f_b = frequency difference.

f_0 = rate of frequency change.

Δf = change in frequency.

T = time.

This method is used both in conventional radar and sonar systems and has also been applied to airborne ultrasonics by Kay[1] for imaging and by Faridian et al[2] in acoustic microscopy.

4.2.3 Pseudo random binary coding

This is a relatively new system which has only become feasible with the development of cheap high speed digital electronics. Here the transmitted pulse is modulated with a binary code that takes so long to repeat as to appear almost random. (Figure 3) If the position within the code of the received signal is known, then by calculating the time at which that section was last transmitted, range data may then be extracted in the same way as in the previous two methods. This ranging method has been used in an ultrasonic level measurement system by Mehrdadi et al[3,4].

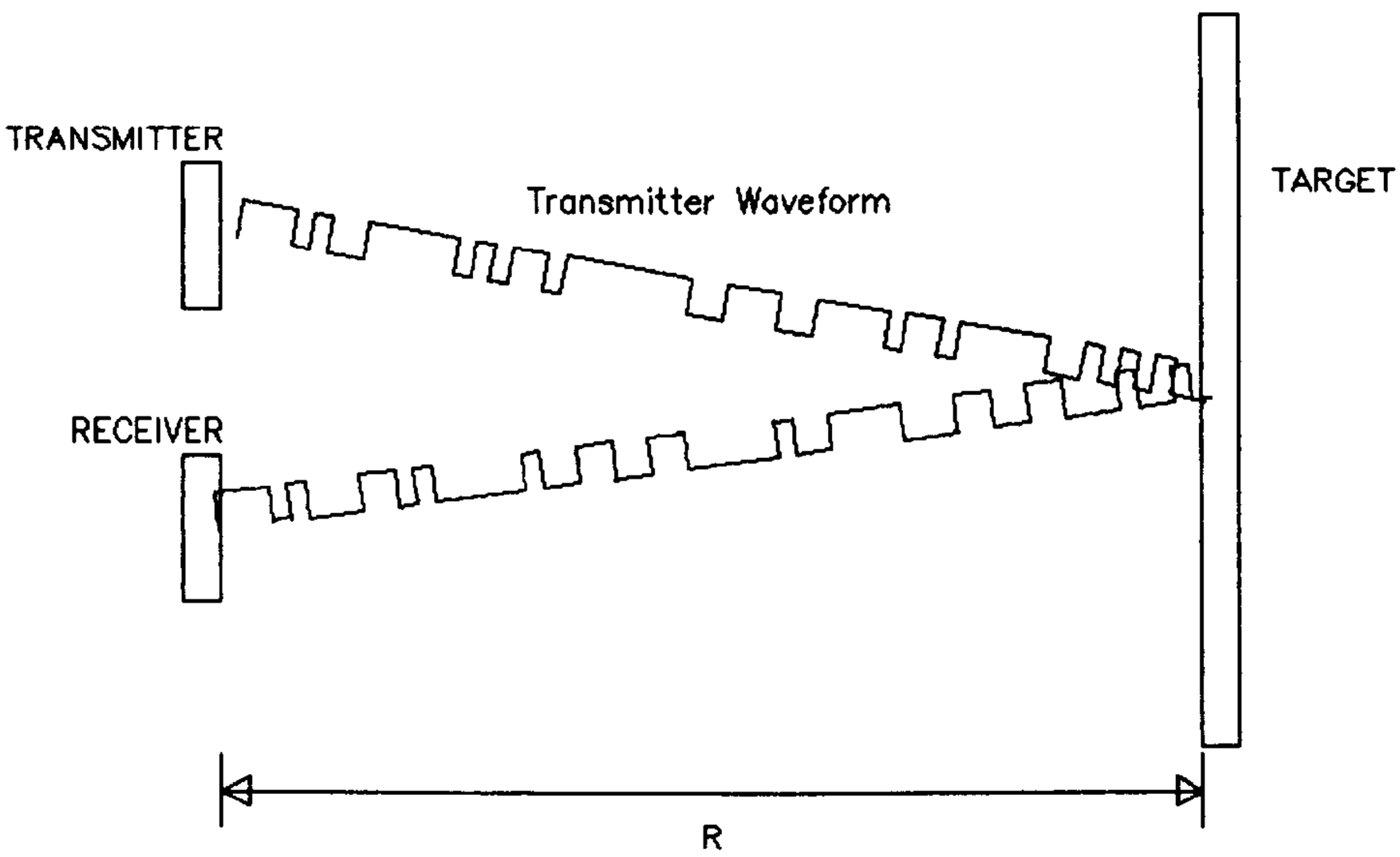

Figure 3 Use of pseudo random binary code method to measure range.

4.3 Bearing measurement

With a single transducer ranging system, the bearing or angular position of the target cannot be found except in so far as the target lies within the transmitter and receiver beam widths. This may be anything up to 360° for an isotropic receiver and transmitter. If bearing is to be measured, then more than one receiving element or a moveable single receiver or transmitter with a narrow beam width must be used.

4.3.1 Mechanical methods

Bearing may be measured by moving the transmitter and or receiver mechanically. Providing the beam widths are relatively narrow the bearing of targets can be obtained to a reasonable degree of accuracy.

The use of a mechanical scanning system is widespread in radar[5] but with the advent of faster and more efficient signal processing systems, most modern radars now employ phased array methods, (section 4.3.2). This is especially so in 3 dimensional radars where it is normal to scan mechanically in bearing and electronically in elevation. Mechanical scanning in airborne ultrasonics has been used by Bull[6] et al, and other workers[7], but has been limited by the only available commercial sensor, which works well in air, being the Polaroid[8]. Other types of sensors are available but they couple poorly with air, these problems have already been discussed in chapter 3. The Polaroid transducer has a beam width of 30° and so gives poor angular resolution. It appears that most workers have only used this transducer because of the lack of availability of a suitable alternative.

4.3.2 Non-mechanical Methods

To obtain bearing information without mechanical rotation more than one receiving or transmitting element must be used. These elements are arranged in an array with an arbitrary spacing between each. If the spacing between elements is equal and they are arranged in a straight line they are usually called linear arrays and if the spacing is unequal they are referred to as sparse arrays. The elements may be arranged in one or two dimensions or any arbitrary position relative to each other. The application of linear arrays only will be described in this section.

The shape of the radiation pattern of an array may then be controlled by varying both the phase and amplitude response of each element[5]. This process is often called beam forming and is best summed up by Curtis[9] who states that: "In its simplest form beam forming can be considered as the process of combining the outputs from a number of omnidirectional transducer elements, arranged in an array of arbitrary geometry, so as to enhance signals from some defined spatial location while suppressing those from other sources".

4.3.3 Conventional array beam forming.

From the principle of reciprocity, which states that the behaviour of a transmitting system will be the same when it is used as a receiver, the operation of an array will be identical if it is transmitting or receiving. In the following calculations, far field conditions are assumed and no allowance has been made for mutual coupling between elements.

A typical linear array is shown in Figure 4. Any array can be considered as

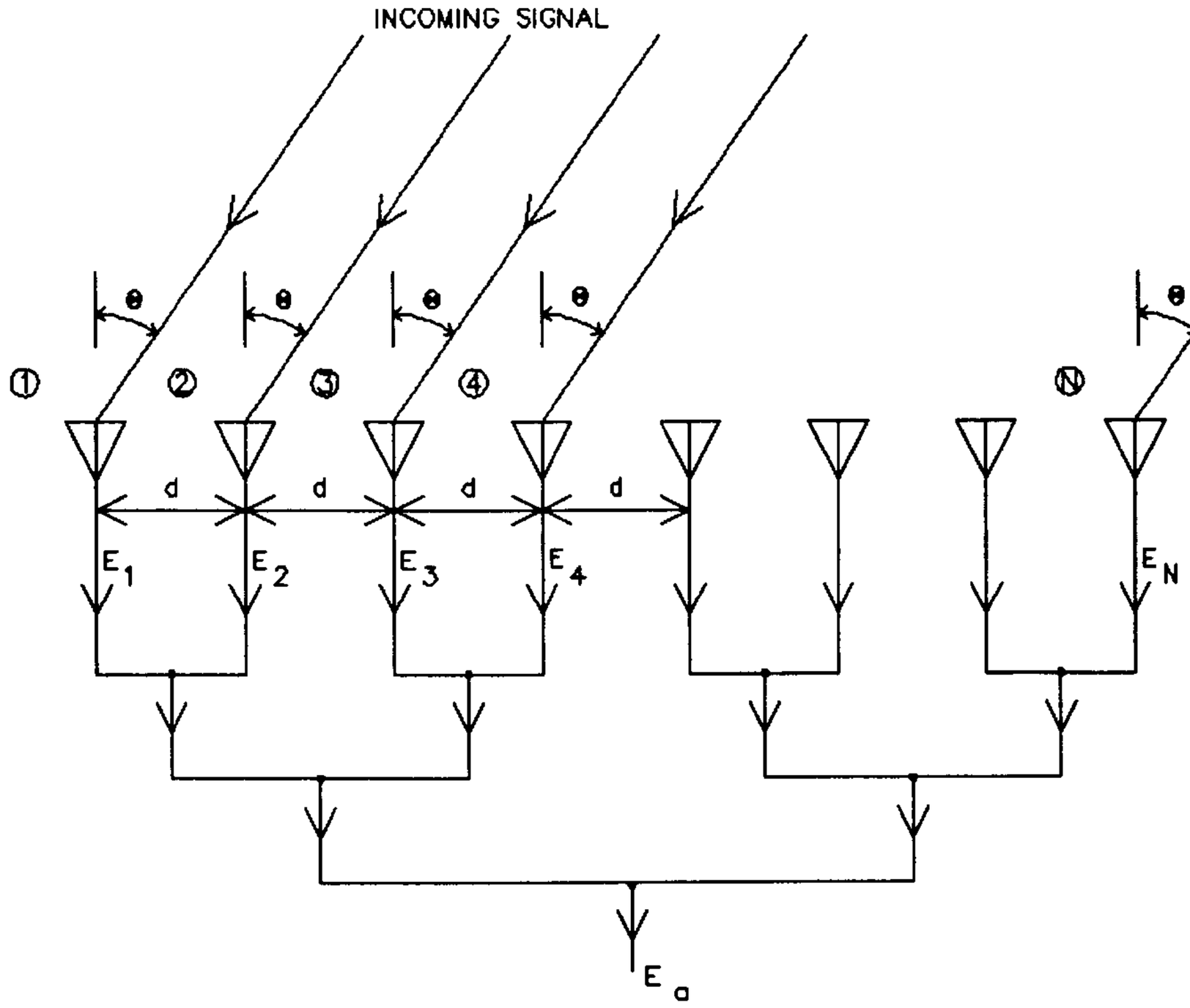

Figure 4 N element linear array.

a series of isotropic elements, the outputs of all the elements $E_1..E_N$ are summed to give the output E_a. If E_1 one is taken as the reference element with zero phase, then from Figure 5 it can be seen that the phase difference ψ between two

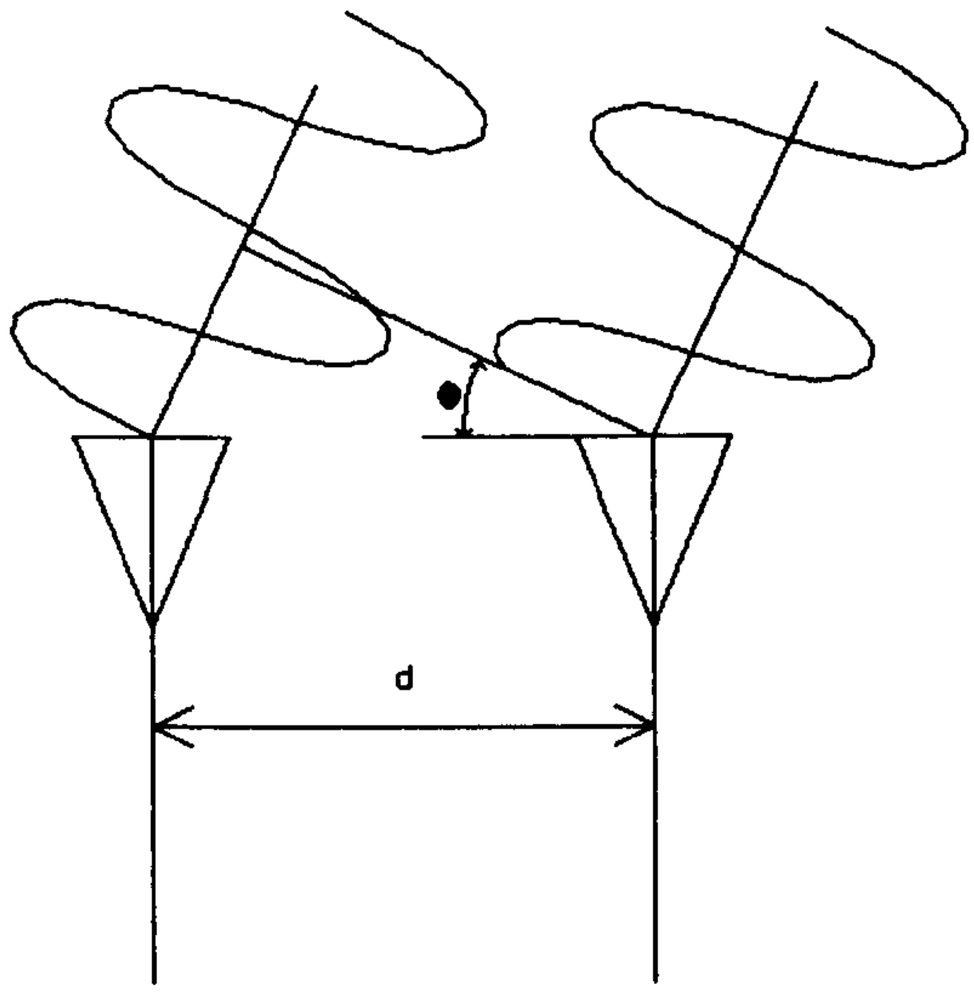

Figure 5 Relative phase difference between elements.

elements of a signal arriving at angle θ is given by:

$$\psi = 2\pi(d/\lambda)\sin\theta \tag{4}$$

where:

d = distance between array elements.

If the outputs of all the elements are summed with equal amplitude and phase weighting, then the output E_a of the whole array is given by:

$$E_a = \sin\omega t + \sin(\omega t+\psi),\ldots \sin(\omega t+(N-1)\psi) \tag{5}$$

where

ω = angular frequency of the received signal.

The sum can also be written as:

$$E_a = \sin\left[\omega t+(N-1)\frac{\psi}{2}\right]\frac{\sin(N\psi/2)}{\sin(\psi/2)} \tag{6}$$

The first factor is a sine wave of frequency ω with a phase shift of $(N-1)\psi/2$. The second term represents an amplitude factor of the form $\sin(N\psi/2)/\sin(\psi/2)$. The field amplitude pattern of the array is the obtained by calculating the magnitude of this equation. This may be written in terms of θ as:

$$|E_a(\theta)| = \left|\frac{\sin[N\pi(d/\lambda)\sin\theta]}{\sin\pi(d/\lambda)\sin\theta]}\right| \tag{7}$$

This equation has nulls when the numerator is zero. These occur when

$$N\pi(d/\lambda)\sin\theta = 0 \tag{8}$$

which happens when $\theta = 0, \pm\pi, \pm2\pi,\ldots,\pm n\pi$. The denominator however is also zero when this occurs. This implies that the field is indeterminate at these points but

by using L'Hopitals rule the maximum field can be shown to occur when $\sin\theta = \pm n\lambda/d$. L'Hopitals rule states that:

$$\lim_{x\to 0}\left[\frac{f(x)}{g(x)}\right] = \lim_{x\to 0}\left[\frac{f'(x)}{g'(x)}\right] \tag{9}$$

These maxima all have the same value and are equal to N. The main lobe of the radiation pattern occurs when $\sin\theta = 0$; the other maxima in the radiation pattern are referred to as grating lobes. These are undesirable in most applications, but they can be avoided if the separation between array elements is a half wavelength or less, since for grating lobes to appear in real space it wouldrequire $\sin\theta > 1$.

An antenna consisting of isotropic elements will have an identical radiation pattern both in front of and behind the array. To avoid ambiguities caused by the presence of two main lobes one half of the array is blanked off. The radiation pattern $G_a(\theta)$ is equal to the normalized square of the amplitude:

$$G_a(\theta) = \frac{|E_a|^2}{N^2} = \frac{\sin^2[N\pi(d/\lambda)\sin\theta}{N^2\sin^2[\pi(d/\lambda)\sin\theta} \tag{10}$$

4.3.4 Beam steering

The beam of an antenna array may be steered electrically by varying the phases of the signals applied to each element.

If the same phase is applied to each element, then the relative difference between elements will be zero and the beam will be at angle $\theta_0 = 0$ (normal to the centre of the array). The beam direction will change if the relative phases

differences are not zero. The direction of the main beam is angle θ when the phase difference $\phi = 2\pi(d/\lambda)\sin\theta$. The phase at each element is thus $\phi_c + m\phi$ where $m = 0,1,2,\ldots(N-1)$ and ϕ_c is any arbitrary phase applied to each element. The normalised radiation pattern when the inter element phase difference is ϕ is given by:

$$G(\theta) = \frac{\sin^2[N\pi(d/\lambda)(\sin\theta - \sin\theta_0)]}{N^2\sin^2[\pi(d/\lambda)(\sin\theta - \sin\theta_0)]} \qquad (11)$$

The maximum occurs when $\sin\theta = \sin\theta_0$.

This equation in effect states that if variable phase shifters are connected to the array elements then the beam may be made to point in any direction. By a similar analysis to that given in section 4.3.2 it can be shown that to avoid grating lobes the element separation must be less than 0.5λ.

4.3.5 Digital beam forming.

The beam steering system described in 4.3.4 has traditionally been implemented by the inclusion of analogue attenuators and phase shifters in the feeds to each element. These are then used during transmit and/or receive to produce the desired radiation pattern. This has several disadvantages; the complexity of the hardware is greatly increased, it is difficult to match precisely the phase and amplitude response of the attenuators and phase shifters between channels and complex control systems are necessary. These problems can be overcome by digitising the received signals at the receiver and then forming the beams either

by the use of specialised digital circuitry or with a computer.

This processing may be performed in either the frequency domain or the time domain. The basics of these methods only are described here and there are many variations on the theme; further details are given in reffs[9,10,11].

4.3.5.1 Time domain processing

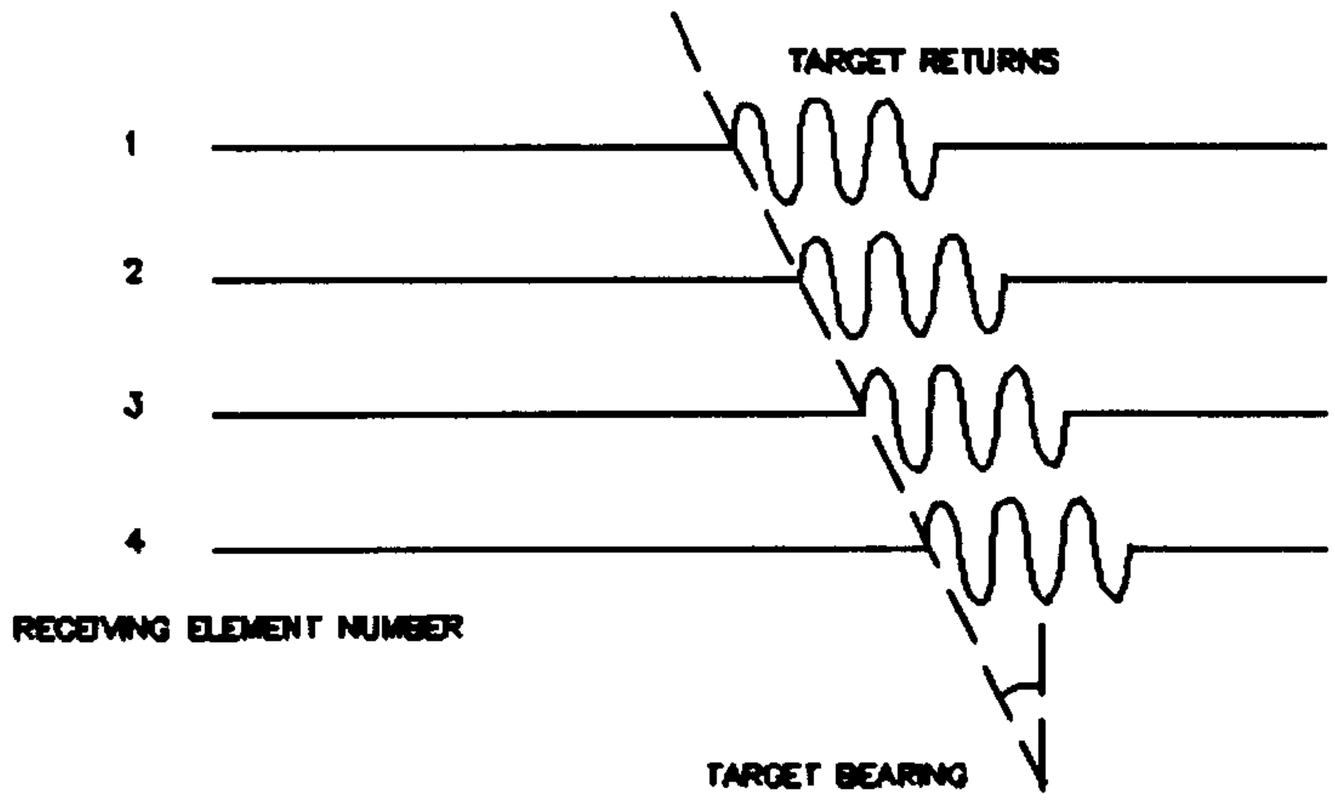

Figure 6: Typical returns from an offset target.

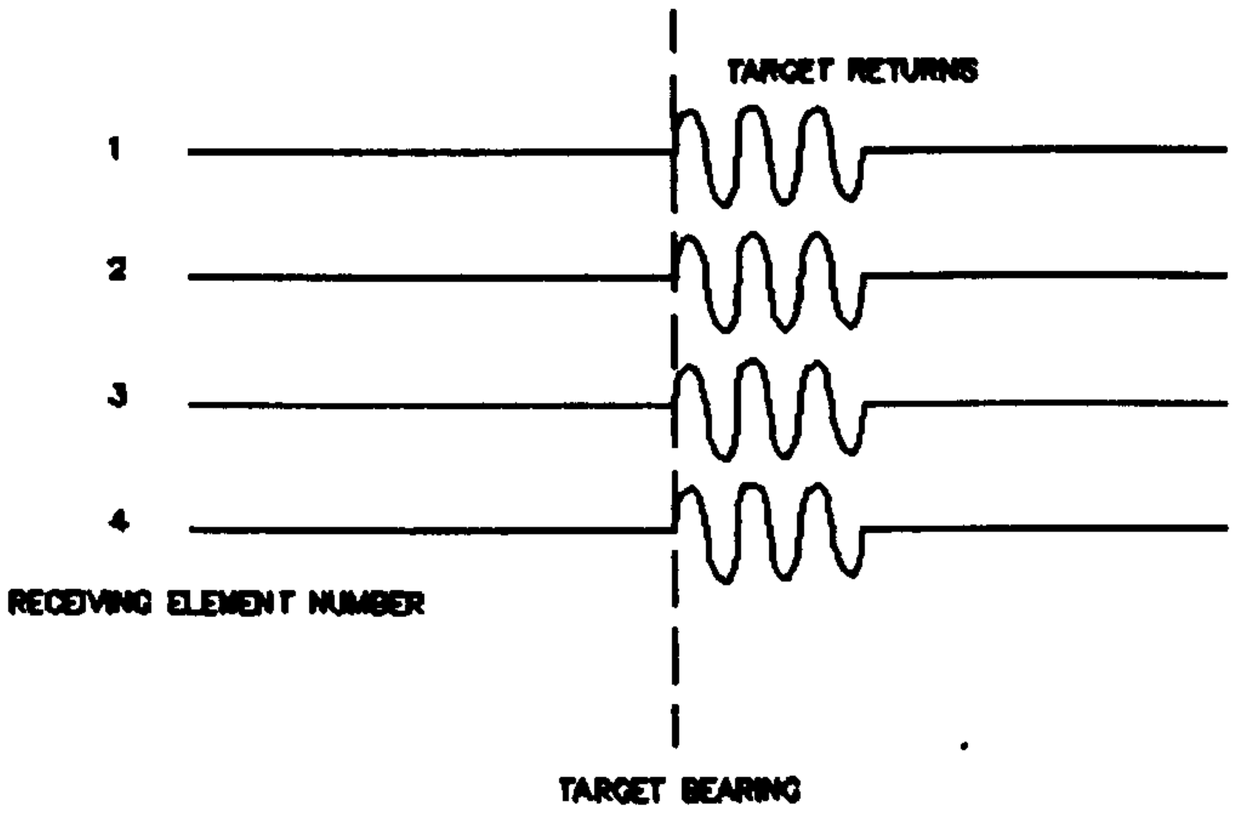

Figure 7: Typical returns from a central target.

Figure 7 and Figure 6 show the typical signals present at the output of a 4 element array. The signals are from a target placed central to the array and a target

offset to one side. If the signals are digitised and stored then they may be viewed as a 4 X n array (n is the number of samples taken from each element) as shown in Figure 8. Since the received data is now stored the data may be processed many times to locate the any targets present. The angular position of any targets present is determined by shifting and adding the array rows and columns until a maximum occurs.

$$\begin{matrix} A_{00} & A_{01} & A_{02} & A_{03} & A_{04} & A_{05} & A_{06} & A_{07} & A_{08} & A_{09} \cdots\cdots A_{0(n-1)} \\ A_{10} & A_{11} & A_{12} & A_{13} & A_{14} & A_{15} & A_{16} & A_{17} & A_{18} & A_{19} \cdots\cdots A_{1(n-1)} \\ A_{20} & A_{21} & A_{22} & A_{23} & A_{24} & A_{25} & A_{26} & A_{27} & A_{28} & A_{29} \cdots\cdots A_{2(n-1)} \\ A_{30} & A_{31} & A_{32} & A_{33} & A_{34} & A_{35} & A_{36} & A_{37} & A_{38} & A_{39} \cdots\cdots A_{3(n-1)} \end{matrix}$$

Figure 8: Matrix representation of array signals.

$$\begin{matrix} A_{00} & A_{01} & A_{02} & A_{03} & A_{04} & A_{05} & A_{06} & A_{07} & A_{08} & A_{09} \cdots\cdots A_{0(N-1)} \\ A_{10} & A_{11} & A_{12} & A_{13} & A_{14} & A_{15} & A_{16} & A_{17} & A_{18} & A_{19} \cdots\cdots A_{1(N-1)} \\ A_{20} & A_{21} & A_{22} & A_{23} & A_{24} & A_{25} & A_{26} & A_{27} & A_{28} & A_{29} \cdots\cdots A_{2(N-1)} \\ A_{30} & A_{31} & A_{32} & A_{33} & A_{34} & A_{35} & A_{36} & A_{37} & A_{38} & A_{39} \cdots\cdots A_{3(N-1)} \end{matrix}$$

Figure 9: Effect of time shift on matrix.

Consider the signals shown in Figure 7. If the samples $A_{00}...A_{30}$ are summed and the process repeated for $A_{(0..3)0}...A_{(0..3)(n-1)}$ then a maximum output will occur at the point in the signals where the target is located. The result is the same as the summation performed in equation (5) with $\psi = 0$; this produces a beam pointing at 0°. The process is directly comparable to conventional beam steering

because the samples are taken at discrete time intervals. A time delay in the time domain is a phase shift in the frequency domain. It therefore follows that if the summation were to be formed after a shift had been applied to each matrix row. The sum formed would be $A_{00}+A_{11}+A_{22}+A_{33}$,the effect of this on the matrix is shown in Figure 9, if this is repeated now for samples between 0 and (n-1) then a progressive time shift has been introduced into channels 0,2 and 3. This time shift is the time domain equivalent of ϕ_c in section 4.3.4.

From Figure 6, it can be seen that if the shift is repeated, the signals will eventually line up and a maximum output will be obtained from the summation. The amount of time shift necessary is directly proportional to the bearing of the target (θ).

The bearing can be calculated from the formula:

$$\sin\theta = \frac{d}{\tau c} \tag{12}$$

where

τ = time interval between samples.

c = speed of propagation.

The process may also be summarised by the equation:

$$S = \sum_{0}^{M-1} x_n(t+\tau_{n,\theta}) \tag{13}$$

where

S = the output along a particular beam.

$x_n(t)$ = signal received on the nth element.

$\tau_{n,\theta}$ = the time delay that must be inserted to form a directional beam at

a bearing of θ.

M = the number of beams.

This digital approach to beam forming is only applicable to receiving arrays.

4.3.5.2 Frequency domain processing

An alternative approach to the time domain analysis of array data is to process the data in the frequency domain. This can be done using a fast fourier transform method (FFT), since the FFT of a signal can be calculated quickly and efficiently using digital signal processing methods.

The technique is best described with reference to Figure 10 and Figure 11. If the outputs from each of the elements are sampled simultaneously then for Figure 10, all the signals are in phase so a DC level will be obtained. If the target is offset as in Figure 11 the outputs of the array elements will now appear as a sampled sine wave. The frequency of this sine wave is directly proportional to the angle of the target θ. If the continuous frequency spectrum of the sampled array output is plotted then frequency component will appear for each bearing which has a target present.

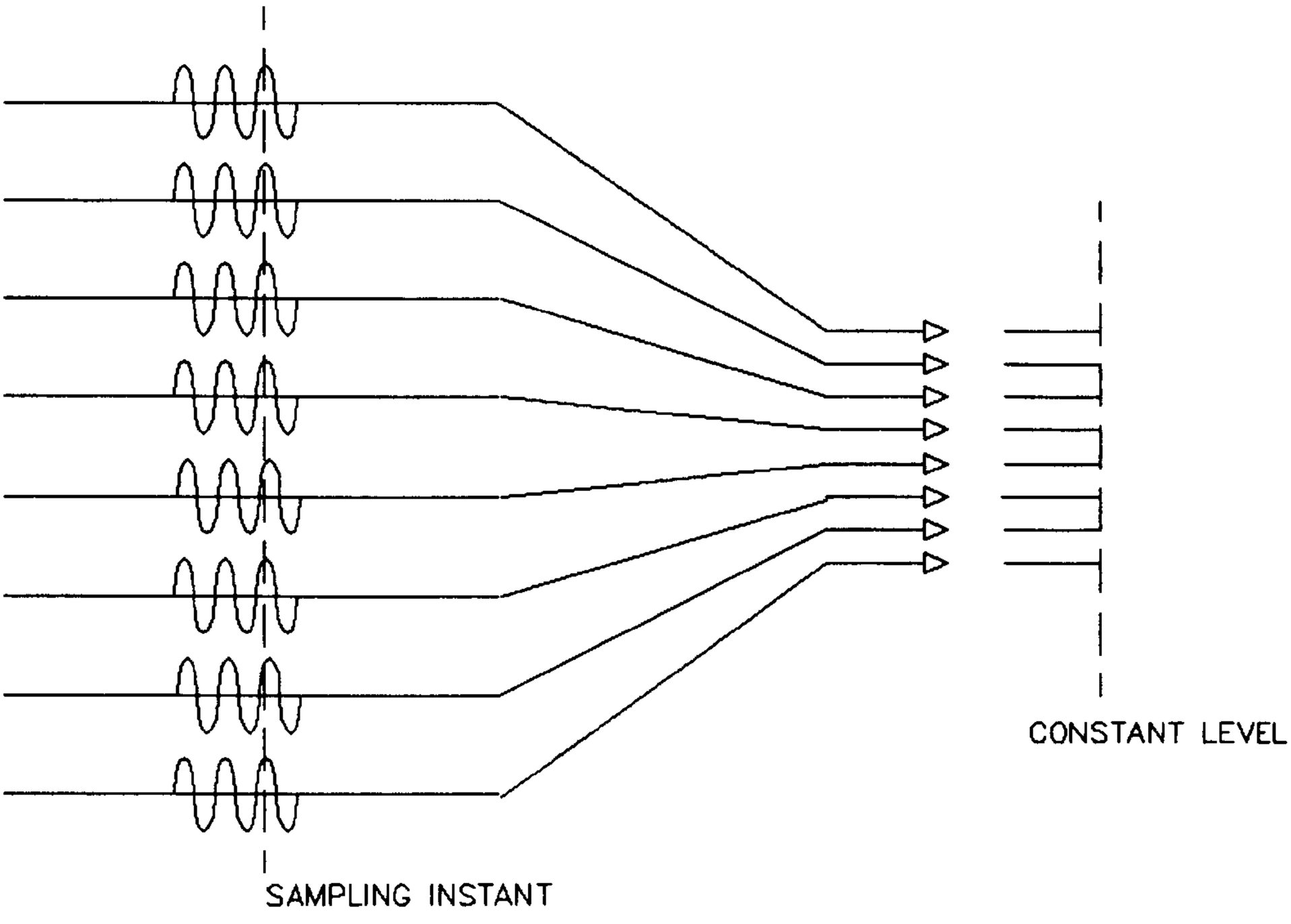

Figure 10: Sampled array output for central target.

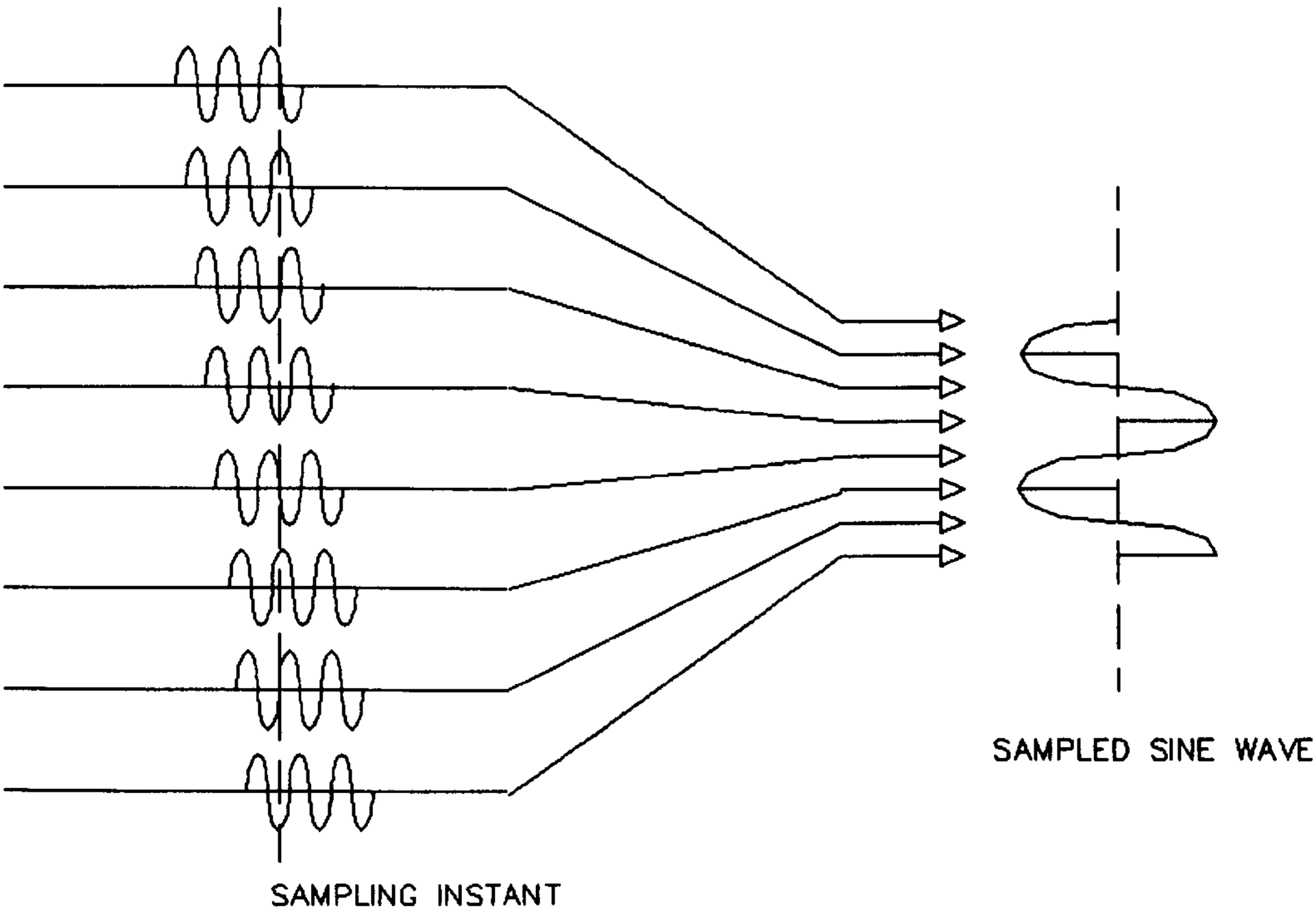

Figure 11: Sampled array output for offset target.

4.4 Angular resolution in beam forming systems.

The angular resolution of an array is defined as the minimum angular distance between two targets which allows them to be individually resolved. In a digital system the resolution is also the minimum angle through which the beam can be steered. The angular resolution of any array beam forming system is limited by the separation of the array elements.

4.4.1 Resolution in an analogue system.

The resolution of an array is governed by Rayleigh's criterion[12] which states that "two components of equal intensity should be considered to be just resolved when the principle intensity maximum of one coincides with the first intensity maximum of the other". This is governed by the maximum width of the array, see Figure 12[13]

If sound is approaching from straight ahead then the beam forming process will produce a maximum output at a bearing of 0°. If the beam is now steered away from this bearing, the output will decrease until a minimum is reached. If the array is considered in two equal halves and the beam is steered through angle α then each element in the top half of the array will cancel its opposite number in the bottom half, and the net output of the array will be zero. Thus if a second wavefront was incident at angle α its maxima would coincide with the minima of a wavefront arriving at 0° and both would be resolved. The resolution for any

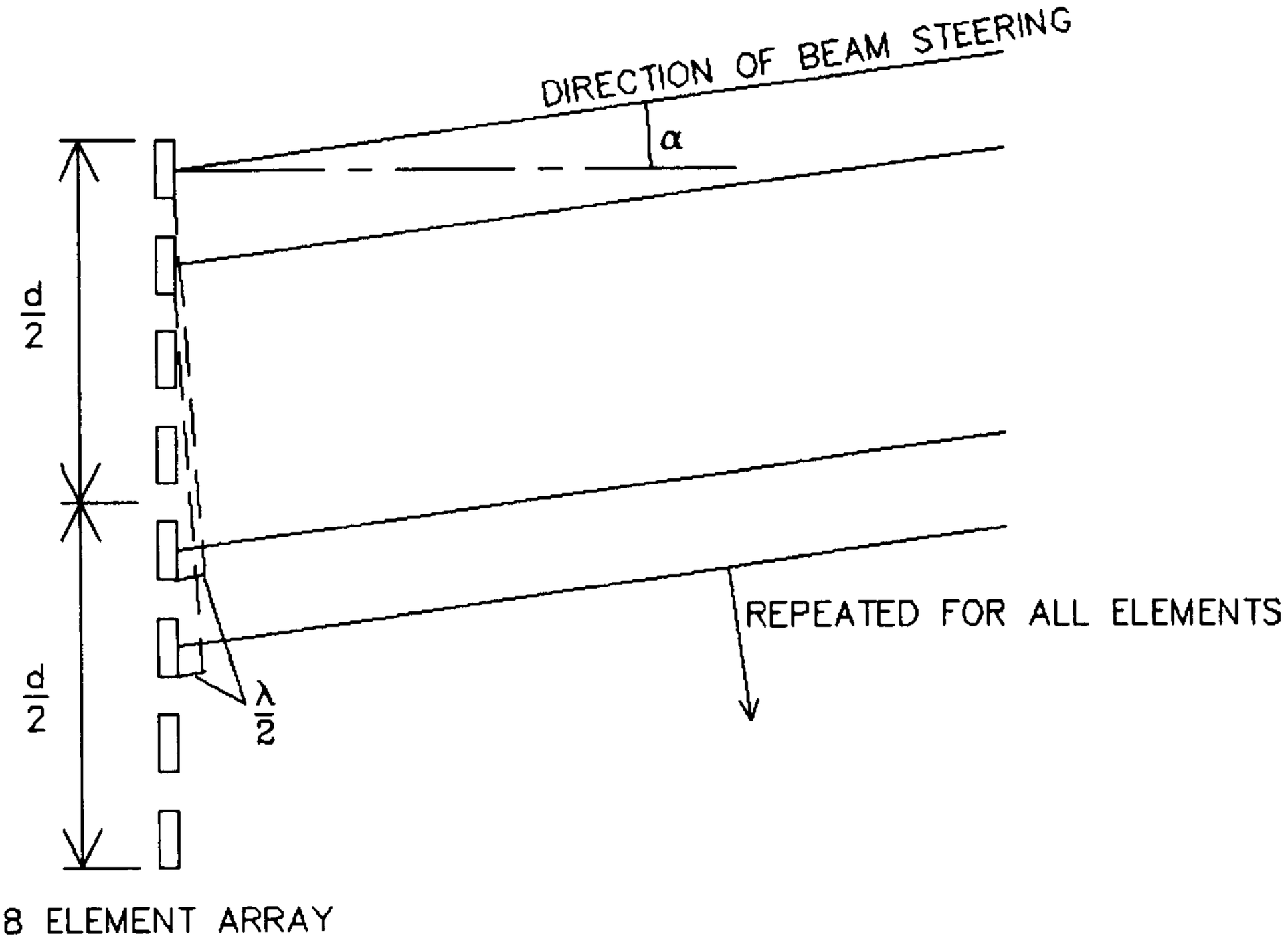

Figure 12: Calculating lateral resolution of an array (after Munro[13])

array width *(d)* can be calculated from:

$$\sin\alpha = \frac{\lambda/2}{d/2} \qquad (14)$$

$$\sin\alpha = \frac{\lambda}{d}$$

From this equation it can be seen that the greater the size of *d*, the greater the resolution of the array.

4.4.2 Resolution in a digital system.

In a digital system the resolution of the array is controlled not only by the Rayleigh criterion but also by the sampling rate. Consider Figure 13; the beams are formed by inserting delays equivalent to the variation in path lengths between

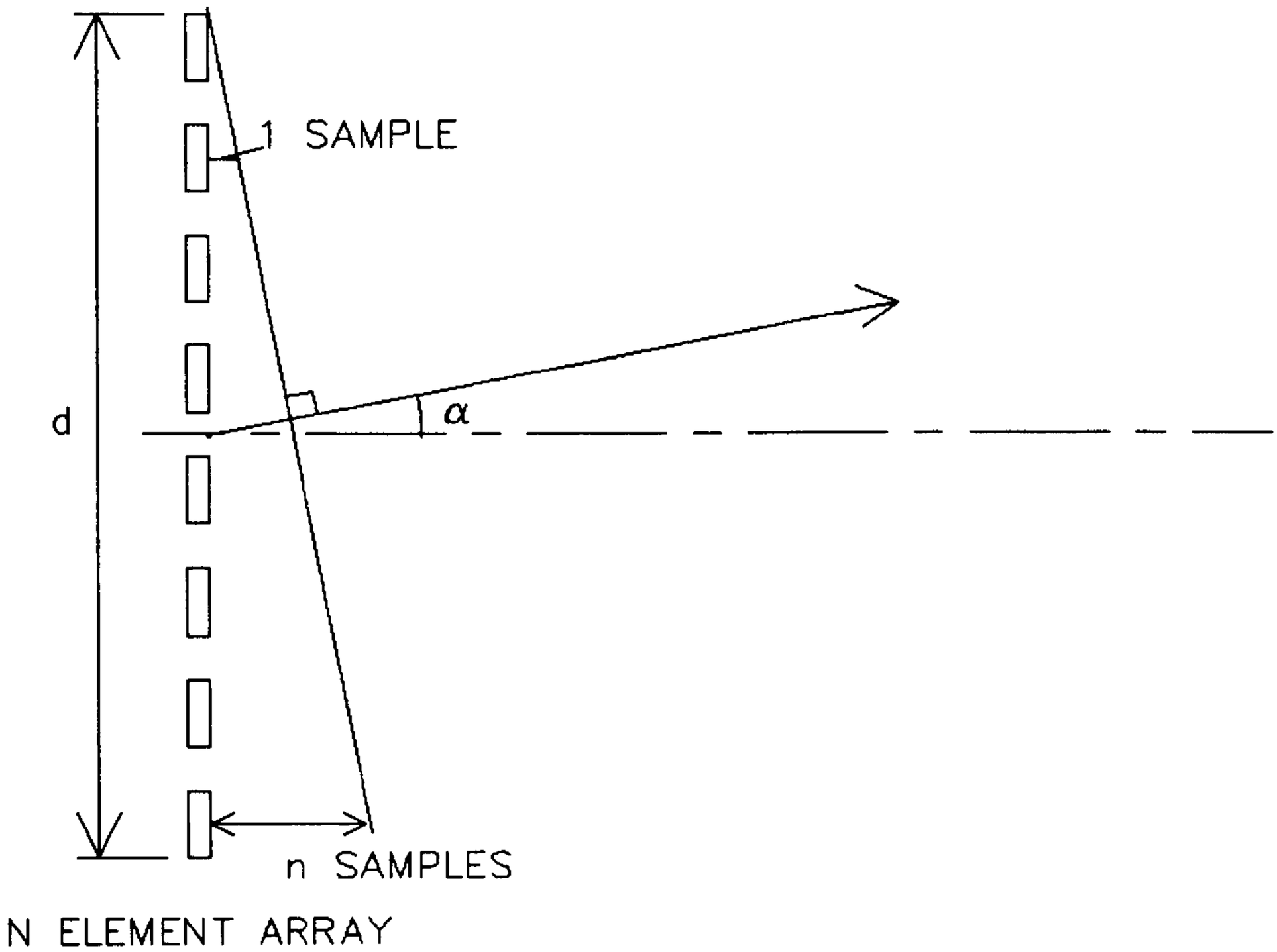

Figure 13: Calculation of array resolution with a digitally sampled signal.

each element and a target. Since the signal is digitised, its value is only known at discrete time intervals. The minimum time delay that can be inserted is therefore equivalent to one sampling interval *(τ)*. Therefore at the *N*th element the minimum time delay that can be inserted is *N(τ)*.

In the far field the maximum theoretical angular resolution (θ_r) of the system is given by

$$\tan\theta_r = \frac{(n-1)\tau C}{2d} \qquad (15)$$

where

n = number of elements.

C = speed of sound.

d = element separation.

The angular resolution is thus limited by the sampling rate and the maximum array element separation d. The Rayleigh criterion still applies but this is usually less that the limitation imposed by the sampling rate. The sampling rate limitation can be removed by using interpolation to artificially increase the sampling rate.

4.5 A new approach to digital beam forming.

This section describes a method by which the $\lambda/2$ limitation on element spacing can be removed with a resulting large increase in resolution without any increase in the sampling rate.

It was noted in section 4.3.3 that due to the periodic nature of the solution equation (7) grating lobes are produced if the element spacing is greater than $\lambda/2$. The periodicity of this solution is due to the continuous nature of the input signal. If the signals received by the array are not continuous but consist of only a few cycles then the envelopes of the received pulses may be approximated by the expression

$$s(t) = \cos\left(\frac{\pi t}{\tau}\right) \qquad |t| < \frac{\tau}{2} \qquad (16)$$

$$s(t) = 0 \qquad \textit{otherwise}$$

The output of the array is thus

$$E(t) = s(t) + s(t+T) + s(t+2T)...s(t+nT) \qquad (17)$$

where

T = envelope arrival time difference between individual elements.

The solution to this equation is not periodic. Grating lobes are not therefore produced so there is no limit to the possible distance between the array elements. The difference between the two processes is shown diagrammatically in Figure 14.

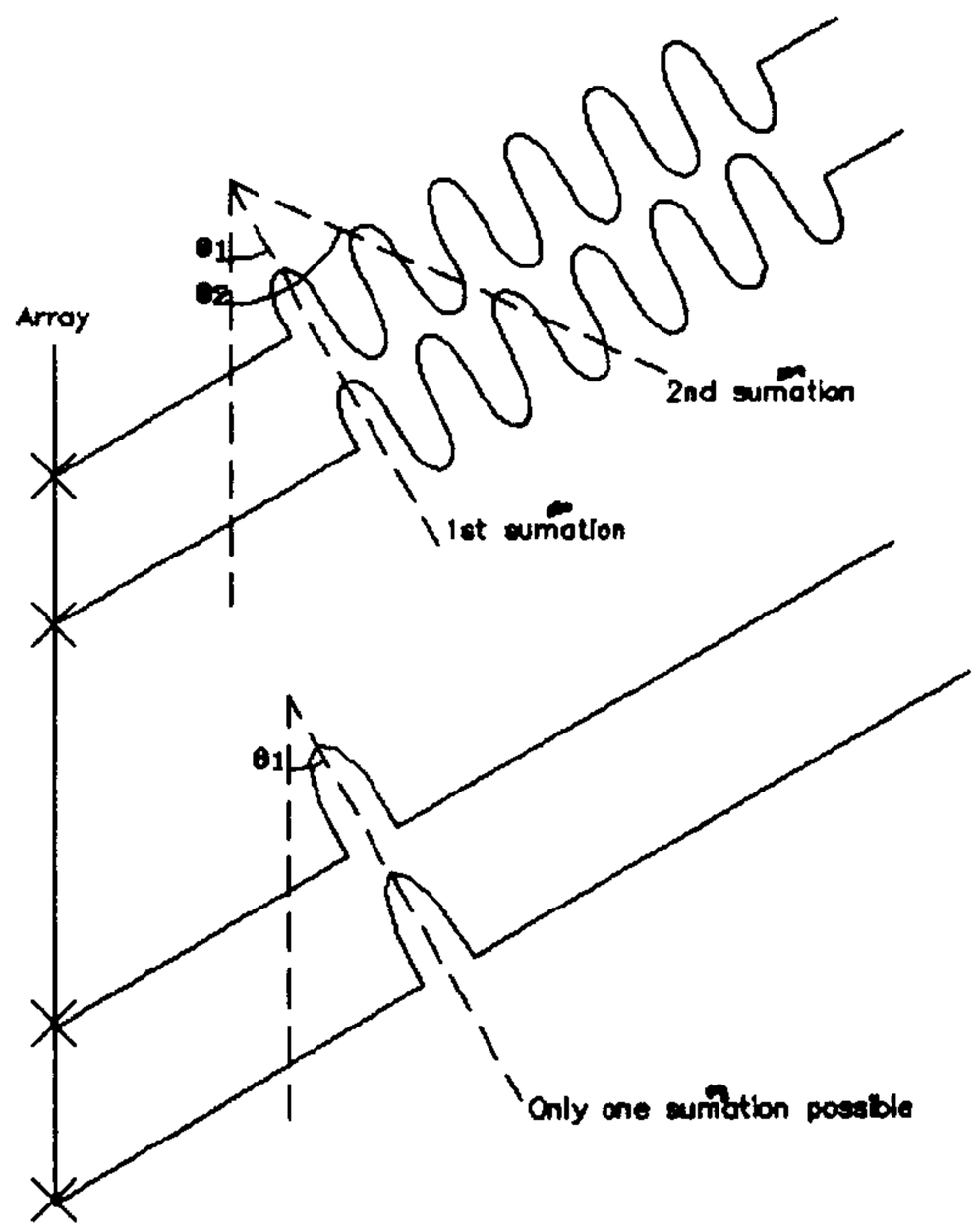

Figure 14 Envelope beam forming compared with traditional CW beam forming.

A possible disadvantage of this approach is beam broadening which will occur if the envelopes are very wide due to the use of a narrow bandwidth transducer. If the received signal consists of a rectangular envelope of width $n\tau$ then the far field angular resolution θ_r will be

$$\theta_r = 2\sin^{-1}\left(\frac{n\tau}{d}\right) \tag{18}$$

For a central target giving an envelope 40τ wide the calculated resultant angular

resolution will be 70° and for a target with an envelope 50τ wide the calculated resultant angular resolution will be 90°. The results of passing simulated data with these envelopes through a far field beam forming algorithm are shown in Figure 15 and Figure 16 respectively.

In the near field the situation is much more complex but the far field expression will still give an approximation of the resolution. Beamplots for a single target in the near field with 40τ wide and 50τ wide envelopes are shown in Figure 17 and Figure 18 respectively. It can be seen that the errors between the calculated far field and measured near field resolutions are 2.5° and 0° respectively. The fact that there is no apparent error in the case of the 50τ wide pulse is probably due to quantisation errors in the beam forming algorithm. This is also the reason why the error with the 40τ wide pulse is exactly 2.5°.

The results presented here are for the worst case of a pure rectangular pulse. In reality the output of the system is likely to be much closer to the pulse described in earlier in this section due to the band limiting effects of the hardware and transducer. It is still however important to ensure that the envelope peak is as sharp as possible or all the advantages obtained from the use of a wide element spacing may be lost.

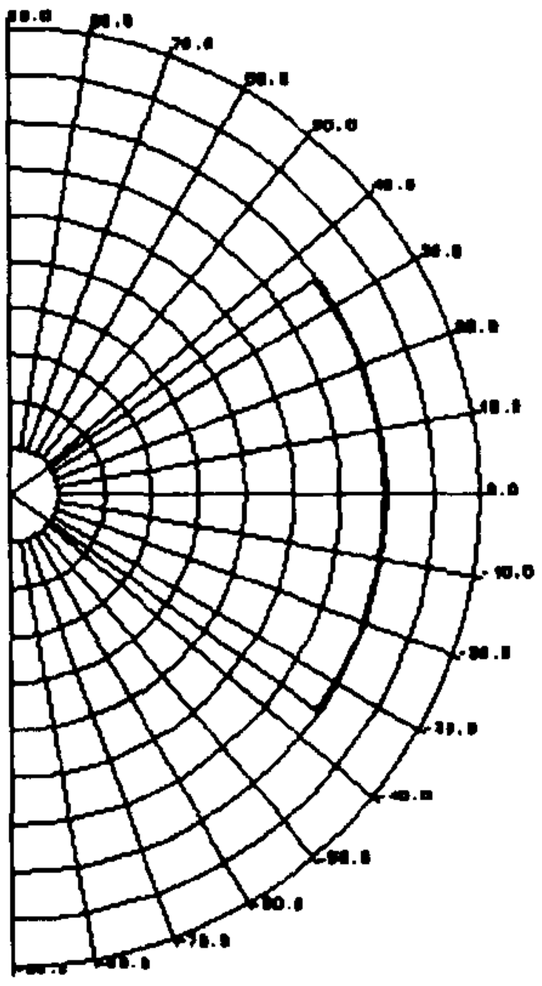

Figure 15: Beamplot for 40τ rectangular pulse (far field).

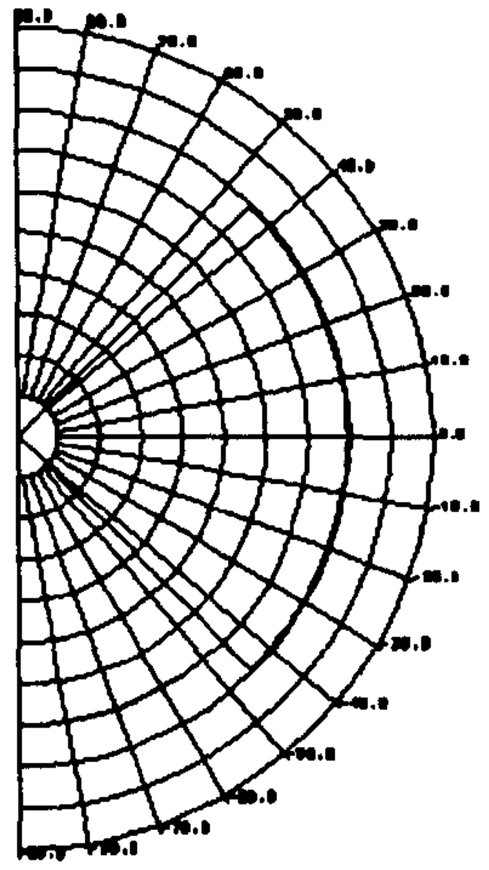

Figure 16: Beamplot for 50τ wide rectangular pulse (far field).

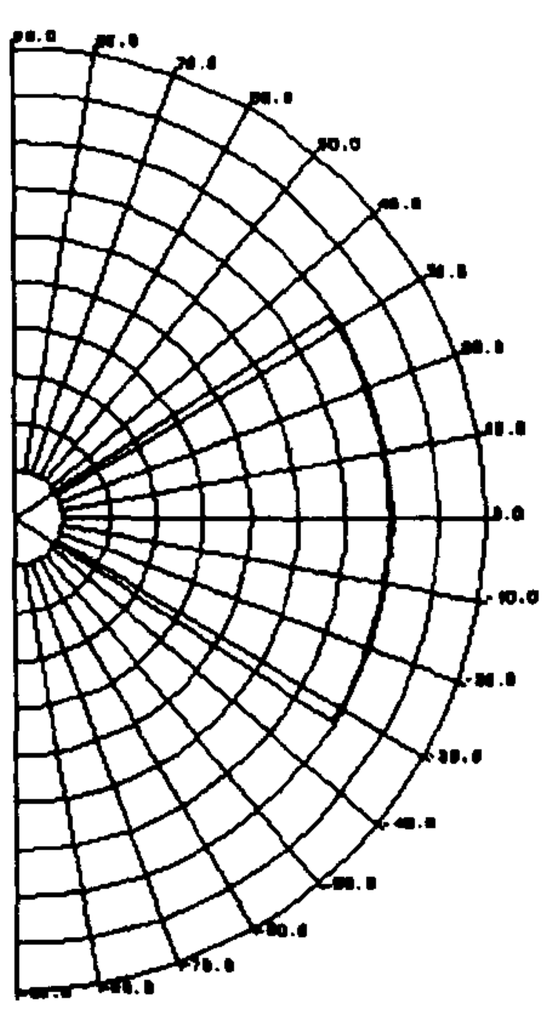

Figure 17: Beamplot for 40τ wide rectangular pulse (near field).

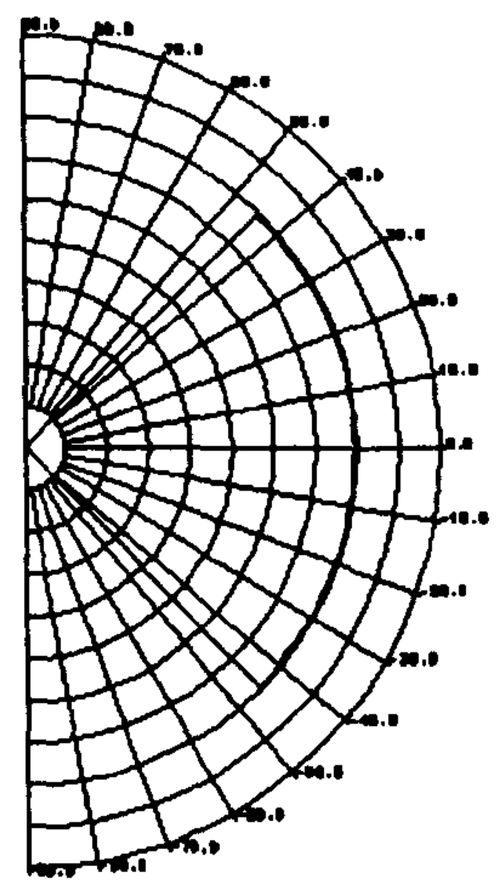

Figure 18: Beamplot for 50τ wide rectangular pulse (near field)

It is possible to compensate for the presence of a very wide pulse by thresholding and truncating the received pulses. This has two main disadvantages; amplitude information is destroyed and the amount of processing is increased. The loss of amplitude information may be significant since this can be used as an aid to target

recognition (see chapter 11). The results of a comparison of this method with traditional beam forming are given in chapter 9.

4.6 Summary

This chapter has described the methods by which range and bearing data may be obtained. Most importantly a different approach to digital time domain beam forming has been presented which completely removes the traditional restrictions on array element spacing. This has allowed a large increase in resolution without the computational penalties that would result from any resolution gains achieved by increasing the sampling rate.

4.7 References

1. L. Kay, "Airborne Ultrasonic Imaging of a Robot Work Space", Sensor review, Vol. 5, No. 1, January 1985, pp8-11.

2. F. Faridian, M. G. Somekh and I. Sakai, "New CW imaging microscope for scanning acoustic microscopy", Electronics Letters, Vol. 22, No. 15, July 1986, pp800-802.

3. B. Mehrdadi, B. Kaghazchi and M. S. Beck, "Non-contacting level measurement of irregular surfaces using coded ultrasound and cross correlation analysis", J. Phys. E. Sci. Instrum., Vol. 15, 1982, pp367-372.

4. J. Wykes, "Non-contacting Level Measurements of Irregular Surfaces Using Coded Ultrasound and Cross Correlation analysis", J. Phys. E. Sci. Instrum., Vol. 15, 1982. pp1386-1387.

5. M. I. Skolnik "Introduction to Radar Systems". McGraw-Hill international. 1984.

6. S. M. Thomas and D. R. Bull, "Neural Processing of Airborne Sonar for Mobile Robot Applications", Proc. IEE Intl. Conf. on Artificial Neural Networks, Bournmouth, UK, November 1991, pp267-270.

7. J. L. Crowley, "World Modelling and Position Estimation for A Mobile Robot Using a Rotating Ultrasonic Ranging Device", IEEE, 1985, pp128-135.

8. "Ultrasonic Range finders" Polaroid Corporation. 1982.

9. T. E. Curtis and R. J. Ward, "Digital Beam Forming for Sonar Systems", IEE proceedings, Vol. 127, Pt. F, No. 4, August 1980, pp257-265.

10. R. A. Mucci, "A Comparison of Efficient Beam forming Algorithms", IEEE transactions on acoustics, speech and signal processing, Vol. 32, No. 3, June 1984, pp548-558.

11. F. Nagi, "Physical Beam Forming and array processing for Sources Location", Ph. D. thesis, University of Nottingham, 1993.

12. M. Born and E. Wolf, "Principle of Optics", Pergamon press, 1980.

13. W. S. H. Munro, "Ultrasonic Phased Arrays for use in Imaging and automatic Vehicle Guidance", Ph. D. thesis, University of Nottingham, 1990.

CHAPTER 5

SYSTEM DESIGN CRITERIA

5.1 Introduction

Chapter 5 provides an overall view of the factors considered in the design of the system. Section 5.2 contains a list of design objectives upon which the system was built. Section 5.3 covers the design and construction of the transducer arrays used. Section 5.4 provides a review of the advantages and disadvantages of both digital and analogue signal processing. It also compares the use of a Digital Signal Processor with other available processing hardware. Section 5.5 describes the design of the data acquisition hardware and the choice of the transmitter waveform. The chapter is summarised in section 5.6. A detailed description of the system as it was actually built is given in chapter 6.

5.2 Design objectives.

The design objectives for the system were formulated primarily to provide a flexible ultrasonic measurement system and a platform for the development of signal processing algorithms. They were also influenced by the results of a feasibility study carried out by Advanced Robotics Research Ltd. This research laid down the following parameters for a robot arm ultrasonic collision avoidance

system[1].

a) Coverage: The sensing system should ideally give complete coverage of the volume of space around the arm.

b) Range: The sensing range (the inner and outer radius of the sensing envelope) should be from less than 30mm to more than 500mm.

c) Accuracy:

i) Systematic Errors in range: A target figure of ±10% should be aimed for.

ii) Random Errors in range: These should be kept below ±5%.

iii) Range Resolution: This should be ±5% of full scale.

iv) Bearing Accuracy: This should ±30%.

e) Speed: Acquisition time should be below 20ms.

g) Environmental Independence: The system should be as independent as possible of any other factors in its operating environment such as humidity, dust, or corrosive gases.

To fulfil the specification and to provide a flexible development platform the following specifications for the system hardware were set.

1: The system must be able to acquire and store the data from a 16 element ultrasonic array operating at a frequency of 100KHz. The acquired data must have sufficient signal to noise ratio to ensure the detection of a 5mm cylinder at a range of 1.5m. It must also be capable of resolving the three

---

[1] These parameters are quoted by kind permission of Advanced Robotics Research Ltd, University Road, Salford, M5 4PP.

corners of a 25mm cube at a range of 0.75m.

***2:** The system must be able to provide a complete set of target data in less than 20ms.*

***3:** The system must be sufficiently flexible to act as a platform for the development of signal processing algorithms.*

***4:** The system must be capable of communicating directly with a PUMA510 robot.*

***5:** The system architecture must be as flexible as possible to allow expansion and improvement without redesigning the whole system.*

The rest of this chapter describes how these design goals where met. The system had to be designed and built in house since there was no commercial system available that could fulfil all these criteria. It was decided at an early stage that the system should utilise the envelope beam forming system described in chapter 7. This allows the maximum resolution to be obtained whilst reducing the processing overhead to a minimum. For the extraction of range data, a pulse echo method had to be chosen since the arrays used have the receivers buried in the transmitter. To function as a receiver a continuous DC bias must be applied to the transmitter (see chapter 3). To transmit the bias to the transducer is switched on and off; this makes it impossible to transmit and receive simultaneously. None

of the continuous wave methods may therefore be used. If the receivers are placed outside the transmitter then, due to the very small divergence of the transmitter output, the field of view is very limited. This problem was encountered in early, non real time, imaging work performed by Pomeroy[1].

5.3 Array Geometry

The ultrasonic arrays used in this work are manufactured by applying an appropriate texture to the surface of a printed circuit board (pcb) and bonding a thin dielectric membrane over the surface. This technique was developed within the Department of Manufacturing Engineering at the University of Nottingham[2] but is not the work of the author. The whole board acts as a transmitter whilst electrically isolated segments are used as receivers. This process allows arrays of any size and geometry to be easily manufactured. The construction of the arrays is described in more detail in[2,3]. Although ultrasonic arrays can be manufactured using a grooved backplane to operate at any frequency[4], the pcb process is currently limited to the production of arrays operating at 100KHz. This frequency provides a good compromise between range and resolution for a system capable of imaging a $1m^2$ workspace. Due to the sizes of board available and the difficulties associated with the handling of large pieces of membrane, arrays are manufactured in a standard eurocard size (100mm $\times$ 220mm). The maximum number of elements on any one board was limited to 16 by the design of the preamplifiers (see chapter 6). For the planned experimental work two configurations of array were chosen, a 16 element array with $\lambda/2$ element spacing

and a 4 element array with 40mm array spacing. On both arrays the elements were 1.7mm wide ($\approx\lambda/2$), which should give a coverage of 180°. In reality, due the structure of the array, a field of view of only 120° was attainable[2]. The two array geometries are shown in Figure 1 and Figure 2. The element spacing for the 4 element array was chosen as the maximum equidistant spacing possible for the size of board.

The transmitter, and hence the aperture, is relatively large compared to the wavelength. This means that the wavefront from the transmitter diverges only very slightly; 0.7° in the case of a transmitter 220mm wide. The area of illumination is thus effectively limited to an area extending directly in front of the transmitter. As a result, two further transducers had to be manufactured with the receiving elements omitted. With the extra transmitters mounted either side of a normal array, the area of coverage was extended to 660mm. The arrays were initially mounted in a simple frame but experiments soon proved this to be unsatisfactory as the arrays showed a tendency to twist, which manifested itself as a skew when the bearings where calculated. To prevent this skew, a machined aluminium backplate was produced and the array and transmitters were firmly clamped to it. As an added precaution the backplate was stress relieved in an oven to eliminate the risk of warpage during use. This resulted in a flat transmitting and receiving array 660mm x 100mm. A photograph of this arrangement is shown in Figure 4.

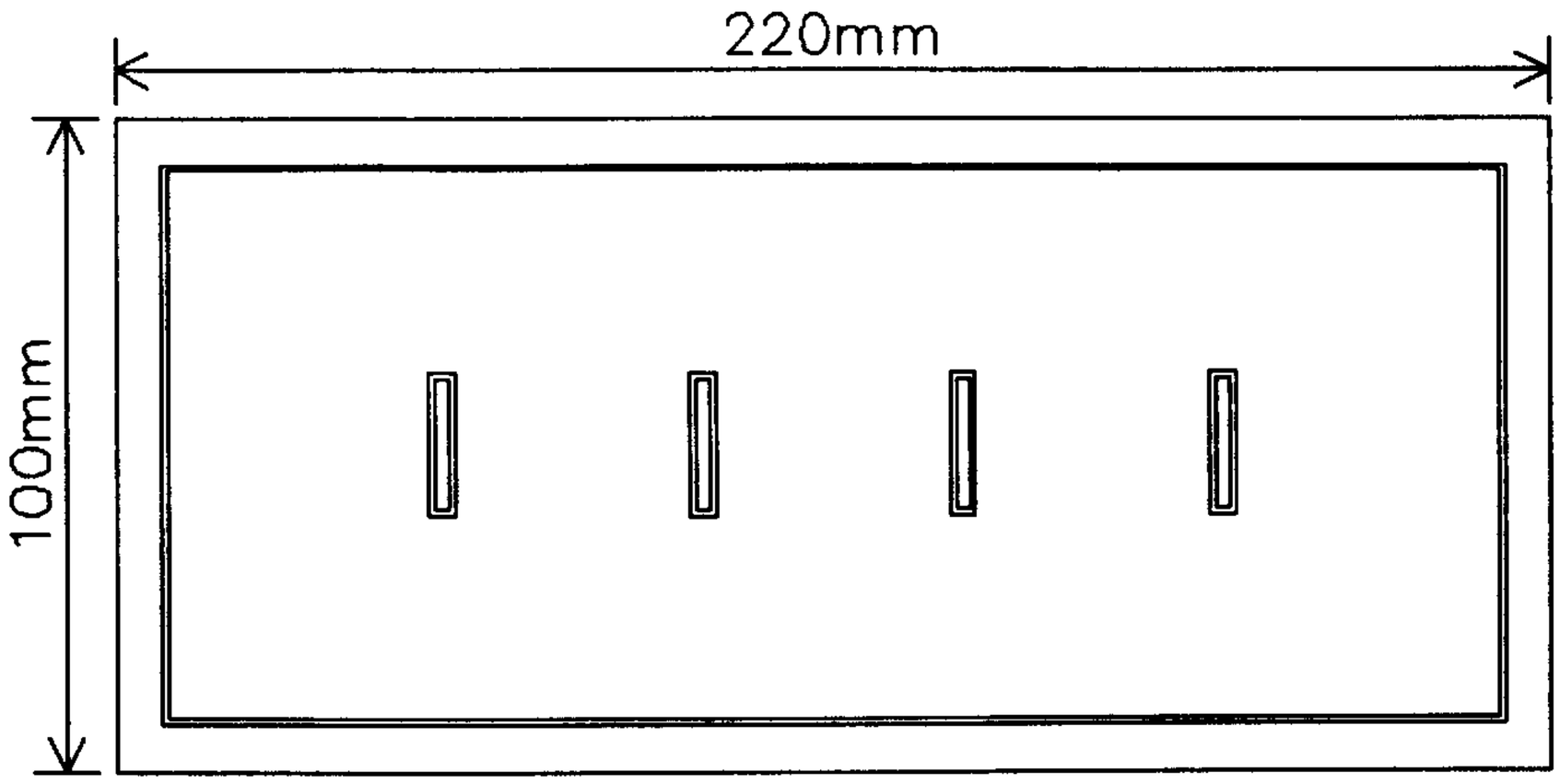

Figure 1: Geometry of 4 element array.

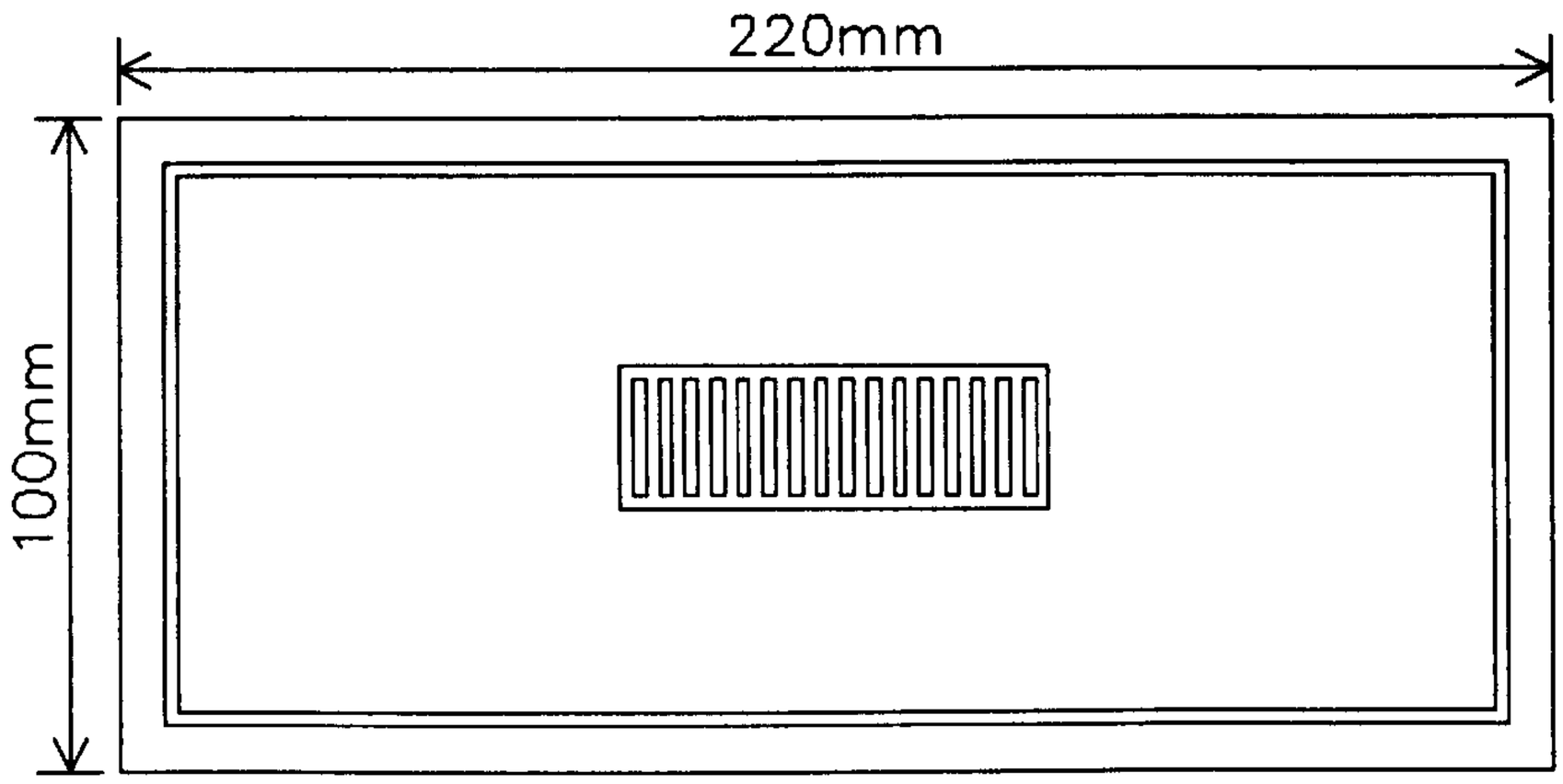

Figure 2: Geometry of 16 element array.

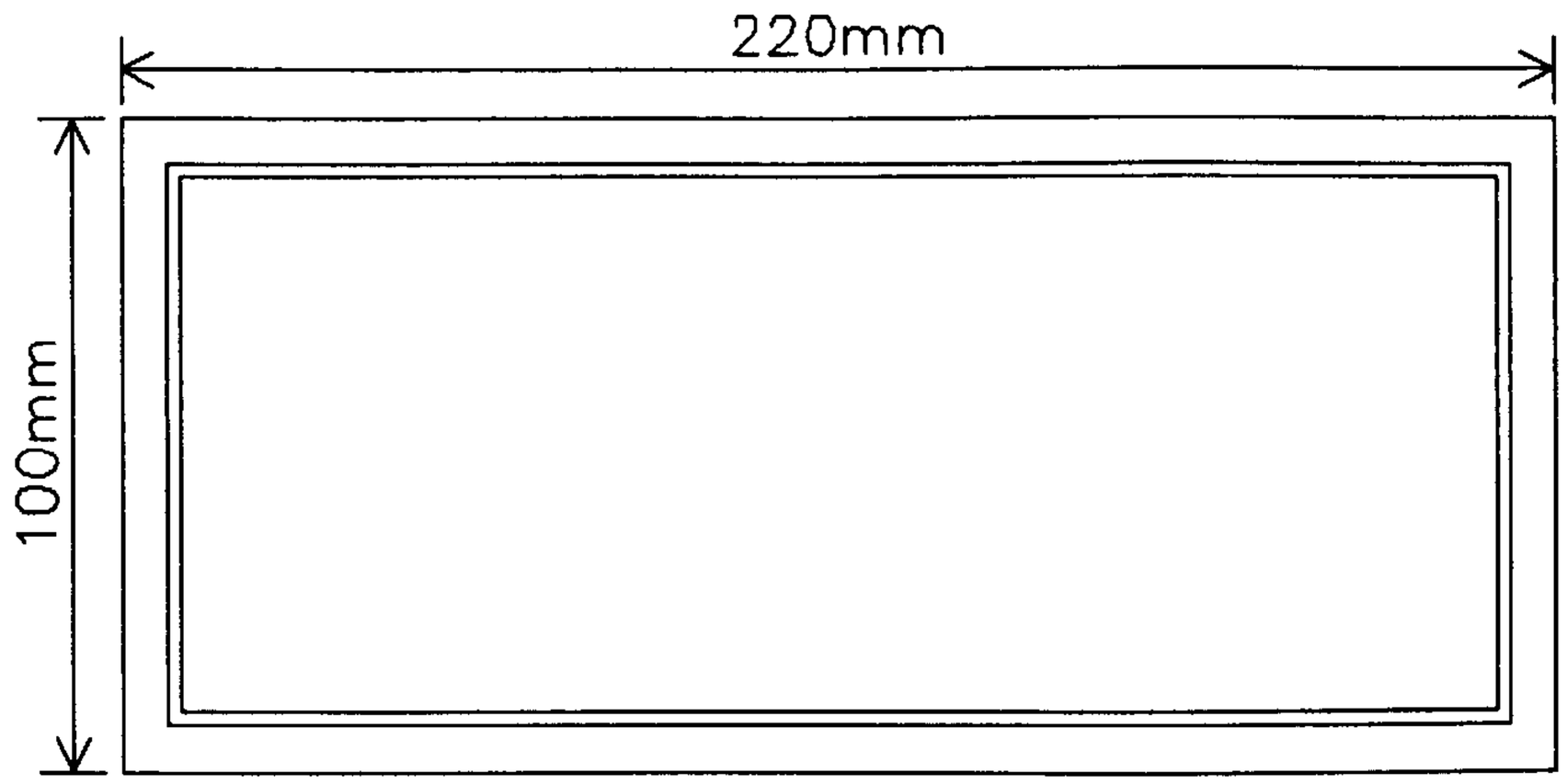

Figure 3: Geometry of transmitter.

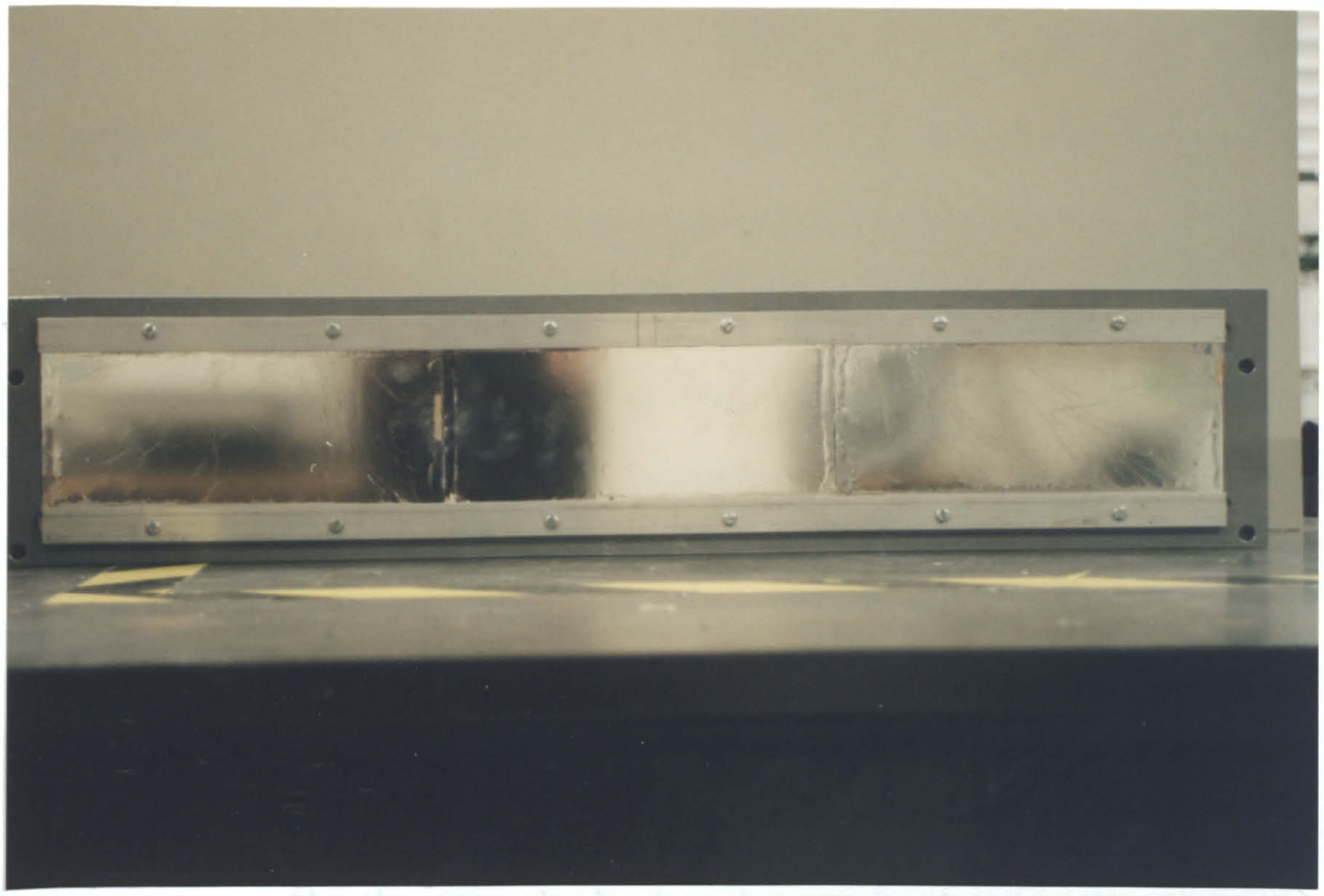

Figure 4: Photograph showing array and transmitters mounted on aluminium backplate.

5.4 Analogue versus digital signal processing

In recent years, there has been an increase in interest in the applications of digital signal processing. The advent of ever faster processors has helped to drive this interest. In most applications the enormous flexibility provided by microprocessor based digital signal processing usually outweighs the increase in hardware complexity compared to an equivalent analogue system or discrete digital system. This is particularly true in a development system where the final signal processing algorithm required cannot necessarily be fully defined at the design stage. This flexibility also allows easy modification of systems in the field. If a digital signal processor is to be used, and signals are to be processed in real time, then it is important to consider the processing burdens that may be placed on the processor. If a large amount of processing is required then it may be wasteful to use the digital signal processing system to perform simple actions such as filtering. For this reason initial signal processing and conditioning is often better performed on a signal using an analogue system. The conditioned signal can then be digitised and transferred for more complex processing on the digital signal processor -see Figure 5. This is the solution that has been adopted in this work.

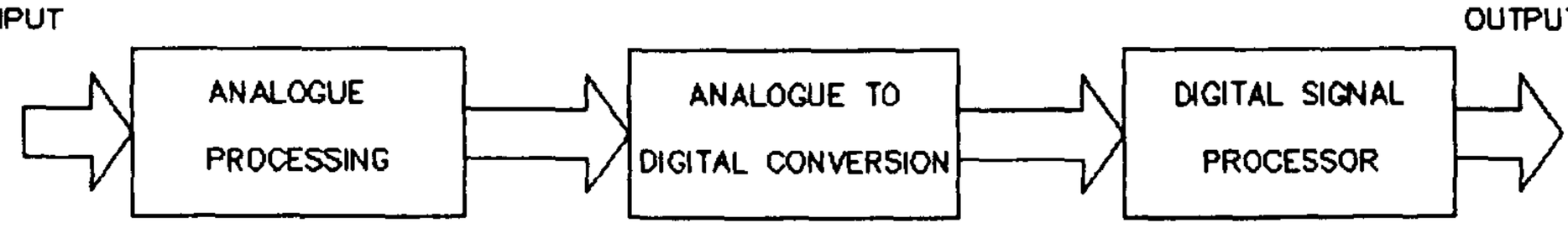

Figure 5: Hybrid signal processing system.

The type of processor chosen for the system was governed by four factors:

1: Cost.

2: Speed.

3: Complexity.

4: Availability.

The basic choice to be made initially was between a multi processor or single processor system. The obvious choice for a multi processor system would be the transputer but this was rejected on the grounds of cost and complexity. Initial analysis showed that a single specialised digital signal processor could achieve the necessary data processing rates. For instance, the Texas Instruments TMS320C30 is capable of performing a parallel 32 bit floating point add and store instruction in 60ns[5]. This compares with the IMS T800 Transputer instruction time of 350ns for a single 32 bit floating point add[6]. Because of the large speed advantage of a digital signal processor, it is capable of performing the work of several transputers and so a single processor solution was chosen. To minimise the amount of in house design and construction work required, the digital signal processor was bought as a commercial system from Loughborough Sound Images Ltd. The processor was mounted on an IBM PC expansion card along with 256k of fast static RAM. The digital signal processing card was mounted in a 25MHz IBM compatible PC. A parallel interface was also supplied with the card allowing easy connection between the processor and data acquisition system.

5.5 Hardware design

This section gives an overview of the design process applied to the data acquisition and processing hardware. The hardware was designed to fulfil the objectives defined in section 5.2. The eventual realisation of this hardware is described in chapter 6.

5.5.1 Signal conditioning

The basic requirement for the input signal to the envelope extraction and digitisation circuits was that the signal should have sufficient amplitude and an adequate signal to noise ratio. This was achieved by a simple amplifier and filter arrangement.

5.5.2 Envelope generation

The signal envelopes may be generated by using a simple envelope detector which, in its simplest form, consists of a rectifier and a lowpass filter, Figure 6. Though this is both simple and effective, it does destroy phase information.

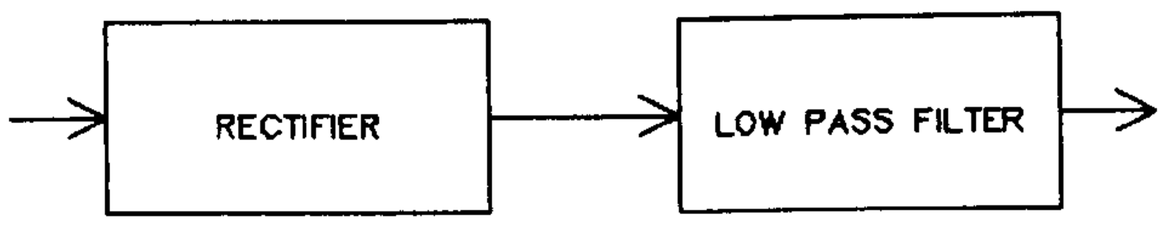

Figure 6: Simple envelope detector.

If the hardware is to be kept flexible to enable its use with more complex signal processing algorithms, then both the real and imaginary parts of the received signal are required and phase data must be preserved. Several methods,

both analogue and digital, may be used to do this. For this system an analogue method was chosen because of its relative simplicity when compared with digital methods. Also, with modern precision semiconductor devices, it was believed that inter channel matching would not be a problem. Initially a single channel was designed and built using discrete components but this was latter rejected on cost and size grounds and was replaced with an integrated circuit based design.

5.5.2.1 Analogue method

The easiest method of extracting the signal envelopes is to mix the signal with an offset frequency and thus shift the spectrum to baseband. This arrangement is shown in Figure 7. There is however a problem with this method in that the phase of the received signal varies depending on the time delay between transmission and reception. The output of the mixer will thus vary according to this phase difference.

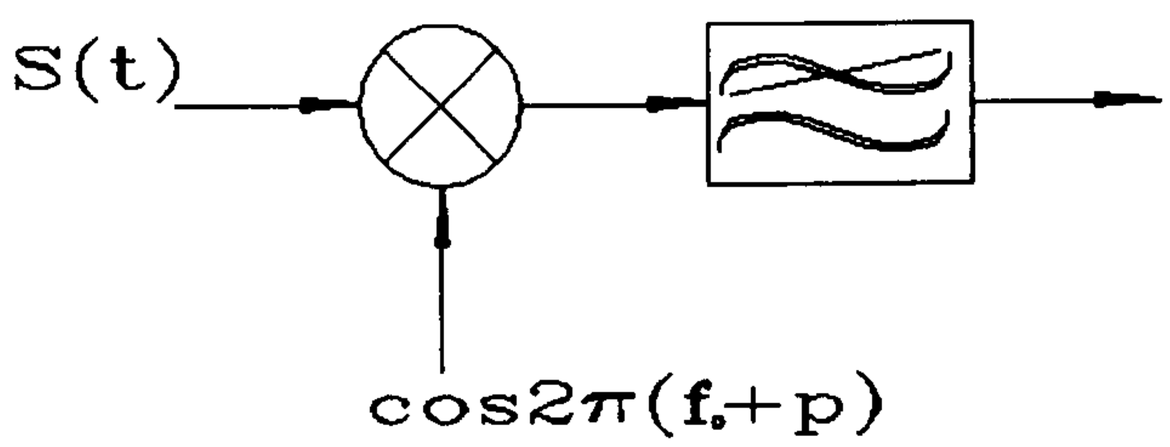

Figure 7: Mixer filter arrangement to shift a bandpass signal to baseband.

This may be overcome by mixing the signal with both a cosine wave and a sine wave of the offset frequency in two separate channels. The theory is as follows:

The transmitted signal *s(t)* may be defined as:

$$s(t) = a(t)\cos\omega_c t \quad (1)$$

where *a(t)* is an amplitude modulation.

The received waveform $s_r(t)$ may similarly be defined as:

$$s_r(t) = a(t-t_1)\cos(\omega_c(t-t_1)+\phi) \quad (2)$$

Where t_1 is the time delay between the transmitted and received signal and ϕ is the phase difference between the signals. This signal is now multiplied by an offset frequency,

$$s_p(t) = \cos(2\pi(f_0-p)) \quad (3)$$

where *p* is a frequency equal to or near to the centre frequency of the bandpass signal. If it is then low pass filtered we have:

$$t-t_1=\tau$$

and

$$s_r(t) = a(\tau)\cos(\omega_p\tau+\phi) \quad (5)$$

using

$$\cos(a+b) = \cos(a)\cos(b) - \sin(a)\sin(b) \quad (6)$$

5.13

we have

$$s_r(\tau) = a(\tau)\cos\omega_p(t)\cos\phi - a(\tau)\sin\omega_p(t)\sin\phi \quad (7)$$

This may be written as:

$$s_r(t)' = \cos(\phi).I - \sin(\phi).Q \quad (8)$$

where:

$$I = a(\tau)\cos(\omega_p(\tau))$$
$$Q = a(\tau)\sin(\omega_p(\tau)) \quad (9)$$

If a second identical channel is used but this time the signal is multiplied by a quadrature signal,

$$s_p(t) = \sin(2\pi(f_0 - p)) \quad (10)$$

then the quadrature version of the down converted signal $s_r(t)''$ will be obtained:

$$s_r(t)'' = a(\tau)\sin(\omega_p(\tau)+\phi) = \sin(\phi).I + \cos(\phi).Q \quad (11)$$

Since:

$$\sin^2+\cos^2 = 1$$

then squaring and adding the two resultant waveforms gives the amplitude of the

resulting envelopes:

$$s_r(\tau)'^{\,2} + s_r(\tau)''^{\,2} = a(\tau)^2 \qquad (13)$$

The output is thus independent of the arbitrary phase shift ϕ.

The phase data may be extracted from:

$$\phi(t) = \tan^{-1}\left[\frac{sr'(t)}{sr''(t)}\right] \qquad (14)$$

A block diagram of the amplitude generation process is shown in Figure 8.

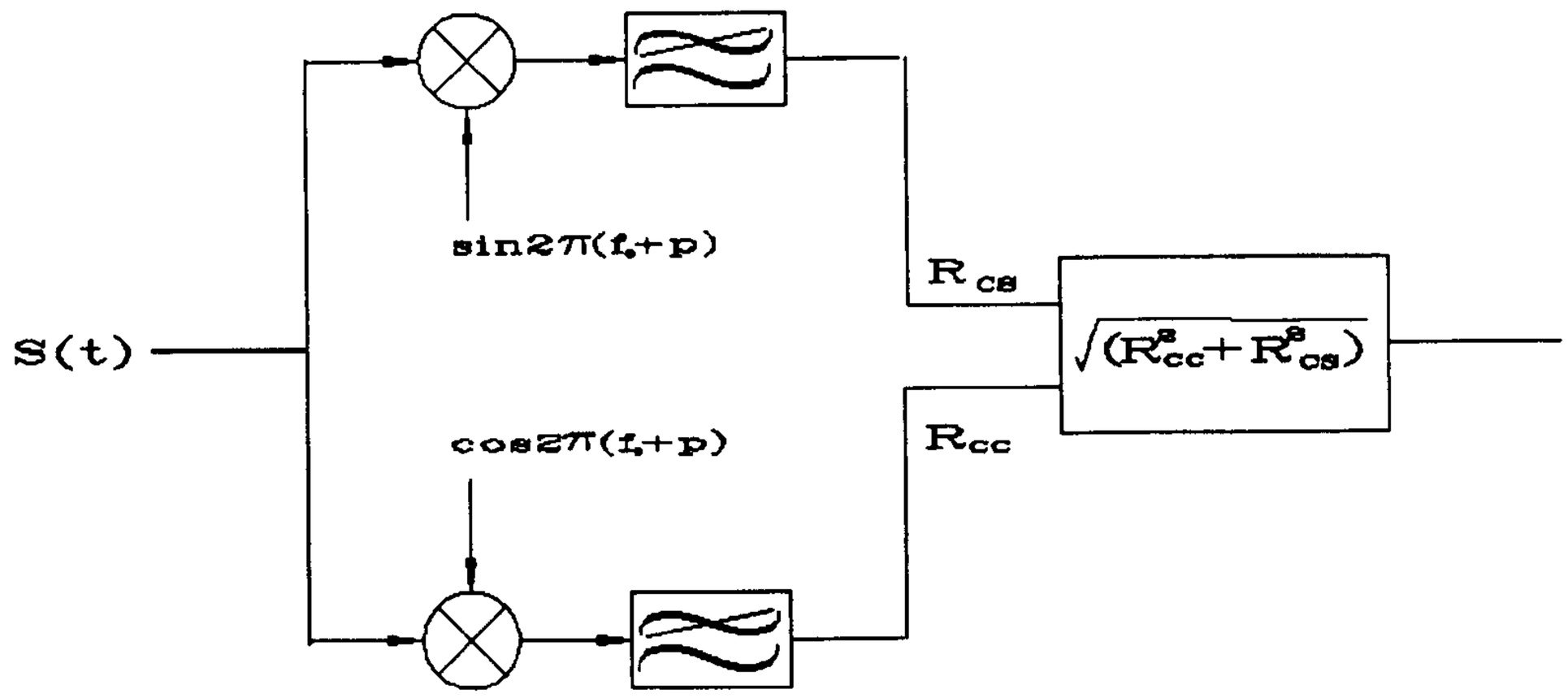

Figure 8: Implementation of down shifting using I and Q techniques.

5.5.2.2 Digital methods

The use of two channels for mixing does have the disadvantage that it is often difficult to match the gains, phases and frequency responses of both channels accurately enough. This problem can be overcome by adopting a digital approach. During the initial system design three method where considered.

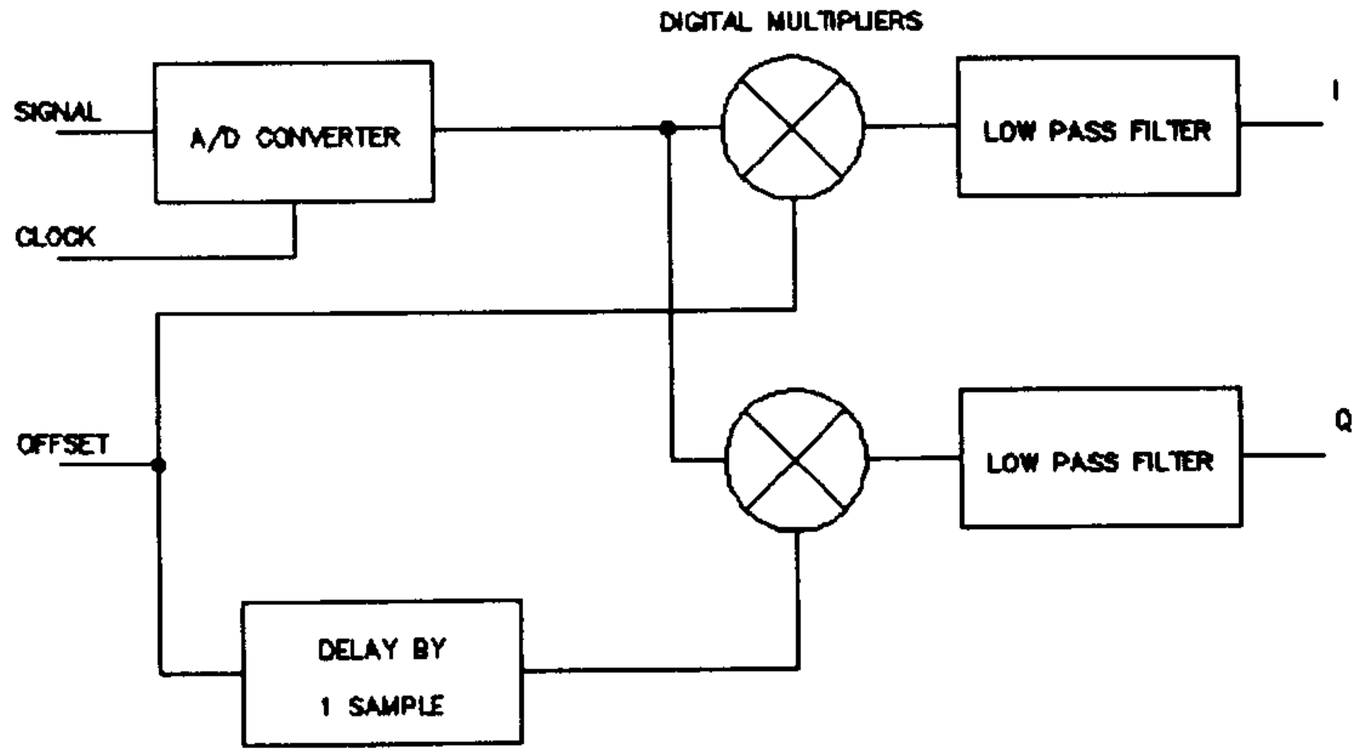

Figure 9: System used by Jackson for digital generation of baseband I and Q signals.

In a method described by Jackson and Mathewson[7], (Figure 9) the input signal is digitised at the input, mixed with samples of the offset frequency by means of digital multipliers and then digitally filtered. The system relies on the fact that the offset frequency can be treated either as a sine or cosine wave depending at which point samples are taken. If the offset frequency is sampled at twice the Nyquist rate and then delayed by one sample, sine and cosine signals are produced. This system has the disadvantage that a fast A/D converter is required since sampling occurs before the input signal has been converted to baseband. The advantage of the system is that the filters and mixers can be realised digitally, giving better stability and providing closer matching between channels.

Another method is that described by Rice and Wu[8] in which the bandpass signal is sampled at uniform intervals and the quadrature component is computed via a digital Hilbert transform Figure 10. Where Fourier transform techniques are used to analyze physical processes, there is often a relationship between the real

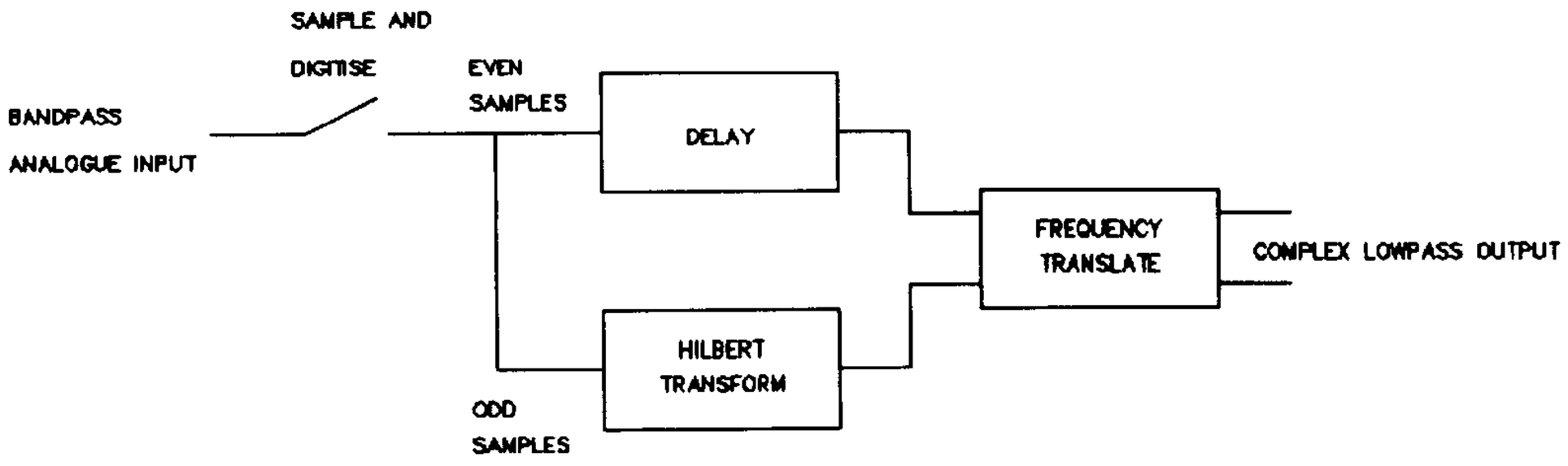

Figure 10: System used by Rice and Wu.

and imaginary parts of the phase and amplitude of the Fourier transform[9]. Such a relationship is called a Hilbert transform relation. The Hilbert transform can thus be used to separate out the real and imaginary parts of a complex signal. The bandpass signal need only be sampled at a rate determined by the Nyquist rate for the signal bandwidth not by the highest frequency present in the passband. The frequency domain periodic representation property of the Fourier transform is then exploited to produce the lowpass complex signal.

A third method is described by Liu, Ghafoor and Stockman[10] in which the input signal is mixed with an offset frequency before sampling and then digitally multiplied to provide inphase and quadrature components. This method has the advantage that not only is the sampling rate much reduced but also there is no need to digitally filter the outputs.

5.5.3. Transmitter waveform generation

In transmitter mode the ultrasonic transducer is made to vibrate by switching the bias on and off (see section 5.3). The actual switching is provided by the transmitter HT driver circuit (the driver is not the work of the author but is described briefly in chapter 6). The driver has to be triggered by a TTL waveform.

For simplicity, a simple software loop was chosen as the method of generating the transmitter waveform. The software addresses and triggers a purpose designed transmitter card and produces an output which changes alternately from 0 volts to +5 volts and +5 volts to 0 volts when the card is addressed. The transmitter waveform therefore consists of a burst of square waves at the required operating frequency. The choice of the burst length and repetition rate depends on several factors:

Frequency: The frequency is determined by the operating frequency of the transducer.

Amplitude: TTL (+5V, 0V).

Pulse width: This limits the minimum range of the system and the range resolution (the latter may be increased using pulse compression which is covered in chapter 8).

Pulse repetition frequency: This limits the maximum range in a pulse echo system (The maximum range may be increased by the use of PRF scheduling, see chapter 8).

The pulse repetition frequency (PRF) is the rate at which the transmitter is fired and the pulse repetition interval (PRI) is the reciprocal of the PRF.

These quantities are shown diagrammatically in Figure 11.

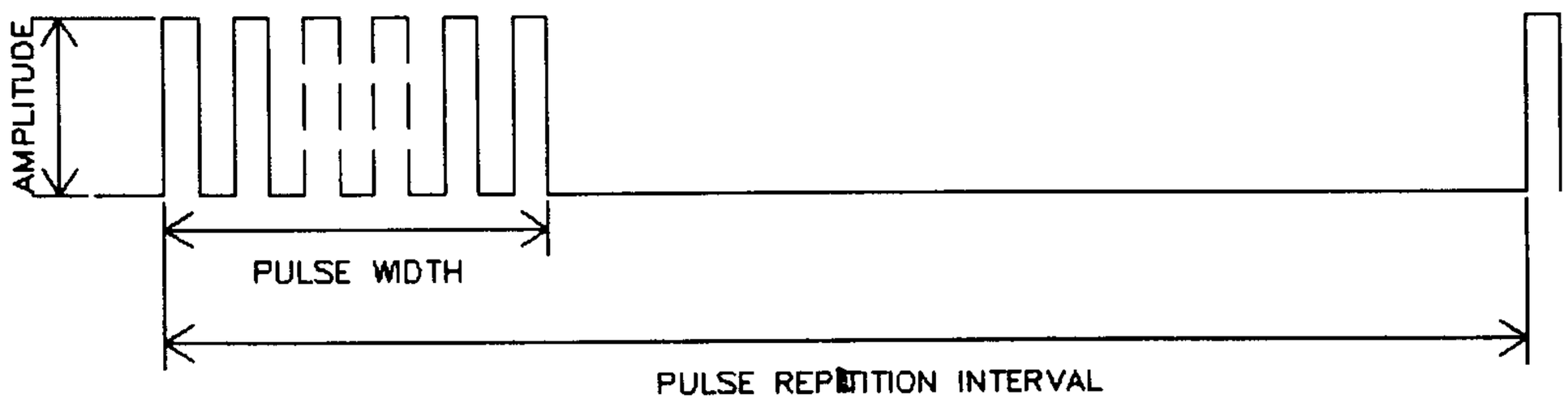

Figure 11: Typical transmitter drive waveform.

Choice of parameters:

Frequency: The frequency is limited by the operating frequency of the transducer and in this case is 100kHz.

Amplitude: Limited to TTL voltage levels.

Pulse width: Ideally the pulse width should be kept as narrow as possible to provide maximum resolution and the smallest possible minimum range. The minimum range of the transducer is set by the pulse width because the array cannot receive at the same time as it is transmitting.

The range resolution is limited by the pulse width through the following mechanism. Consider two targets close together. If the transmitted pulse is incident on the first target then a portion will be reflected back to the receiver. This process of reflection continues for as long as it takes the entire pulse to pass over the target. If during this time the front of the pulse is incident on the second target then a second reflection will take place and the two reflections will merge. It is the separation between two targets at which the two pulses can be resolved that is the range resolution. This process is shown diagrammatically in Figure 12.

The standard definition is based on the Rayleigh criteria and it is said that the two targets may be resolved when the separation of two pulses is greater than the 3dB points of the signals.

The width of the pulse that can be produced is limited by the response of the transducer. For an ideal pulse the transducer should have an infinite bandwidth giving zero rise and decay times. The capacitive transducer has

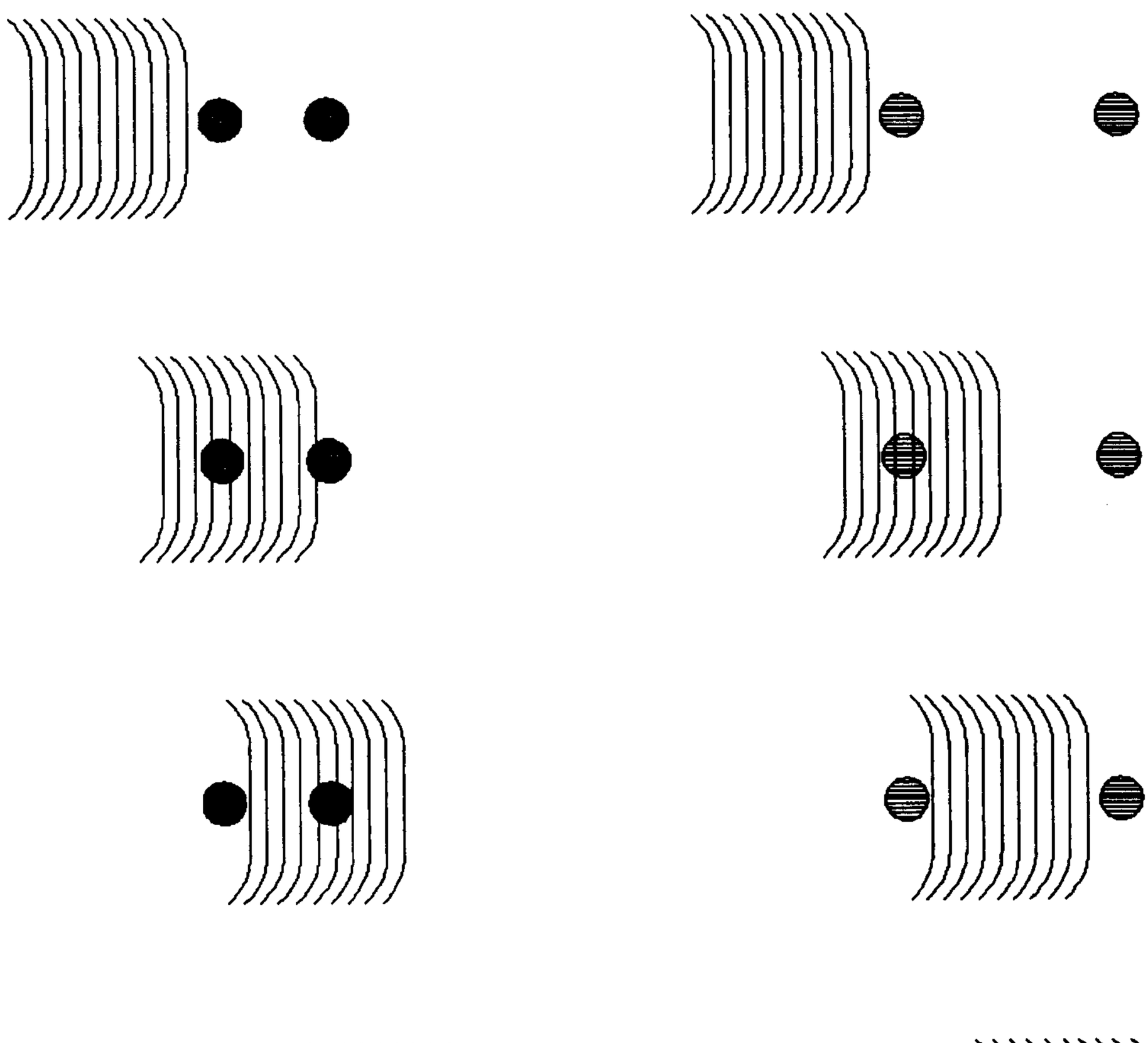

Figure 12: Effect of pulse width on resolution.

generally a better response than the other types of transducer available[11], but is still not ideal. The transducer used in this work has a bandwidth of 25kHz[2]. The effect of driving the transmitter with 1,2,3,4 and 5 cycles is shown in Figure 13 to Figure 17 respectively. The waveforms were recorded on a LeCroy 9400 digital oscilloscope using a Brüel and Kjær microphone No. 4138 and a Brüel and Kjær Measuring Amplifier type 2608. The results were taken with the transmitter transmitting into free space and the microphone placed 150mm from the centre of the array. The minimum pulse width that can be produced is 5 cycles wide, this is produced by stimulation with 3 cycles at a frequency of 100kHz. Stimulation with fewer cycles does not result in a shorter pulse but reduces the energy in the pulse. Stimulating with any more than 3 cycles does not increase the energy in the pulse but increases the pulse length.

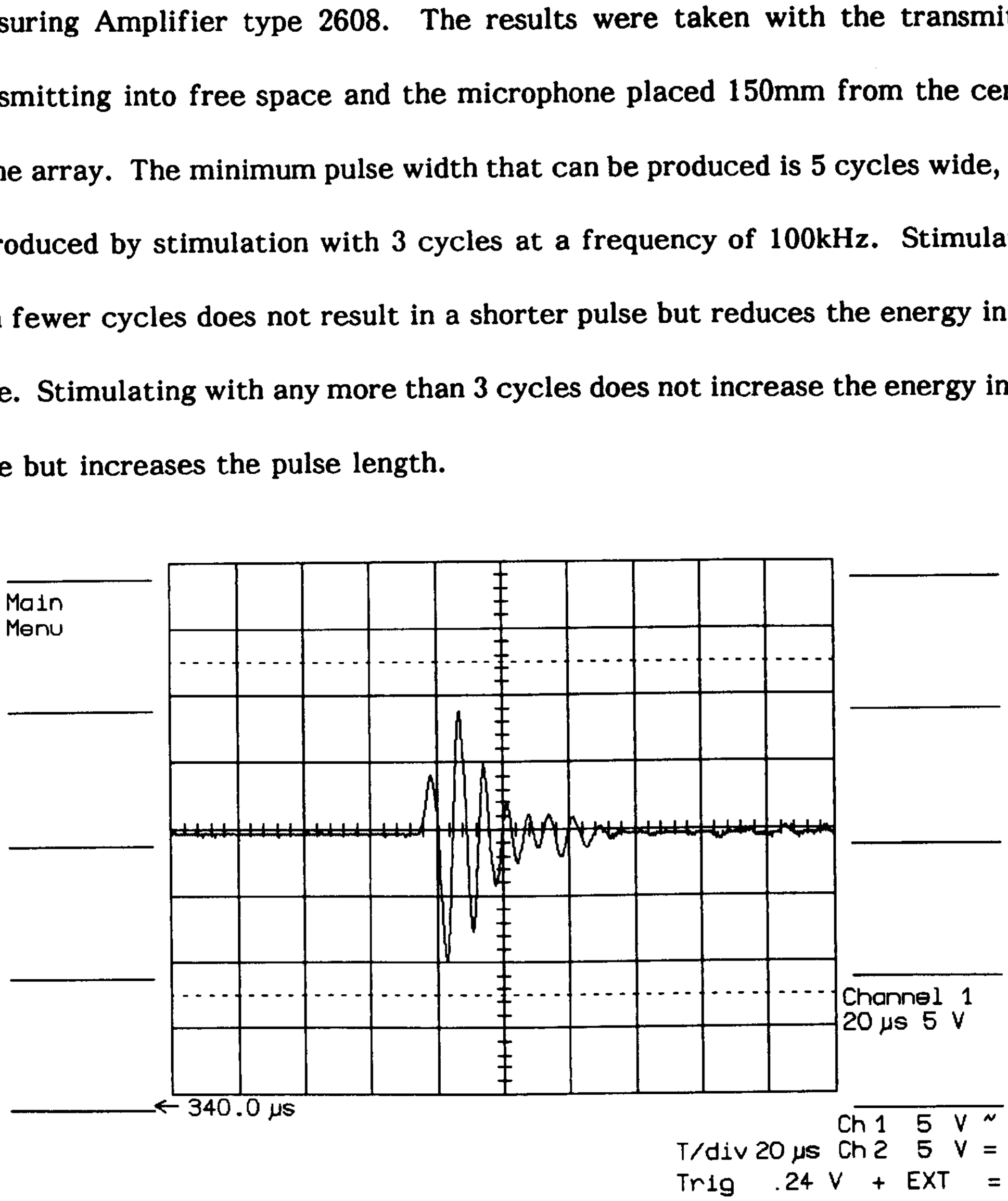

Figure 13: Resultant transmit waveform with a 1 cycle driving waveform.

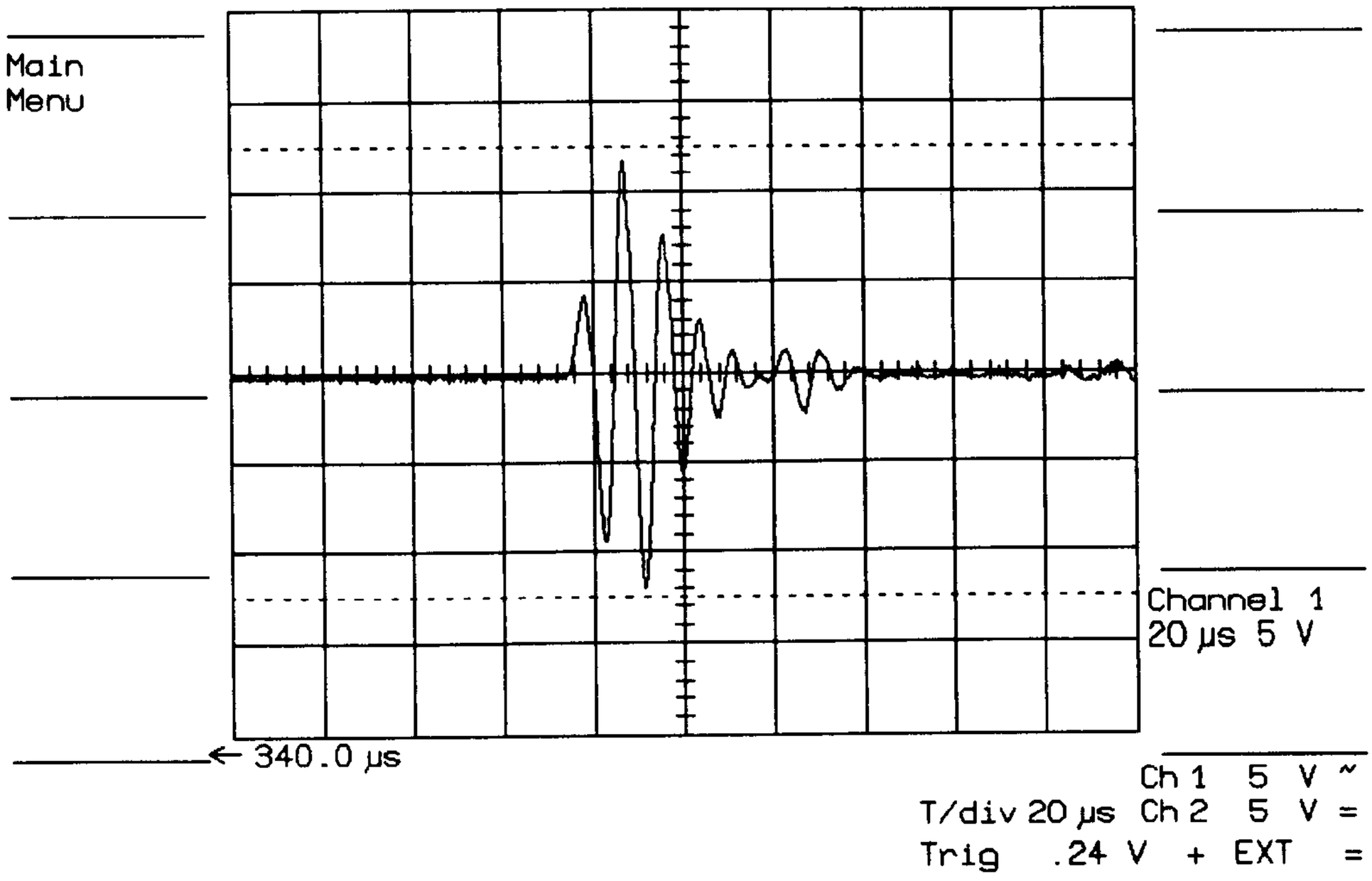

Figure 14: Resultant transmit waveform with a 2 cycle driving waveform.

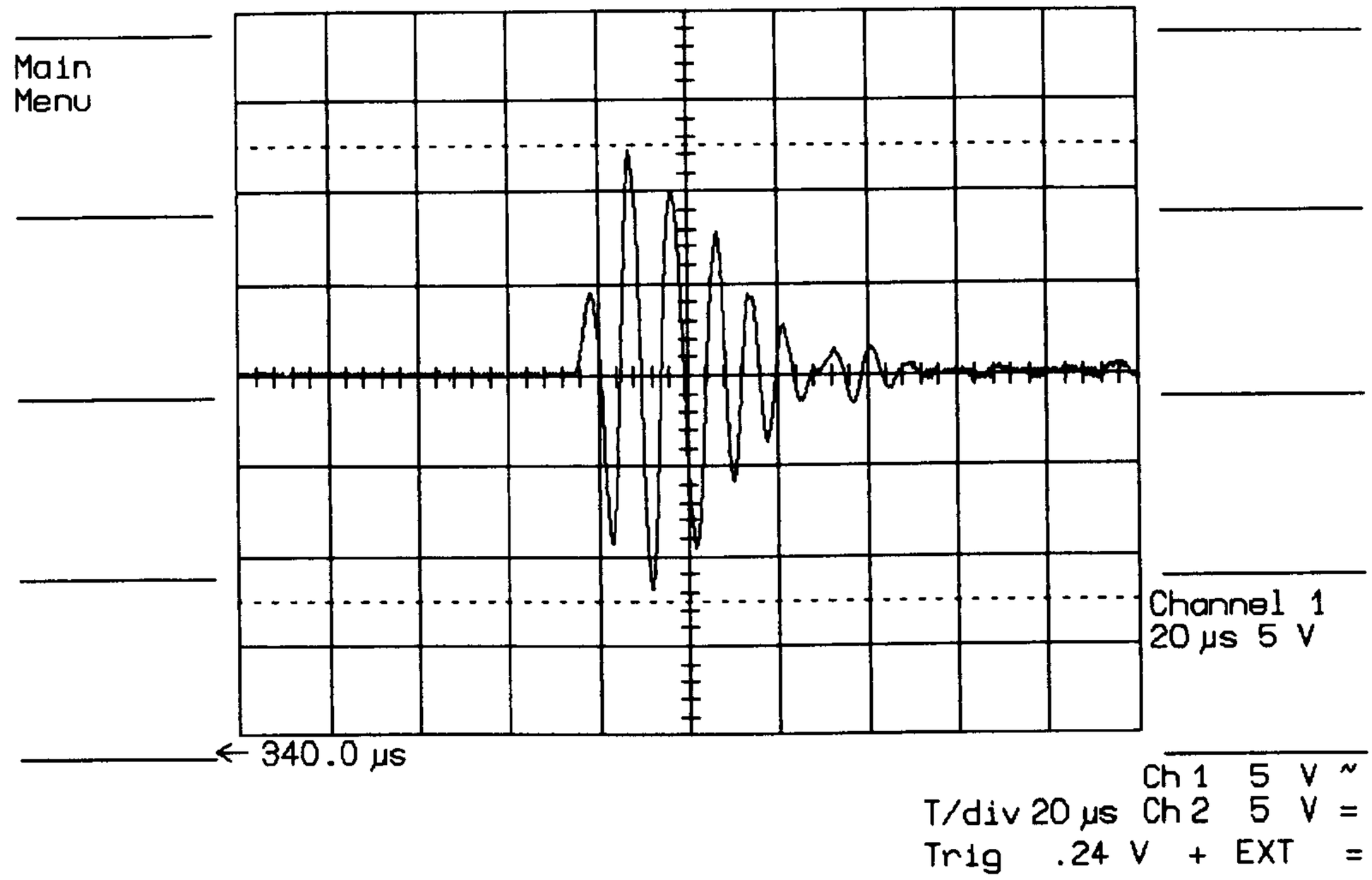

Figure 15: Resultant transmit waveform with 3 cycle driving waveform.

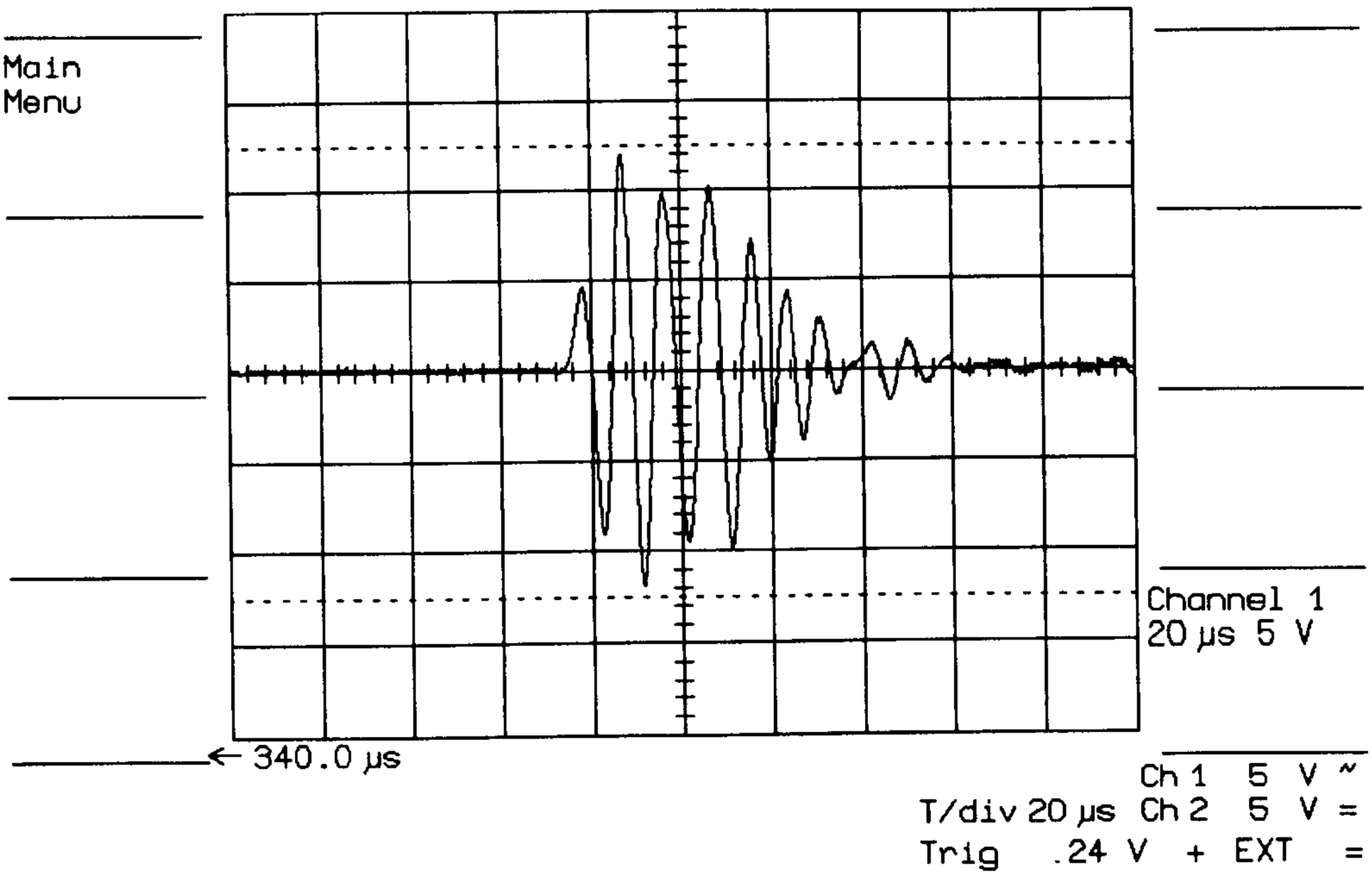

Figure 16: Resultant transmit waveform for 4 cycle driving waveform.

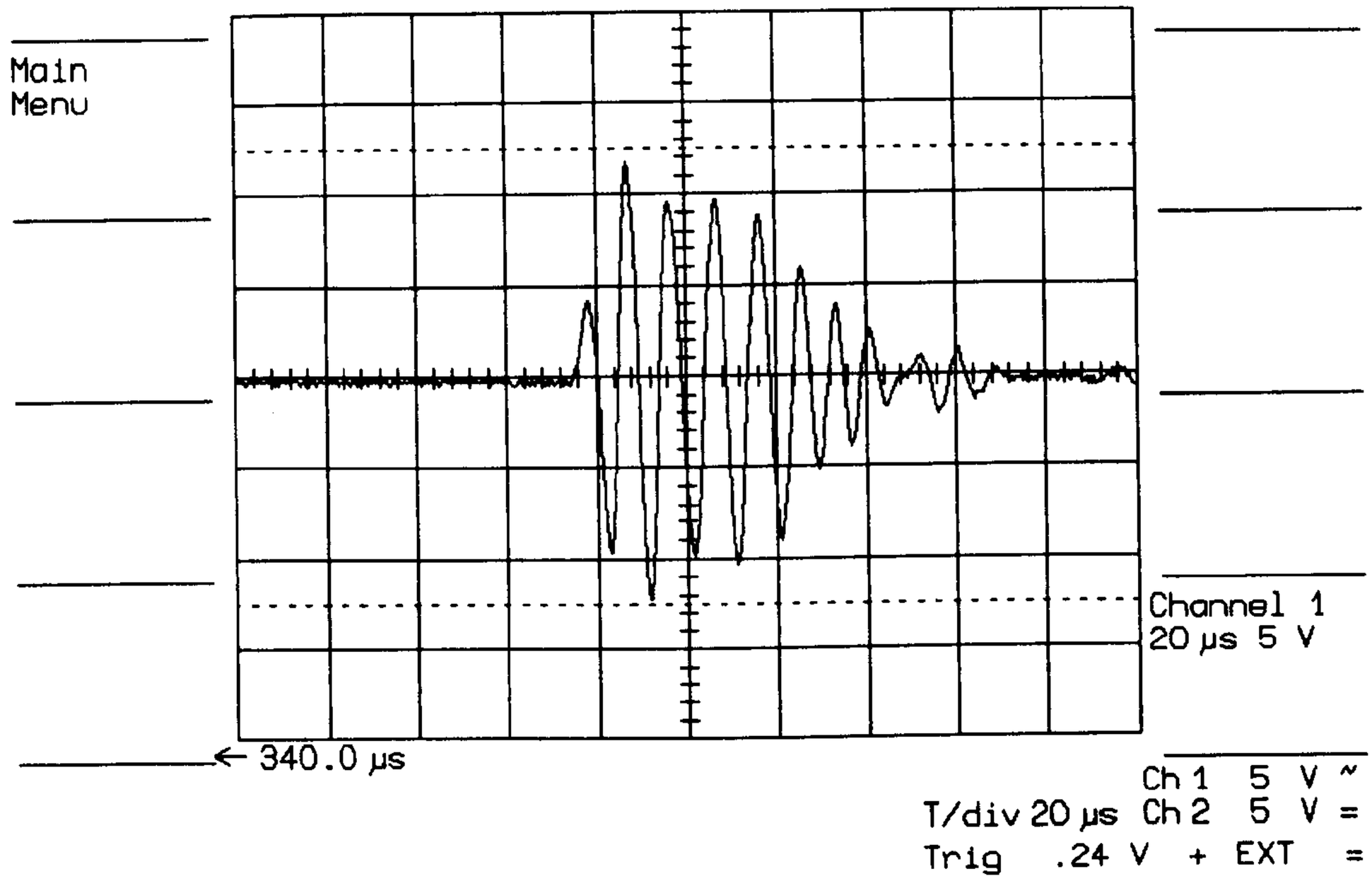

Figure 17: Resultant transmit waveform with 5 cycle driving waveform.

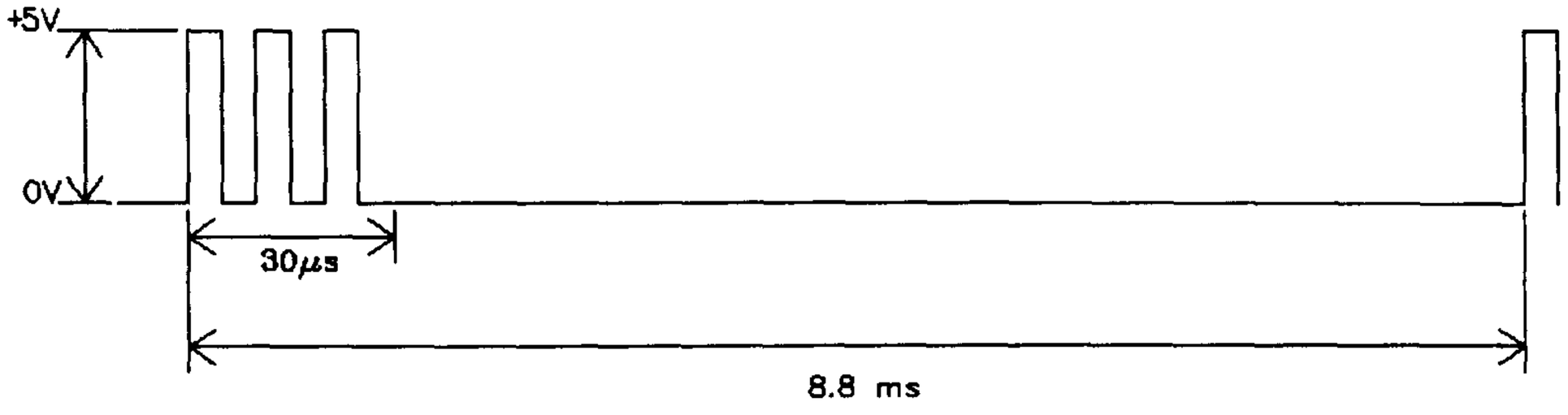

Figure 18: Final transmitter drive waveform.

The final parameters for the transmit waveform are shown below in table 1 and a sketch of the waveform is shown in Figure 18.

PARAMETER	VALUE
Frequency	100KHz
Amplitude	0V - 5V
Pulse width	3 cycles
PRI	8.8ms

Table 1: Final drive waveform transmitter parameters.

The value chosen for the PRI is arbitrary and gives a maximum range of 1.5m in dry air at 20°C.

5.5.4 General design features.

It was decided to build the system as a series of memory mapped modules connected via buffers to the DSP expansion bus. This approach was chosen for four reasons:

1: The system would be easy to design and test in stages.

2: The system could easily be modified and expanded.

3: The data handling and timing functions could all be driven directly by DSP software, thus avoiding the design and construction of complicated timing and control circuitry.

4: The highest possible data transfer rates could be achieved.

Initially, four data acquisition modules were constructed combining the data acquisition and envelope generation functions. The data acquisition card was based around two 200kHz analogue to digital converters, one for the I channel and one for the Q channel. The sampling rate was chosen as reasonably priced A/D converters were available at this speed and the resulting resolution of the system would be adequate at 1.25° (see chapter 9). To allow the system to operate with a 16 element array a 16:1 multiplexer was designed to form the input to each channel.

5.6 Summary

This chapter has given an overview of the design criteria used when the system was being initially developed. The construction of the system and the design of each of the modules is covered in chapter 6, an evaluation of this hardware is then given in Appendix C.

5.7 References

1. S. C. Pomeroy, "Ultrasonic Phased Arrays for Robotics Modelling and Experimental Implementation", Ph. D. Thesis, University of Nottingham, 1989.

2. W. S. H. Munro, "Ultrasonic Phased Arrays for Use in Imaging and Automatic Vehicle Guidance", Ph. D. Thesis, University of Nottingham, 1990.

3. W. S. H. Munro and C. Wykes, "Arrays for 100Khz Air-borne Ultrasound", accepted for publication , Ultrasonics, 1993.

4. H. Carr, "Electrostatic Transducers for Air-borne Ultrasound", Ph. D. Thesis, University of Nottingham, 1989.

5. K. Lin, G. A. Frantz and R. Simar, "The TMS320 Family of Digital Signal Processors", Proceedings of the IEEE, Vol. 75, No. 9, September 1987, pp1143-1159.

6. G. Harp, "Transputer Applications", Pitman, 1989.

7. M. C. Jackson. and P. Mathewson. "Digital Processing of bandpass signals ," GEC Journal. Vol. 4, 1986. pp32-41.

8. D. W. Rice and K. H. Wu. "Quadrature sampling with high dynamic range," IEEE Transactions on Aerospace and Electronic Systems. AES-18. Nov 1982. pp736-739.

9. A. V. Oppenheim, "Digital Signal processing", Prentice Hall International, 1975.

10. H. Liu, A. Ghafoor and P. H. Stockman, "A new quadrature sampling and processing approach", IEEE Transactions on Aerospace and Electronic Systems, Vol. 25, No. 5, 1989, pp733-747.

11. P. Kleinschmidt and V. Mágori, "Ultrasonic Robotic Sensors for Exact Short Range Distance Measurement and Object Identification", Proc. IEEE Ultrasonics symposium, 1985, pp457-462.

CHAPTER 6

SYSTEM HARDWARE CONSTRUCTION

6.1 Introduction.

Chapter 6 provides a description of the construction and layout of the system hardware. Section 6.2 gives an overview of the digital signal processor chosen. Section 6.3 covers the design of each element of the hardware in detail and Section 6.4 describes the construction methods used. All circuit descriptions have been kept to block level since all designs are based around standard circuits elements. A system block diagram is also provided in Figure 1. It should be noted that, although the hardware can accept arrays with up to 16 elements, for clarity only a four element array is shown connected.

6.2 Digital Signal Processor Overview.

The reasons for the use of a digital signal processor have already been discussed in chapter 5 but it is necessary to have a basic understanding of the architecture of the TMS320C30 in order to appreciate how the DSP interacts with the data acquisition hardware. A knowledge of the internal layout of the chip is also vital to understand the function of software written in TMS320C30 assembly language.

The TMS320C30 chip is based on a Harvard Architecture design (multiple buses) but the data and program memory have been united to provide the advantages of both Harvard and Von Neuman architectures[1]. A block diagram of the device is shown in Figure 2. A more detailed description of chip operation is given in the users guide[2].

The internal structure of the chip may be loosely divided into:

1: On-chip memory and cache.

2: CPU with register file.

3: Peripheral bus and peripherals

4: Interconnecting buses.

The on-chip memory consists of two blocks of RAM (1k x 32), one block of ROM (4k x 32) and an instruction cache (64 x 32). The CPU contains an ALU (arithmetic logic unit), a floating point multiplier and a 32-bit barrel shifter. A barrel shifter allows a full 32 bit shift to be applied in one instruction cycle. The register file (Figure 3) contains 8 x 40-bit extended precision registers, 8 x 32-bit auxiliary registers and 12 x 32-bit control registers. The on chip peripherals provided are 2 serial ports, two timers and a DMA (direct memory access) controller. These communicate with the rest of the chip via a dedicated peripheral bus. Multiple interconnecting buses are provided to handle program, data and DMA operations in parallel.

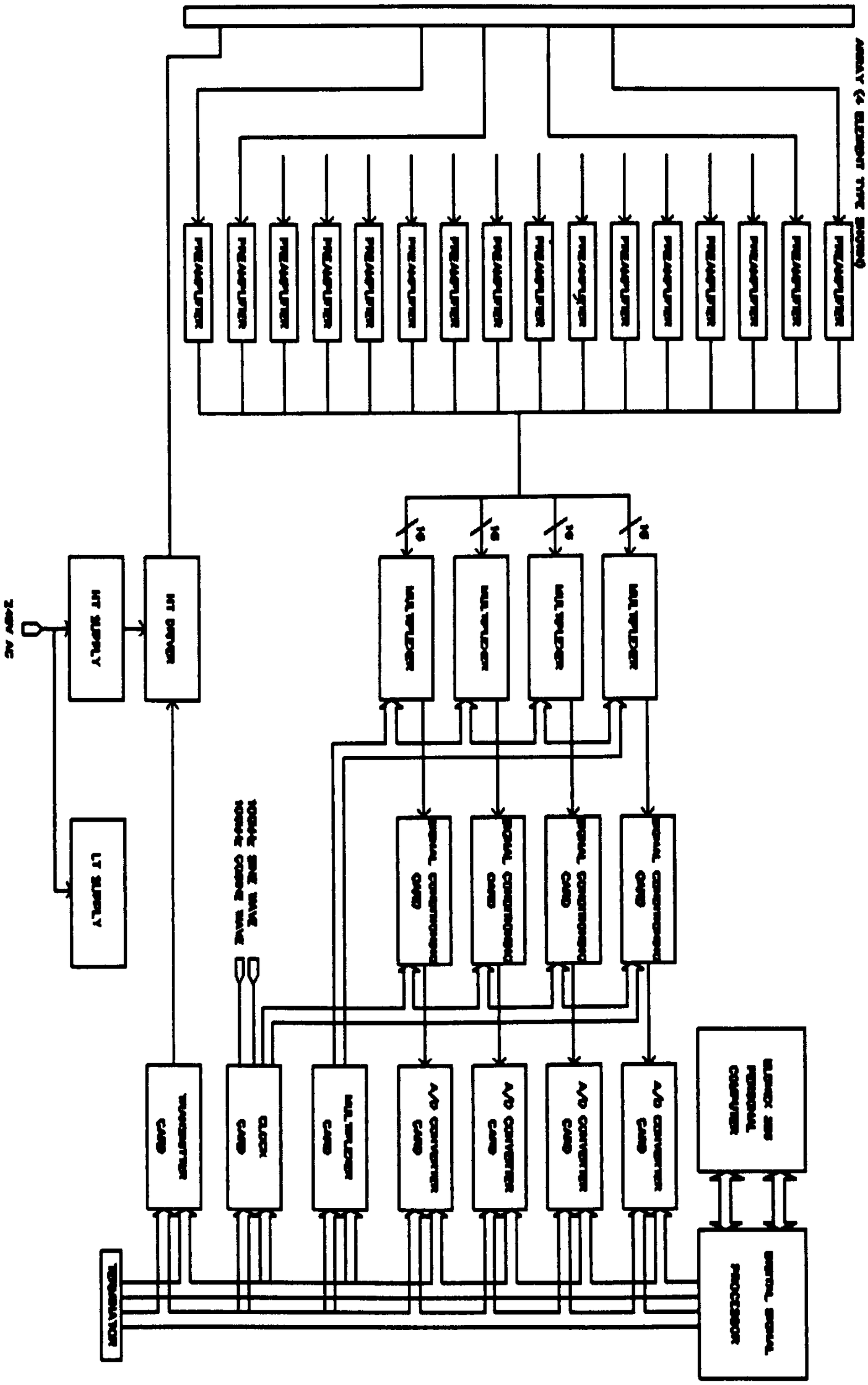

Figure 1 System block diagram

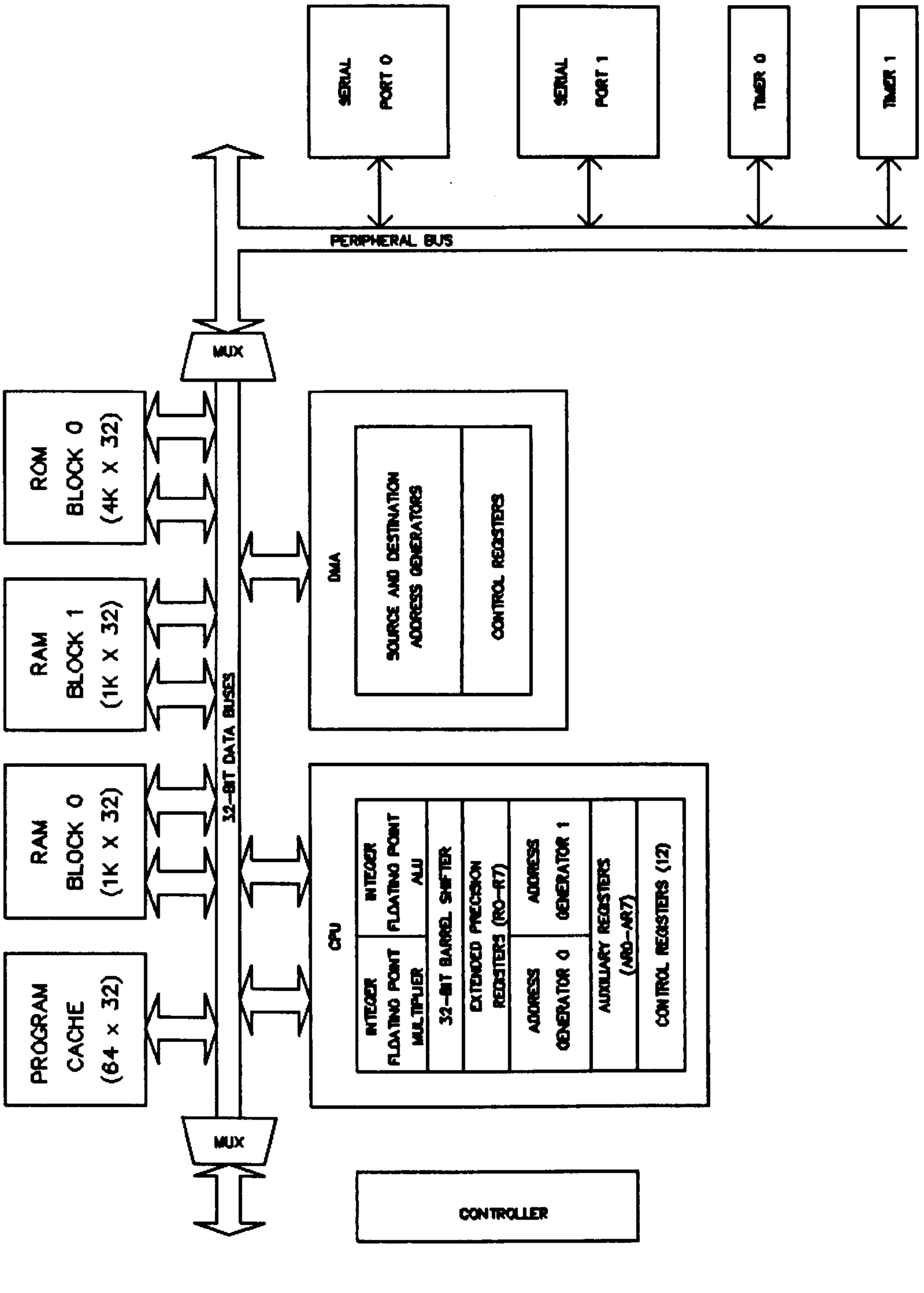

Figure 2: Block diagram of Texas Instruments TMS320C30 digital signal processor chip.

REGISTER NAME	ASSIGNED FUNCTION
R0	EXTENDED-PRECISION REGISTER 0
R1	EXTENDED-PRECISION REGISTER 1
R2	EXTENDED-PRECISION REGISTER 2
R3	EXTENDED-PRECISION REGISTER 3
R4	EXTENDED-PRECISION REGISTER 4
R5	EXTENDED-PRECISION REGISTER 5
R6	EXTENDED-PRECISION REGISTER 6
R7	EXTENDED-PRECISION REGISTER 7
AR0	AUXILIARY REGISTER 0
AR1	AUXILIARY REGISTER 1
AR2	AUXILIARY REGISTER 2
AR3	AUXILIARY REGISTER 3
AR4	AUXILIARY REGISTER 4
AR5	AUXILIARY REGISTER 5
AR6	AUXILIARY REGISTER 6
AR7	AUXILIARY REGISTER 7
DP	DATA PAGE POINTER
IR0	INDEX REGISTER 0
IR1	INDEX REGISTER 1
BK	BLOCK SIZE
SP	SYSTEM STACK POINTER
ST	STATUS REGISTER
IE	CPU\DMA INTERRUPT ENABLE
IF	CPU INTERRUPT FLAGS
IOF	I/O FLAGS
RS	REPEAT START ADDRESS
RE	REPEAT END ADDRESS
RC	REPEAT COUNTER
PC	PROGRAM COUNTER

Figure 3: CPU Register file

Several interfaces are provided to communicate with the outside world. These are:

1: Two buses (primary and expansion).

2: Two serial ports and two timers.

3: Two external flags.

4: Hold and hold-acknowledge signals.

The primary bus contains a 24-bit address bus and a 32-bit data bus. The expansion bus contains a 13-bit address bus and a 32-bit data bus. It also has two strobes, one for memory and one for I/O accesses. Both buses have the facility for up to seven wait states to be inserted by software or hardware; this allows easy interfacing with slow memory or peripherals. Since the other means of communication are not used in this application they will not be described here but they are fully described in reference[1].

The system has a 60ns instruction cycle which results in an operating speed of over 16 million instructions per second (MIPS) and over 33 million floating-point operations per second (MFLOPS). The use of a 24-bit address bus width gives an overall memory space of 16 million 32-bit words.

To simplify the design of the system, the DSP based section was purchased as a ready made development board manufactured by Loughborough Sound Images Ltd (LSI). This is supplied as a PC AT plug-in board complete with TMS320C30 processor, 256k words of SRAM and serial and parallel interfaces. This was housed in an Elonex 25MHz 386 personal computer. Connection to the data acquisition system is made by a 50 way ribbon cable connected to the LSI DSPlink[3]

connector, using a 50 way plug and socket mounted in a spare PC expansion slot. DSPlink is a standard DSP interface developed by LSI which allows processor independent hardware interfacing.

6.3 System description.

The system was designed to be as flexible as possible. With this in mind, it was built as a series of discrete modules each constructed on a separate printed circuit board. Each module is plugged into a common bus built to the format of the LSI DSPlink[3] but with the addition of -5V, +12V and -12V power supplies. One extra signal "STARTCONV" has also been provided; this is described in 6.3.3. In order to minimise noise pickup inter-module analogue signal connection is via a screened cable connected to the relevant board by sub-miniature bayonet (SMB) plugs and sockets.

6.3.1 Transducer preamplifiers.

Each array element is connected directly to a preamplifier tuned to a centre frequency of 100kHz with a gain of 38dB and a bandwidth of 50kHz. The preamplifiers are constructed using Surface Mount Technology; this allows 16 such amplifiers to be mounted on a printed circuit board measuring 160mm x 100mm. Each amplifier can thus be mounted almost directly behind the corresponding receiver element. This helps to limit signal attenuation and noise. It should be noted that the preamplifiers are not the work of the author. Further details may be found in reference[4].

6.3.2 Transmitter drive electronics.

The 180 VDC bias supply for the transmitter is provided by a simple linear power supply. During transmission, this is switched on and off at the required frequency. Switching is performed by a MOSFET which is triggered by a TTL signal from the transmitter board described in chapter 5. It should be noted that the transmitter drive electronics are not the work of the author. Further details may be found in reference[3].

6.3.3 Analogue to digital conversion cards.

A block diagram of the analogue to digital conversion card is shown in Figure 4 and a photograph of the completed card is given in Figure 6. The card may be broken down into sections, the digital section, consisting of buffering, address decode and data latches, and the analogue section consisting of input amplifier, mixers, lowpass filters level shifters and analogue to digital converters. The analogue section is described first.

The analogue signal enters the board via a screened "SMB" connector and is fed to an AC coupled differential amplifier with a voltage gain of 10. After amplification the signal is split and applied to the inputs of two Analogue Devices (AD) 534 precision IC multipliers and mixed with two externally generated 100kHz sine waves, the inputs to the two mixers being in phase quadrature. After mixing, the two signals are filtered by a pair of National Semiconductor LMF60 6th order switched capacitor Butterworth lowpass filters. These are controlled by an external clock running at 1.228MHz (clock 1); this gives a cutoff frequency of 25.6kHz. After filtering, the signals are level shifted and scaled before being fed

to two AD7575 analogue to digital converters. The level shifting and scaling circuit effectively increases the dynamic range of the converters from 0 to +2.46V to ±5V. The AD7575 8-bit converters used have a conversion time of 5μs and a built in track and hold to ensure accurate conversion timing. They are supplied with an external 4MHz clock signal (clock 2). When conversion is complete the digitised output is stored in a latch.

Consider now the digital section of the board. The board can operate in two modes; these are referred to as 'master mode' and 'slave mode'. In master mode if the board is addressed then a signal is produced called STARTCONV, this not only starts the A/D conversion on the board but is also fed to the bus. This means that conversion is started on all other boards present in the system. This facility allows for conversion to be synchronised. At the same time any data from a previous conversion is stored in the latch circuits and 'tri-stated' to the bus, in 'slave mode' The A/D converters are not effected when the board is addressed but any data stored in the latches by the action of the externally generated STARTCONV signal is 'tri-stated' on to the bus by the signal DSEND.

The operating mode of the board is determined by the generation of the signal MSTR/SLV. This signal is produced when the 2 least significant bits of the address are zeros. The board address is set using 8 switches it can be set anywhere between 0x0801000 and 0x0801FFF. On the system, four boards are used, the addresses of which are shown in Table I.

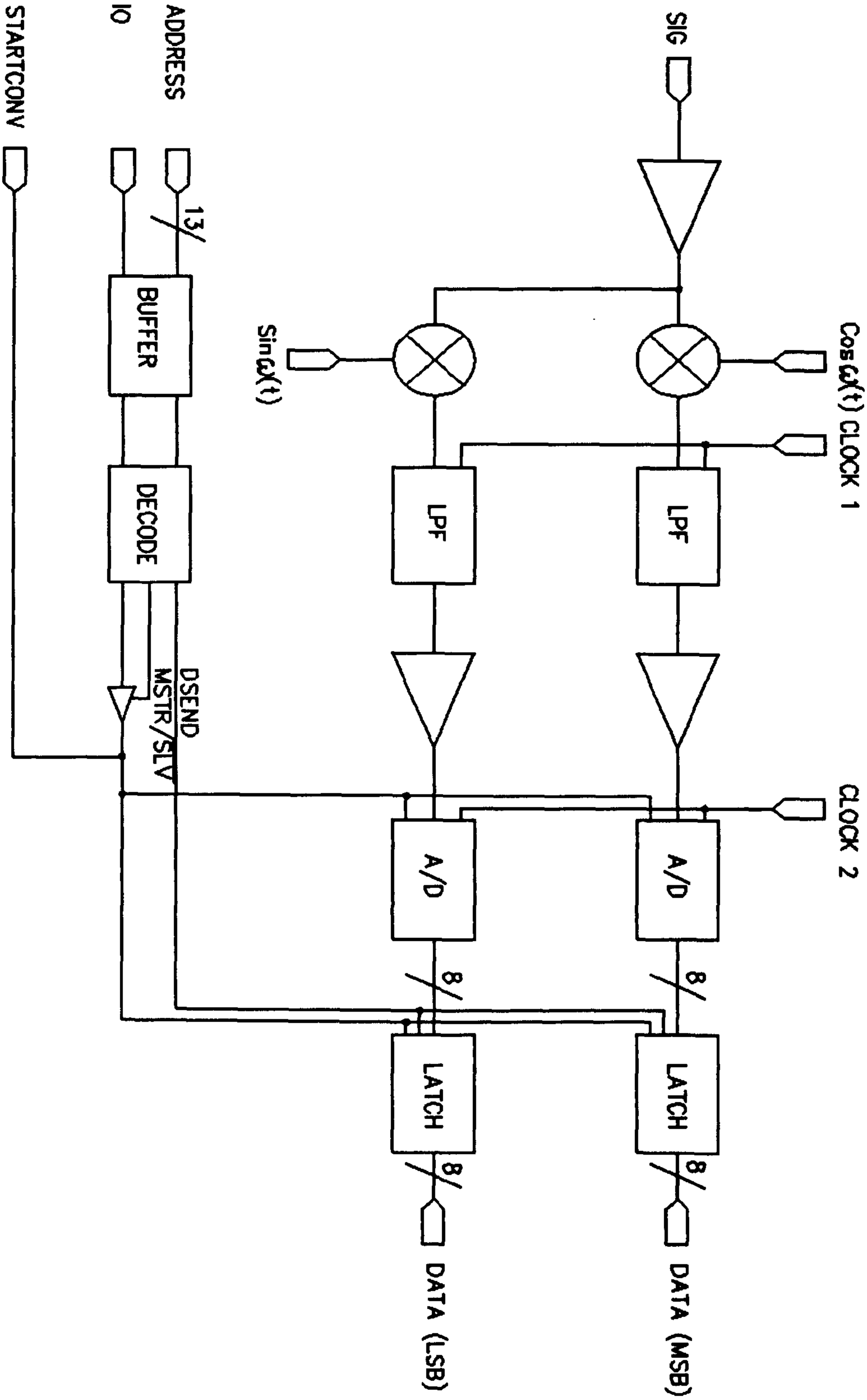

Figure 4: Block diagram of analogue to digital converter card.

6.3.4 Transmitter card.

A block diagram of the transmitter card is shown in Figure 5 and a photograph of the completed card is shown in Figure 7.

When the transmitter address is called up by the DSP an output pulse is generated by the address decode circuit. This is used to toggle the output of a latch. This output is used to switch the bias via a line driver circuit and the mosfet switching circuit described in section 6.3.2. The transmitter output is connected to a BNC socket located on the front panel.

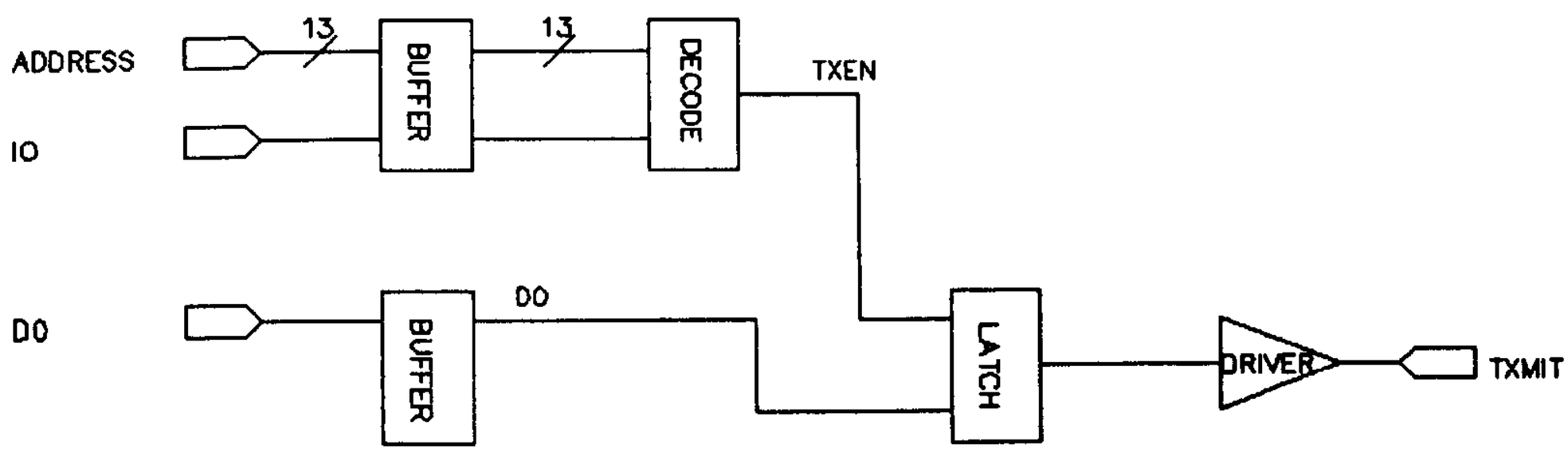

Figure 5: Block diagram of transmitter card.

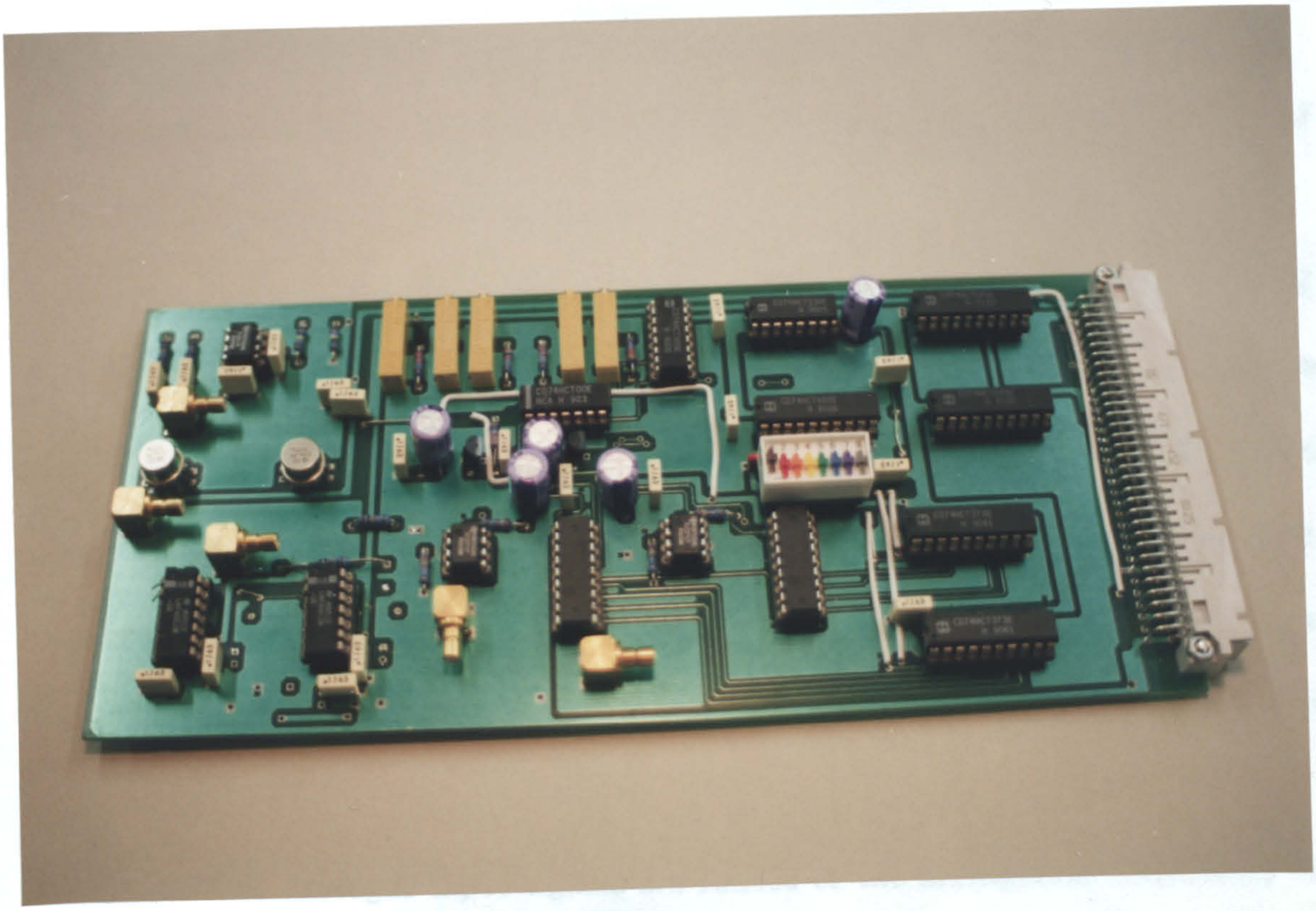

Figure 6: Photograph of completed A/D card.

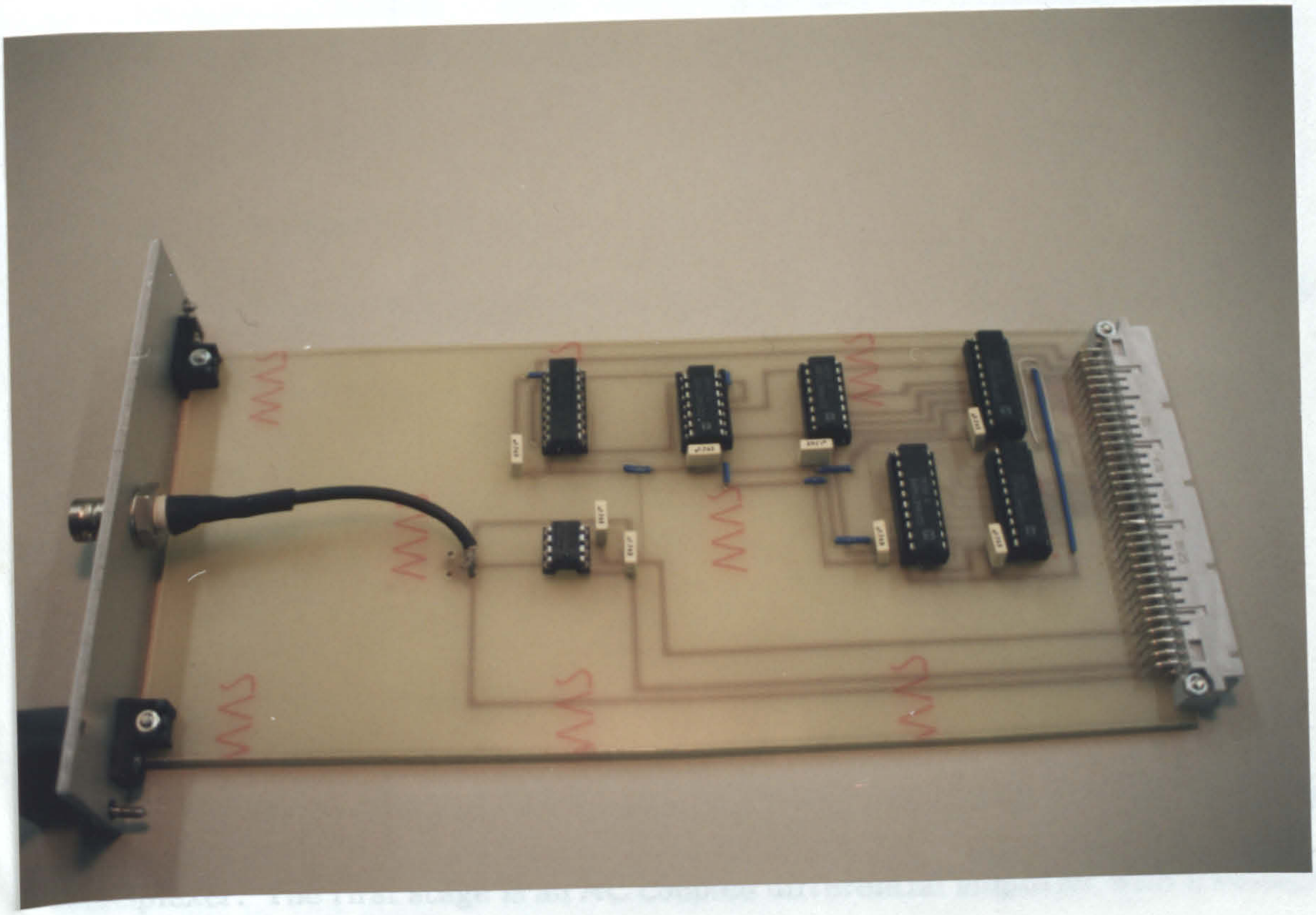

Figure 7: Photograph of completed transmitter card.

6.3.5 Multiplexer card.

A block diagram of the multiplexer card is shown in Figure 8 and a photograph of the completed card is shown in Figure 10.

The card is based around 4 Plessey DG526 16:1 multiplexer chips all of which share a common address decode circuit. The memory map for this card is shown in Table I. When a multiplexer is addressed a chip select signal is produced and the internal data bus buffer is enabled by the signal DEN. This allows the channel to be set by writing a hexadecimal number between 0 and F to the data bus. The signal WR is also checked to ensure that a write and not a read is occurring.

The 16 analogue input signals are routed to the multiplexer chips from 16 BNC connectors located on the front panel via screened cables. The output signals are connected to 4 internally mounted "SMB" sockets.

6.3.6 Signal conditioning card.

A block diagram of the signal conditioning card is shown in Figure 9 and a photograph of the completed card is shown in Figure 11.

Figure 9: Block diagram of signal conditioning card.

The analogue signal enters the signal conditioning card directly from the multiplexer. The first stage is an AC coupled differential amplifier with a voltage gain of 2 the signal is then filtered by a active second order 100kHz bandpass

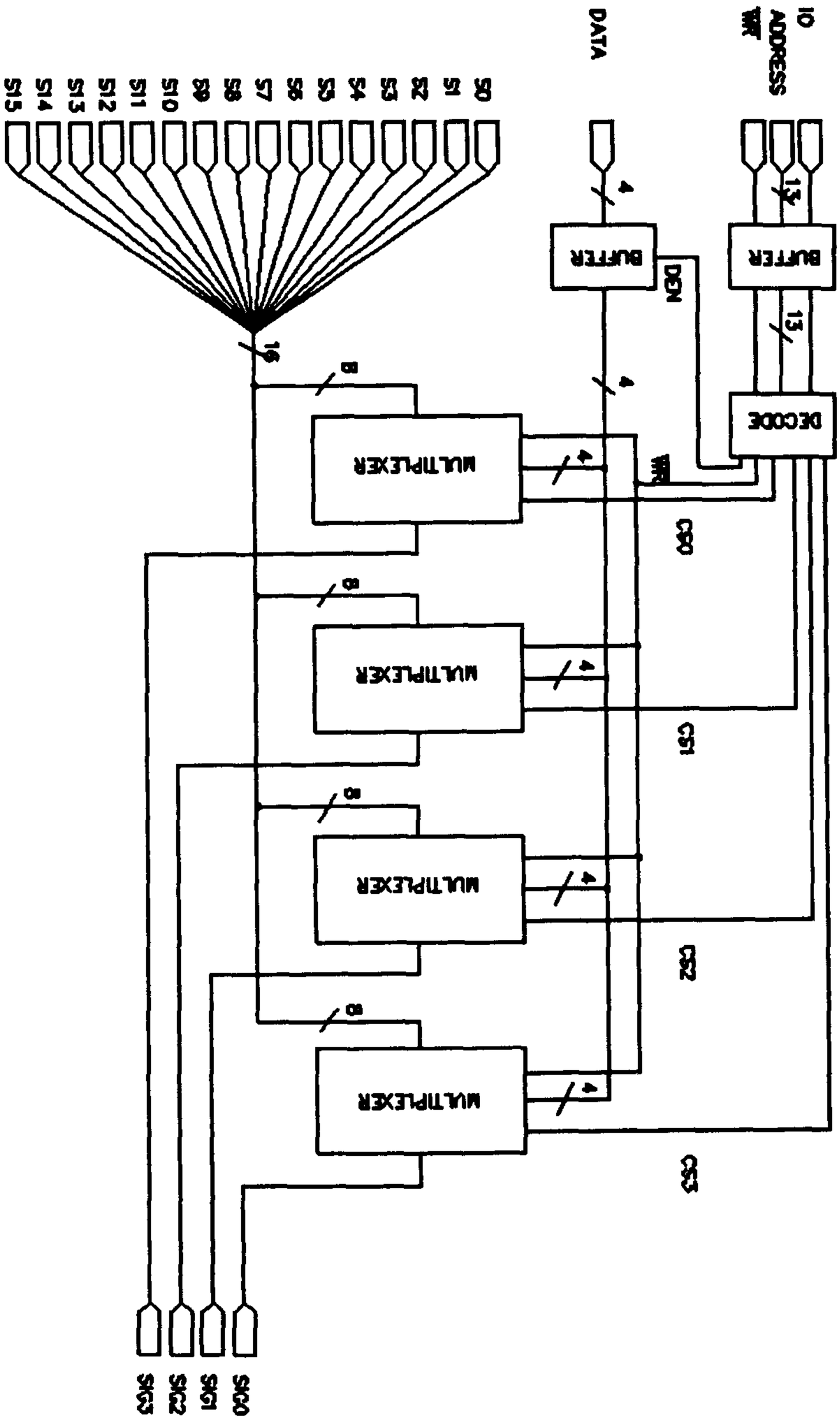

Figure 8: Block diagram of multiplexer card.

filter with Q factor 3 and a voltage gain of 15. After filtering the signal is amplified by a further amplifier with voltage gain adjustable between 1 and 10. The output of this stage is fed to the analogue to digital conversion card via a screened cable.

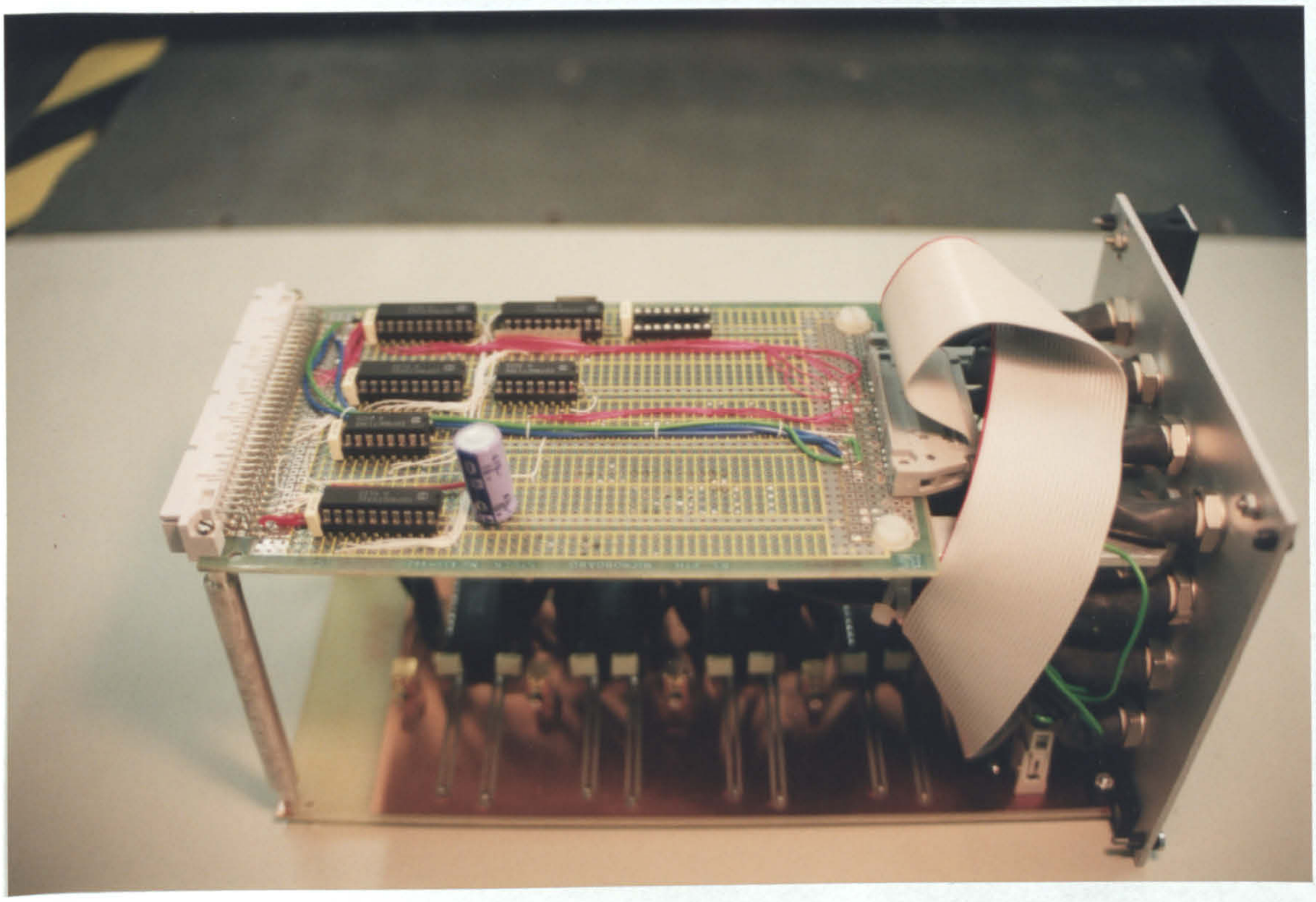

Figure 10: Photograph of completed multiplexer card.

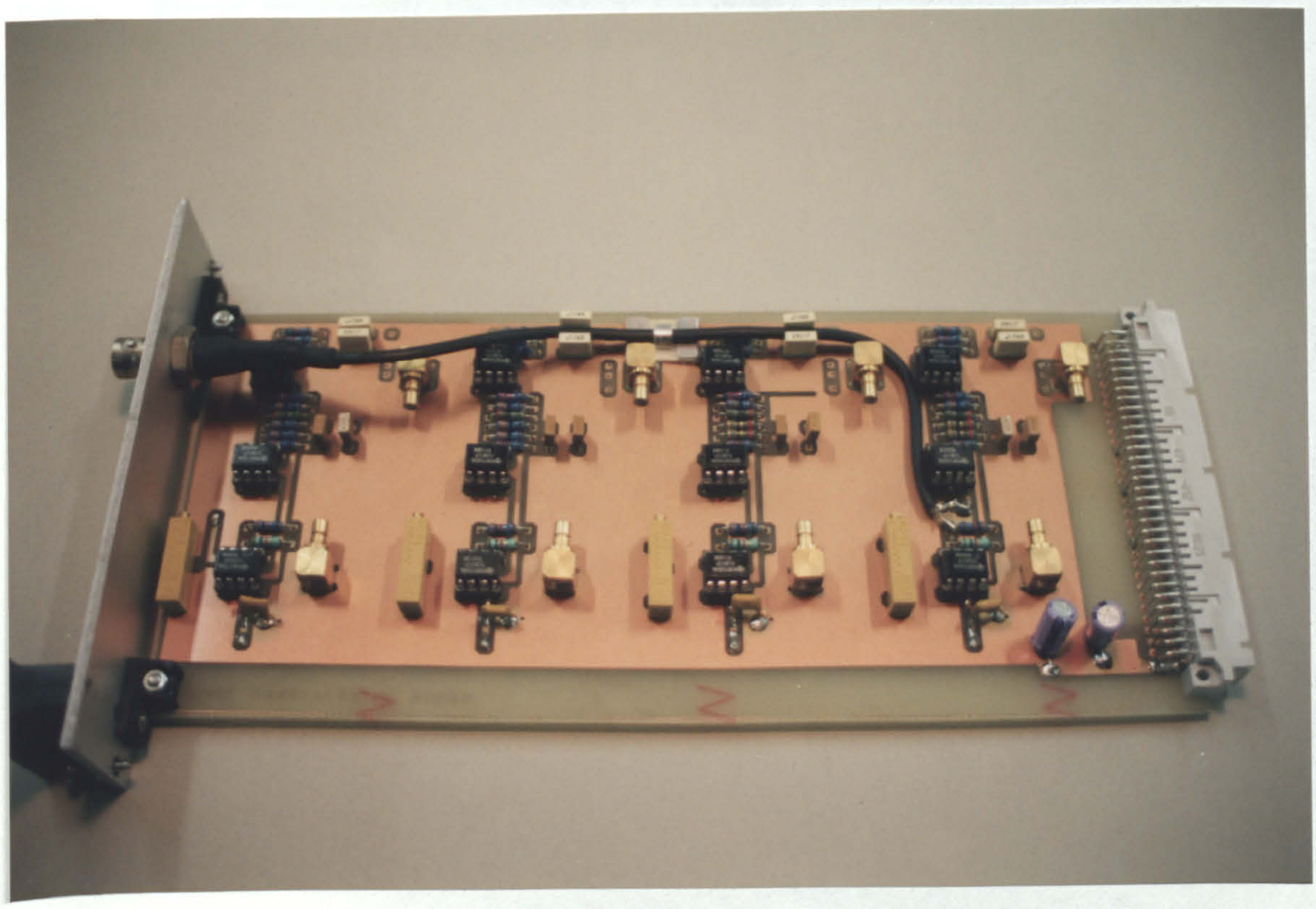

Figure 11: Photograph of completed signal conditioning card.

6.3.7 Clock card.

This consists of two crystal oscillators which provide the two system clocks (clock 1 and clock 2) described in 6.3.3. This board also distributes the two mixer inputs which are supplied by two external signal generators. Connection is made via two BNC sockets mounted on the front panel.

6.4 Construction.

The system was constructed around a standard 19 inch rack. Inter module communication is provided by a 64 way backplane mounted at the rear of the rack. Each circuit board terminates in a 64 way male connector which mates with a corresponding connector on the backplane. The backplane is passively terminated by a series of resistors connected to all address, data and signal lines. Power is provided by three separate power supplies mounted behind the backplane. Two of these provide a ∓5V supply and a ∓12V supply for the analogue electronics. The third supply provides +5V for the digital electronics. All the boards are constructed on printed circuit boards. These where all manufactured in-house except for the analogue to digital conversion cards. The convertor printed circuit boards were, manufactured by an outside contractor due to their complexity and the need for plated through holes.

ADDRESS	HARDWARE DEVICE
0x0801100	ANALOGUE TO DIGITAL CONVERSION CARD 1
0x0801101	ANALOGUE TO DIGITAL CONVERSION CARD 2
0x0801102	ANALOGUE TO DIGITAL CONVERSION CARD 3
0x0801103	ANALOGUE TO DIGITAL CONVERSION CARD 4
0x0801200	MULTIPLEXER CARD CHANNEL 1
0x0801201	MULTIPLEXER CARD CHANNEL 2
0x0801202	MULTIPLEXER CARD CHANNEL 3
0x0801203	MULTIPLEXER CARD CHANNEL 4
0x0801300	TRANSMITTER CARD

Table I: Hardware memory map.

6.5 References.

1. P. Pamapamichelis and R. Simar, "The TMS320C30 Floating-Point Digital Signal Processor", IEEE Micro Magazine, Vol. 8, No. 6, December 1986, pp10-28.

2. Third Generation TMS320 User's Guide, Texas Instruments, 1988.

3. "TMS320C30 PC System Board Technical Reference Manual", Loughborough Sound Images Ltd, March 1991.

4. W. S. H. Munro "Ultrasonic Phased Arrays for Use in Imaging and Automatic Vehicle Guidance", Ph. D. thesis, University of Nottingham, 1990.

CHAPTER 7

TARGET LOCATION

7.1 Introduction.

Chapter 7 provides a detailed description of the methods used by the author to locate targets in range and bearing. Both the theoretical basis and actual implementations will be described. The basic theory of the methods used has already been discussed in chapter 4. Practical results are presented in chapters 9 and 10.

Section 7.2 covers a simple digital beam forming method which is expanded in 7.3 and 7.4 to include dynamic focusing and aperture compensation. A method of reducing the computational load and memory requirements is also described in these sections. Section 7.5 deals with the application of further processing to improve the resolution and accuracy of both methods. Section 7.6 describes an interpolated beam former using a 16 channel $\lambda/2$ array. Section 7.7 describes a method in which range bearing solutions are only calculated for a location when there is a high likelihood of a target being present at that location. A summary of the contents of this chapter is provided in section 7.8.

7.2 Linear beam forming.

The theory behind linear beam forming has already been discussed in detail in

chapter 4. The practical application of this method was implemented as an assembly function. Assembly language was chosen both for speed and because it allows full exploitation of the large register set available on the TMS320C30. This makes it easier to write efficient, and therefore fast, code.

The software written to perform the beam forming process is described here in the form of pseudo code. The full assembly language listing for the far field beam former is shown in Appendix B.

The right hand and left hand sweeps of the beam former are performed by two different programs. The left hand beam former, which forms beams from the far left to the centre of the angle of view of the array, is described first.

Pseudo code far field beam former (left hand):

Load starting skews to registers.

for 0 to number of beams {

Load data start addresses to address registers.

Add offsets to set starting range.

Load beam storage address to address register.

For 0 to beam length {

Form summation and store at beam storage address

Increment beam storage address and data address registers.

}

Subtract offsets to set next beam skews.

}

The loading of a set of initial starting skews allows the beams to be formed from the outer edge of the angle of view. This makes later data handling more convenient but is not necessary to the functioning of the beam former. The offsets for the far field case are either 0, 1, 2 or 3 dependent on which array element the data has come from. An almost identical program is used to form the right hand beams where offsets are added to set the next beam skews. The starting skews in this case are zero since the beam is required to start from 0°.

Pseudo code far field beam former (right hand):

Load starting skews (0) to registers.

for 0 to number of beams {

Load data start addresses to address registers.

Add offsets to set starting range.

Load beam storage address to address register.

For 0 to beam length {

Form summation and store at beam storage address

Increment beam storage address and data address registers.

}

add offsets to set next beam skews.

}

7.3 Focused beam forming.

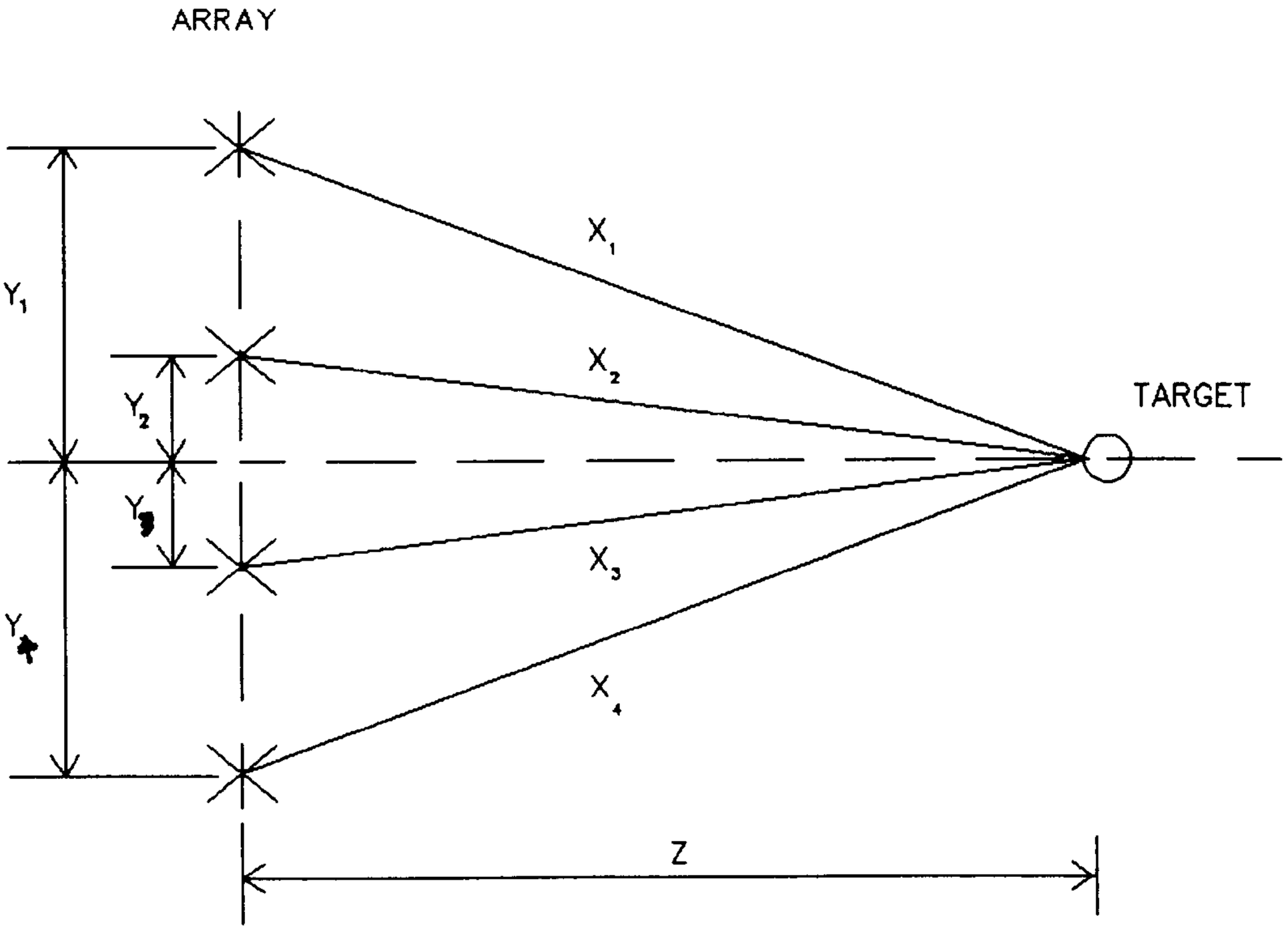

Figure 1: Focusing on a central target

So far it has been assumed that all the beam forming summations can be performed along a straight line. This is, however, only the case for targets in the far field region (chapter 3) and does not apply for near field targets. With a very wide aperture, as is used in the current system, the majority of targets lie in the near field. To obtain improved results, this must be taken into account during processing. From Figure 1 and Figure 2, it is apparent that the length of each individual path between target array element is not equal to the distance to the centre of the array, Z. If the values to be calculated are range Z and angle θ, (see Figure 2), a series of offsets must be calculated for $X_1..X_4$ so that the data is summed along a curved, rather than straight, address plane. This has the effect of focusing the beam on the target.

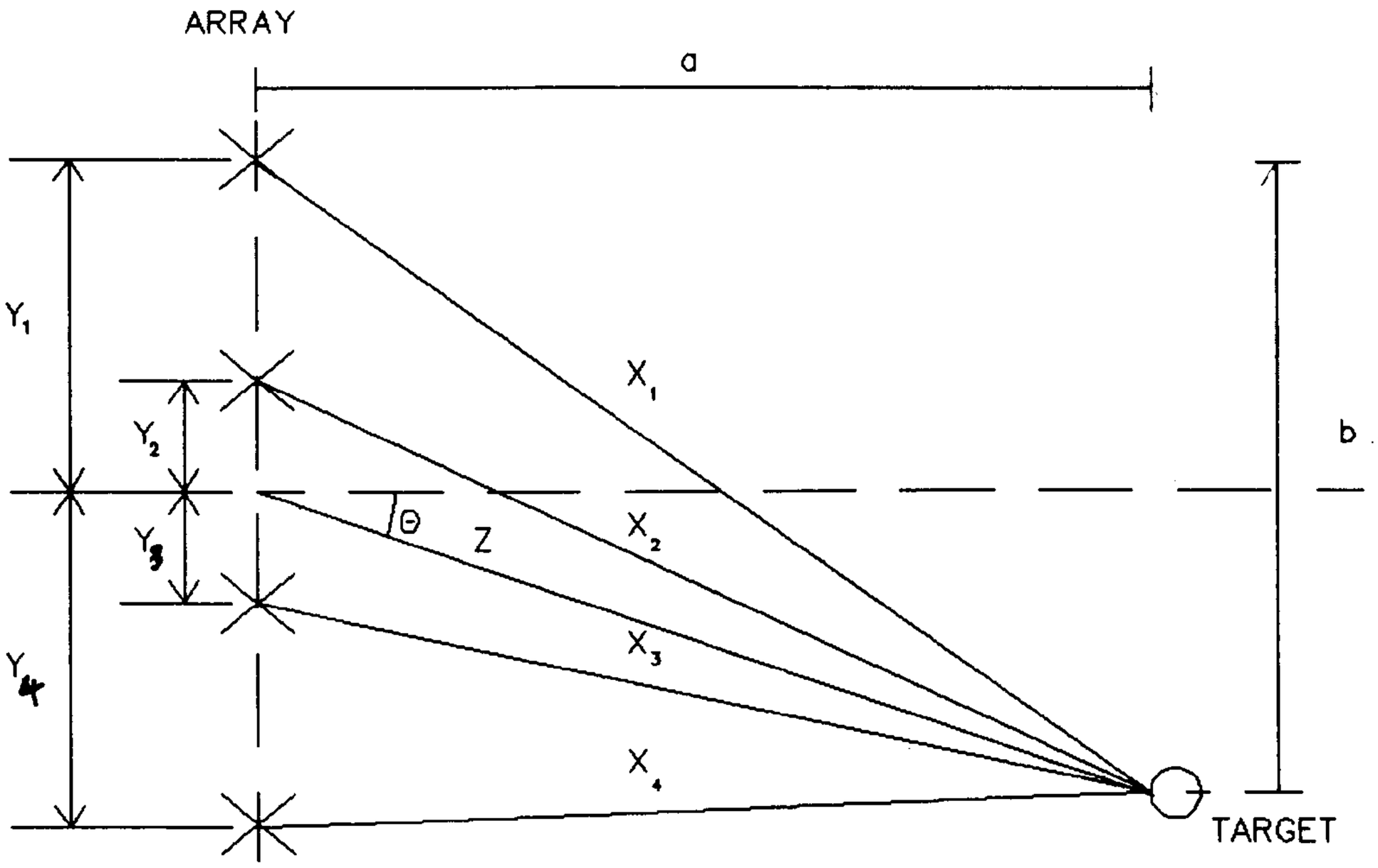

Figure 2: Focusing on a single offset target.

The offsets can be calculated for any range and bearing by use of the following formula:

$$O_n = X_n - Z \qquad (1)$$

O_n = Calculated offset.

X_n = Target to element distance.

Z = Distance to centre of array.

X can be calculated at any range and bearing from:

$$X_n = \sqrt{a^2 + b^2} \qquad (2)$$

a and b may be calculated using simple trigonometry:

$$\begin{aligned} a &= Z\cos\theta \\ b &= y_n + Z\sin\theta \end{aligned} \qquad (3)$$

Therefore:

$$O_n = \sqrt{Z^2\cos^2\theta + (y_n + Z\sin\theta)^2} - Z \qquad (4)$$

This gives the path length difference, this may also be expressed in terms of time between samples:

$$O_n = \frac{\sqrt{Z^2\cos^2\theta + (y_n + Z\sin\theta)^2} - Z}{c\tau} \qquad (5)$$

where

c = speed of sound in air.

τ = time between samples.

y_n = array element separation.

7.3.1 Partial focusing.

The focusing offsets can either be calculated dynamically or they can be pre-calculated and stored. Pre-calculation provides much faster operation but suffers from the disadvantage of requiring a large quantity of memory. To form 47 beams each 1m long would require in excess of 94,000 offsets. Three possible methods by which this figure may be reduced are discussed in this section. The first is to produce offsets for only one side of the sweep and then reverse the order of the offsets for the second half of the sweep. This will reduce the number of offsets required to 48,000. The number is not reduced by half since the central beam at 0° must still be generated. A second method by which the number can be further

reduced is by dividing the beam into a series of regions and only generating offsets for the start of these regions. The beam former then performs a linear beam form within the region. This process has been called partial focusing.

A method of reducing the amount of computation required for digital beam forming has also been suggested by O'Donnell[1]. The method he describes relies on the similarities in the focusing coefficients that exist between adjacent beams. The system is particularly appropriate in beam splitting applications where the beams tend to be very close together. In beam splitting a coarse beam is produced during transmit which is then split into further beams during receive. No attempt was made to apply this method here as the difference in the values of the focusing coefficients between beams was considered too great.

7.3.2 Limitations of partial focusing.

This section analyses the penalties that are incurred by using partial focusing to increase processing speed. Memory constraints limit the size of the focusing zone to a minimum of 5 samples, this has the effect of sampling the focusing offsets at five sample widths. As with any digitally sampled system there is the likelihood of errors if the sampling rate is not high enough. There are two main sources of error present due to this approach. The first is rounding which will occur in any memory based digital beam forming system because the offsets must be integers; an address cannot be modified by a floating point value. The second source of error arises from the assumption that the progression is linear within the focusing zones. This is not however the case due to the non-linear nature of the focusing offsets. At longer ranges as the situation becomes more of a far field case, the

offsets are more linear and there should be less errors introduced by linear beam forming between offsets. The offsets generated for both short range (75mm - 160mm) and long range (750mm - 835mm) are shown in Appendix E. The effect of increasing range on the linearity of the offset can be seen from these values. The effect of these errors on accuracy is measured in chapter 9 and the use of partial focusing is compared with full focusing.

7.3.3 Practical implementation.

The practical implementation of this is again realised in the form of an assembly language program, a full listing of which is given in Appendix B. The main difference between this and the far field beam former described in section 7.2 is that there are no skews generated by the program since all the offsets required are generated externally. It is important to note that after the end of a focusing region is reached, the region width is subtracted to allow the next offset to be added. This prevents the increment accumulating.

Pseudo code for focused beam former:

for 0 to number of beams {

Load data start addresses to address registers.

Add offsets to set starting range.

Load beam storage address to address register.

For 0 to beam length {

Add next offset to data start address registers.

For 0 to region_width {

Form summation and store at beam storage address

Increment beam storage address and data address registers.

}

Subtract region_width from data start address registers.

}

}

In the practical implementation, the offsets are pre-calculated by a computer program and stored in file. During beam former operation this file is down loaded to the DSP board memory.

To compare the effect of using a partially focused beam former, with a fully focused beam former another DSP program was written where the offsets were calculated individually during each beam form. The offsets could not be pre-calculated because of insufficient memory. The software implementation for this was written in C and Spox as time was not considered to be critical.

7.4 Beam forming with wide aperture.

In these calculations, it has been assumed that the transmitter is a point source located in the centre of each array element. In reality the transmitter is a flat plate and produces a flat wave front[2]; the calculations must therefore be modified to take this into account. If this is not done then significant errors may

result, especially if the transmitter is very wide in relation to the element spacing.

From Figure 2 it is apparent that the transmitted signal comes from the point on the transmitter closest to the target. This is then reflected at an angle on to the receiving element. In conventional ultrasonic ranging systems[3] it is always assumed that the target range is equal to half the 'roundtrip' time multiplied by the speed of sound in air. If this is used in this case, then the target will appear closer than it really is. To compensate for this, the transmission path length must be subtracted to give the target range. The transmission path length(l) for a particular range and bearing may be calculated from:

$$l = Z\cos\theta \qquad (6)$$

This can be converted to an offset for the beam forming algorithm using the formula:

$$O_t = O_n + \frac{Z\cos\theta}{c\tau} \qquad (7)$$

where

O_t = Total offset.

This is implemented with the same program as the focused beam former but with different offset values.

7.5 Interpolation beam forming.

The resolution of digital beam forming is limited by sampling rate. A common method used to overcome this is to artificially increase the sampling rate using

interpolation. This has been implemented using a fast Fourier transform method to increase the sampling rate. It was decided not to use the more usual implementation[4] of this method, which involves the interpolation of all the acquired data before beam forming because of the very large amount of data that would have resulted and the massive processing overhead that would have been incurred. An alternative method was devised in which a coarse beam form is first performed and the output scanned for targets; when a target is found, data corresponding to the target is interpolated and a second much more accurate beam form is performed. This is represented as a pseudo code program below:

Beam form all data.

Locate all targets.

for 0 to number of targets{

Un beam form target to find data in array output vectors.

Interpolate data around target.

Do second beam form.

Store new range and bearing.

}

This has been implemented on the DSP using a mixture of assembly language and C. This method could also be applied to improve the accuracy of the direct method described in 7.7.

7.6 A 16 channel interpolated beam former.

A fully interpolated beam former was implemented to test the feasibility of using a 16 channel $\lambda/2$ array with envelope beam forming. The sampling rate was increased to 1MHz. Due to the size of resulting arrays of data the beam former could only operate over a field of view of ±25°.

7.7 Direct method.

The method, described in 7.4, whilst being an effective and accurate way of determining target bearing, suffers from the major drawback that it is computationally very intensive. If the data received from the array could be pre-scanned, and all possible targets identified, then the range and bearing need only be found for individual targets. This would result in a substantial saving in time and processing effort. This approach has been called the direct method.

7.7.1 Solution of target equation.

A set of equations can be derived to give the cartesian co-ordinates of target from any two sets of range data.

Figure 3 shows a target located in front of the array and offset to one side.

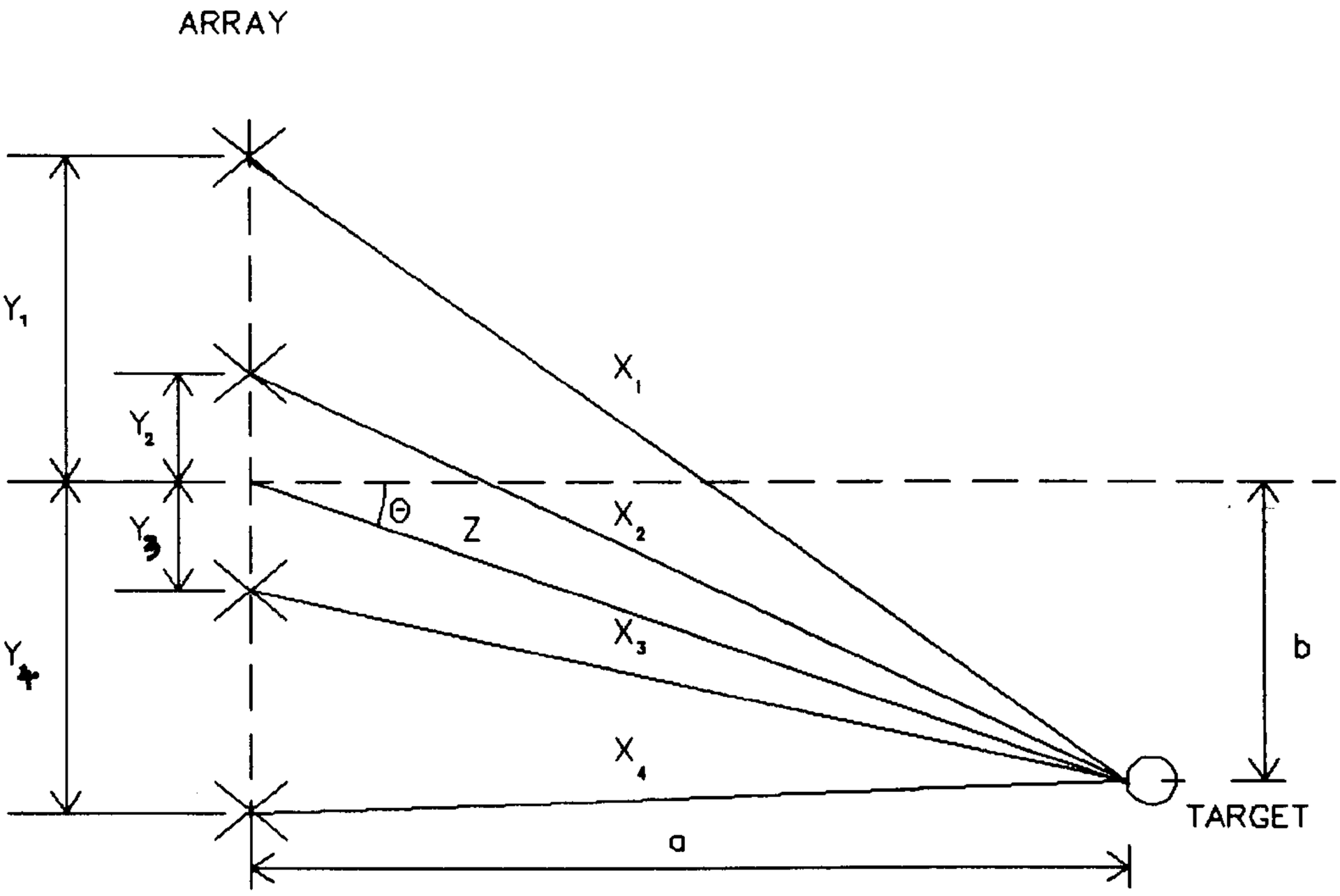

Figure 3: Diagram of array with a single offset target.

The cartesian co-ordinates a and b can be calculated from the polar co-ordinates Z and θ:

$$\begin{aligned} a &= Z\cos\theta \\ b &= Z\sin\theta \end{aligned} \qquad (8)$$

The output from any channel of the data acquisition system represents the roundtrip time for a pulse of sound to travel between array and target. This is directly proportional to the outward distance 'a' plus the return distance 'X_n'.

The distance 'x_{rn}' measured by the hardware is therefore:

$$x_{rn} = x_n + a \qquad (9)$$

The value of y_n is dependent on the geometry of the array and is constant for any particular array.

Therefore the return distance from target to array is:

$$x_n = \sqrt{a^2+(b-y_n)^2} \tag{10}$$

If the outward distance is included then:

$$x_{rn} = \sqrt{a^2+(b-y_n)^2} + a \tag{11}$$

$$x_{rn}-a = \sqrt{a^2+b^2-2by_n+y_n^2} \tag{12}$$

Squaring both sides:

$$x_{rn}^2-2ax_{rn}+a^2 = a^2+b^2-2by_n-y_n^2 \tag{13}$$

This process may be repeated for all x and y values to give a complete set of four equations.

$$\begin{aligned} x_1-2a &= \frac{1}{X_1}(b^2-2by_1-y_1^2) \\ x_2-2a &= \frac{1}{x_2}(b^2-2by_2-y_2^2) \\ x_3-2a &= \frac{1}{x_3}(b^2-2by_3-y_3^2) \\ x_4-2a &= \frac{1}{x_4}(b^2-2by_4-y_4^2) \end{aligned} \tag{14}$$

Subtracting and re-arranging gives a set of 6 equations which can be used to calculate a range bearing solution from any two elements.

$$0 = b^2\left(\frac{1}{x_1} - \frac{1}{x_2}\right) - 2b\left(\frac{y_1}{x_1} - \frac{y_2}{x_2}\right) + \left(\frac{y_1^2}{x_1} - \frac{y_2^2}{x_2}\right) - (x_1 - x_2) \quad (15)$$

$$0 = b^2\left(\frac{1}{x_1} - \frac{1}{x_3}\right) - 2b\left(\frac{y_1}{x_1} - \frac{y_3}{x_3}\right) + \left(\frac{y_1^2}{x_1} - \frac{y_3^2}{x_3}\right) - (x_1 - x_3) \quad (16)$$

$$0 = b^2\left(\frac{1}{x_1} - \frac{1}{x_4}\right) - 2b\left(\frac{y_1}{x_1} - \frac{y_4}{x_4}\right) + \left(\frac{y_1^2}{x_1} - \frac{y_4^2}{x_4}\right) - (x_1 - x_4) \quad (17)$$

$$0 = b^2\left(\frac{1}{x_2} - \frac{1}{x_3}\right) - 2b\left(\frac{y_2}{x_2} - \frac{y_3}{x_3}\right) + \left(\frac{y_2^2}{x_2} - \frac{y_3^2}{x_3}\right) - (x_2 - x_3) \quad (18)$$

$$0 = b^2\left(\frac{1}{x_2} - \frac{1}{x_4}\right) - 2b\left(\frac{y_2}{x_2} - \frac{y_4}{x_4}\right) + \left(\frac{y_2^2}{x_2} - \frac{y_4^2}{x_4}\right) - (x_2 - x_4) \quad (19)$$

$$0 = b^2\left(\frac{1}{x_3} - \frac{1}{x_4}\right) - 2b\left(\frac{y_3}{x_3} - \frac{y_4}{x_4}\right) + \left(\frac{y_3^2}{x_3} - \frac{y_4^2}{x_4}\right) - (x_3 - x_4) \quad (20)$$

These may be solved as quadratics and the results used to find the value of '*a*'.

This approach gives much better resolution than normal beam forming. The increase in resolution occurs because there need only be one sample difference

between array element 1 and array element 4 to locate a target. From equation (15) in chapter 4 section 4.4 the maximum angular resolution for an array with 4 elements with a separation of 40mm and a sampling rate of 200kHz the maximum resolution is 2.5°.

With the direct method the equation becomes:

$$\tan\theta = \frac{\tau C}{d} \qquad (21)$$

where d is the separation between the two receiving elements in use.

Using elements 1 and 4 of the array this evaluates to 0.82°.

7.7.2 Practical implementation.

To implement this system the output of the array must first be pre-scanned to identify any possible targets and find their range. Next they must be matched to form pairs of range values which are associated with the same target. A pseudo code version of the software developed is shown below:

Acquire data.

Pass data through threshold and find peak.

Store ranges of all targets in range table (save amplitude for analysis).

For 0 to length of range table{

Pick value from 1st element and look for range value within ±Qmm.

Calculate range and bearing and store in target table along with matching amplitude.

}

This method works very well with a limited number of targets and is capable of detecting the corners of a 25mm cube. It is however prone to errors when complex target scenes are encountered. The code for this was written in a mixture of assembly language and C.

7.8 Summary

This chapter has covered the implementation of two methods of locating the position of a target. The first method is well known but the second method has been developed by the author. The digital beam forming system has been greatly speeded up by the use of a soft focusing method, also developed by the author, and the standard focusing algorithm has been modified for use with a very wide aperture transmitter ($\approx 200\lambda$). A full presentation and analysis of all the practical results obtained using these methods is provided in chapter 9 and chapter 10.

7.9 References

1. M. O'Donnell, "Efficient Parallel Receive Beam Forming for Phased Array Imaging Using Phase Rotation", Proceedings IEEE ultrasonics symposium, 1990, pp1495-1498.

2. W.S.H. Munro , "Ultrasonic phased array for use in imaging and automatic vehicle guidance", Phd. Thesis, University of Nottingham, 1990.

3. R. Kuc. "A spatial Sampling Criterion for Sonar Obstacle Detection", IEEE transactions on pattern analysis and machine intelligence. Vol. 12, No.7, JULY 1990.

4. R. A. Mucci, "A Comparison of Efficient Beam Forming Algorithms", IEEE transactions on acoustics speech and signal processing, Vol. 32, No. 3, June 1984, pp548-558.

CHAPTER 8

IMPROVING SYSTEM ACCURACY

8.1 Introduction

Chapter 8 provides a detailed description of the methods employed to improve the accuracy and reliability with which targets can be extracted from signals generated by the data acquisition system. The processing used is designed both to eliminate the presence of false targets and to increase the resolution of measurement. Section 8.2 compares the methods available for detecting the arrival time of the received signals. Section 8.3 investigates the application of matched filtering to improve resolution and increase signal to noise, section 8.4 describes a further method used to increase resolution of the system. Section 8.5 describes the most common ways in which false targets are generated and describes ways in which they can be removed. Finally the chapter is summarised in section 8.6.

8.2 Target detection.

The primary objective of the ultrasonic measurement system is to obtain accurate range measurements for any targets present within the system field of view. To locate a target accurately, using the pulse echo method described in chapter 4, the precise time of arrival of its echo must be measured; there are several ways of

doing this. The time of arrival may be taken as the time when the amplitude of a signal exceeds a preset level (thresholding) or the position of the peak amplitude of the signal may be taken. These two methods are discussed in detail and their reliability assessed when used to detect the presence of targets using the ultrasonic location system. The inaccuracies present in both these methods are shown to be directly related to the signal to noise level.

8.2.1 Thresholding.

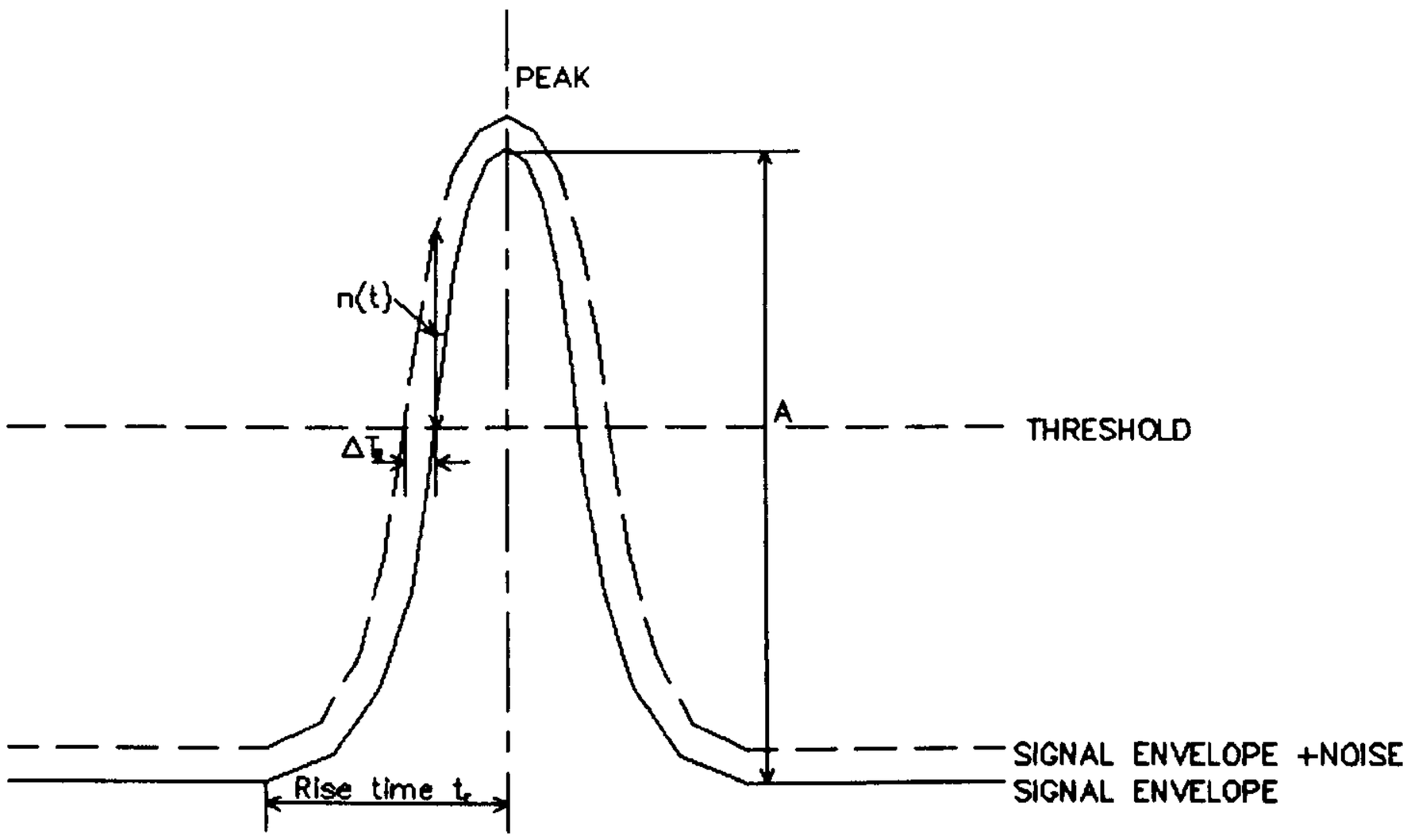

Figure 1: Effect of noise on a typical signal envelope.

A typical signal envelope is shown in Figure 1. If a thresholding system is used to measure the arrival time of the signal then the error due to noise (ΔT_R) may be written[1]:

$$\Delta T_R = \frac{n(t)}{A/t_r} \qquad (1)$$

where

n(t) is the noise in the vicinity of the threshold crossing.

A is the signal amplitude.

t_r is the rise time.

The presence of noise in the system has the effect of shifting the leading and trailing edges of the pulse and thus altering their relative arrival times. For large signal to noise ratios (SNR) the slope of the pulse is effectively unchanged by the presence of noise but for low SNR the effect may be significant. Equation (1) may be rewritten as:

$$[(\Delta T_R)^2]^{1/2} = \delta T_R = \frac{t_r}{(A^2/n^2)^{1/2}} = \frac{t_r}{(S/N)^{1/2}} \qquad (2)$$

where *S/N* is the signal to noise power ratio.

Values of δT_R were calculated for three types of target a 5mm dia

Target	SNR (dB)	δT_R (μs)	δR (mm)
25mm Cylinder	17.5	0.9	0.15
5mm Cylinder	16.2	1.2	0.2
Corner	9.3	5.9	1.0

Table 1: Calculated error for different target types.

cylinder, a 25mm diameter cylinder and a corner. The signal to noise ratios used were measured at the with the targets positioned at a range of 500mm from the array. The amplitudes of the signal and noise were measured using the output

from the data acquisition system. The resulting values are shown in Table 1 along with the equivalent range error δR. The range error values assume dry air at a temperature of 20°C.

From these calculations it is evident that the inaccuracy in range measurement is dependent on the relationship between the threshold value and the peak of the signal. This ratio can vary significantly even when no noise is present. This can be compensated for by using an adaptive threshold where the threshold is always a fixed fraction of the pulse amplitude. Both a fixed threshold and an adaptive thresholding system were implemented in software and tested. The standard deviations of the measured ranges were calculated for 100 firings for the three targets used to calculate the theoretical errors. The adaptive threshold was set to measure the time from the point at which the pulse has reached half its maximum amplitude. This is the point at which the rate of change of amplitude is maximum so the error due to noise should be a minimum. The results are shown in Table 2 and Table 3.

Target	Standard Deviation (mm)
25mm Cylinder	0.35
5mm Cylinder	0.46
Corner	0.51

Table 2: Results using a fixed threshold.

The same three targets where used in each case and placed at a range of 500mm from the array. The three targets where chosen so that the returns would have three different amplitudes with the 25mm cylinder having the largest and the

Target	Standard Deviation (mm)
25mm Cylinder	0.31
5mm Cylinder	0.36
Corner	0.46

Table 3: Results using an adaptive threshold.

corner having the smallest. It can be seen that in all cases the standard deviations for the adaptive threshold are less than those for the fixed threshold. The accuracy of the measurements also decreases with SNR as predicted by equation (2). The calculated range error does not agree very well with the measured range error but the measured values of SNR used for the calculated values were instantaneous and not averaged.

8.2.2 Peak detection.

An alternative target detection system method to that discussed in section 8.2.1 is the use of a peak detector. With a peak detector the accuracy of the measurement system depends on the sharpness of the peak. If the peak is relatively flat then small noise spikes may cause errors. If the noise is relatively constant there will be little effect on the range. The precise effect is impossible to calculate since the process is random. A peak detector system was implemented in software and tested. The standard deviations were calculated over 100 firings for the three targets and the values used to calculate the theoretical errors. The results obtained are shown in Table 4. The targets used where identical to those used in section 8.2.1.

Target	Standard Deviation (mm)
25mm Cylinder	0.17
5mm Cylinder	0.19
Corner	0.26

Table 4: Results using a peak detector.

8.2.3 Comparison of target detection methods.

It can be seen that in all cases the standard deviations for the adaptive threshold are less than those for the fixed threshold. The best method is the use of a peak detector as this has the lowest standard deviation of the three. The peak detector only works in this system because the peaks of the envelopes are relatively sharp; if the pulses were flattened then the precise position of the peak would be difficult to find. In this situation, an adaptive threshold would be likely to provide the most accurate method of determining the time of arrival of an ultrasound pulse.

8.3 Matched filtering.

As discussed in the previous section, the use of a wide pulse prevents the use of a peak detector. It also decreases the range resolution of the sensor. In some applications a wide pulse width may be advantageous since it allows the transmitted energy to be increased. Thereby improving the sensitivity of the transducer, and the disadvantages of a wide transmitted pulse can be overcome by the use of a matched filter. A classical description of a matched filter is that

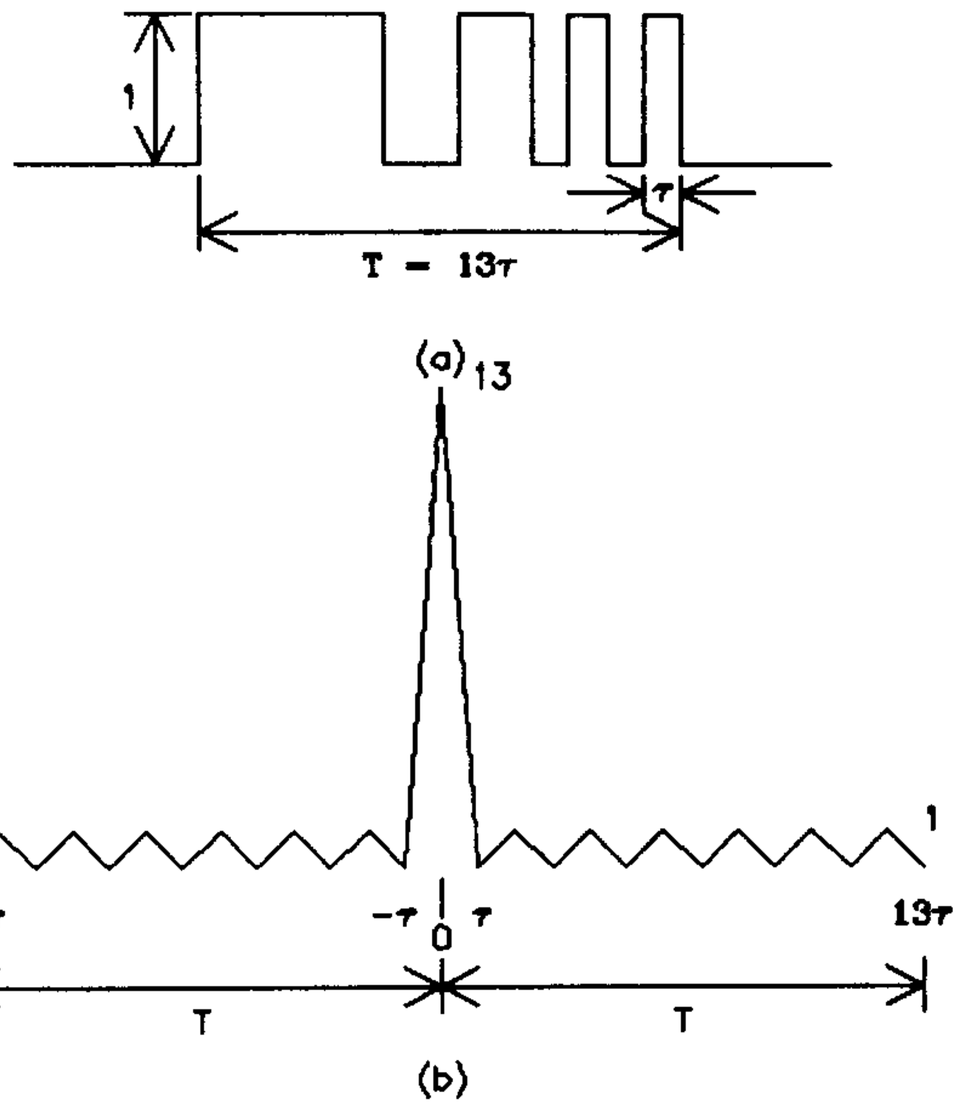

Figure 2: Barker code waveform.

given by North[2]; "The matched filter is the filter which optimises the signal to noise power ratio in the presence of additive white Gaussian noise". In effect a matched filter is a device that will give an output only when a specific waveform is detected. It can be shown that the response of a matched filter is the autocorelation function (ACF) of the signal[3]. The effectiveness of a matched filter in a receiver can be optimised by careful choice of the transmitted waveform, one such waveform which is common in radar is called a Barker code[1]. An example of a Barker code is shown in Figure 2 (a) and its ACF is shown in Figure 2 (b) it can be seen that the ACF has a narrow and pronounced peak with small and equal time sidelobes. The example shown has 13bits, this is the maximum known code length[1] which will produce the type of ACF shown in Figure 2, but they exist in lengths from 2 bits. Barker codes have been applied to ultrasonics by Peremans et al[4] in a long range application. The work is repeated here to test its efficacy in a short range application and to show that the hardware and software are flexible enough to implement such a system. In Peremans[4] work,

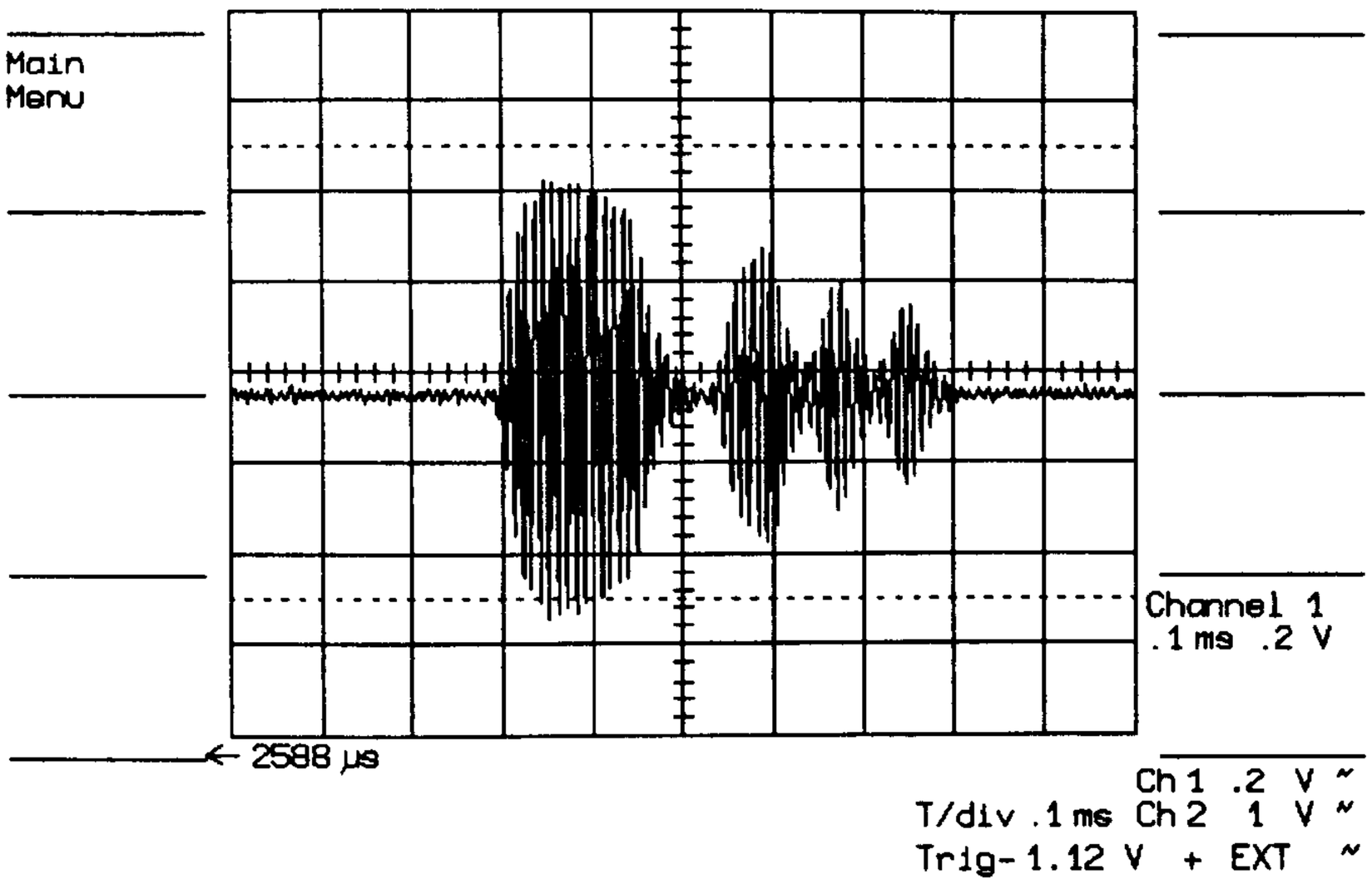

Figure 3: Transmitted waveform with 13 bit Barker code.

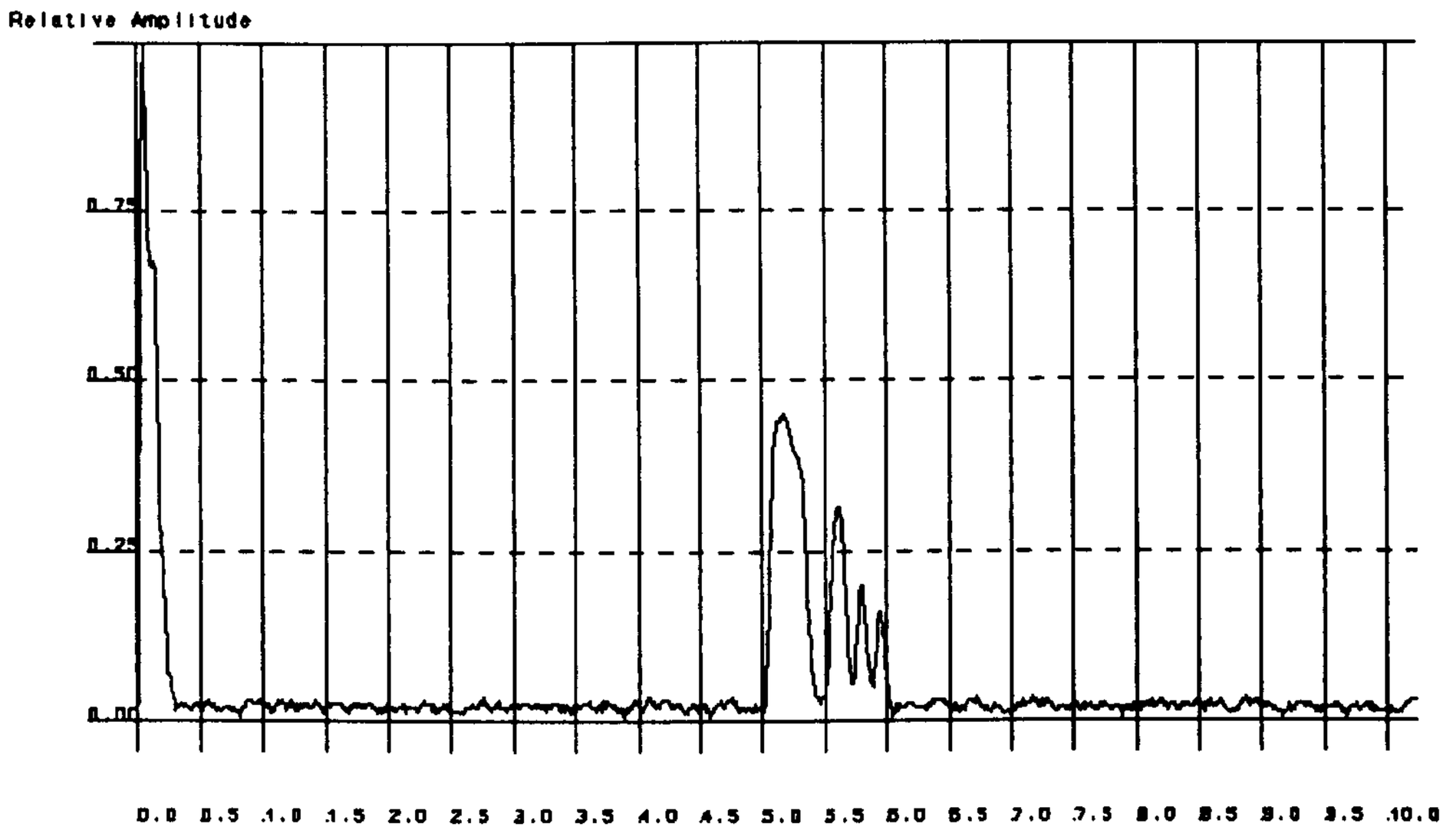

Figure 4: Received 13 bit Barker code waveform.

the 13bit Barker code shown was used resulting in a transmitted pulse length of 0.6ms. With a 0.6ms pulse length the minimum range is 105mm at 20°C. This compares with a minimum range of 3.5cm with the single transmitter pulse.

8.3.1 Practical implementation.

The resulting transmitted waveform is shown in Figure 3 and the received waveform from a single target at 500mm is shown in Figure 4. The same target is shown in Figure 5 after matched filtering.

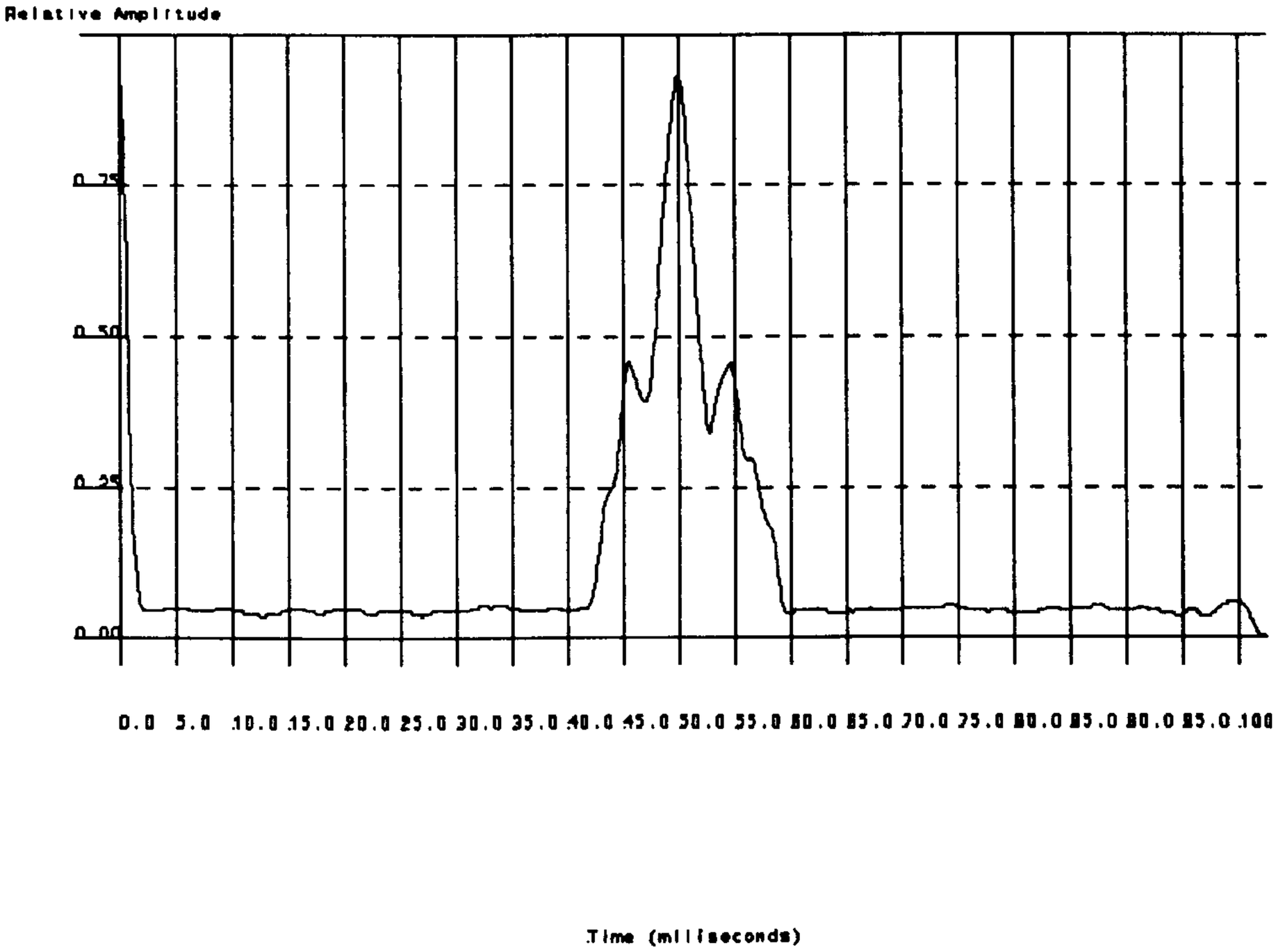

Figure 5: Received 13 bit Barker code waveform after matched filtering.

The waveform shown in Figure 3 was produced by modifying the assembly language program used to drive the transmitter card in the data acquisition system. Each binary pulse of the code consisted of a pulse of ultrasound five cycles wide (1) or a pause of 50μs (0). On reception the received envelopes were passed through a matched filter. The matched filter was produced by storing a replica of the transmitted waveform in the DSP memory and performing a correlation with the incoming signal.

With an uncoded pulse the range resolution is proportional to the width of

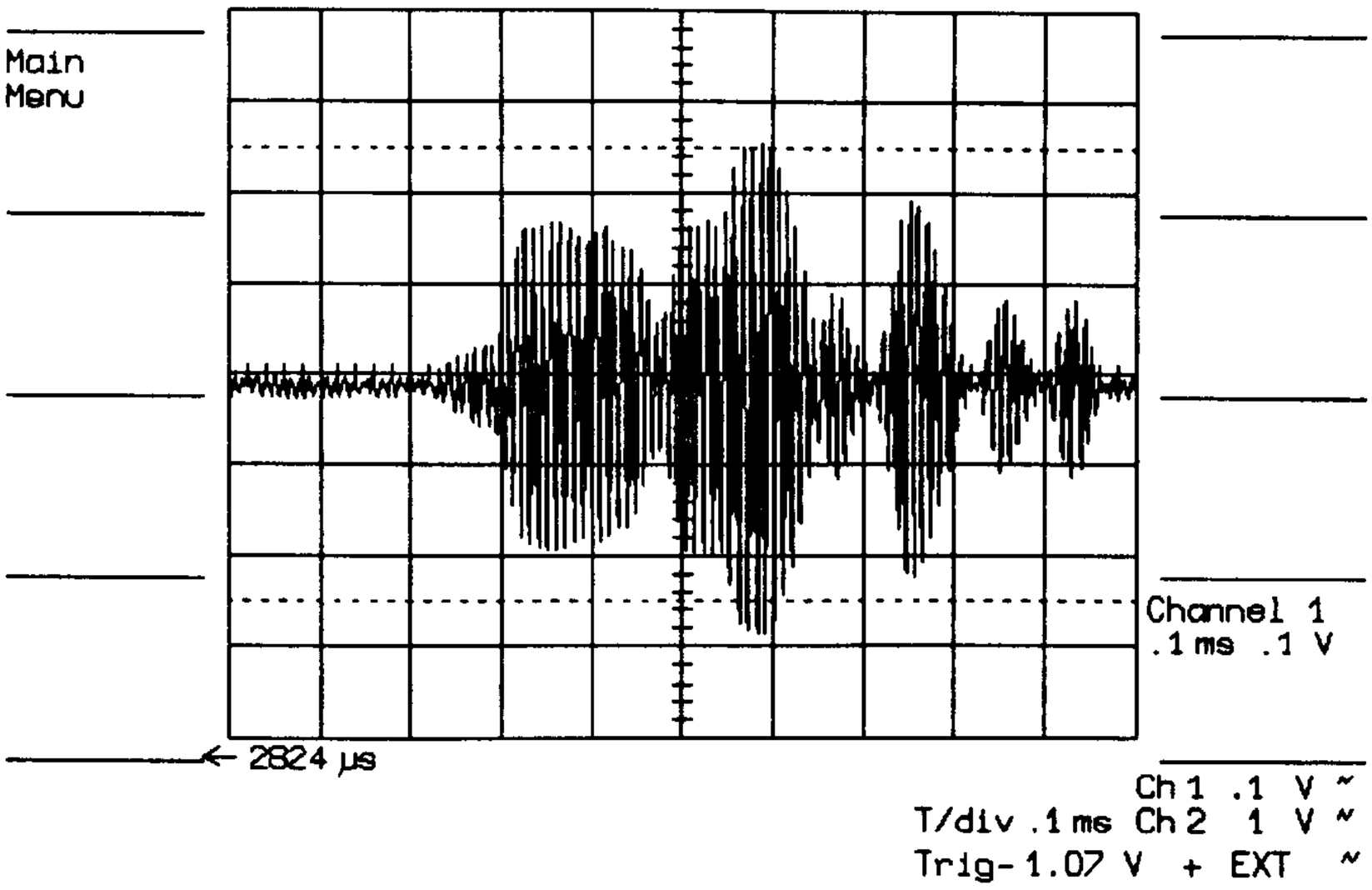

Figure 6: Unprocessed received signal for two targets 4cm apart.

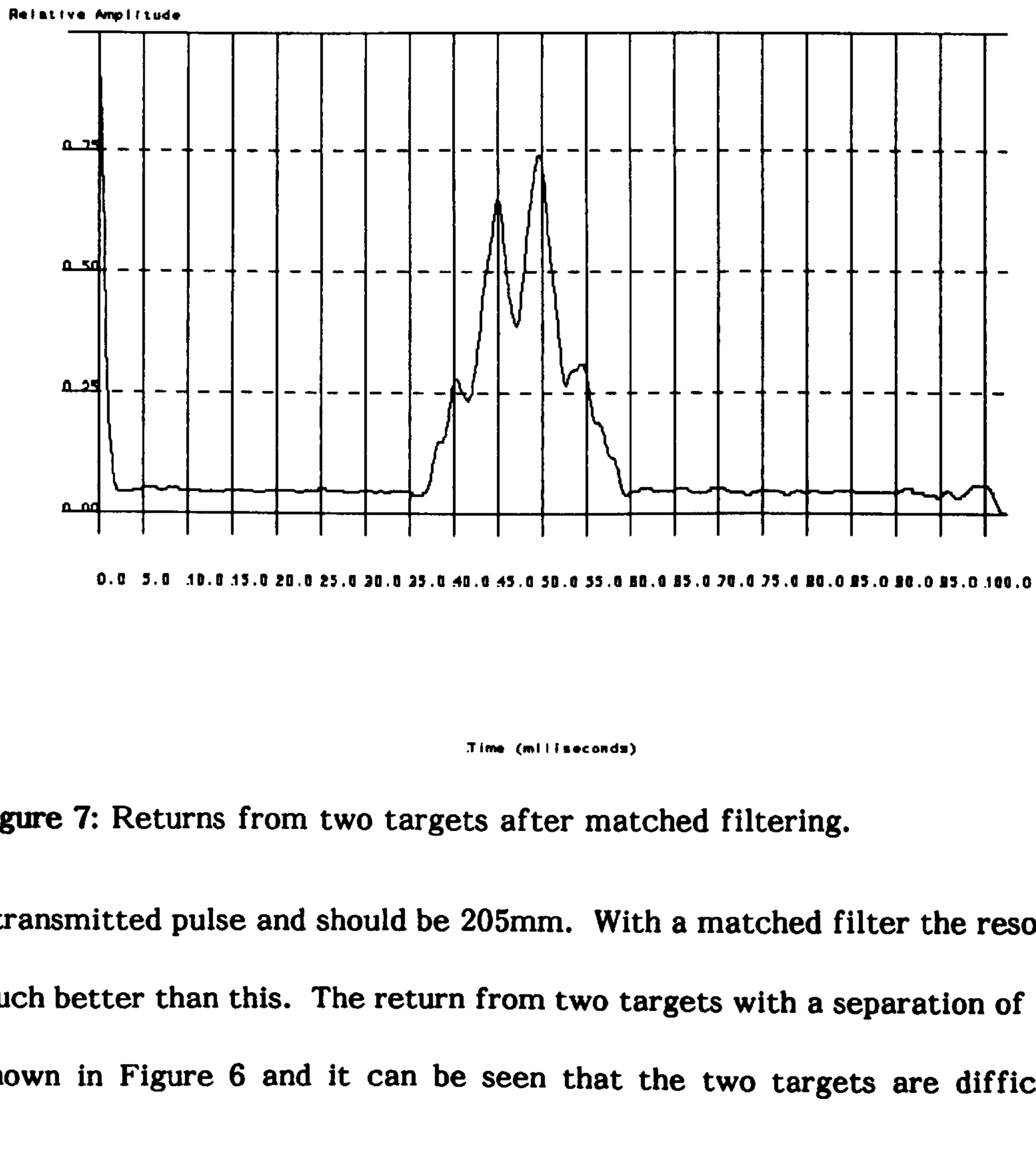

Figure 7: Returns from two targets after matched filtering.

the transmitted pulse and should be 205mm. With a matched filter the resolution is much better than this. The return from two targets with a separation of 50mm is shown in Figure 6 and it can be seen that the two targets are difficult to

distinguish before filtering. The same targets are shown in Figure 7 after matched filtering and can be easily distinguished. The advantage of using a matched filter is an increase in signal to noise ratio. It can be seen in Figure 7 that the signal to noise ratio is greater than in the unfiltered returns. This improvement in signal to noise becomes more apparent in the presence of high levels of noise and when interfering signals from other ultrasound sources are present.

It should be noted that the outputs from the matched filter presented here are not ideal. There are two large sidelobes present on the filter outputs. These are probably caused by the transmitted waveform not being a true barker code since it does not fall to zero in between bits and the amplitude is not constant due to transmitter effects.

8.4 Increasing resolution.

It was shown in chapter 7, that if standard digital beam forming algorithms are to be effective the signal must be sampled at well above the Nyquist rate. This can cause severe problems when the system is to be implemented in real-time or near real-time as the amount of data acquired often exceeds the available system bus bandwidth. In non real-time systems, very large areas of memory may be required.

If the system has a degree of prior knowledge about the location of targets, then the sampling rate in areas where targets are present can be increased by the use of interpolation. This prior information could possibly be obtained by using a very coarse beam forming system to scan the data first.

There are many different methods available for the interpolation of sampled

band limited signals[5]. A common method is linear interpolation; this was tried but proved too computationally intensive. Fourier transform interpolation[6] was however implemented successfully; this is described in section 8.4.1.

8.4.1 Fourier transform interpolation

If the FFT of a sampled signal of length N_1 is calculated, then a sampled frequency spectrum will result. The frequency function can then be separated by adding zeroes at n $=N_1/2$ to give a frequency function of length N_2. When an inverse FFT is performed on the stretched spectrum, a time function will result with a sampling rate increased by a factor of N_2/N_1. An illustration of this process is shown in Figure 8. This is the method used to produce the interpolated beam former discussed in chapter 7.

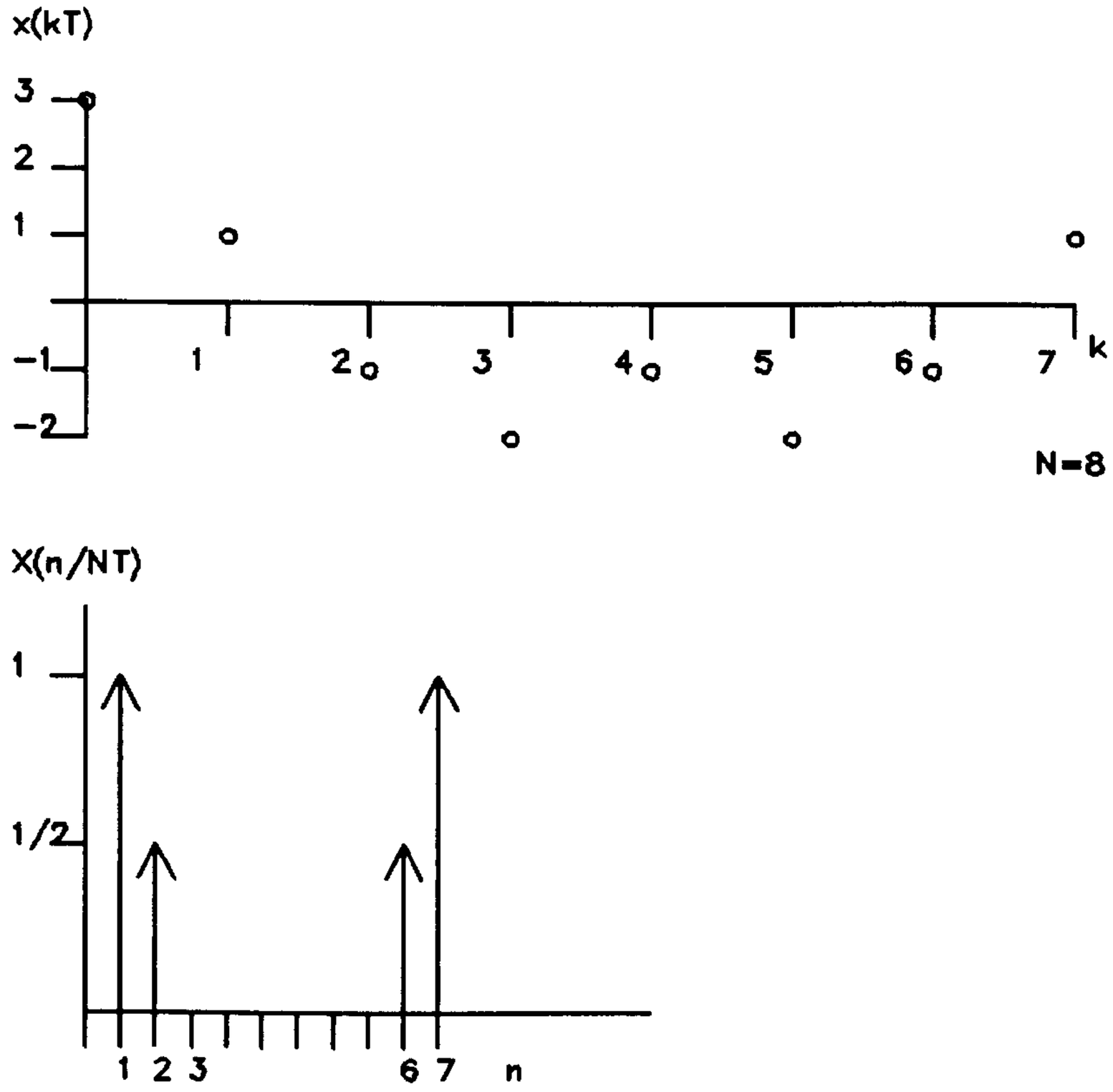

Figure 8: Diagram showing the principle behind FFT interpolation (after Brigham[6]).

8.5 Removal of false targets.

Another source of range error is the detection of spurious targets. These are targets which do not exist but are generated by the environment within which the system is used.

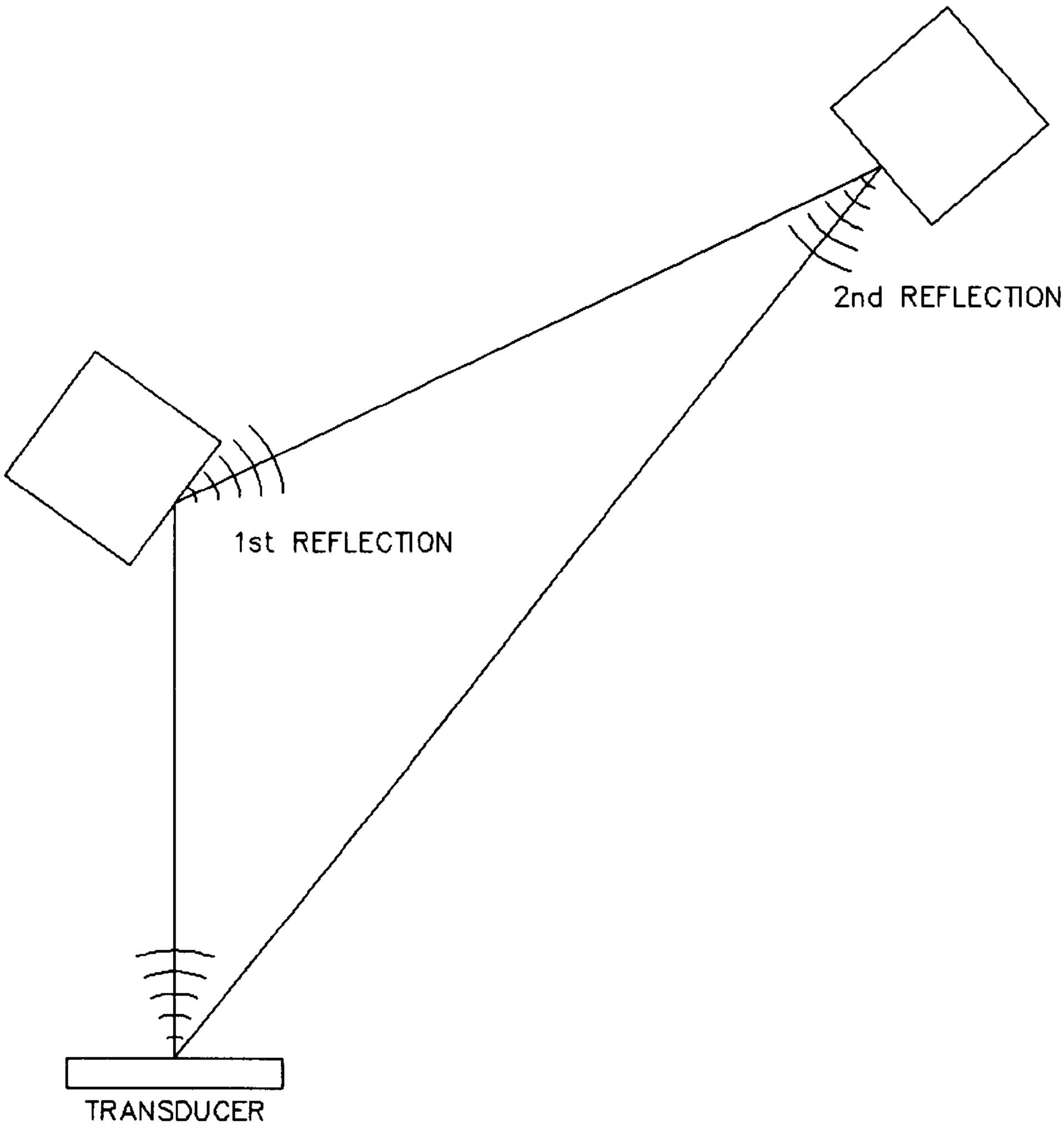

Figure 9: Generation of multiple reflections.

Spurious target returns are usually generated in one of three ways; multiple echoes, second time around echoes or noise spikes. Multiple echoes occur when

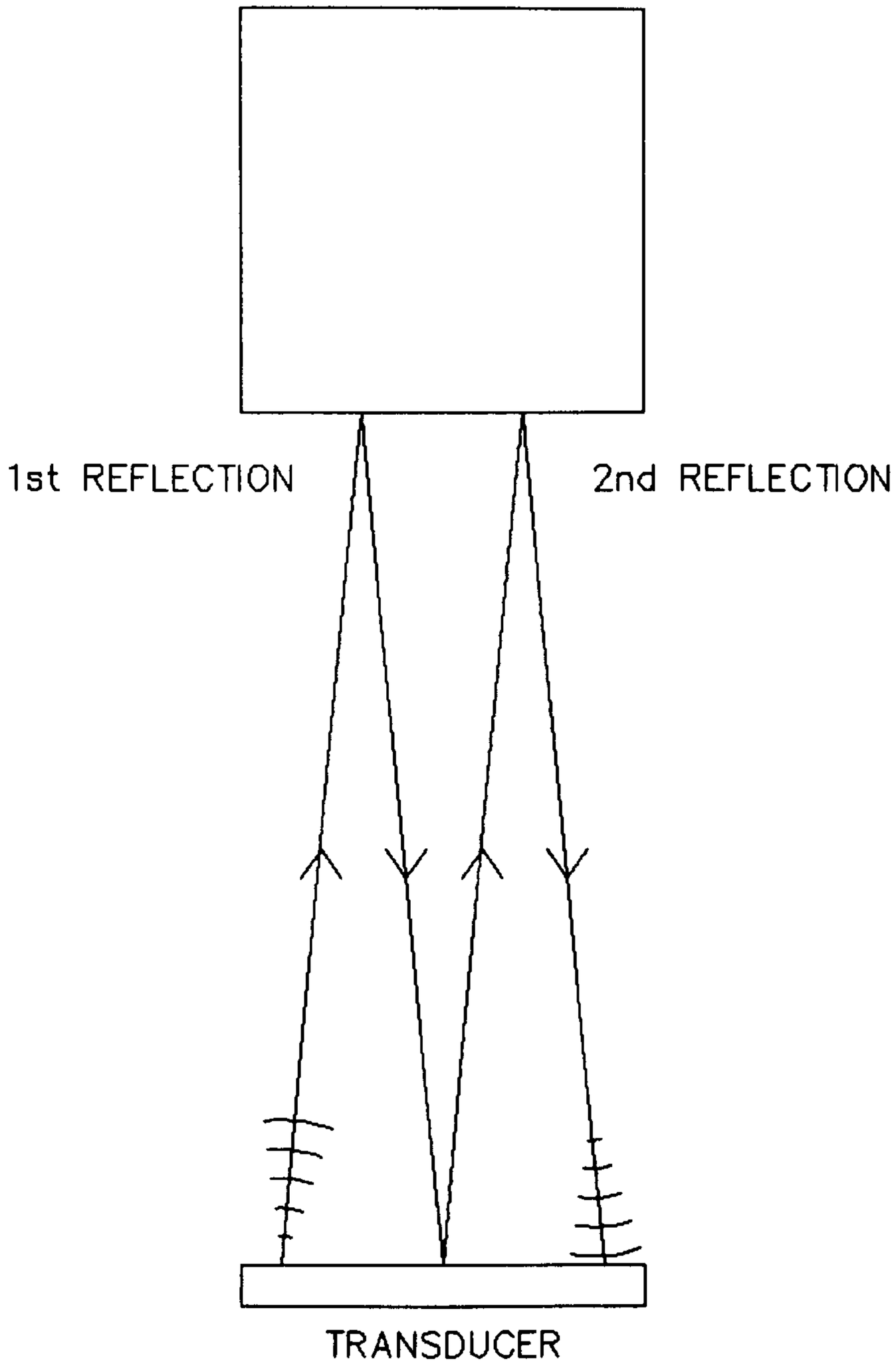

Figure 10: Multiple returns generated by the presence of a large target close to the transducer.

the received signal has been deflected by more that one object, Figure 9. This results in the appearance of a target at a false range and bearing. Multiple echoes may also occur when a large target is placed close to the transducer Figure 10. Second time around echoes occur when an echo is received from a target beyond the normal range of the system Figure 11. This happens when the transmitter is fired before all the energy from a previous firing has returned. The second time around return from a target appears

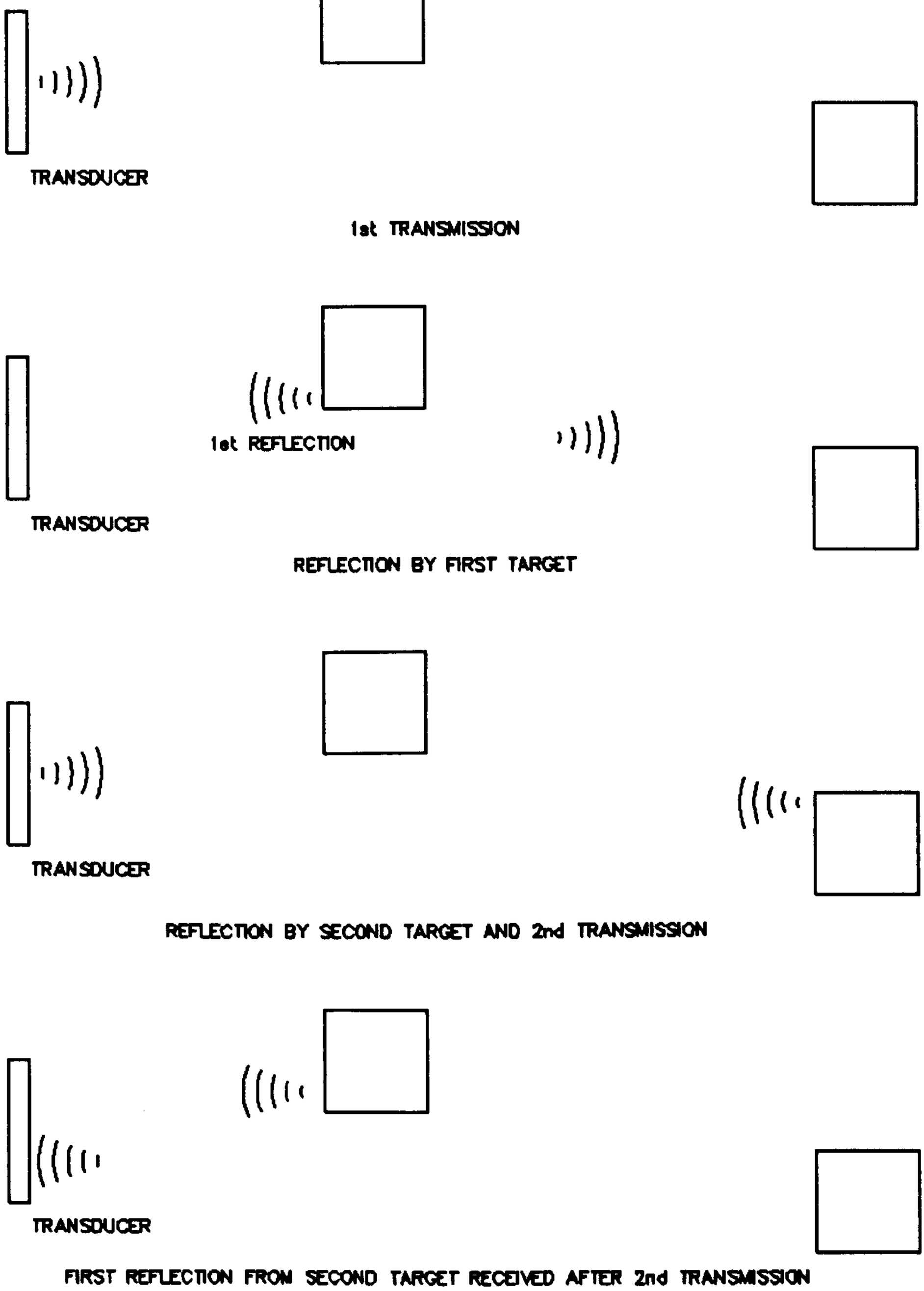

Figure 11: Generation of second time around echoes.

as a target at a much reduced range. The occurrence of these echoes is particularly common at high transmitter firing rates. At slow rates all the energy from the last firing will have dissipated before the transmitter fires again. Noise spikes may be generated by other ultrasonic systems, mechanical shocks, collisions and gas discharges.

8.5.1 Multiple PRF

The use of several different pulse repetition frequencies (PRF) is a common radar technique which is used for the removal of second time around returns[7,8]. The PRF of a radar system is the rate at which the transmitter is fired. It is especially used in short range radar operating with a high PRF[9].

The principle of the system relies on varying the time separation between transmitter firings. Figure 12 shows the idealised returns that would be received for the situation shown in Figure 11. The single PRF returns are exactly as shown in the figure. If the time between firings is varied then the 2nd time around echo will appear to move in time relative to the transmit pulse. If two such firings are compared and only targets which remain static in relation to each other are used then all 2nd time around targets will be removed. This is again shown in Figure 12.

This use of a multiple PRF also has the benefit of removing most of the types of noise interference described in section 8.5 as such noise seldom correlates between transmitter firings.

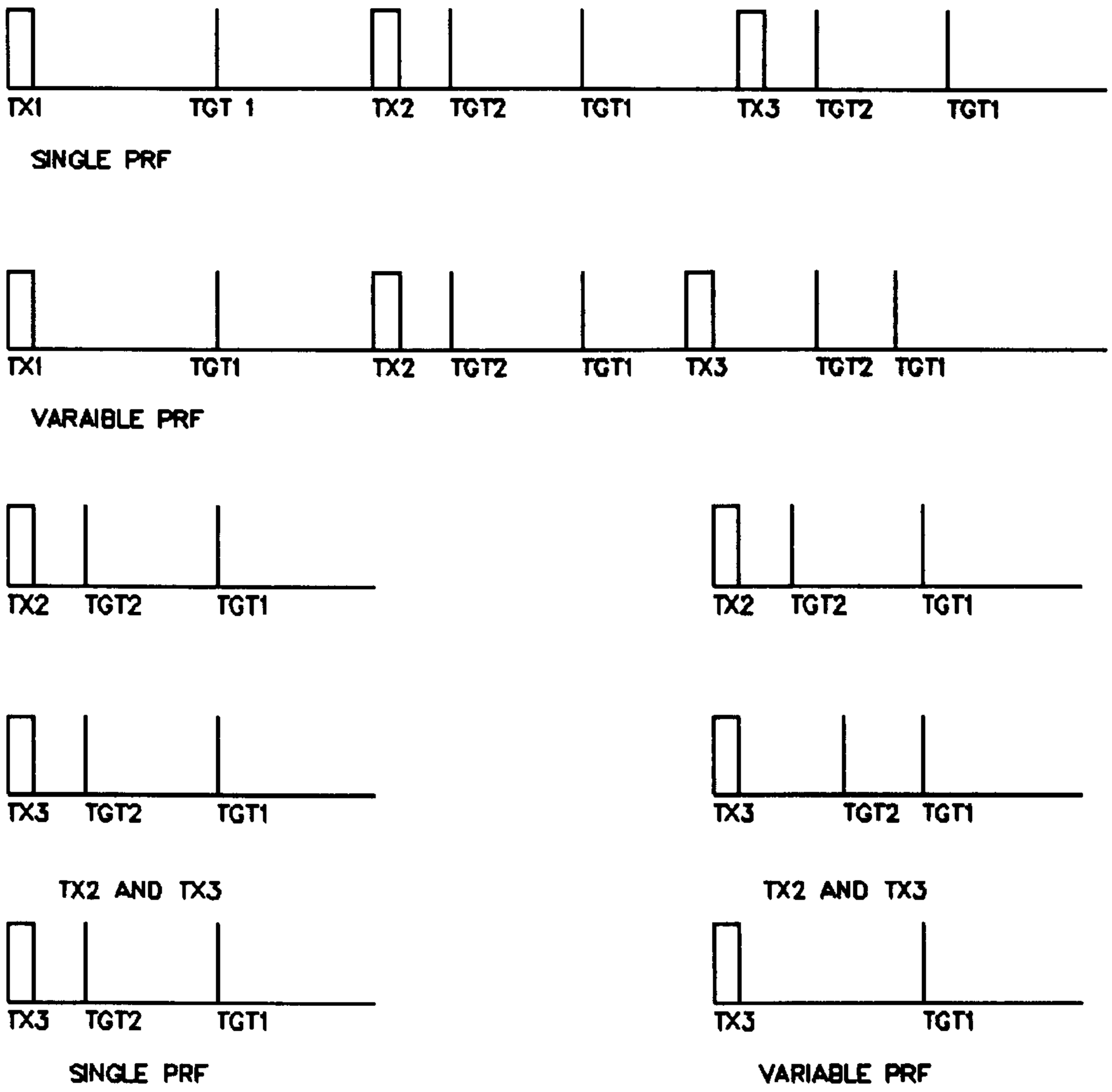

Figure 12: Effect of varying PRF on Idealised target returns from Figure 11.

8.5.2 Practical Implementation.

The system described in 8.5.1 has been successfully implemented in software as a DSP function. The PRF is changed by altering the number of A/D samples taken between transmitter firings. Two sets of data are captured by the DSP and then compared. The process is effectively a logical 'and' but the comparison must be made in such a way as to compensate for the difference in amplitudes that may occur between the two data sets. In the system a sample by sample comparison is performed. A sample is accepted as valid if two samples with an amplitude

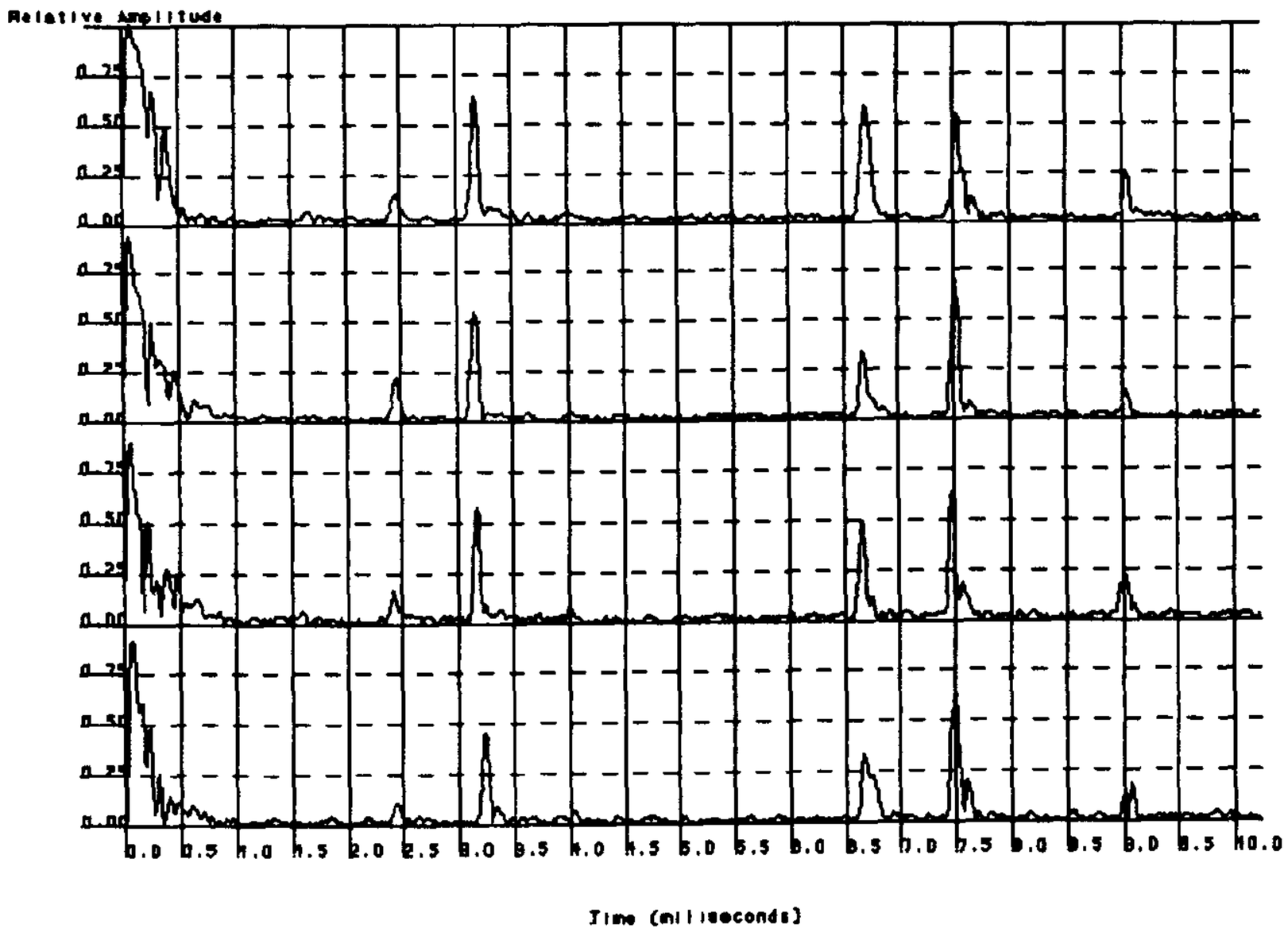

Figure 13: Returns from targets with single PRF.

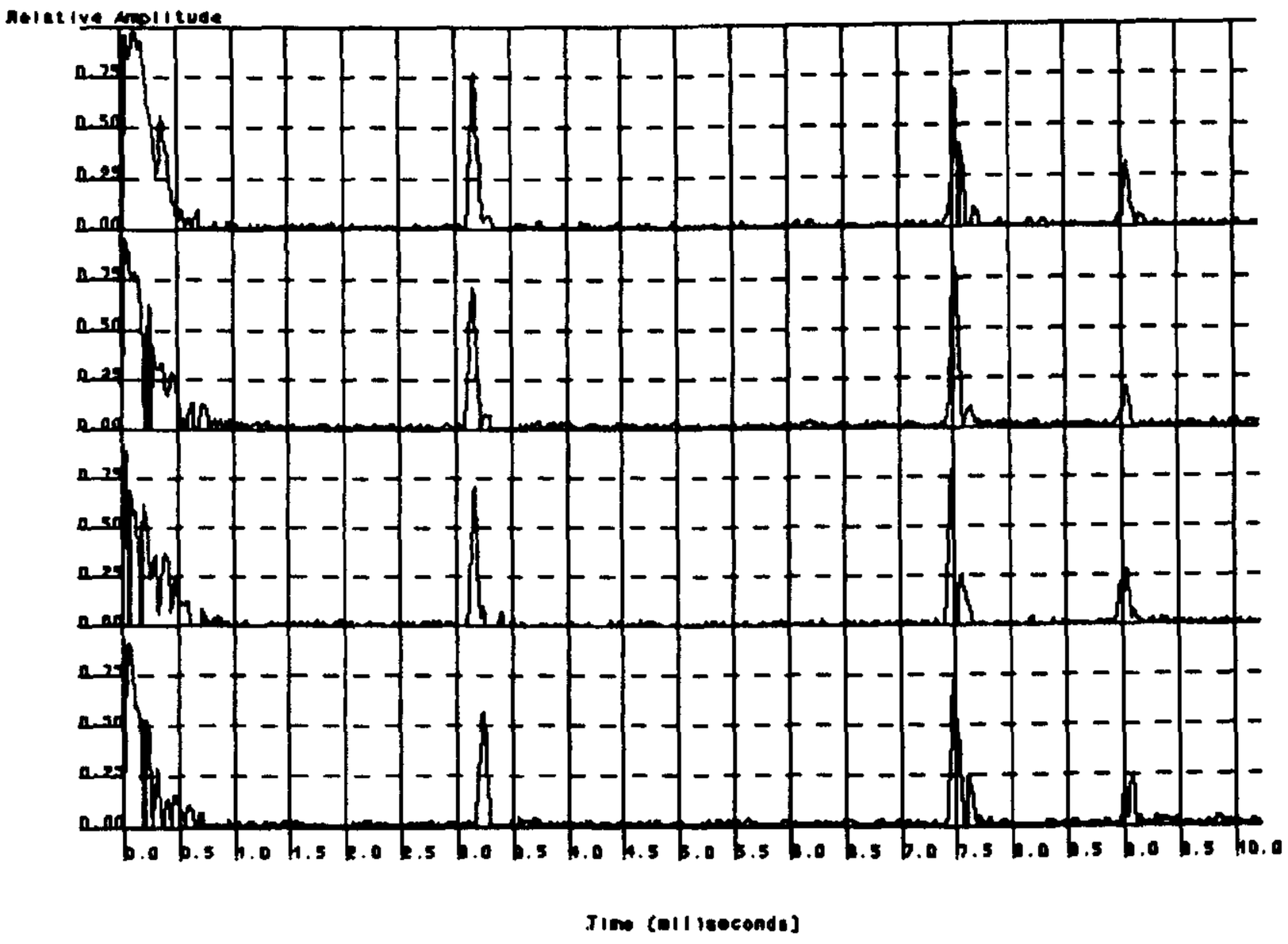

Figure 14: Target returns with multiple PRF.

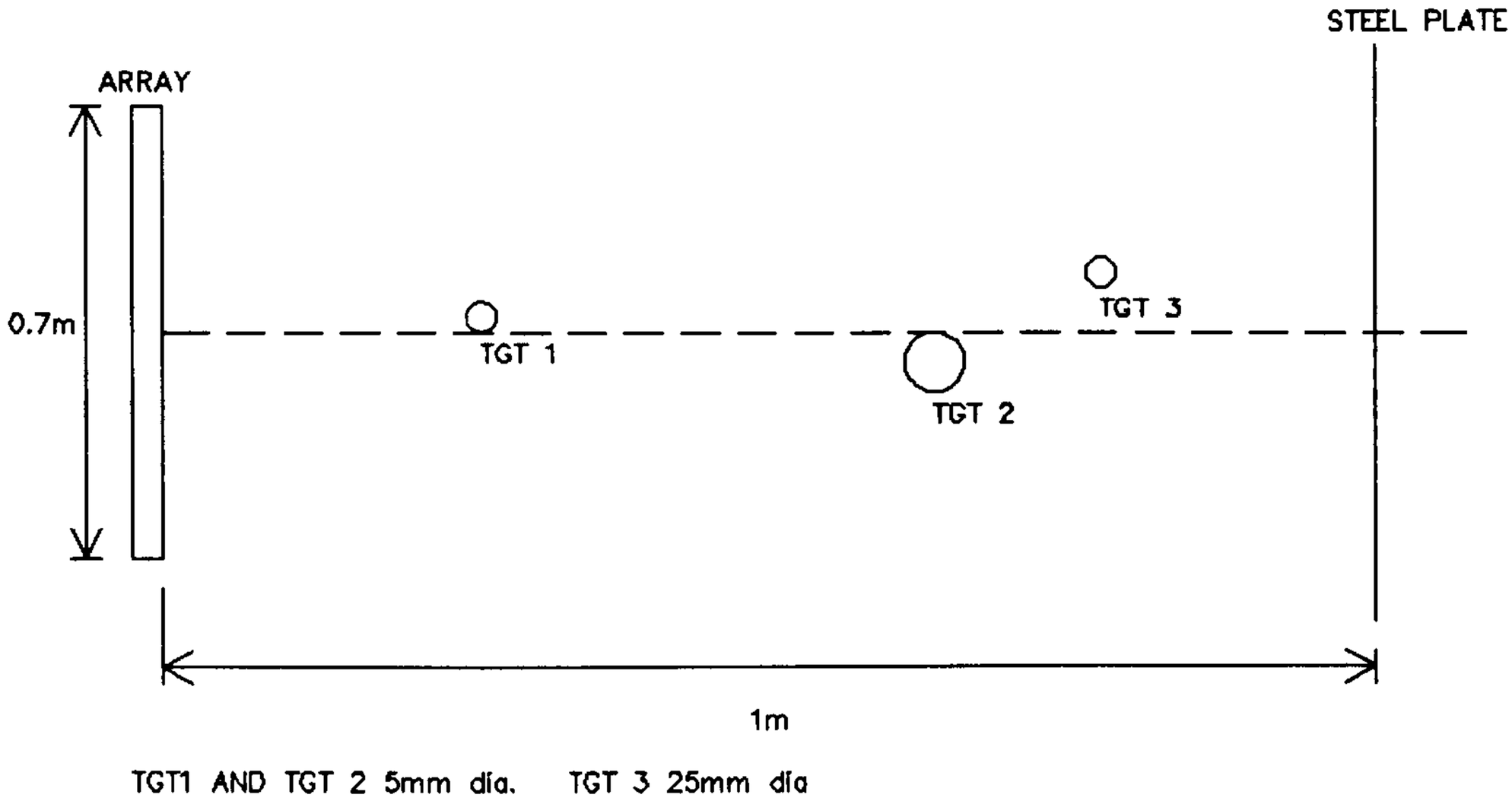

Figure 15: Target layout used to test MPRF system.

difference within ∓25% are adjacent. The effectiveness of this technique is shown in Figure 13 and Figure 14. It can be seen that the 2nd time around returns have completely disappeared and the background noise level is significantly reduced with the MPRF system active. The data was obtained with the target layout shown in Figure 15. The steel plate shown was inserted to simulate the presence of objects in front of a solid vertical surface. This is a situation that is likely to occur regularly due to the widespread occurrence of vertical surfaces in a real environment. This technique is therefore particularly suited to use in robot anti-collision systems.

8.5.3 Removal of multiple reflections.

Multiple PRF cannot remove false targets produced by multiple reflections. False targets generated by large targets placed close to the transmitter (Figure 10) can be removed by searching the returns for equally spaced targets but this may result

in real targets being discarded. Multiple reflections of the type shown in Figure 9 can only be detected by doing range amplitude comparisons. This relies on the assumption that the return will be smaller than expected because of the slight scattering effect of the first reflection. This method is not very robust because local environmental factors can cause significant reductions in signal amplitude. Interference by these two types of multiple reflection can be a limiting factor in the application of airborne ultrasonics.

8.5.4 Removal of noise spikes.

Spurious targets generated by the presence of noise spikes can be removed by the use of averaging. In this process the received signals from several transmissions are stored and summed. A noise spike that appears in single set of received data will be well below the level of the signal from a real target which appears in all the sets of data. One disadvantage of using averaging is the increase in processing time, another is the requirement for everything to be stationary during the averaging period. The use of averaging will also increase the signal to noise level of the system. The received signals for a 5mm cylinder placed in front of the array are shown in Figure 16, Figure 17 and Figure 18. To simulate the presence of a noise spike a second target was place in front of the array for one firing of the transmitter (see Figure 16), Figure 17 shows the same target after 5 averages and Figure 18 shows it after 10 averages. It can be seen that the spike has disappeared after the 10th average. There is also an improvement in the signal to noise ratio.

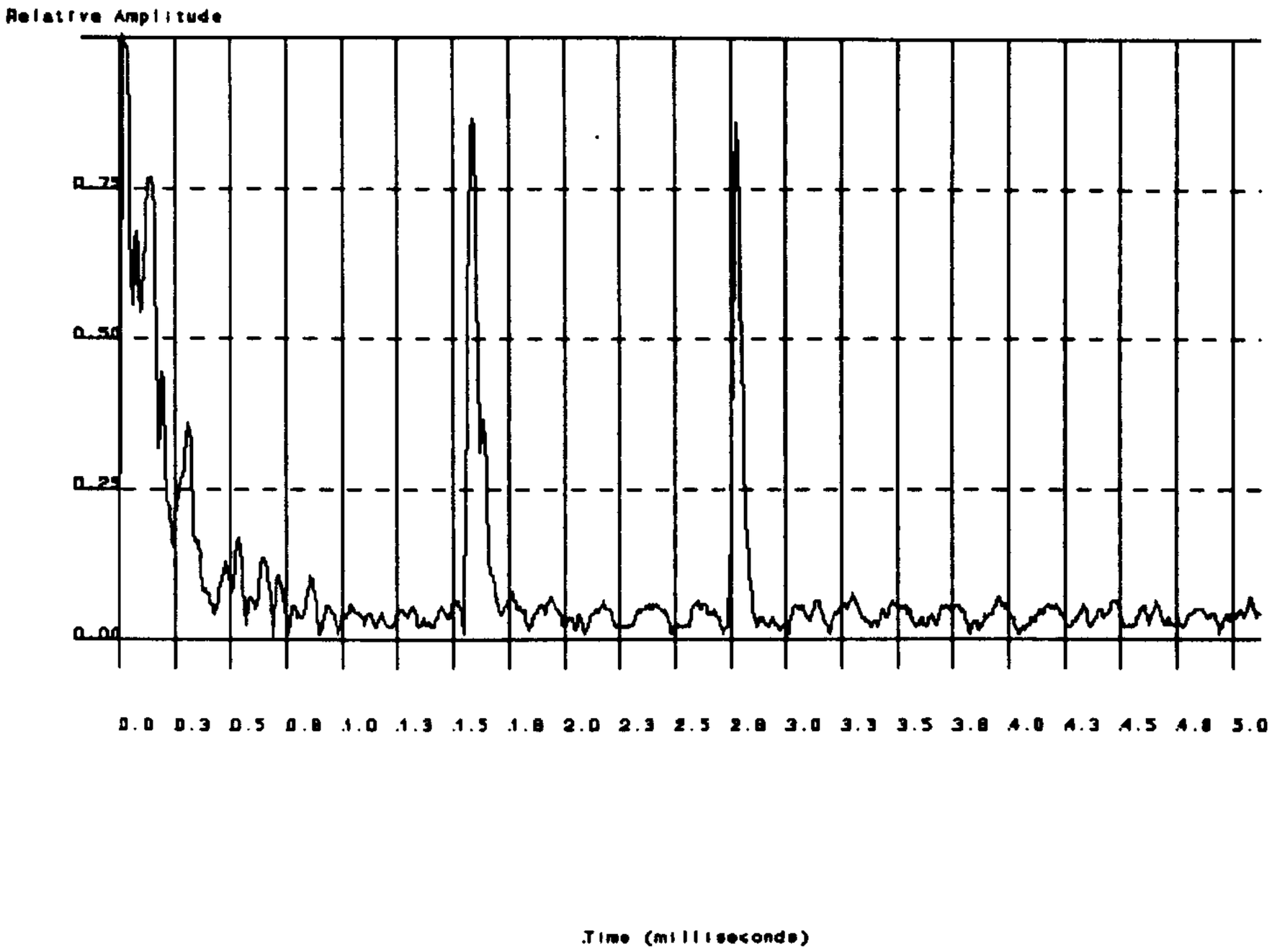

Figure 16: Unaveraged signal.

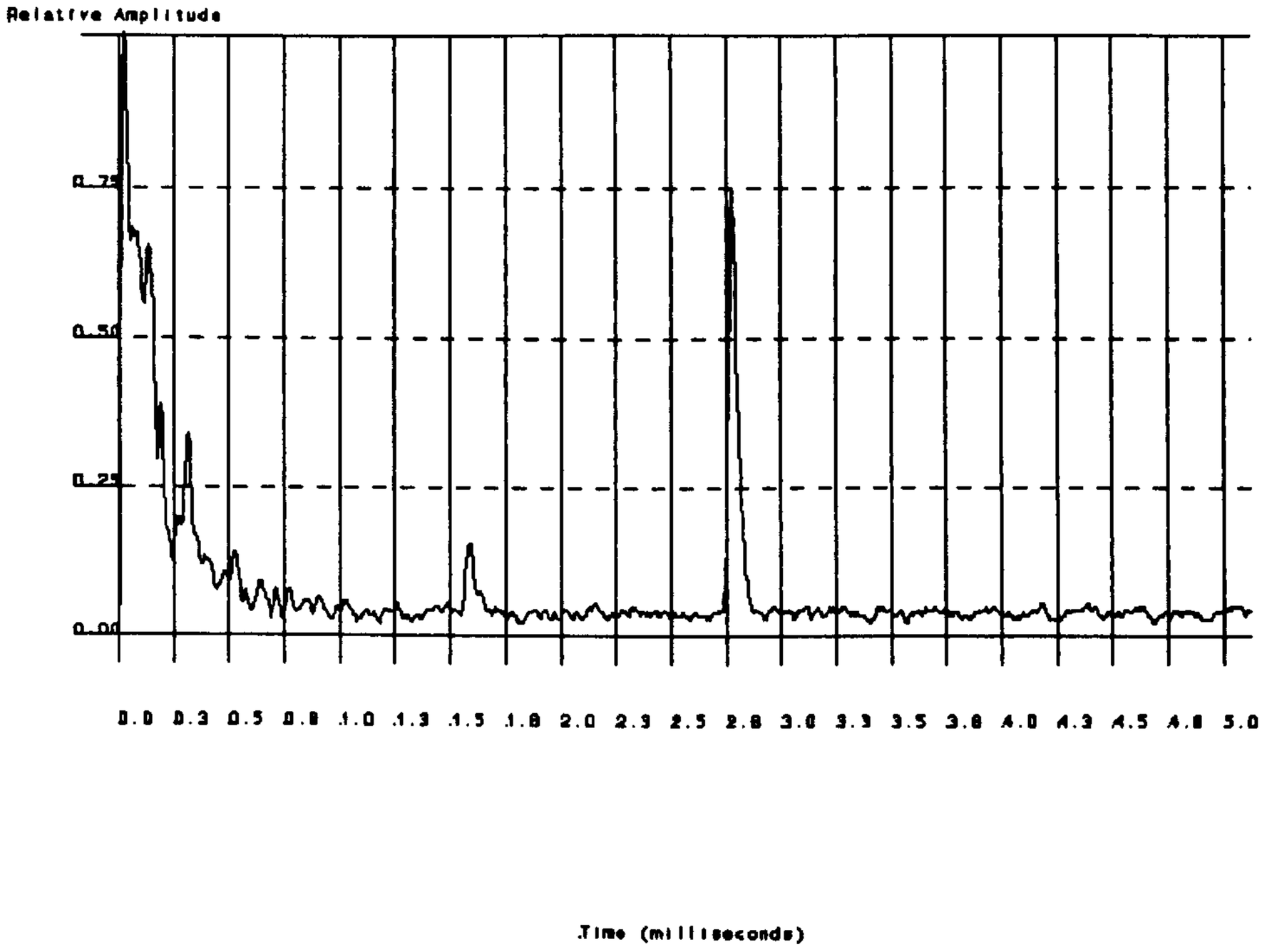

Figure 17: Partially averaged signal.

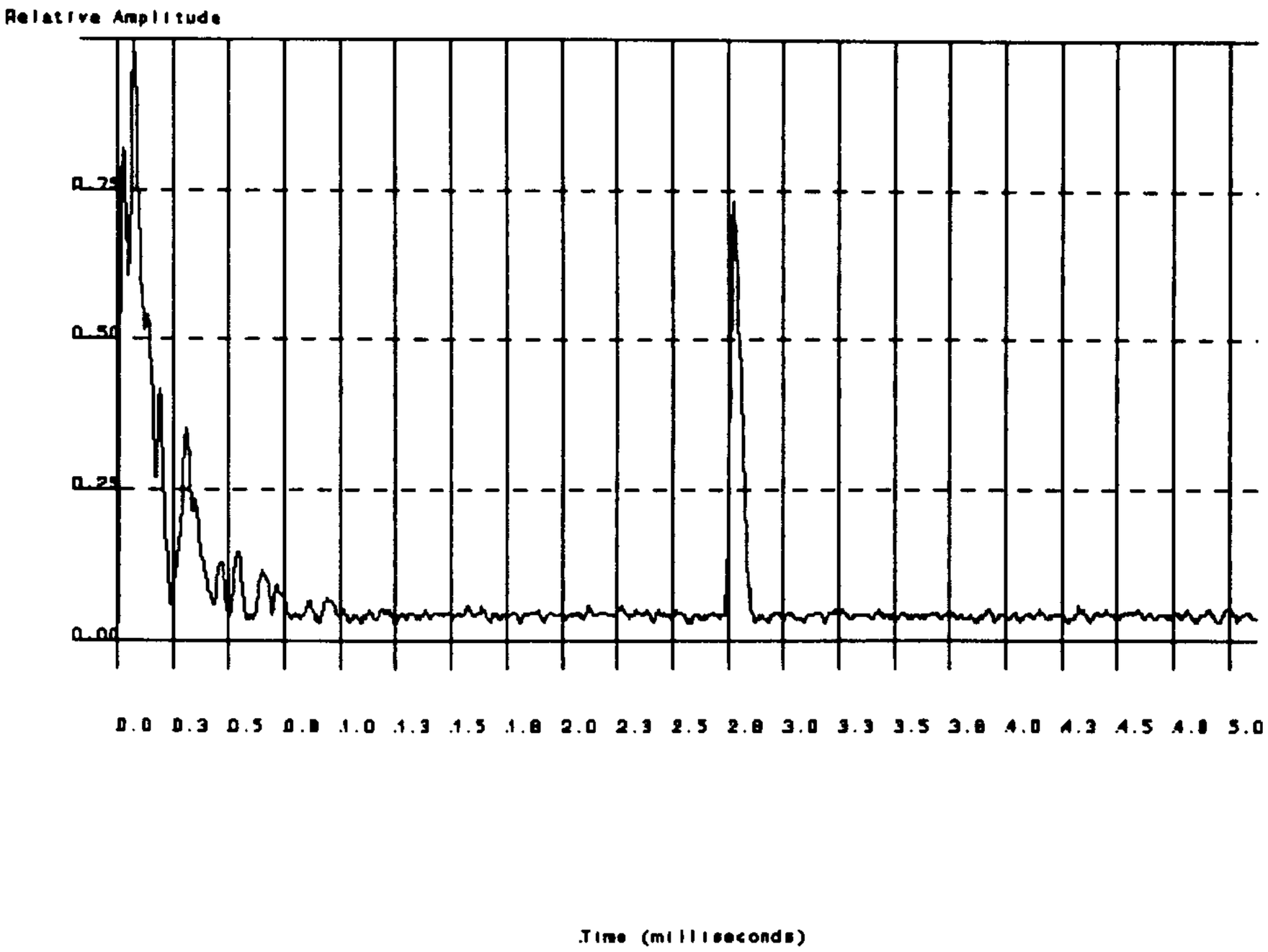

Figure 18: Fully averaged signal.

Another method that can be used to remove the effects of noise spikes is integration, in this method the signals are simply added until a target passes a set threshold. The theory is that only real targets will be present for sufficient firings of the transmitter to exceed the threshold. A disadvantage of this method is that it takes longer to detect weak targets than strong targets. This is the method used by the polaroid ranging system[10].

8.6 Summary.

The methods described in this section can be used to improve the quality of the signal used by the beam former. A multiple PRF system has been used in the final system and has proved highly effective in removing second time around echoes. As far as the author is aware a multiple PRF system has not been used, to remove

second time around returns, in an airborne ultrasonic ranging system before. Such a system has been used to remove interference from other transmitters by Borenstein and Koren[11]. Matched filtering was not used in the final system but may be required if the system was to be used in a noisy environment. Matched filters are often used in radar pulse compression systems to increase resolution but this is unnecessary in this system since a narrow pulse is available already. An interpolation system is of great use when it is wished to increase the resolution of system without modifying the hardware. Such an implementation of interpolation has already been described in chapter 7.

8.7 References.

1. M. I. Skolnik, "Introduction to Radar Systems", McGraw Hill, 1984.

2. D. N. North, "An Analysis of the Factors Which Determine Signal/Noise Discrimination in Pulsed-Carrier Systems", Proceedings of the IEEE, Vol. 51, July 1963, pp1016-1027.

3. A. W. Rihaczek, "Principles of High Resolution Radar", McGraw Hill, 1969.

4. H. Peremans, K. Audenaert and J. M. Campenhout, "A High-Resolution Sensor Based on Tri-aural Perception", IEEE Transactions on robotics and automation, Vol. 9, No. 1, February 1993, pp36-48.

5. R. W. Shafer and R. R. Rabiner, "A Digital Signal Processing Approach to Interpolation". Proceedings of the IEEE, Vol. 61, No 6, June 1973.

6. E. O. Brigham, "The Fast Fourier Transform and its Applications", Prentice International, 1988.

7. K. Gerlach, "Second Time Around Radar Return Suppression Using PRI Modulation", IEEE Transactions on Aerospace and Electronic Systems, Vol. 25, No. 6, 6 November 1989.

8. S. A. Hovanessian, "An Algorithm for Calculation of Range in a Multiple PRF Radar". IEEE Transactions on Aerospace and Electronic Systems, VOL. 12, No. 2, March 1976.

9. S. A. Hovanessian, "Medium PRF Performance Analysis", IEEE Transactions on Aerospace and Electronic Systems, Vol. 18, NO. 3, MAY 1982.

10. Polaroid Corporation, "Ultrasonic Ranging System Manual", 1984.

11. J. Borenstein and Y. Koren, "Noise Rejection for Ultrasonic Sensors in Mobile Robot Applications",Proc IEEE International conference on robotics and automation, Nice France, 1992, pp1727-1732.

CHAPTER 9

MEASUREMENT SYSTEM PERFORMANCE

9.1 Introduction.

Chapter 9 provides a detailed analysis and presentation of the experimental results obtained during this research. The evaluation covers the performance the of the system as a measurement tool and quantifies the measurement capability of the whole system. The chapter begins in section 9.2 with a comparison of the results obtained using envelope beam forming in comparison to traditional beam forming. Section 9.3 contains an introduction to the extraction of data from raw beam former outputs. Section 9.4 provides a mathematical analysis of the total errors found within the system and section 9.5 analyses the theoretical resolution of the system. Sections 9.6 and 9.7 contain a detailed analysis of the overall performance together with a comparison of soft and full focusing. Finally the results are summarised in section 9.8.

9.2 Comparison of envelope and traditional beam former.

This section contains the results of a comparison between the envelope beam forming method and the traditional beam forming method described in chapter 4.

For a system operating at 100KHz with a sampling rate of 200KHz the angular resolution for a $\lambda/2$ array is 41°. The only way of improving this is to

increase the sampling rate. The data acquisition system used to acquire the bandpass data has a sampling rate of 500KHz which gives a resolution of 8.35°. The resolution obtained with the high sampling rate is better but is still poor when compared with a 40mm array operating with a sampling rate of 200KHz which has a theoretical maximum resolution of 1.25°. The actual useable resolution was found to be 2.5° due to noise on the envelope peaks causing instability. It is also important to remember that the reduction in sampling rate gives a significant increase in processing speed and a reduction in memory requirements.The experimental results shown below where generated by a program running on an IBM PC. The data for the envelope beam plots was obtained from the base band data acquisition system described in chapter 6. The non envelope data was obtained using a data acquisition system which acquires the bandpass signal directly from the array at a sampling rate of 500KHz. In all the following results the target used is a single 5mm diameter wire at a range of 300mm from the centre of the array.

9.2.1 Envelope beam forming with 40mm array.

The result of applying envelope beam forming to the output of an array, with a 400mm element spacing is shown in this section. The array used had 4 elements with a spacing of 40mm (11.66λ). Beamplots are shown in Figure 1, Figure 2 and Figure 3 for targets with bearings of 0°, 15° and 35° respectively. In all cases the targets can be clearly resolved and there are no sidelobes present.

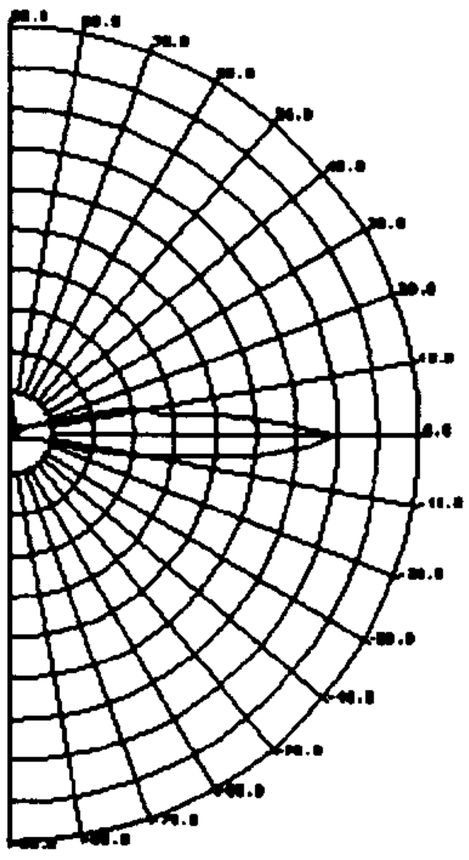

Figure 1: Output of Envelope beam former for target at 0°.

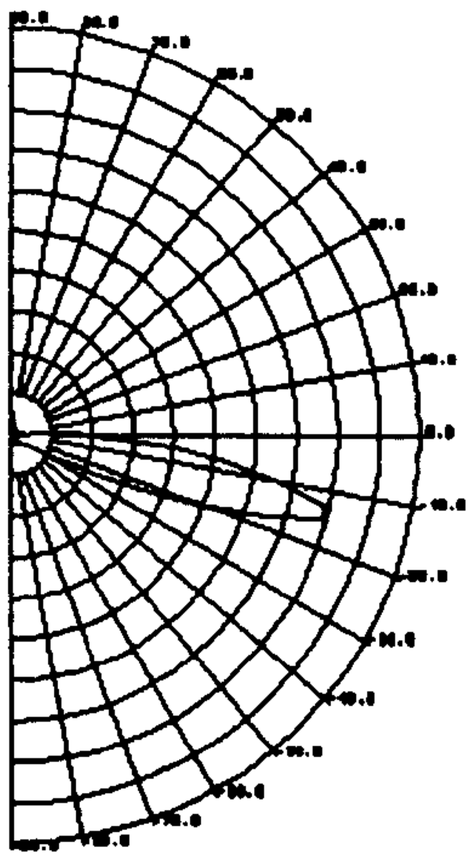

Figure 2: Output of Envelope beam former target at a bearing of 15°

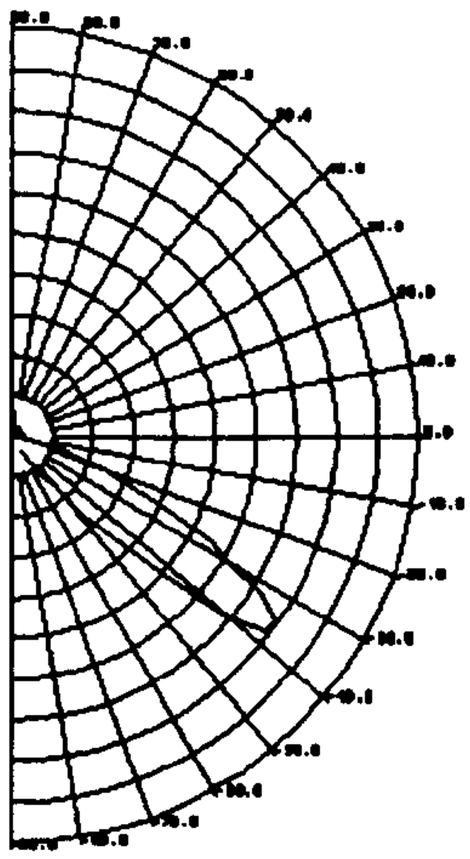

Figure 3: Out put of Envelope beam former for target at 35°.

9.2.2 Traditional beam forming with 40mm array.

The result of applying traditional beam forming the output of an array is shown in this section. The array used had 4 elements with a spacing of 40mm (11.66λ). According to theory the angle of the first grating lobe (θ_g) is given by

$$\theta_g = \pm\sin^{-1}\left(\frac{\lambda}{d}\right) \qquad (1)$$
$$\theta_g = \pm 4.9°$$

This effectively makes the array unusable. The array used had 4 elements with a spacing of 40mm. Beamplots are shown in Figure 4, Figure 5 and for targets with bearings of 0° and 15° respectively.

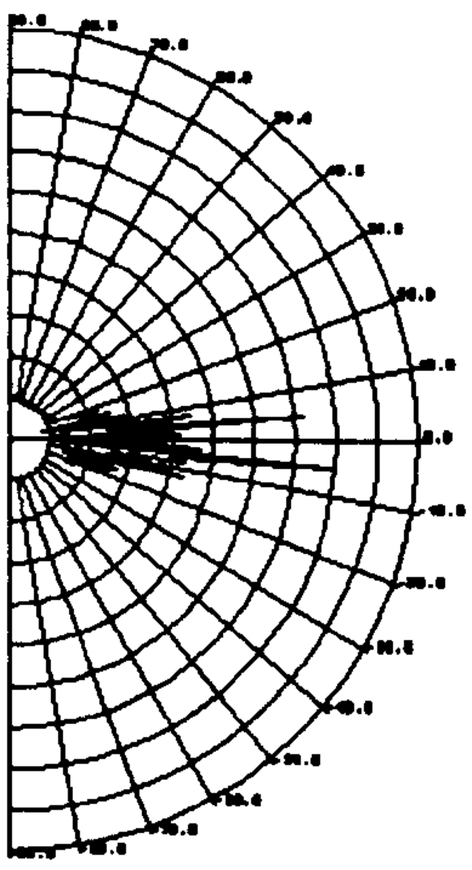

Figure 4: Beamplot for traditional beam former with a single target at 0°

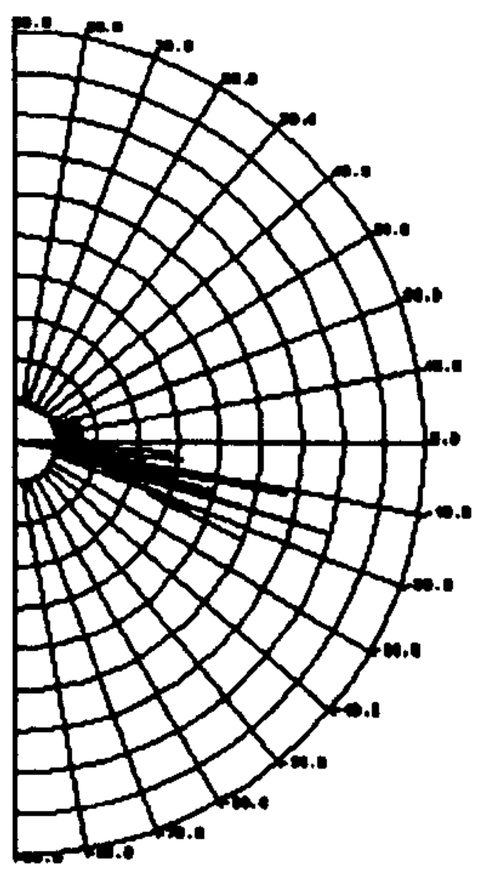

Figure 5: Beamplot for traditional beam former with a single target at 15°.

It can be seen that in both cases the target is impossible to locate due to the grating lobes. It is worth noting that the grating lobes taper off with increasing bearing, this is due to the narrow received pulse width (5 cycles). The grating lobes would be present at all multiples of 4.9° for a true continuous wave signal.

9.2.3 Traditional beam forming with $\lambda/2$ array.

The result of applying traditional beam forming to the output of an array is shown in Figure 6 and Figure 7. Beamplots are shown for targets with bearings of 0°and 18° respectively (the target was placed at 18° to ensure it fell in the next area of resolution of the system). The array used had 4 elements with a spacing of 1.715mm ($\lambda/2$).

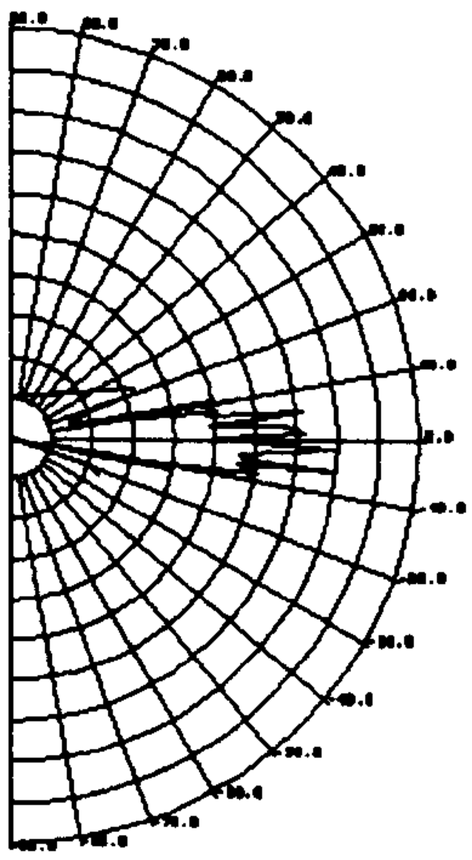

Figure 6: Beamplot for traditional beam former with single target at 0°.

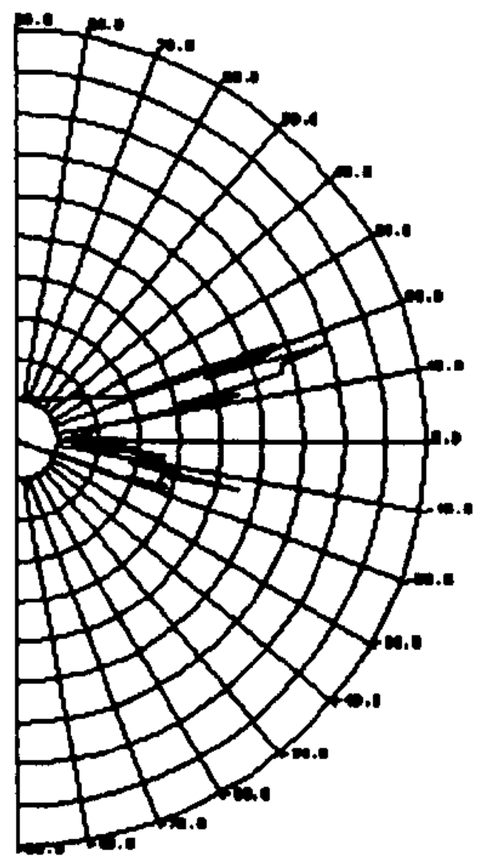

Figure 7: Traditional beam former output with a single target at 18°.

It can be seen that the side lobe levels in the beamplots are much lower than with the 40mm array but the resolution is poorer. The unevenness of the beamplot in comparison to the envelope beam former is probably due to the higher sampling rate and relatively small differences between the received signals. This makes the system much susceptible to noise.

9.2.4 Envelope beam forming with (λ/2) array.

The result of applying envelope beam forming the output of a λ/2 array is shown in this section. The plots are for targets at 0°and 15° respectively. It can be seen from Figure 8 and Figure 9 that the position of the target cannot be determined from the beamplots.

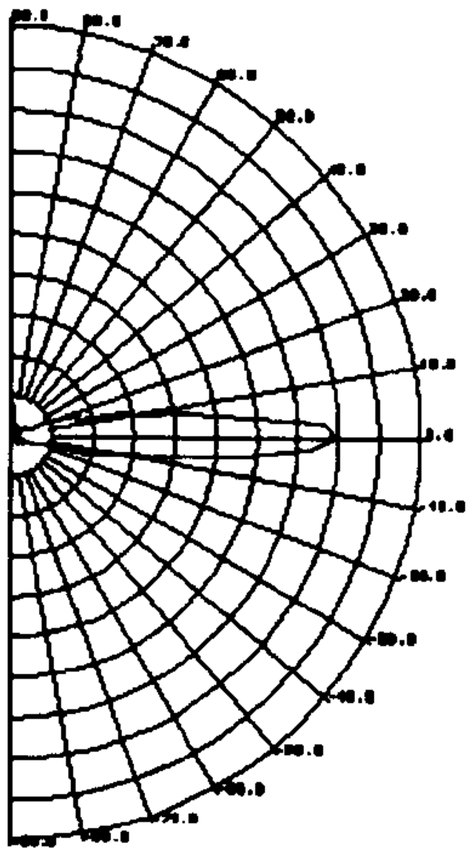

Figure 8 Beamplot for envelope beam former with a single target at 0°.

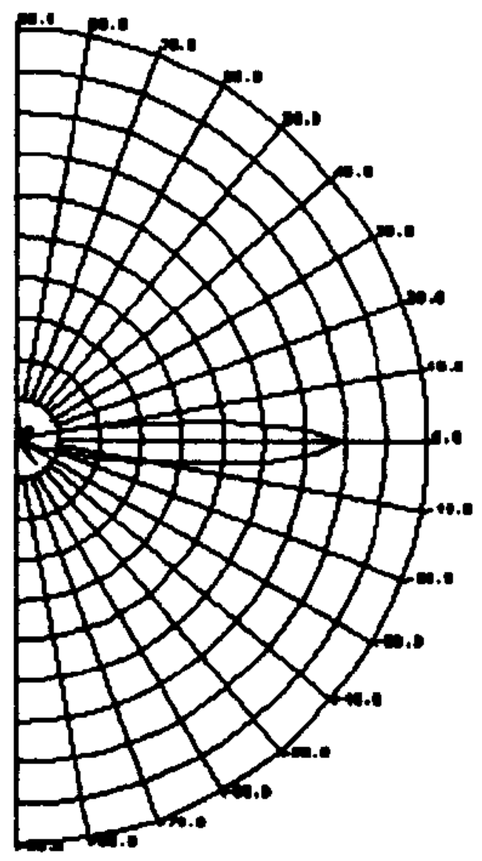

Figure 9: Envelope beam former output for target at 15°.

The use of this combination of processing is of little use since the resolution is almost as wide as the array angle of view. All targets will appear to have a bearing of 0°.

9.3 Beam former output.

When the system is used purely as a measuring instrument the output of the beam former is processed to extract the position of the largest target present. This produces a beam number and the number of samples along the beam at which the

target occurs. This is then converted to x, y co-ordinates relative to the centre of the array. An offset is added to the position to compensate for the delay which occurs between the start of the transmitter waveform and the first triggering of the analogue to digital converters.

9.4 Error analysis.

All measurement systems are prone to errors. This section covers the sources of error which may be present in an ultrasonic measurement system. There are two main classes of errors which must be considered, systematic and random errors. Systematic errors are examined and analyzed in section 9.4.1. whilst random errors are examined and analyzed in 9.4.2. This section starts with a brief introduction to the methods by which the effect of errors on a measurement system may be calculated.

If a system measures two values X and Y with errors δX and δY, then if

$$Z = X + Y \tag{2}$$

it can be shown that[1]

$$\pm\delta Z^2 = \delta X^2 + \delta Y^2 \tag{3}$$

since it is unlikely that δX and δY will have extreme values together. For that to be true, the errors should be normally distributed.

It can also be shown that if

$$Z = f(P,Q,R...) \tag{4}$$

(where f is any function)

$$\delta Z^2 = \left(\frac{\partial f}{\partial p}\right)^2 \delta P^2 + \left(\frac{\partial f}{\partial Q}\right)^2 \delta Q^2 + \left(\frac{\partial f}{\partial r}\right)^2 \delta R^2 + \ldots \tag{5}$$

In the ultrasonic measurement system described here range and bearing values are found by solving the following equations

$$\begin{aligned} R &= \sqrt{a^2 + b^2} \\ \theta &= \tan^{-1}\frac{a}{b} \end{aligned} \tag{6}$$

From chapter 7:

$$a = \frac{-\left(\frac{y_1}{x_{r1}} - \frac{y_2}{x_{r2}}\right) + \sqrt{\left(\frac{y_1}{x_{r1}} + \frac{y_2}{x_{r2}}\right)^2 - 4\left(\left(\frac{1}{x_{r1}} - \frac{1}{x_{r2}}\right)\left(\frac{y_1^2}{x_{r1}} - \frac{y_2^2}{x_{r2}}\right) - (x_{r1} - x_{r2})\right)}}{2\left(\frac{1}{x_{r1}} - \frac{1}{x_{r2}}\right)} \tag{7}$$

and

$$b = -\frac{1}{2x_{r1}}\left(a^2 - 2ay_1 - y_1^2\right) + \frac{x_{r1}}{2} \tag{8}$$

The beam forming process is an iterative solution of the above equation.

There are two quantities involved in these equations. These are x_{rn}, the roundtrip distance from transmitter to target and back to the receiving element, and the element spacing y_n. Any errors in these quantities will introduce errors

into the calculated range and bearing.

The following calculation of the errors was performed assuming a 'worst case' situation with a range of 1m and a bearing of 50°. This is the maximum theoretical bearing that can be achieved due to limitations in the field of view of the receiver elements.

9.4.1 Systematic errors.

Systematic errors are those which are introduced by the limited accuracy of the calibration of the measuring system and are independent of external factors.

Systematic errors are likely to be present in both the array geometry and the roundtrip distance between target and array. Here a one dimensional array is used so the only geometry which need be considered is the separation of the elements y_n. The roundtrip distance x_{rn} is calculated from the time of flight t and the speed of sound c. Thus from

$$x_{rn} = ct \tag{9}$$

the systematic error in x_{rn} from equation (5) is

$$\left[\frac{\delta x_{rn(TotalSystematic)}}{x_{rn}}\right]^2 = \left[\frac{\delta c}{c}\right]^2 + \left[\frac{\delta t}{t}\right]^2 \tag{10}$$

Thus there are two potential sources of error present in x_{rn} and these are covered in sections 9.4.1.1 and 9.4.1.2. The effect of errors in y_n is covered in section 9.4.1.3. The effect of these errors on the range and bearing values produced are

then calculated and presented in section 9.4.1.4.

9.4.1.1 Systematic timing errors.

The time of flight is determined by the position of a peak in the sampled received signal and the accuracy with which this can be found is limited by the DSP chip timer accuracy. The timing of the DSP is specified by the manufacturer to an accuracy of only 1% but has a stability of 0.0001% at a temperature of 25°C[2]. In the measurement system described here the accuracy can be improved to 0.02%[3] using a frequency counter or digital oscilloscope to measure the clock frequency.

9.4.1.2 Systematic errors in the speed of sound.

The speed of sound in air is proportional to humidity and temperature (see chapter 3). Variations of ambient temperature and humidity can be compensated for by entering a value at the start of each run of the system. From chapter 3 the speed of sound in air, depending on temperature and humidity, is given by

$$c = \sqrt{\frac{\gamma RT}{M_{mol}}} \tag{11}$$

Since

$$\delta c = \frac{\partial c}{\partial T}\delta T + \frac{\partial c}{\partial \gamma}\delta \gamma + \frac{\partial c}{\partial M_{mol}}\delta M_{mol} \tag{12}$$

we have

$$c = \alpha T^{\frac{1}{2}}$$

$$\frac{\partial c}{\partial T} = \frac{1}{2}\alpha T^{-\frac{1}{2}} \qquad (13)$$

$$\frac{\partial c}{c} = \frac{1}{2}\frac{\partial T}{T}$$

By a similar process of differentiation for humidity, which affects both the ratio of specific heats γ and the molecular weight M_{mol} of air:

$$\frac{\delta c}{C} = \frac{1}{2}\frac{\delta T}{T} + \frac{1}{2}\frac{\delta \gamma}{\gamma} - \frac{1}{2}\frac{\delta M_{mol}}{M_{mol}} \qquad (14)$$

It has already been shown in chapter 3 that an increase in humidity causes γ to increase but the density decreases. There is thus a degree of cancelation between the two quantities but the decrease in density is greater than the increase in γ so there is a net increase in the speed of sound with increasing humidity.

Under typical laboratory conditions the temperature may vary between 20°C and 25°C whilst relative humidity may vary between 20% and 50%.

For every 1% change in temperature

$$\frac{\delta c}{c} = [0.0018] \qquad (15)$$

So under laboratory conditions the maximum error due to temperature changes,

without compensation, will be

$$\frac{\delta c_{(temperature)}}{c} = [0.045] \tag{16}$$

For every 1% change in humidity

$$\frac{\delta c}{c} = 0.00004 \tag{17}$$

The maximum error due to humidity changes, without compensation, will be

$$\frac{\delta c_{(humidity)}}{c} = [0.0012] \tag{18}$$

If both temperature and humidity are to be compensated for and the measurement accuracy of the two parameters is 0.1°C and 0.1% respectively, then the total error is:

$$\frac{\delta c}{c} = \sqrt{[0.00017]^2 + [0.000005]^2} = [0.00017] \tag{19}$$

When corrections for temperature and humidity are made, the maximum error in c is 0.017%.

9.4.1.3 Array geometry errors.

The value of y_n is dependent on the manufacturing tolerance of the array and is ±0.5mm. This can however be measured to an accuracy of 0.1m using a vernier

calliper. Therefore

$$\frac{\delta y_{n(manuf)}}{y_n} = [0.0025] \tag{20}$$

The thermal expansion and contraction of the array is also another possible source of error that must be considered. The thermal linear expansion of copper is 0.000016 K^{-1} (accurate to 3%). Assuming a temperature change from 20° to 25° the change in element separation due to thermal expansion would be $8x10^{-8}$ or 0.00032mm. Thus the error due to thermal expansion can be ignored and the total error in y_n is

$$\frac{\delta y_n}{y_n} = 0.0025 \tag{21}$$

9.4.1.4 Total systematic errors:

The total error in x_{rn} is:

$$\left[\frac{\delta x_{rn(TotalSystematic)}}{x_{rn}}\right]^2 = \left[\frac{\delta c}{c}\right]^2 + \left[\frac{\delta t}{t}\right]^2 = [0.0002]^2 + [0.00017]^2 \tag{22}$$

so

$$\frac{\delta x_m}{x_m} = 0.00037 \tag{23}$$

or approximately 0.04%.

The total systematic errors in range and bearing can be calculated by using the

errors obtained and applying then to the worst case situation described in section 9.4. It then follows that:

$$\left[\frac{\delta\theta_{(Systematic)}}{\theta}\right]^2 = \left[\frac{\delta\theta_{xrn(Systematic)}}{\theta}\right]^2 + \left[\frac{\delta\theta_{yn(Systematic)}}{\theta}\right]^2 \quad (24)$$

$$\left[\frac{\delta R_{(Systematic)}}{R}\right]^2 = \left[\frac{\delta R_{xrn(Systematic)}}{R}\right]^2 + \left[\frac{\delta R_{yn(Systematic)}}{R}\right]^2 \quad (25)$$

The total systematic errors are thus

$$\frac{\delta\theta_{(Systematic)}}{\theta} = [0.0002] \quad (26)$$

$$\frac{\delta R_{(Systematic)}}{R} = [0.0002] \quad (27)$$

These correspond to errors of 0.2mm in range and 0.01° in bearing.

9.4.2 Random errors.

Random errors are those which occur due to factors which vary randomly. There are no random errors present in the array element separation y_n so only the roundtrip distance x_{rn} is affected by random errors. There are three main potential sources of random error in the system. These are variations in the speed of sound caused by random temperature variations within the measurement area, drift in the DSP timer operating frequency and the presence of noise.

The total random error in the measurement of x_{rn}, $x_{rn(Total\ Random)}$ is therefore

$$\left[\frac{\delta x_{rn(TotalRandom)}}{x_{rn}}\right]^2 = \left[\frac{\delta c_{(random)}}{c}\right]^2 + \left[\frac{\delta t_{(random)}}{t}\right]^2 + \left[\frac{\delta x_{rn(noise)}}{x_{rn}}\right]^2 \qquad (28)$$

The stability of the crystal oscillator is quoted by the manufacturer as 0.0001% at a temperature of 25°C. By the same method used in section 9.4.1 the error due to this random error may be calculated.

$$\frac{\delta t_{random}}{t} = [0.000001] \qquad (29)$$

The magnitude of the error due to temperature fluctuations cannot be calculated since the temperature variation within the workspace is unknown. However it can be found experimentally by measuring the variation in the time-of-flight of a pulse of ultrasound scattered from a fixed target. This was done by recording the signal on a digital oscilloscope with a sampling rate of 100MHz, and assessing the position of the peak visually; the resulting waveform is shown in Figure 10. This was repeated many times and the variation in measured time due to such fluctuations was found to be less than ±0.5μs which is significantly less than the sampling interval of the ultrasonic measuring system. The time period over which this occurred was 3.5ms and so 1μs represents an error 0.03%. The random error due to variations in the speed of sound due to temperature in still air is thus

$$\frac{\delta c_{random}}{c} = [0.0003] \qquad (30)$$

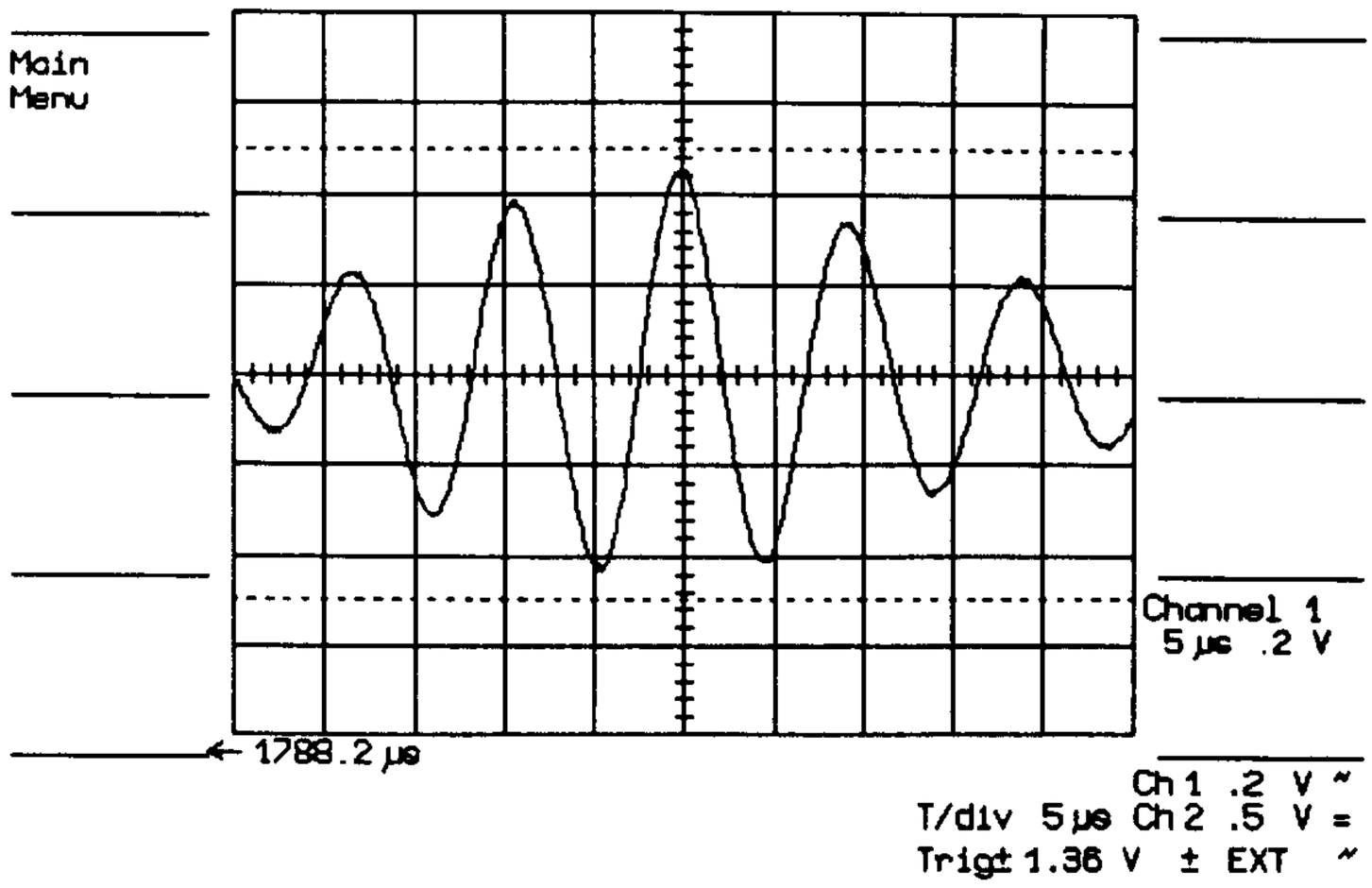

Figure 10: Display of waveform used to measure variation of time of flight with time.

The above process was then repeated for turbulent air. A fan heater was placed such that the output was directed across the measurement space. The heater was positioned at 500mm from the array and 1m to the side. The fluctuation in time of flight was then measured and found to be ±2µs; this is still less than the sampling rate. The time period over which this occurred was 3.5ms and so 4µs represents an error of 0.1%. The random error due to variations in the speed of sound due to temperature in turbulent air is thus

$$\frac{\delta c_{random}}{c} = [0.001] \tag{31}$$

It has been shown in chapter 8 that the range error due to noise is dependent on the method used to detect the target. In this case, a peak detector is used to detect the presence of a target. The total random error due to noise has been

calculated as

$$\frac{\delta x_{rn(noise)}}{x_{rn}} = [0.0001] \quad (32)$$

The total random error in still air is thus

$$\frac{\delta x_{rn(TotalRandom)}}{X_{rn}} = [0.0003] \quad (33)$$

The total random errors in range and bearing can be calculated from:

$$\left[\frac{\delta\theta_{(Random)}}{\theta}\right]^2 = \left[\frac{\delta\theta_{xrn(Random)}}{\theta}\right]^2 + \left[\frac{\delta\theta_{yn(Random)}}{\theta}\right]^2 \quad (34)$$

$$\left[\frac{\delta R_{(Random)}}{R}\right]^2 = \left[\frac{\delta R_{xrn(Random)}}{R}\right]^2 + \left[\frac{\delta R_{yn(Random)}}{R}\right]^2 \quad (35)$$

Since there are no random errors due to y_n the total random errors are

$$\frac{\delta\theta}{\theta} = [0.0005] \quad (36)$$

$$\frac{\delta R}{R} = [0.0005] \quad (37)$$

These correspond to errors of 0.48mm in range and 0.02° in bearing.

9.4.3 Total error

The total error is the sum of all the errors described in 9.4.1 and 9.4.2. These

values are summarised in Table 1.

Table 1: Summary of errors.

Error source	Systematic	Random
time	0.02%	0.05%
temperature	0.02%	0.0001%
humidity	0.0005%	--
array geometry	0.25%	--
array expansion	0.0324%	--
noise	--	0.01%

The total errors are

$$\frac{\delta\theta}{\theta} = [0.0007] \tag{38}$$

$$\frac{\delta R}{R} = [0.0007] \tag{39}$$

The maximum likely error in the system is therefore:

Range error: 0.7mm

Bearing error: 0.35°

The most significant of the random errors is that due to random variations of temperature within the workspace. In a turbulent environment greater errors may be encountered. It is also important to remember that this is very much a worse case situation and it will be seen that the actual errors obtained from the practical system are much less.

To allow the significance of each error to be assessed individually the range

and bearing errors introduced by each error source are listed in Table 2.

Table 2: Effect of individual errors on range and bearing.

Error source	Systematic %		Random %	
	Range	Bearing	Range	Bearing
time	0.03	0.003	0.0006	0.0006
temperature	0.03	0.003	0.046	0.046
humidity	0.0007	0.007	--	--
array geometry	0.19	0.004	--	--
array expansion	--	--	--	--

9.5 Measurement resolution.

The resolution of an instrument is defined as the smallest change in measurand which can be detected by the system. In a simple digital instrument, it is given by the least significant digit of the display, but it is somewhat more complex here.

Both range and angle are found from the position of the peak in a set of summed time-varying signals. The resolution with which this can be determined is limited by the resolution with which the peak can be found. At best, this corresponds to the sampling rate, Δt, though it may be worse than this for low signals or high noise levels.

The best range resolution which is obtained is given by

$$\delta d \approx \frac{c\Delta t}{2}$$

The sampling interval, Δt, is 5μs so that the best range resolution is 1.7mm at 20°C.

The smallest beam spacing obtainable is determined by the sampling interval since at least one sampling interval has to be introduced between adjacent channels to produce a change of angle. Thus, the best angular resolution achievable is given by

$$\delta\theta \approx \frac{c\Delta t}{L}$$

where

$$L = y_n(N-1) \tag{42}$$

and N is the number of elements.

The inter-element spacing is 40mm, so that the best angular resolution is 2.5°. The resolution could be improved in the near-field case by using variable beam-spacing, but this would add to the complexity of the processing and has not been done. To increase the resolution in both the near and far field either the element separation or the sampling rate must be increased.

When the system is used to locate a target, the position of the target has to be calculated in cartesian co-ordinates given by

$$x = d$$

$$y = d \tan\theta$$

giving resolutions of

$$\delta x = \delta d$$

$$\delta y = \frac{\partial(d\tan\theta)}{\partial\theta}\delta\theta + \frac{\partial(d\tan\theta)}{\partial d}\delta d$$

$$= \frac{d}{\cos^2\theta}.\delta\theta + \tan\theta.\delta d$$

Thus, δx is 1.5mm, and δy varies from 2.2mm at a distance of 100mm to 22mm at a distance of 1m.

9.6 Analysis and presentation of experimental results.

In this section the results of the experiments used to verify the measurement performance of the system are presented. In each case two sets of results are presented, those obtained using soft focusing and those using full focusing. Section 9.6.1 covers measurement of the range accuracy of the system, section 9.6.2 covers the measurement of the bearing accuracy.

To obtain accurate measurements of the positional measurement accuracy of the system, a linear stage was used. This allows precise and repeatable positioning of a target with an accuracy specified by the manufacturer of 0.001mm. The stage is controlled by the measuring system via an IEEE488 interface using purpose written software which runs in conjunction with the control software on an IBM compatible PC. This software is described briefly in appendix A. The experimental layout is shown in Figure 11.

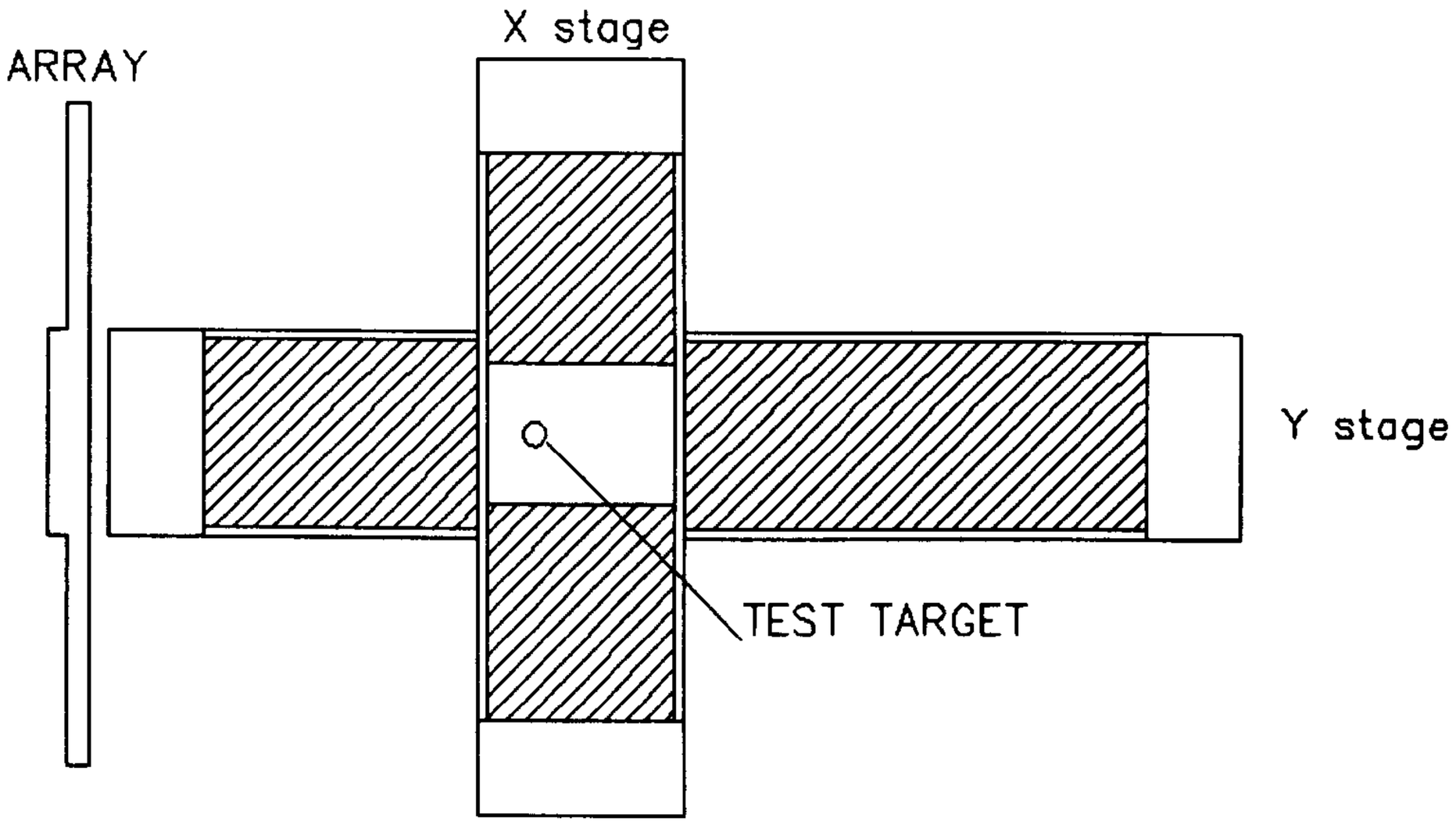

Figure 11: Diagram showing general layout for system testing.

9.6.1 Range accuracy.

The range accuracy of the system was obtained by moving a target along the centre of a beam (constant bearing) and comparing the stage position with the output of the ultrasonic measurement system. The results are presented as a series of error plots where the difference between the measured and actual position are plotted against range. This was repeated for bearings of 0°, 10°, -10°, 20° and -20°. The plots for soft focus are shown in section 9.6.1.1 (Figure 12 to Figure 16) and those for full focus are shown in section 9.6.1.2 (Figure 17 to Figure 21). It can be seen that the error in all cases is within 5mm. Whilst this is greater than the error figures derived in section 9.4, the situations where this error occurs are due to other factors which are explained later.

9.6.1.1 Soft focus range accuracy results.

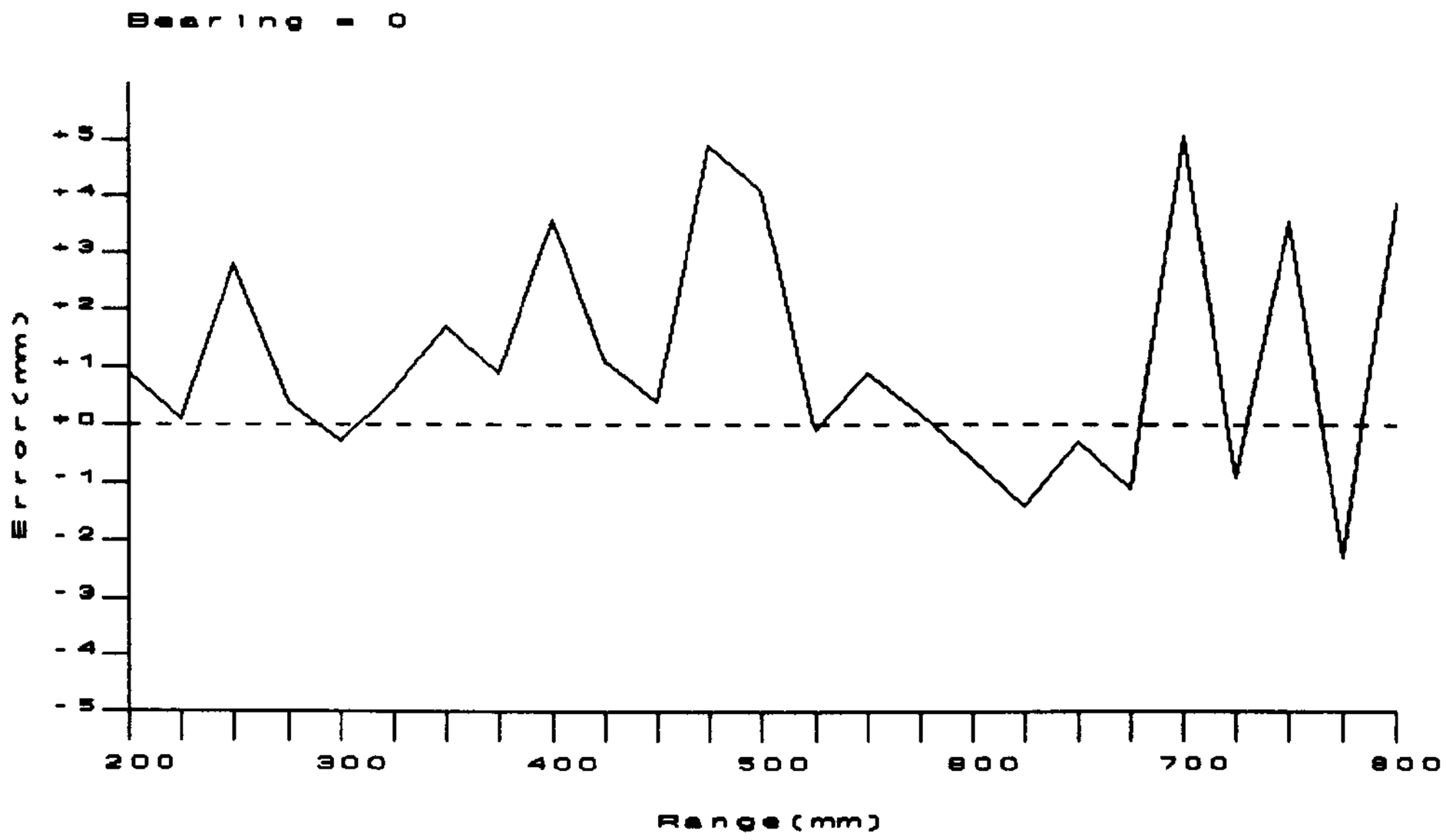

Figure 12: Range error plot target at bearing -20°.

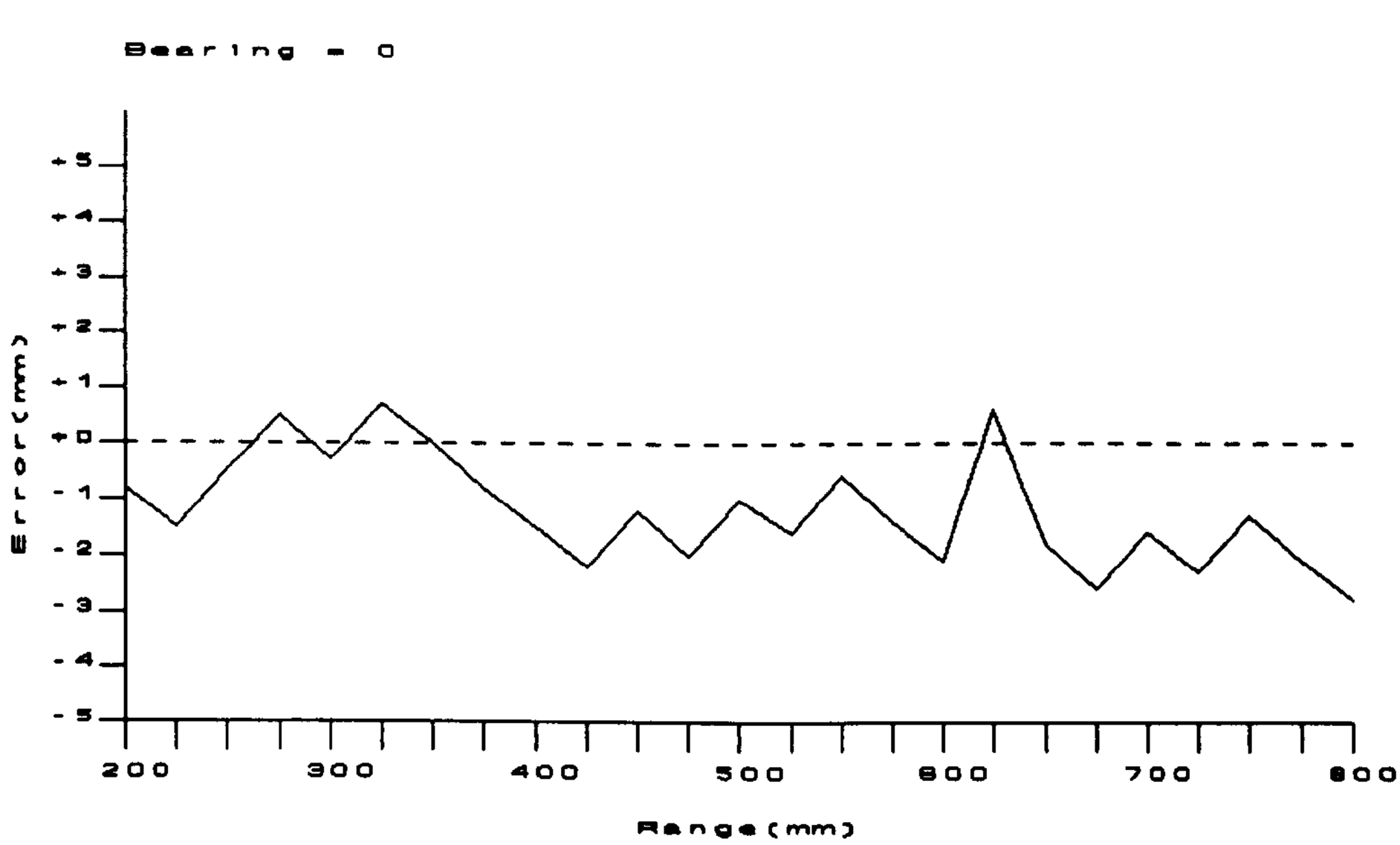

Figure 13: Range error plot for target at a bearing of -10°.

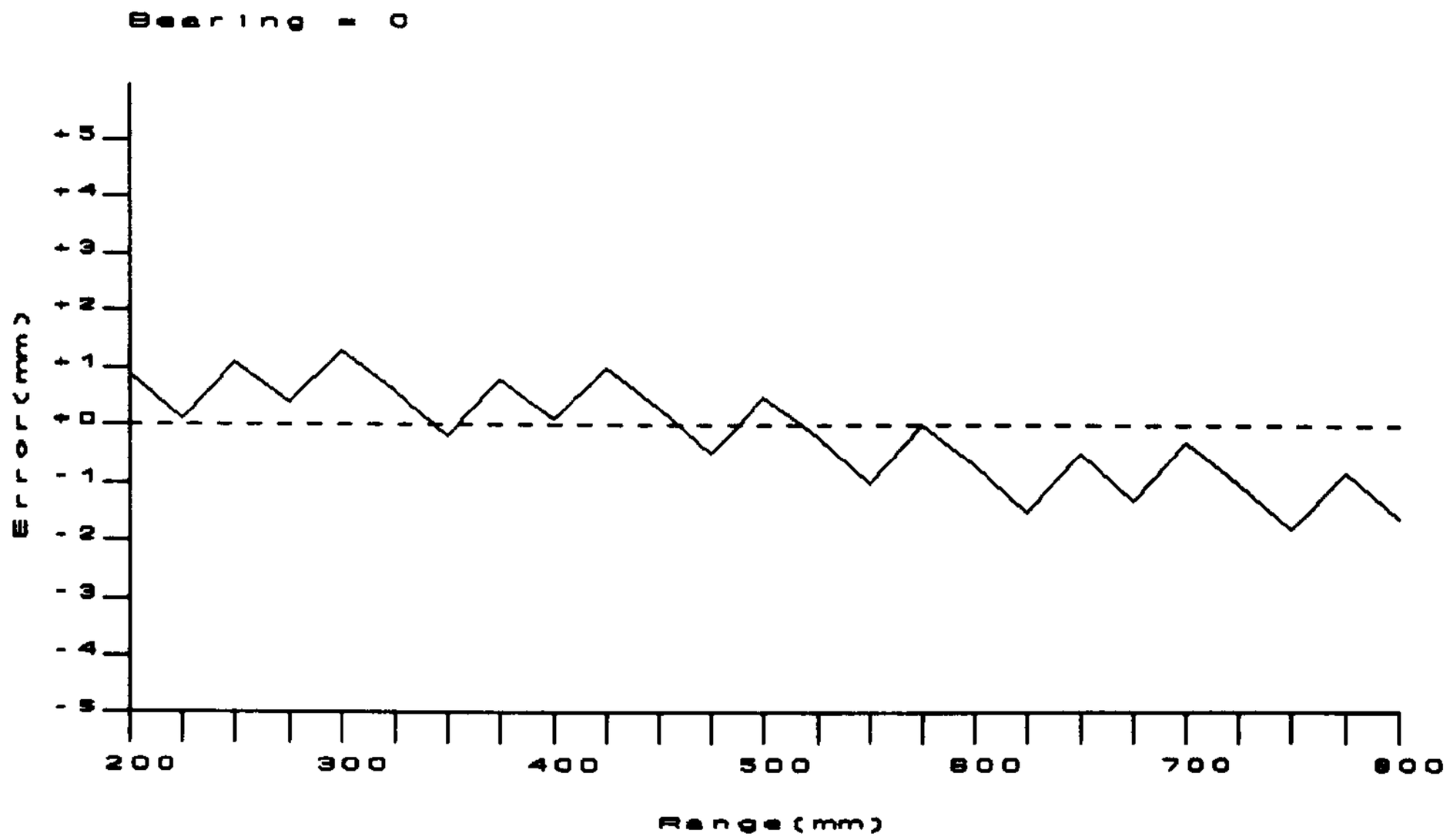

Figure 14: Range error plot for target at bearing 0°.

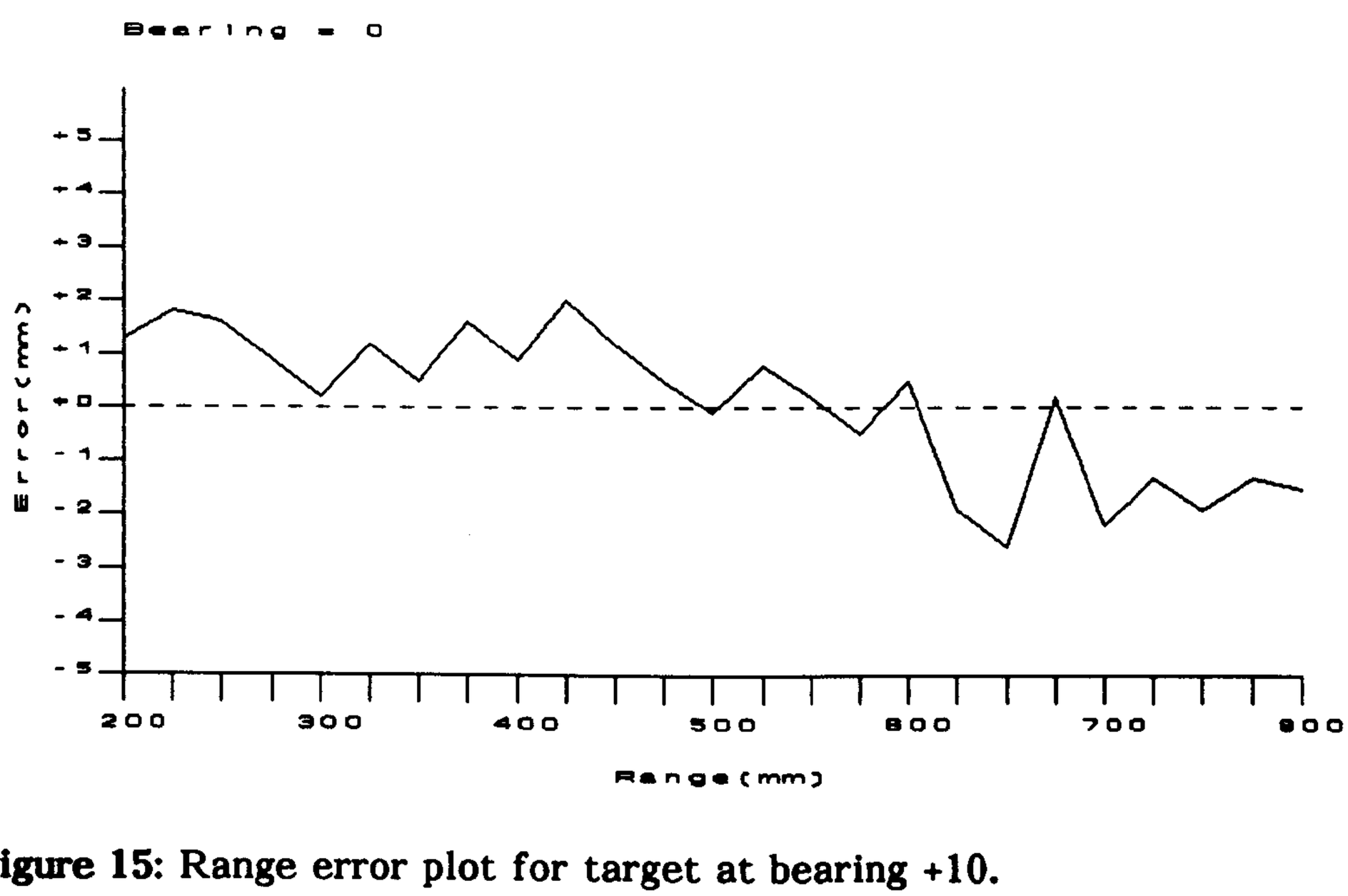

Figure 15: Range error plot for target at bearing +10.

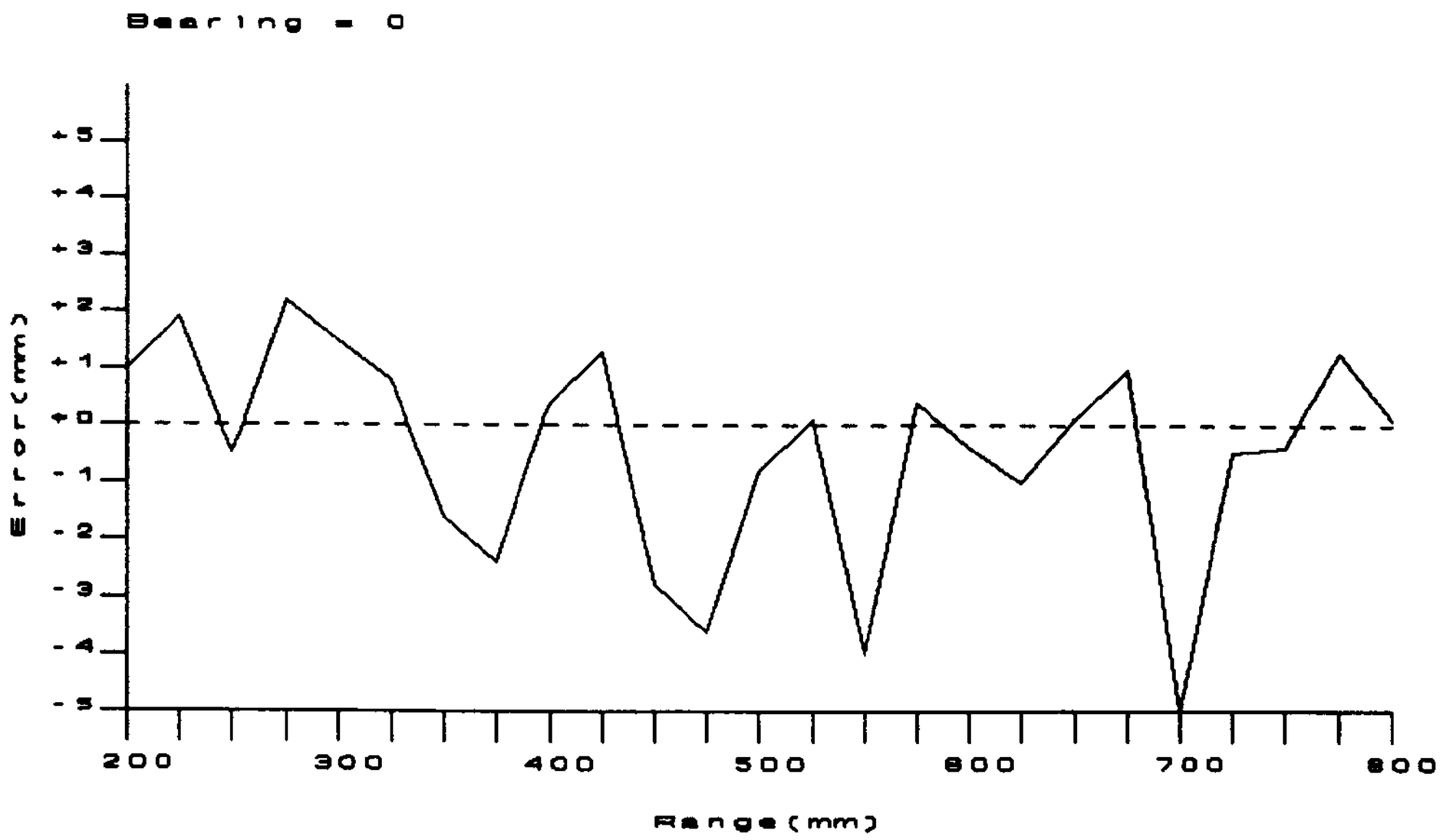

Figure 16: Range error plot for target at bearing 20°.

9.6.1.2 Full focus range accuracy results.

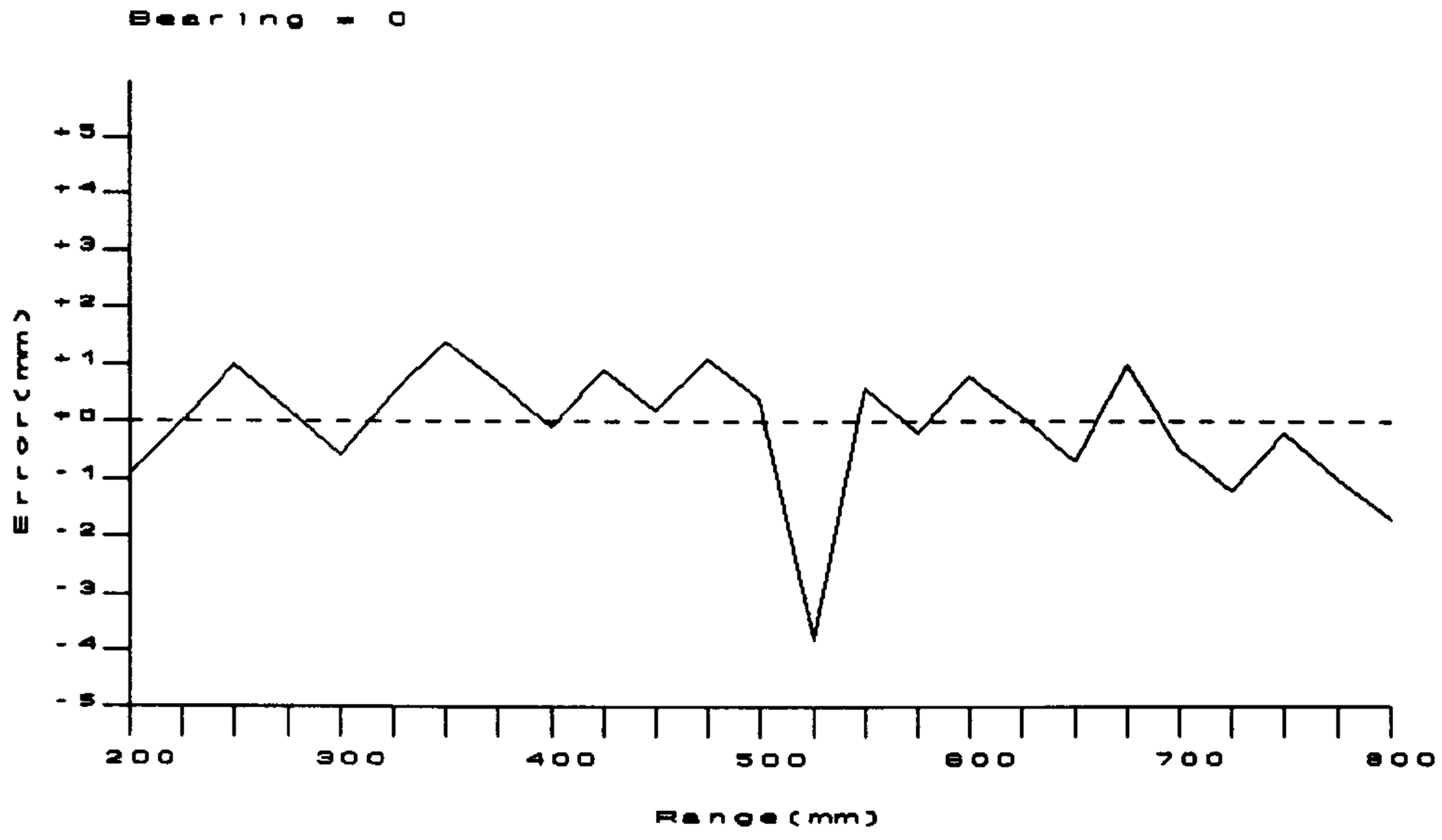

Figure 17: Range error plot for target at a bearing of -20°.

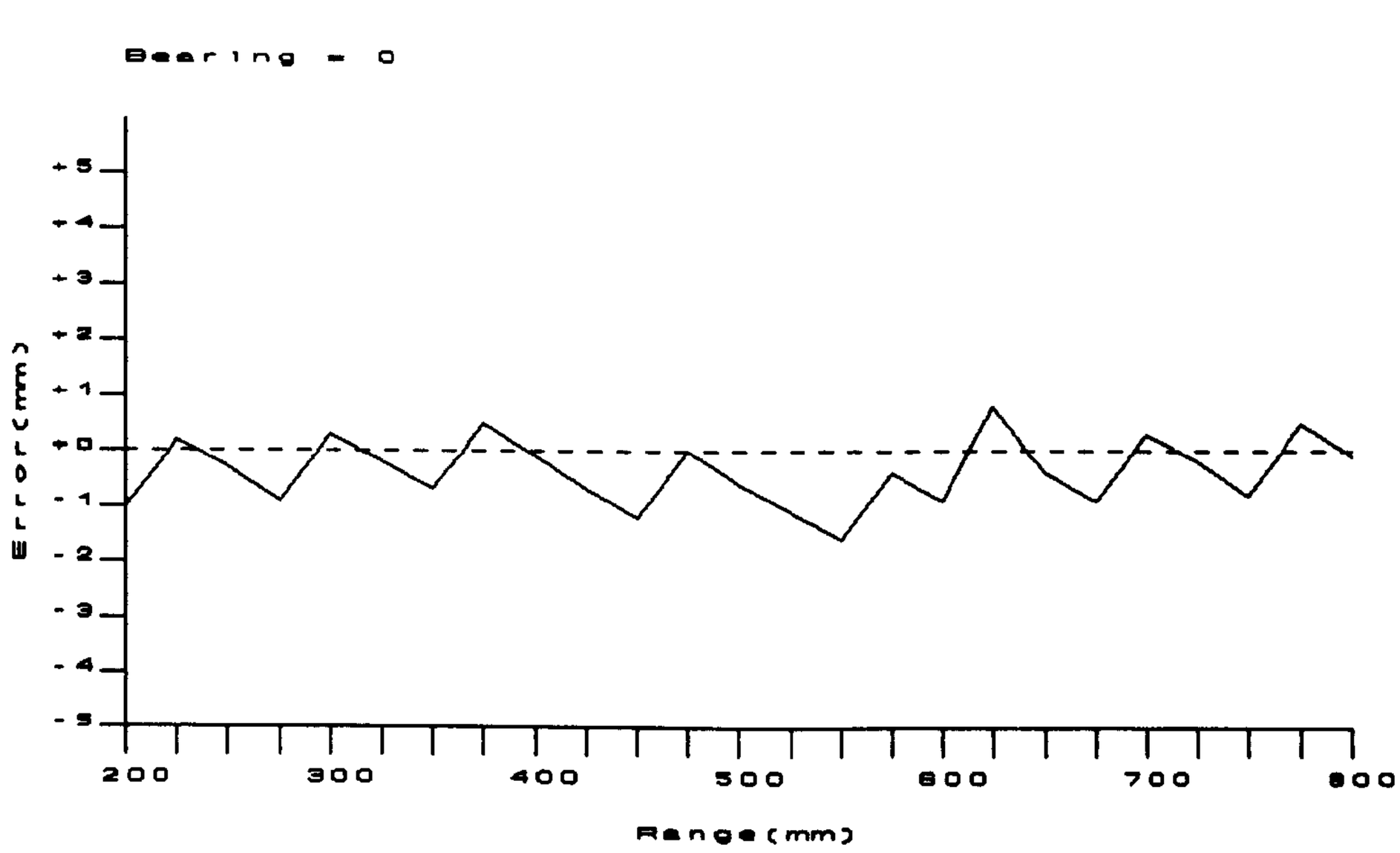

Figure 18: Range error plot for target at bearing -10°.

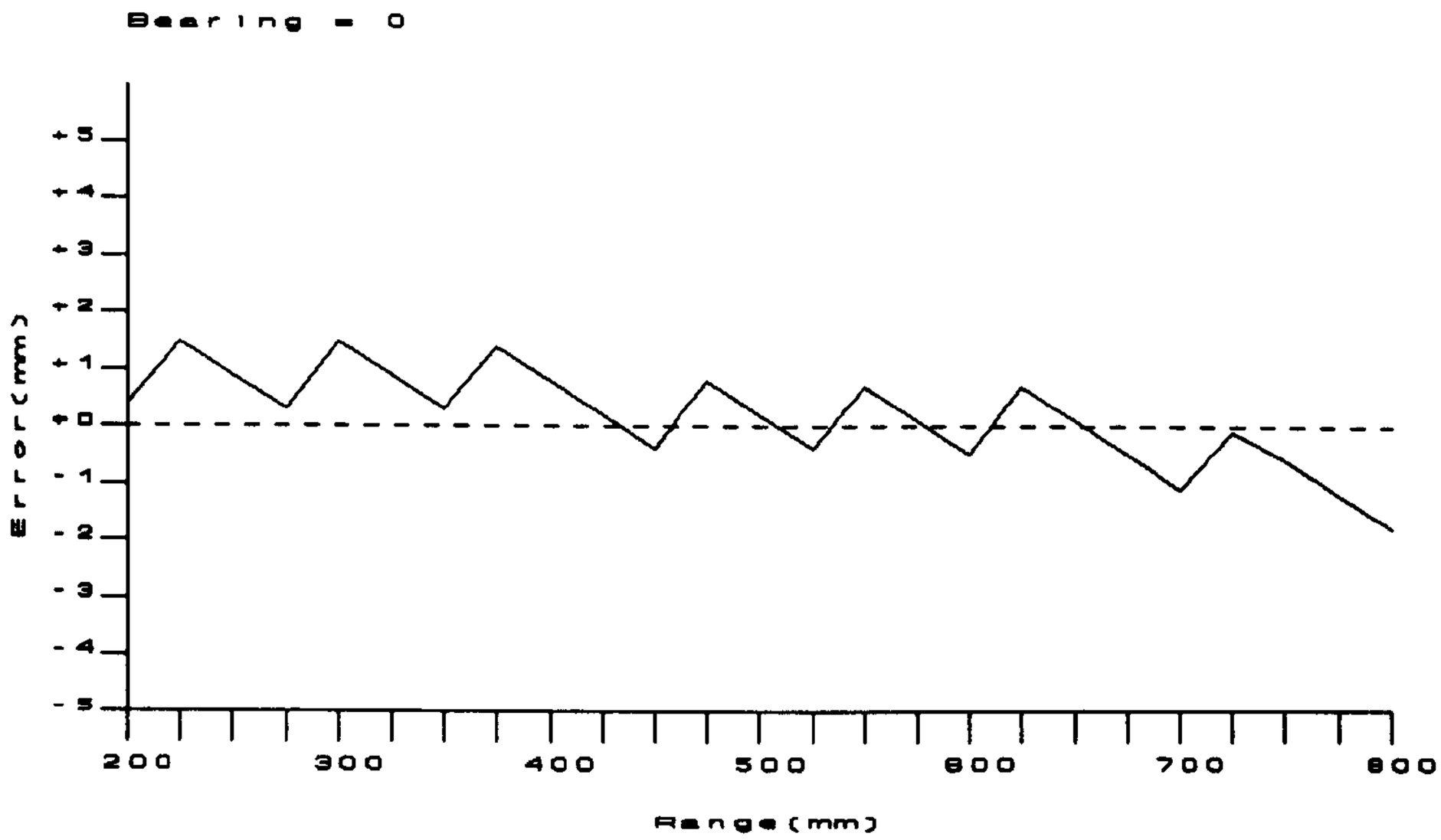

Figure 19: Range error plot for target at bearing 0°.

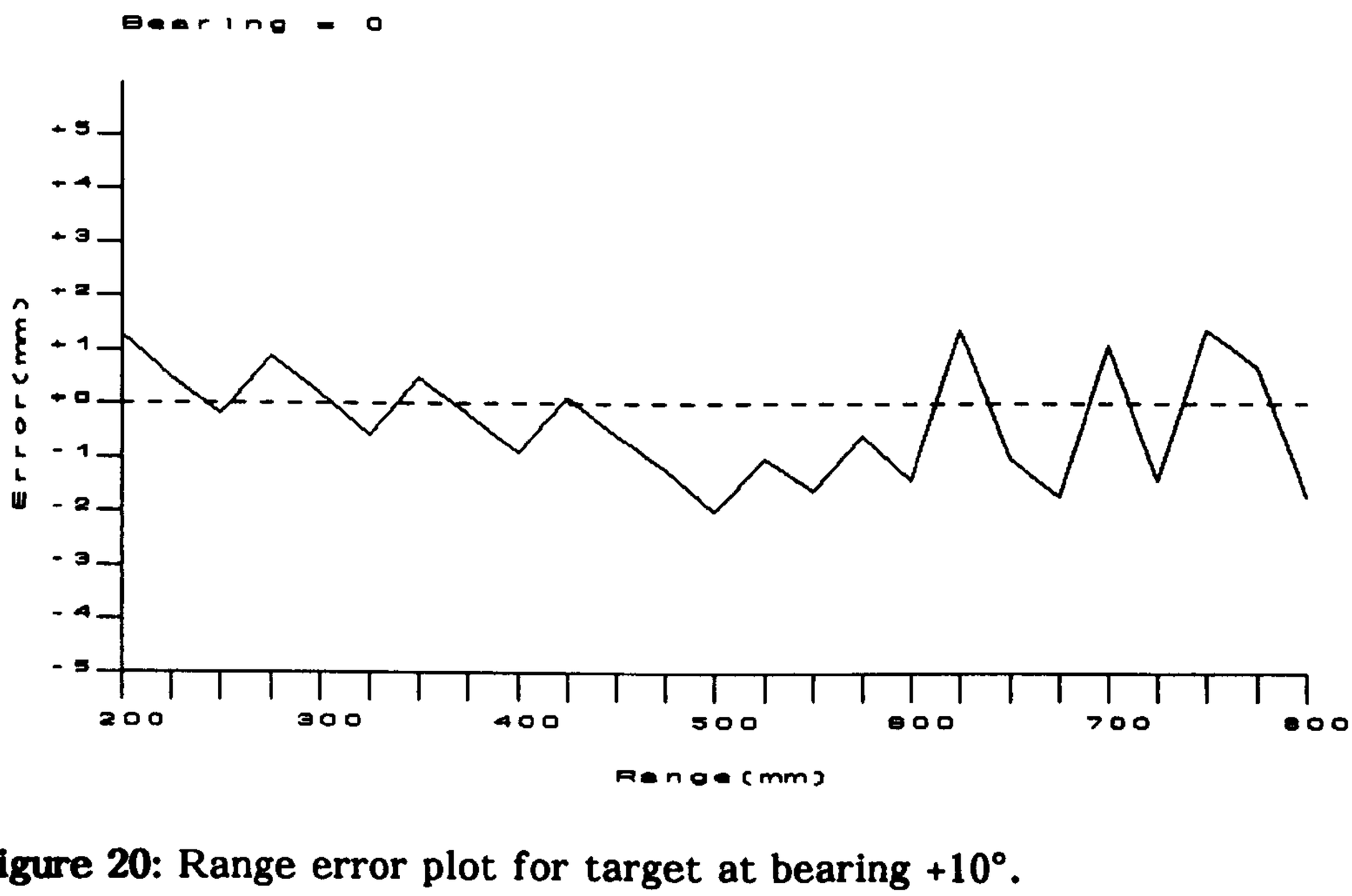

Figure 20: Range error plot for target at bearing +10°.

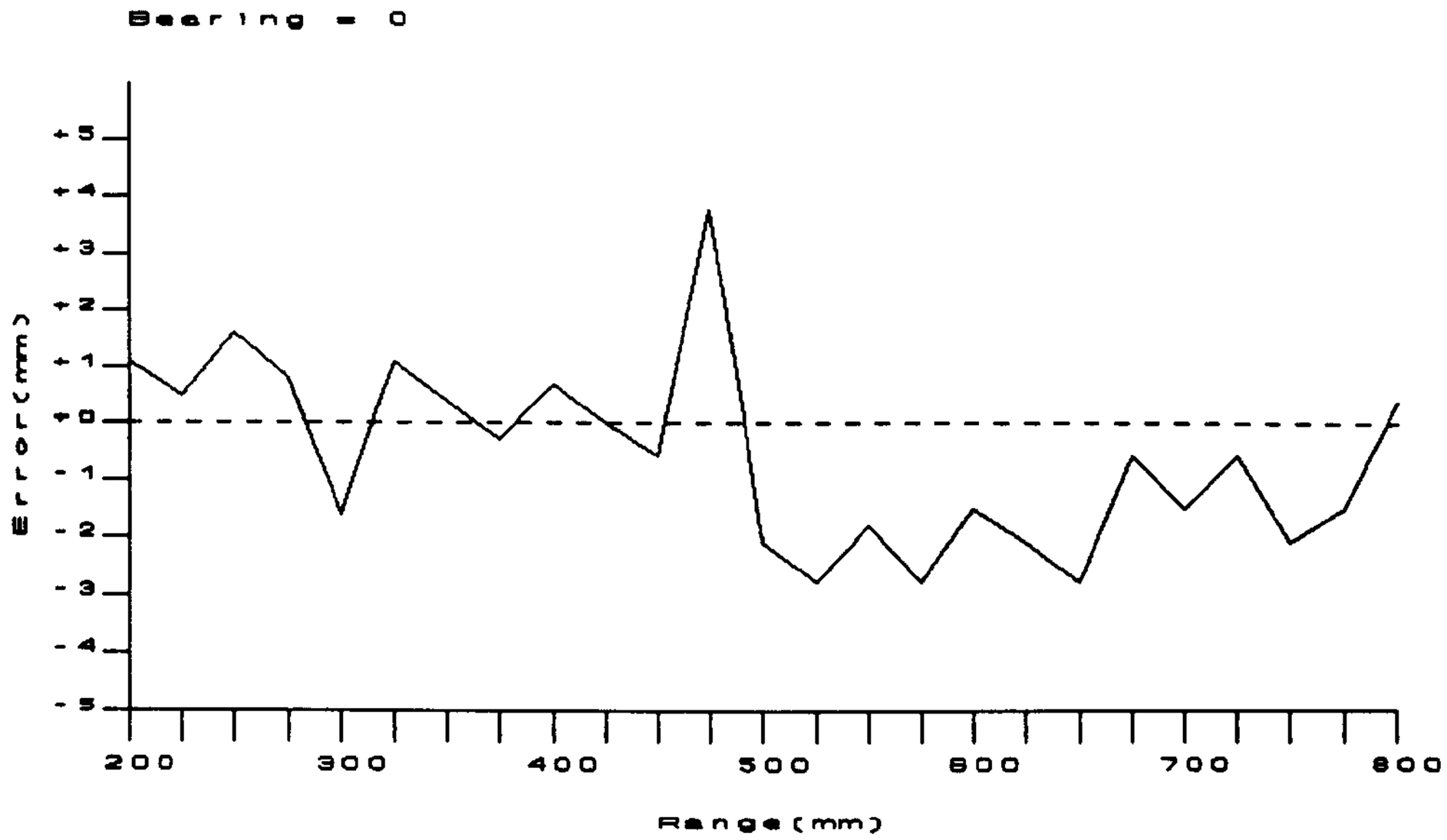

Figure 21: Range error plot for target at bearing 20°.

9.6.1.3 Summary

The first thing that is apparent is that the soft focus system is less accurate than the analysis in sections 9.4 and 9.5 would suggest. This is as predicted in chapter 7 and confirms the expected trade off of speed for accuracy. The error is particularly noticeable at larger angles, again as predicted. The results from the hard focus system are all within the predicted resolution except for those at ±20° and approximately 500mm and at 0° and 800mm. These ±20° values are outside the predicted resolution because they coincide with the junctions between the transmitters and the array. This results in an area of low transmitter output and thus a poor signal to noise ratio. The inaccuracy in the 0° plot is probably due to a combination of a random error above the level predicted and a maximum systematic error. The results from the +20° bearing are less accurate than the -20° bearing because the transmitter output was found to be less on that side. This power output difference is due to unknown factors during manufacture. The

presence of systematic errors are apparent in some of the results and these manifest themselves as a gentle slope in the range error plots. The system has been proved capable of operating within the prescribed limits.

9.6.2 Bearing accuracy.

The bearing accuracy of the system was obtained by moving a target parallel to the front of the array (constant range) and comparing the stage position with the output of the ultrasonic measurement system. The results are presented as a series of plots the measured and actual position are plotted on the same axis. This was repeated for a series of ranges between 200mm an 550mm. The plots for soft focus are shown in section 9.6.2.1 (Figure 22 to Figure 29) and those for full focus are shown in section 9.6.2.2 (Figure 30 to Figure 37). Most of the results fall within the resolution of the system but some of the beams appear slightly broadened or narrowed the reasons for this are explained in section 9.6.2.3.

9.6.2.1 Soft focus bearing accuracy results.

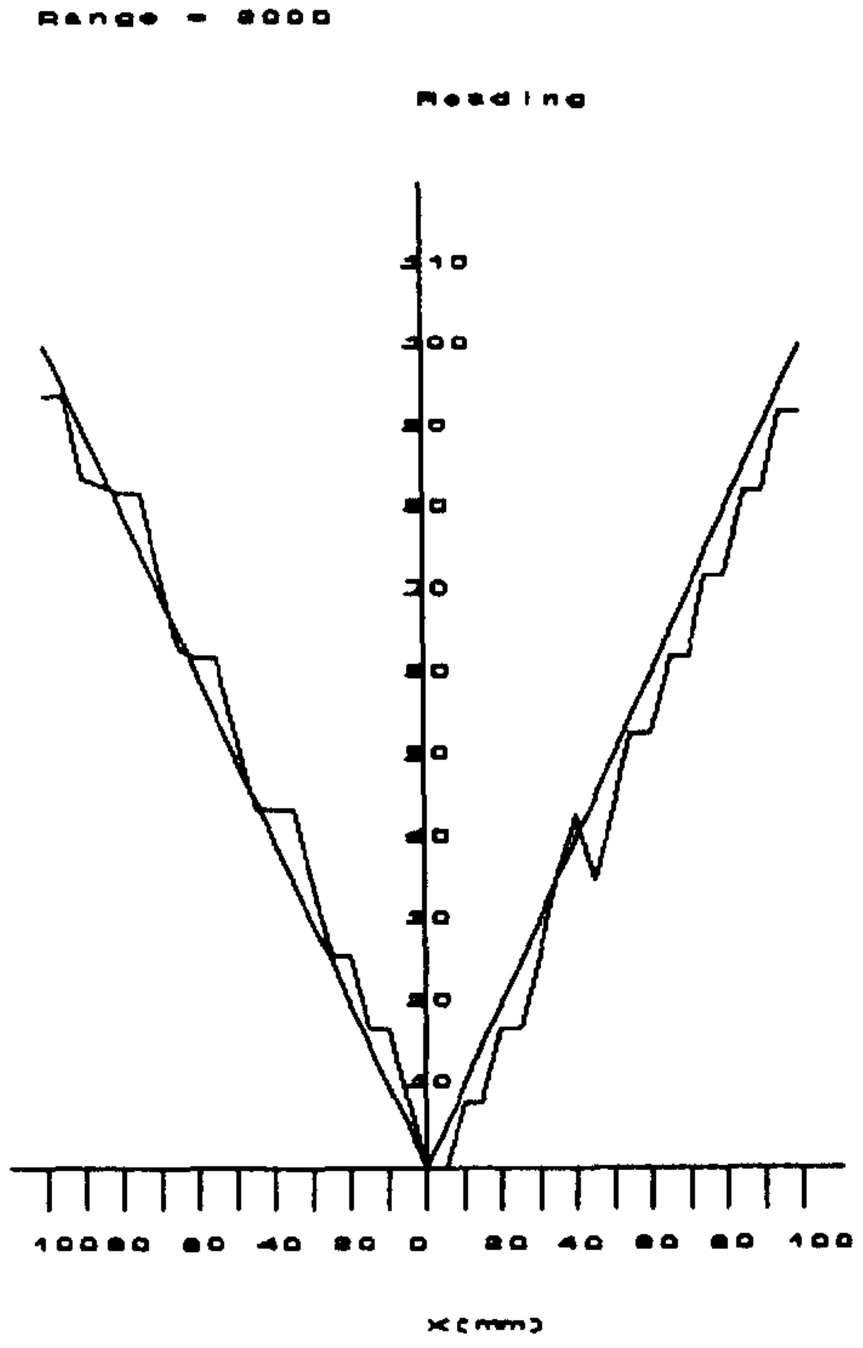

Figure 22: Bearing error plot for 200mm range.

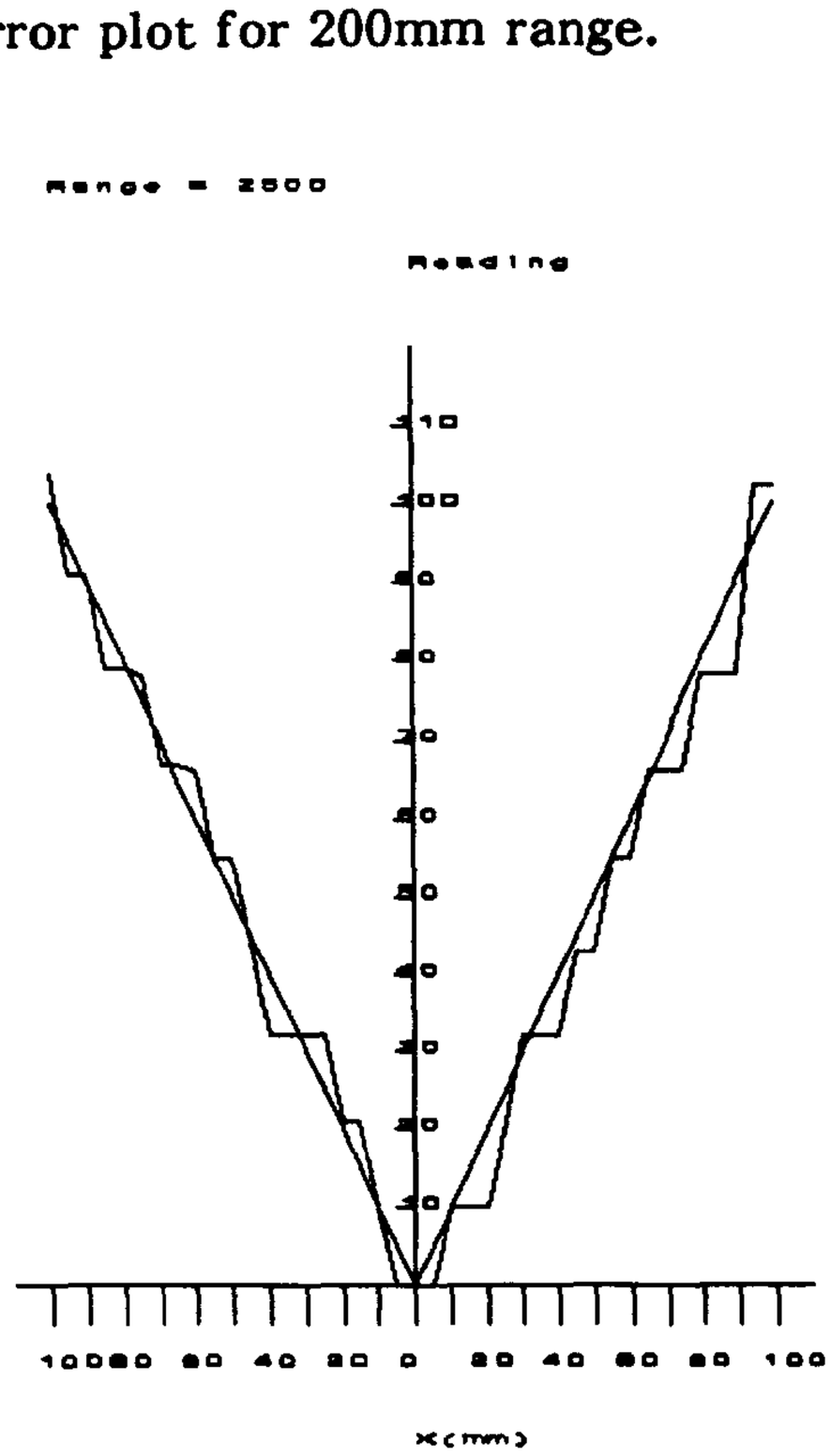

Figure 23: Bearing error plot for 250mm range.

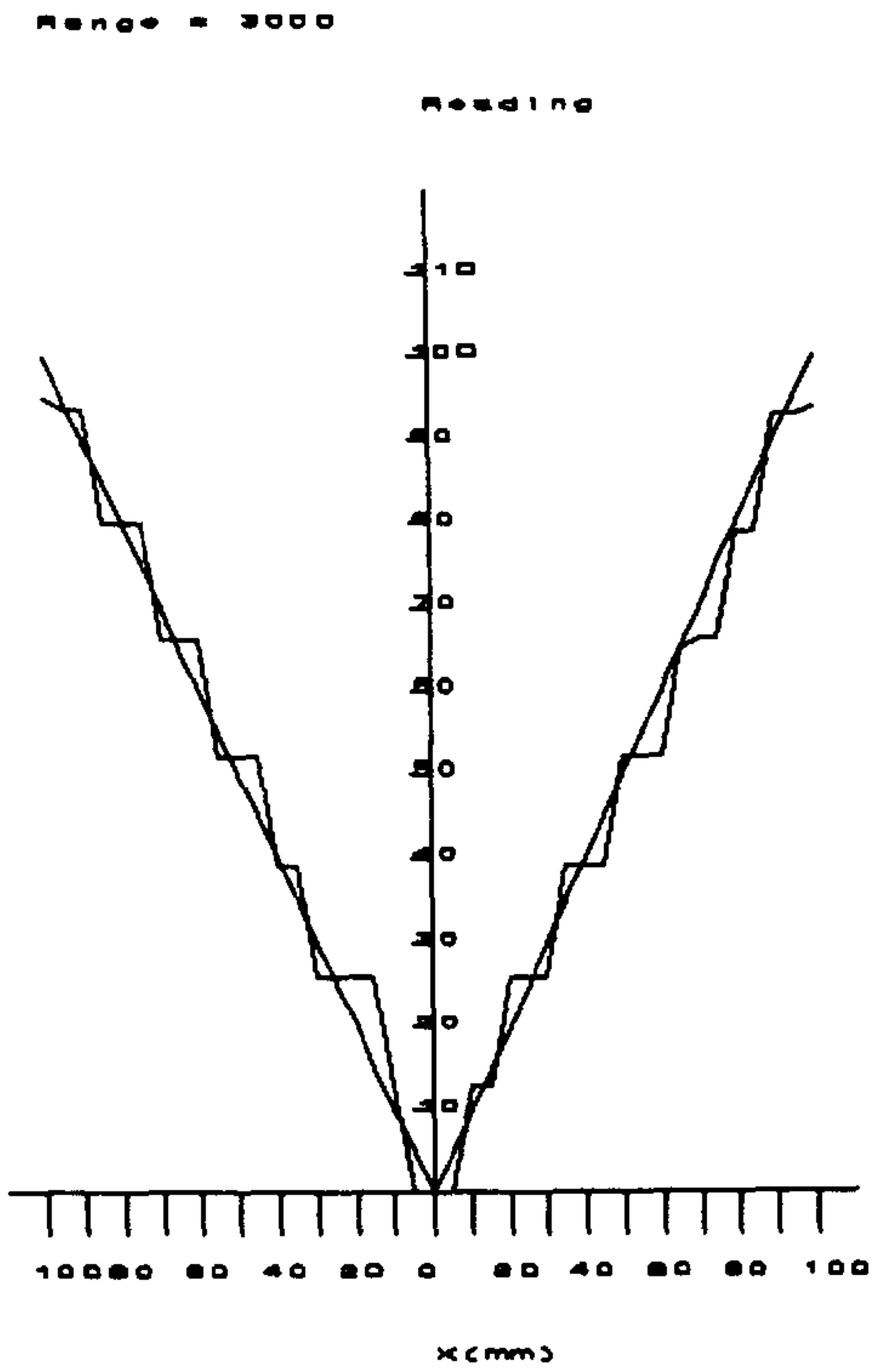

Figure 24: Bearing error plot for 300mm range.

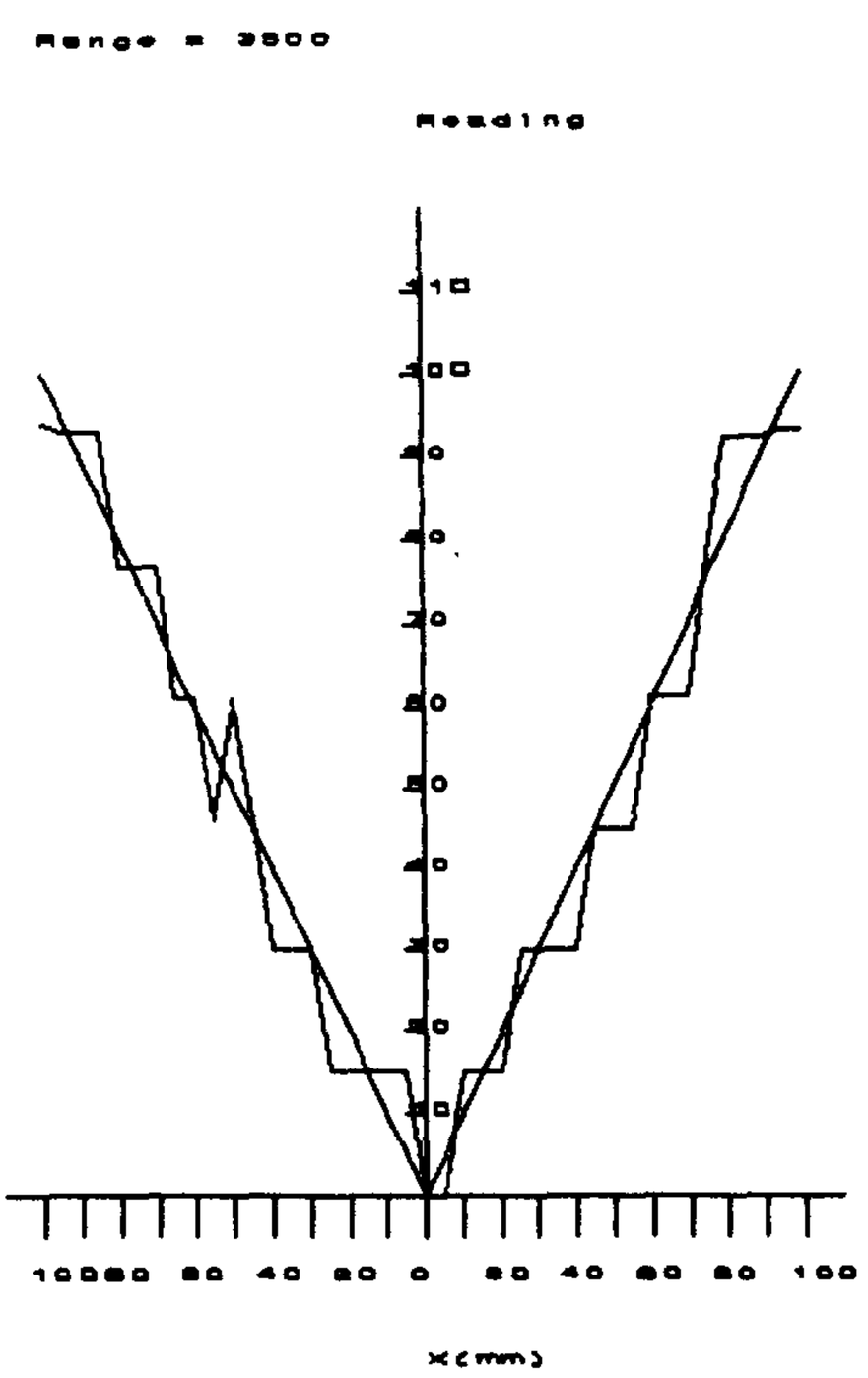

Figure 25: Bearing error plot for 350mm range.

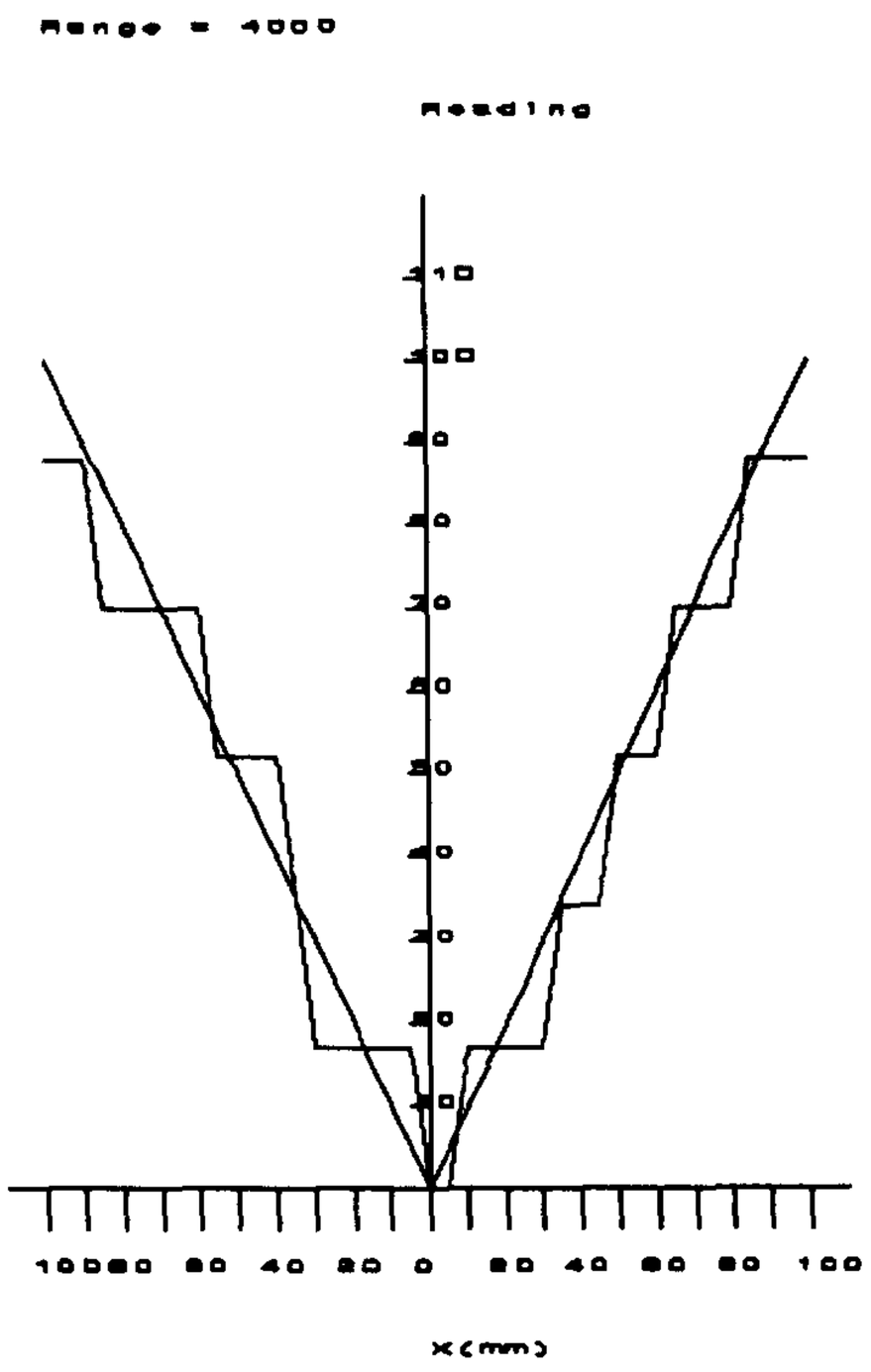

Figure 26: Bearing error plot for 400mm range.

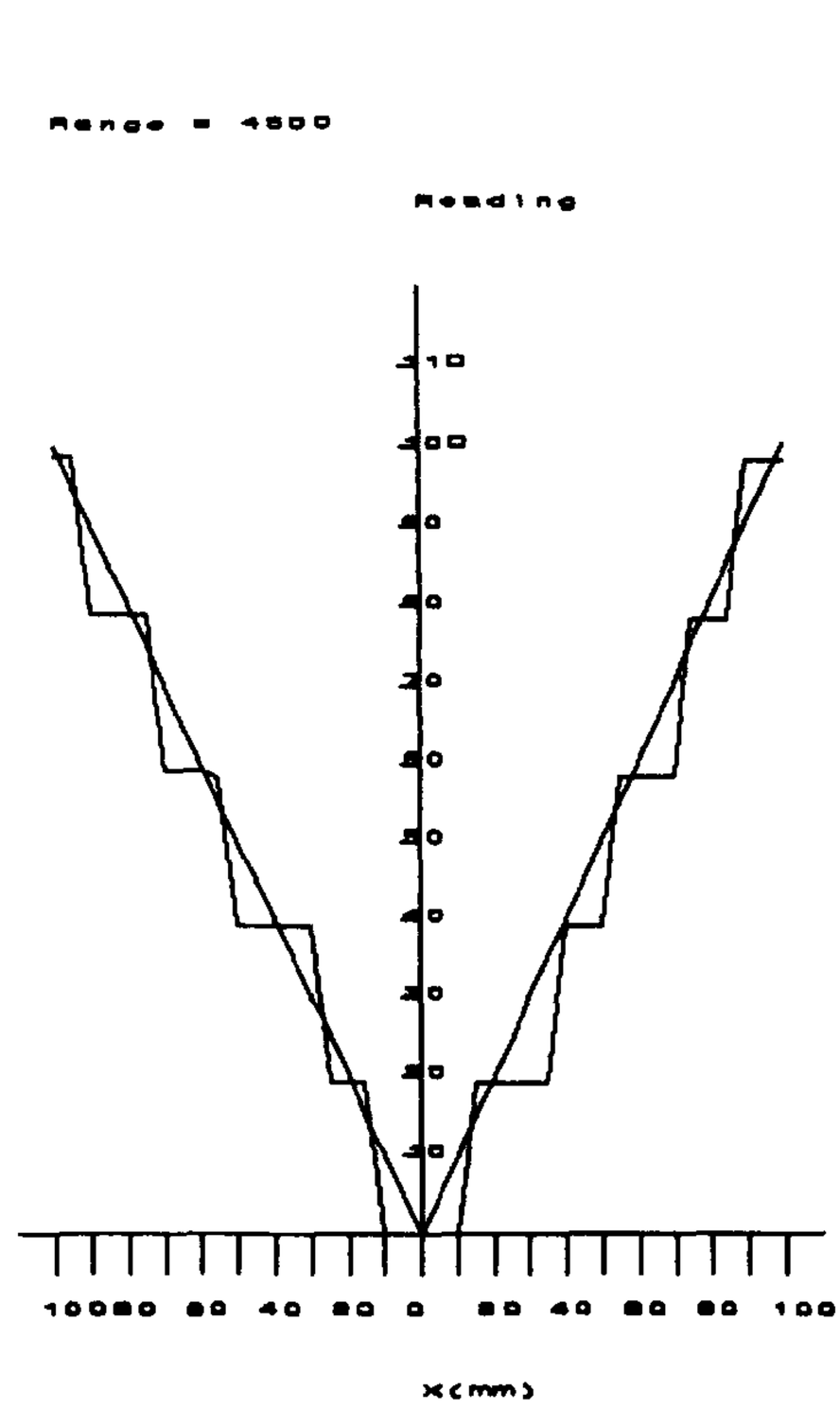

Figure 27: Bearing error plot for 450mm range.

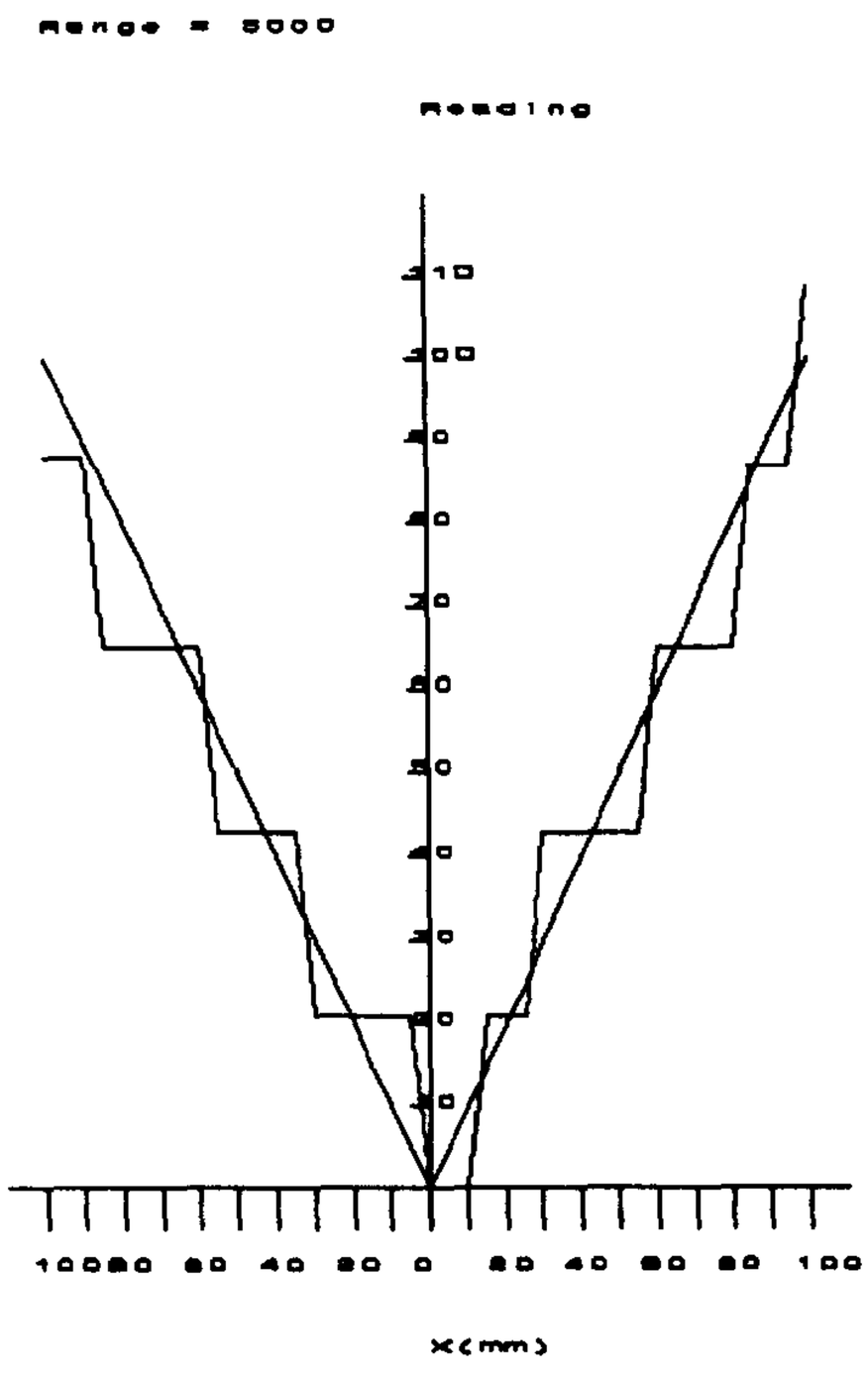

Figure 28: Bearing error plot for 500mm range.

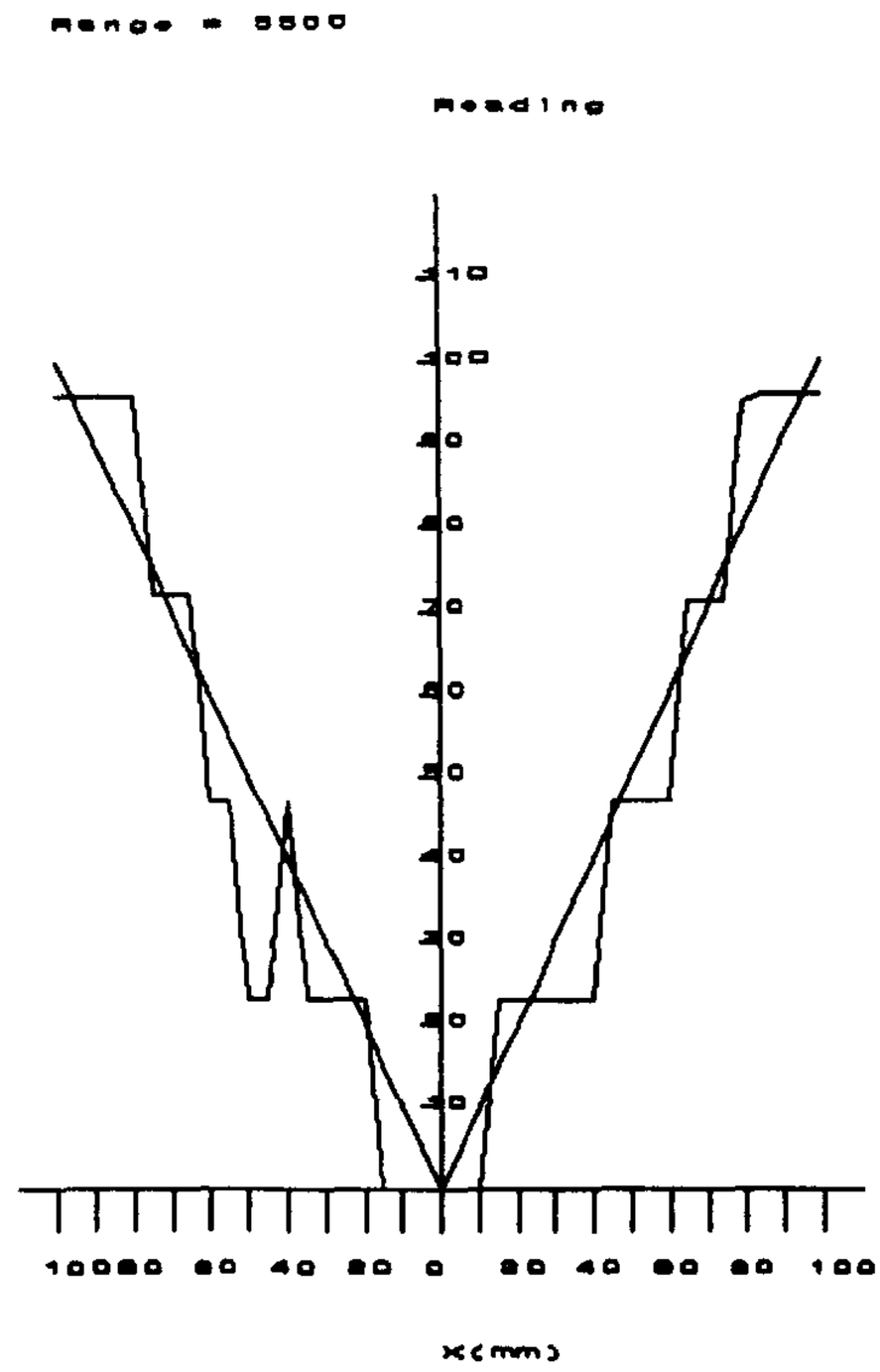

Figure 29: Bearing error plot for 550mm target.

9.6.2.2 Full focus bearing accuracy results.

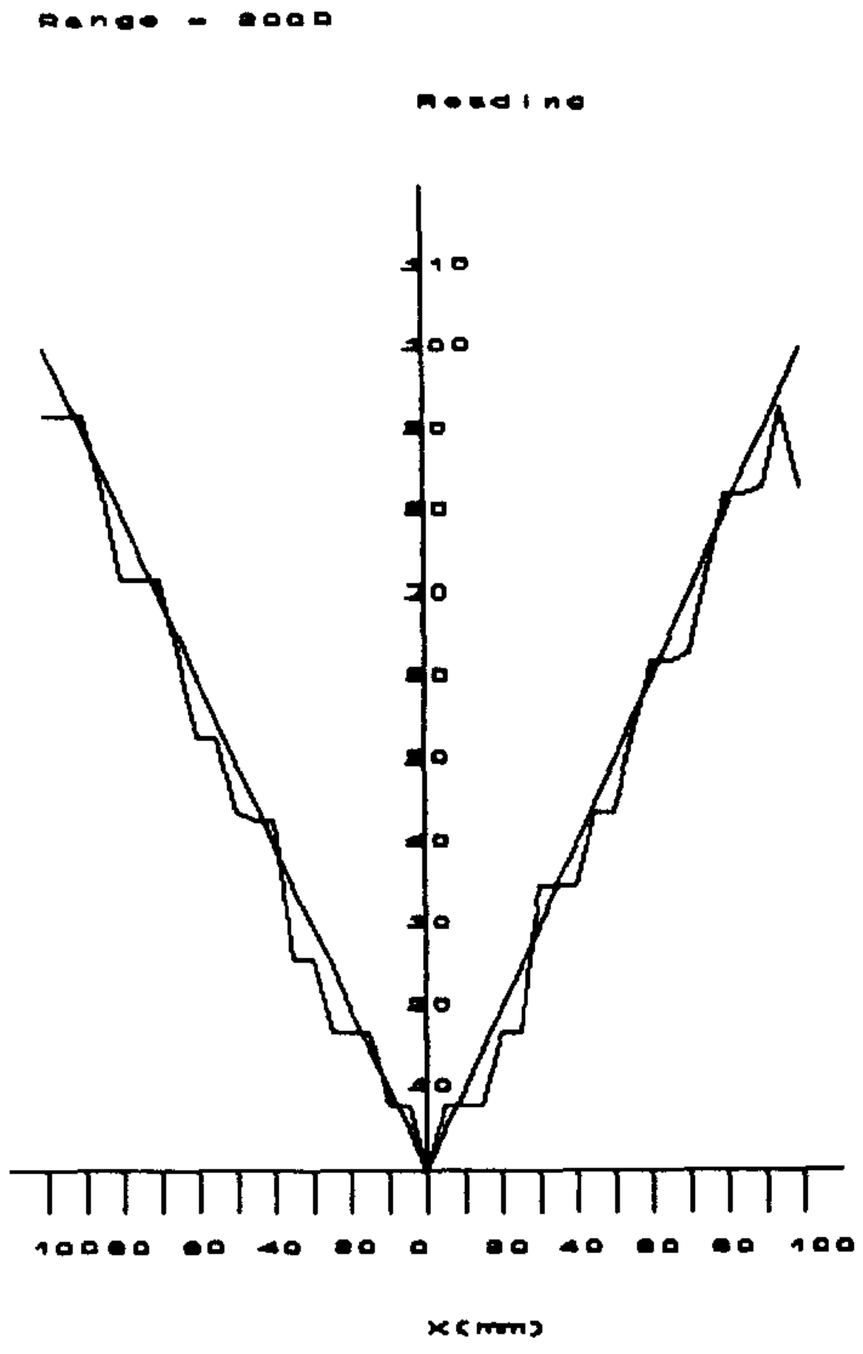

Figure 30: Bearing error plot for 200mm range.

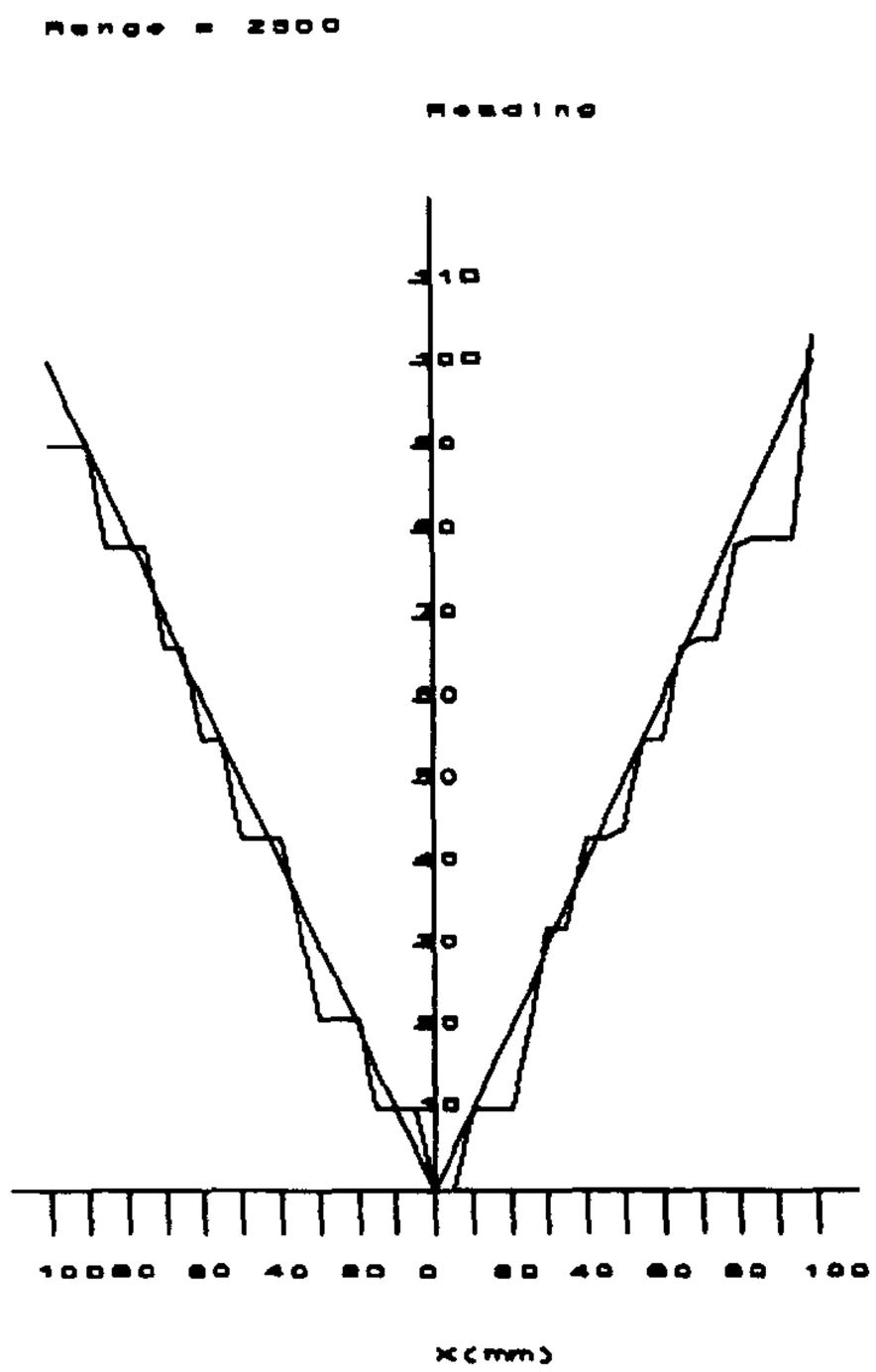

Figure 31: Bearing error plot for 250mm range.

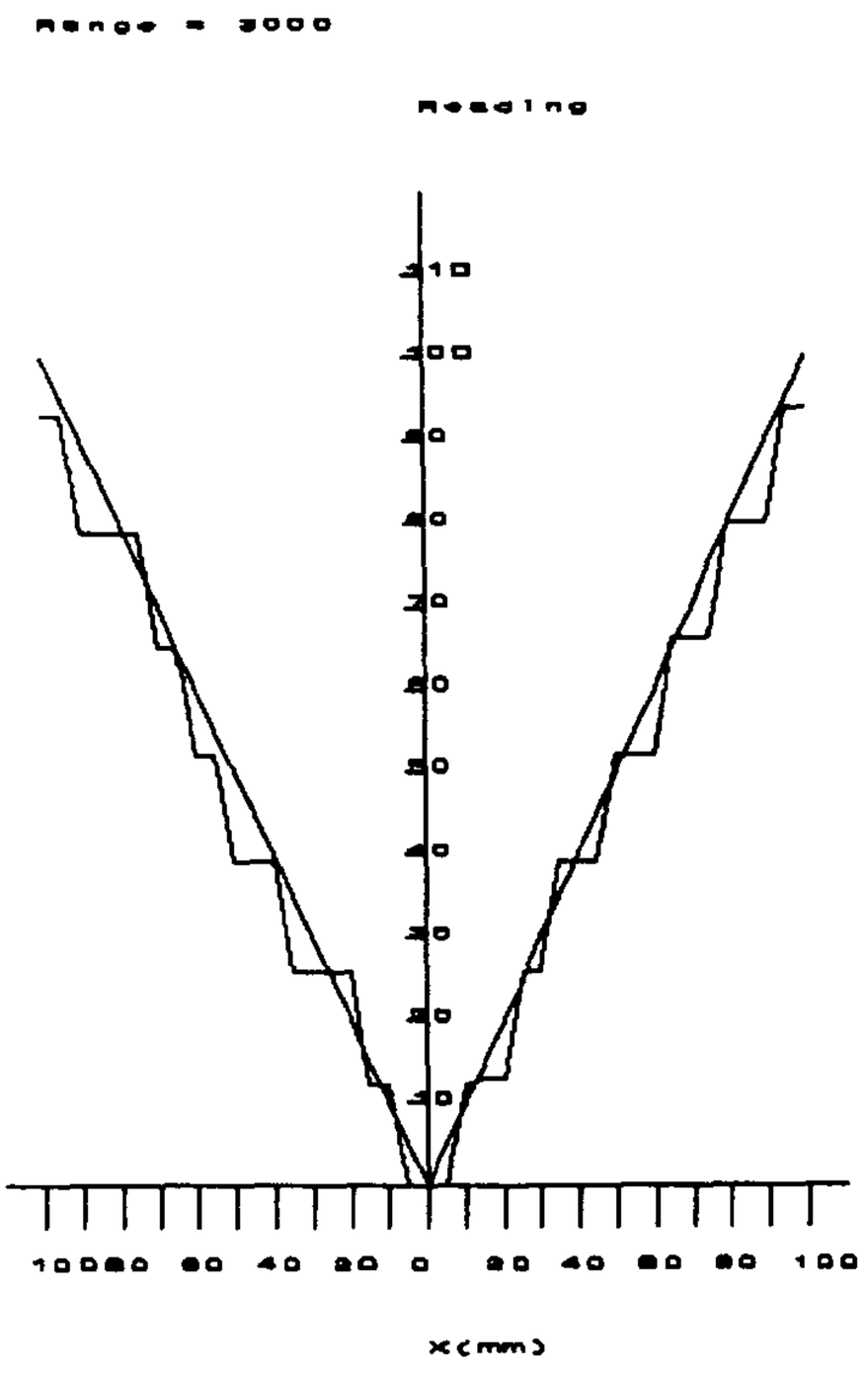

Figure 32: Bearing error plot for 300mm range.

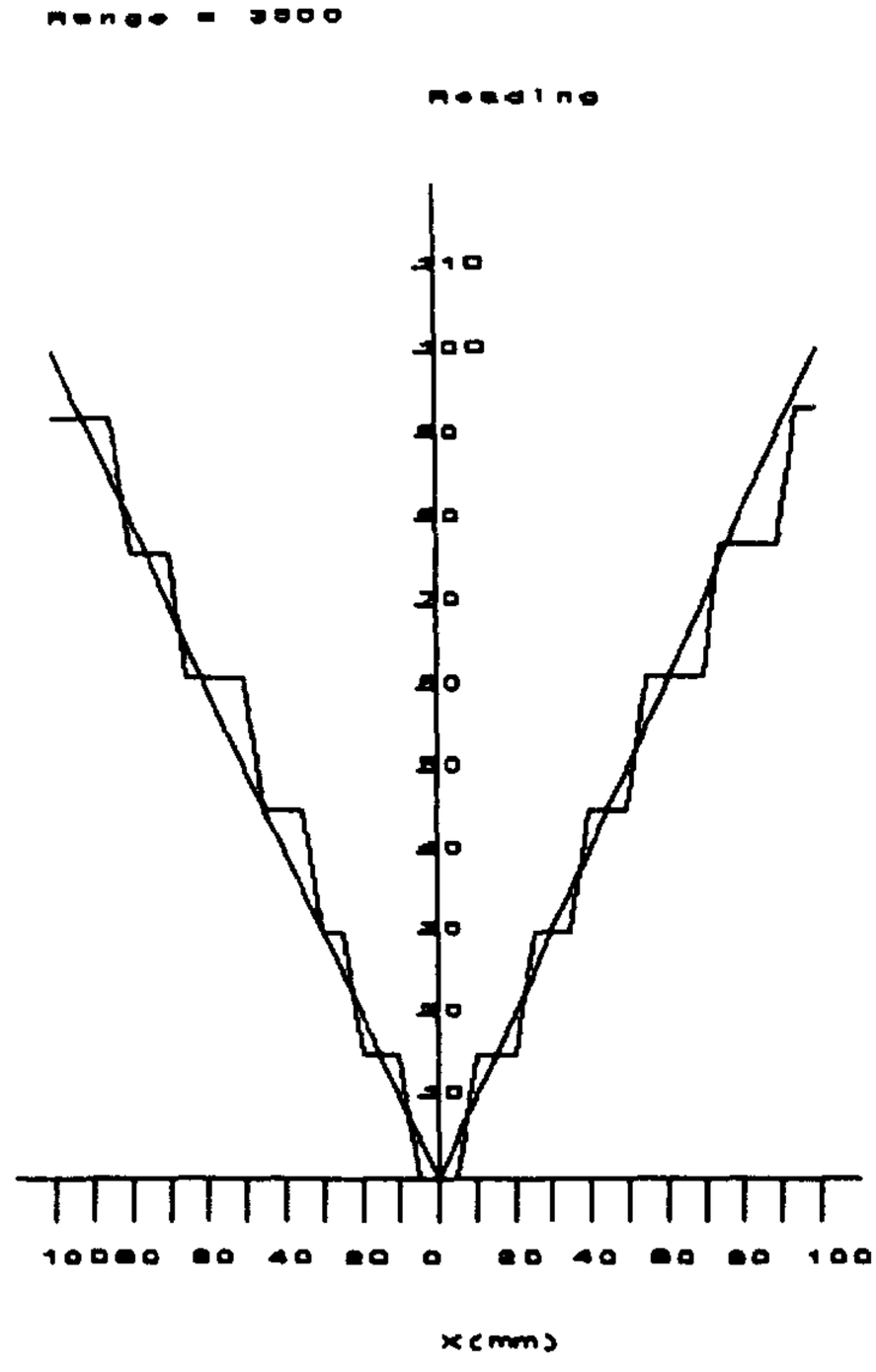

Figure 33: Bearing error plot for 350mm range.

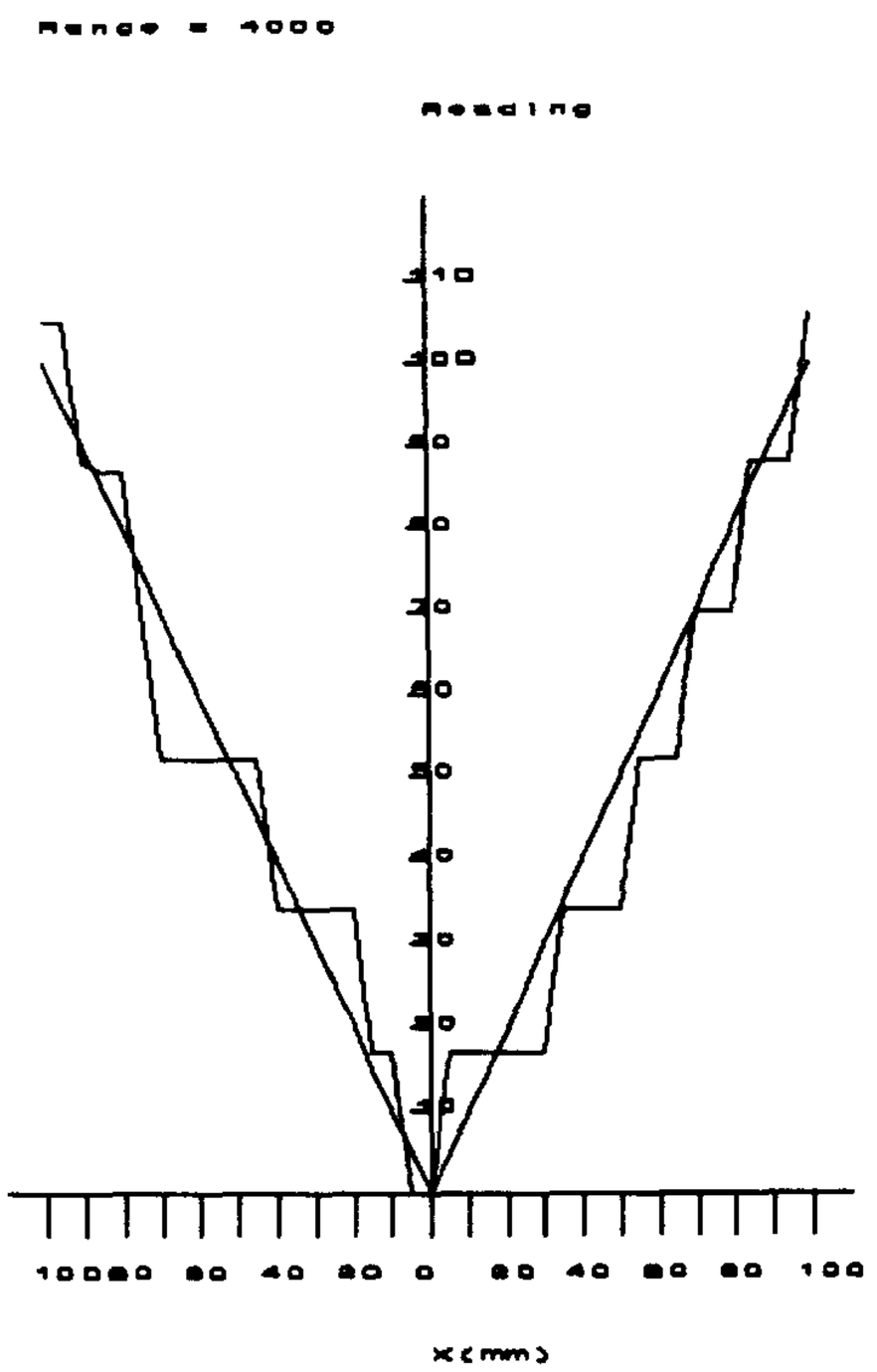

Figure 34: Bearing error plot for 400mm range.

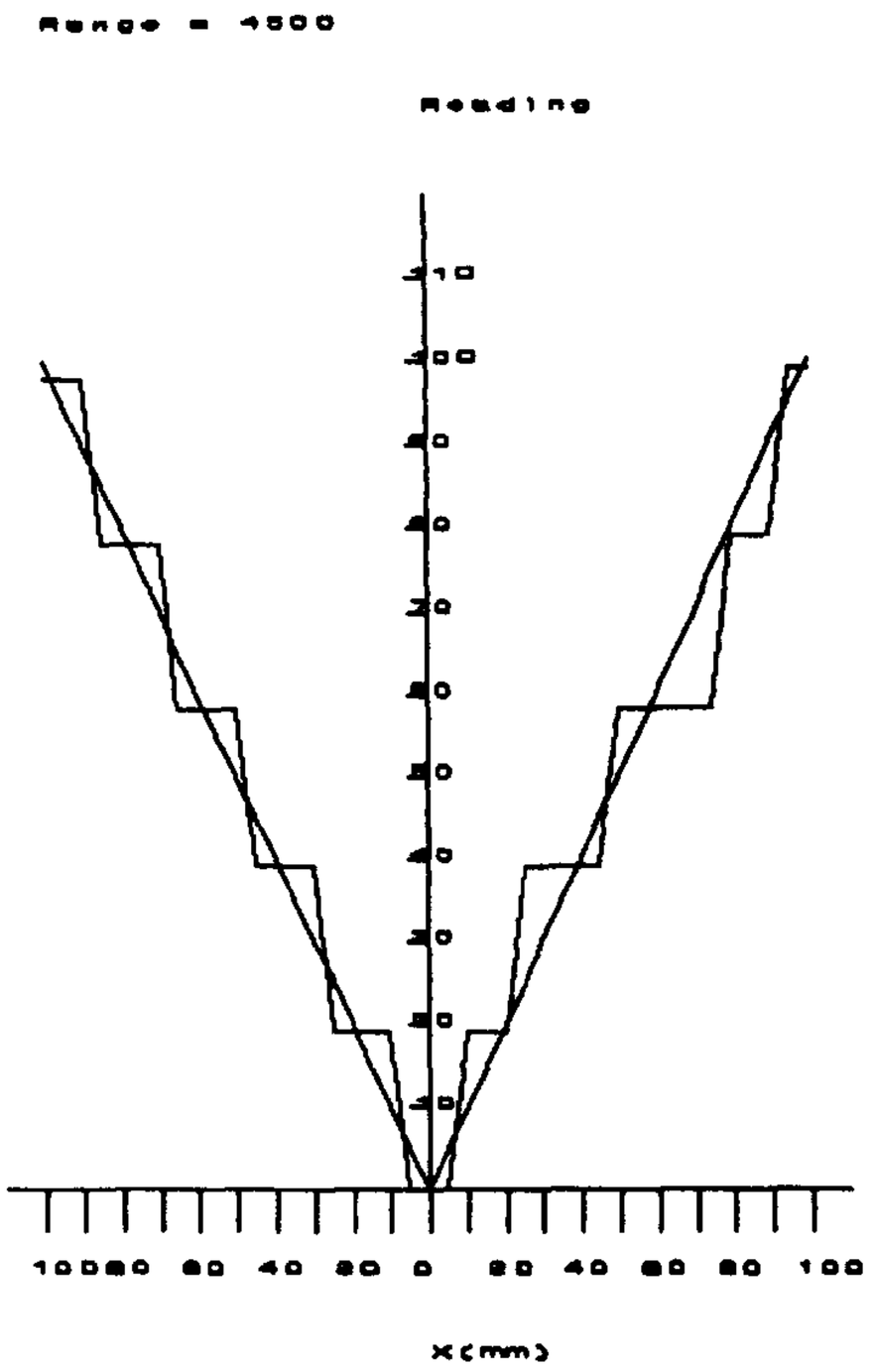

Figure 35: Bearing error plot for 450mm range.

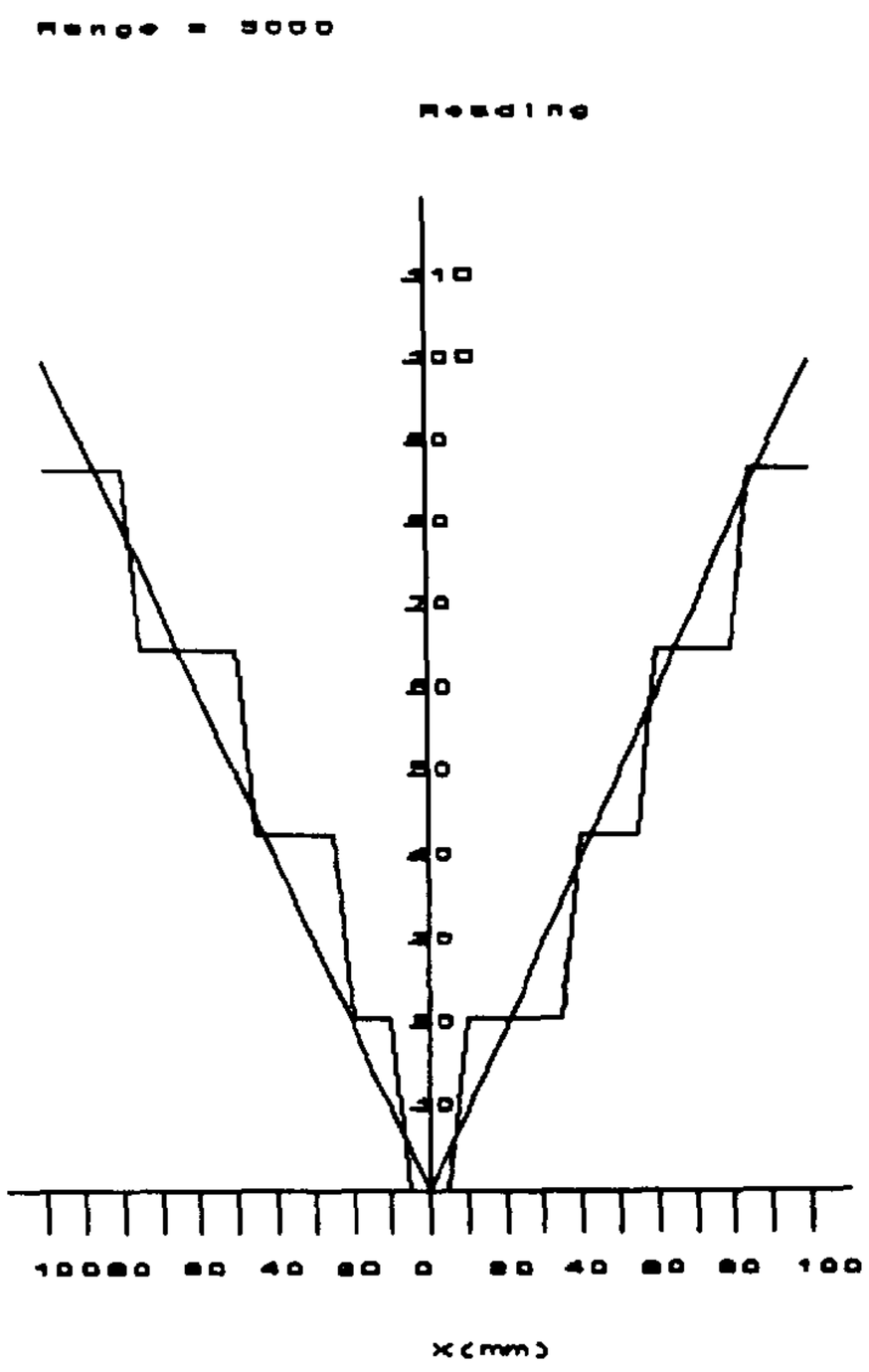

Figure 36: Bearing error plot for 500mm range.

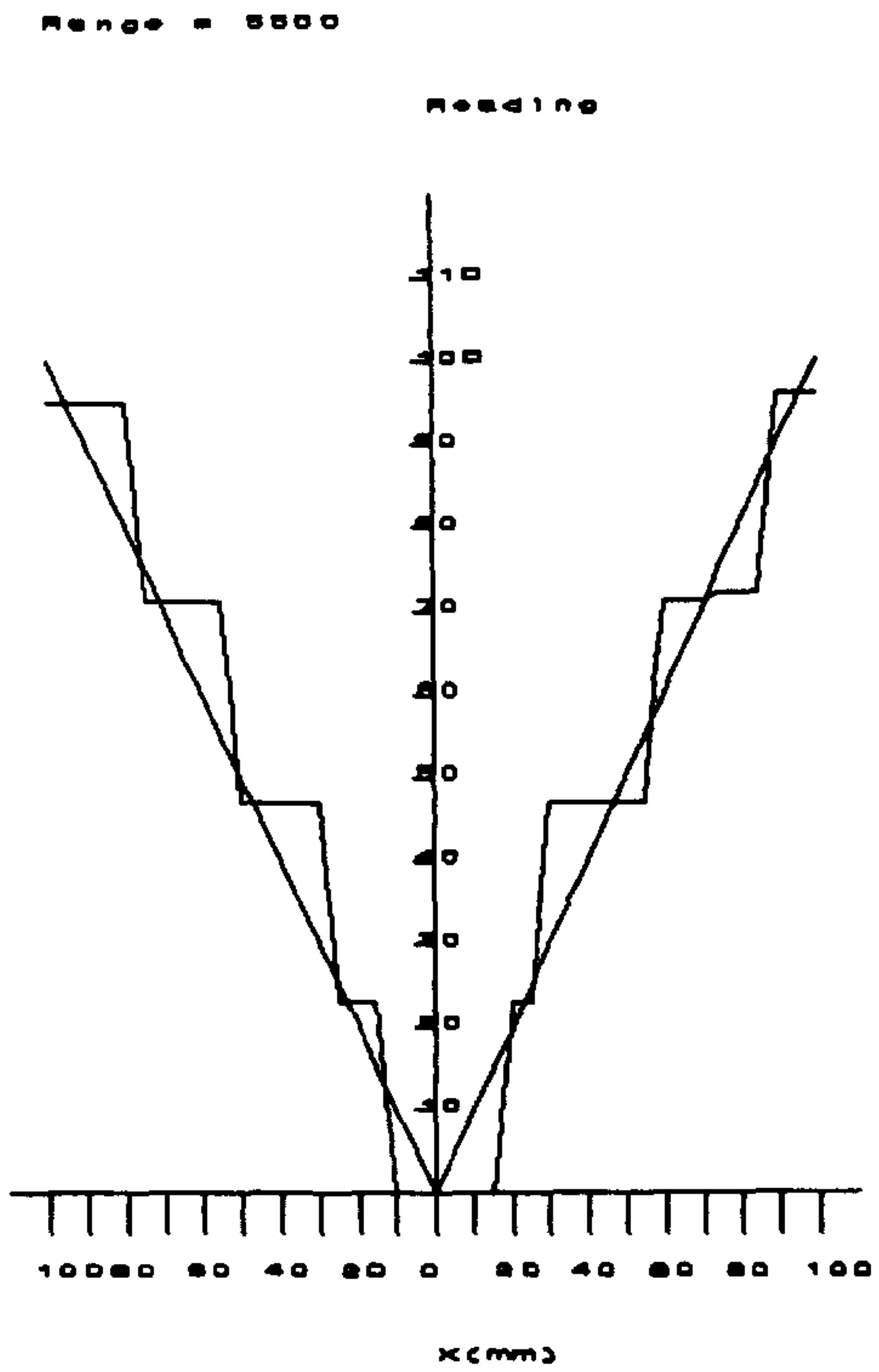

Figure 37: Bearing error plot for 550mm target.

9.6.2.3 Summary

Comparison between the results for bearing measurements show that there is little to choose between full and soft focusing. This is probably due to the lower resolution expected in bearing compared with that expected in range. It can be seen that in some cases the target has actually jumped beams due to the presence of noise and errors when the target is close to the edge of a beam. Taking the soft focus 350mm plot as an example, the beams at this range should have a width of approx 15mm. This is not the case in all the measurements taken but two factors must be considered; firstly there is always the possibility of jitter occurring near the boundary between two beams (see section 9.7), secondly positions used to measure accuracy were picked arbitrarly and not to coincide with beam centres. In the range accuracy experiments, where the target bearing was picked to maintain the target centrally in a beam it was recorded as remaining in the correct beam at all times. The overall effect of this, and random and systematic errors, is to broaden or narrow adjacent beams.

9.7 Beam stability.

In any system which relies on the division of a signal into a series of discrete quantisation there is bound to be an area of uncertainty between levels. The width of this region is dependent on the level of noise within the system (see chapter 8) and the presence of random measurement errors (see section 9.4.2).

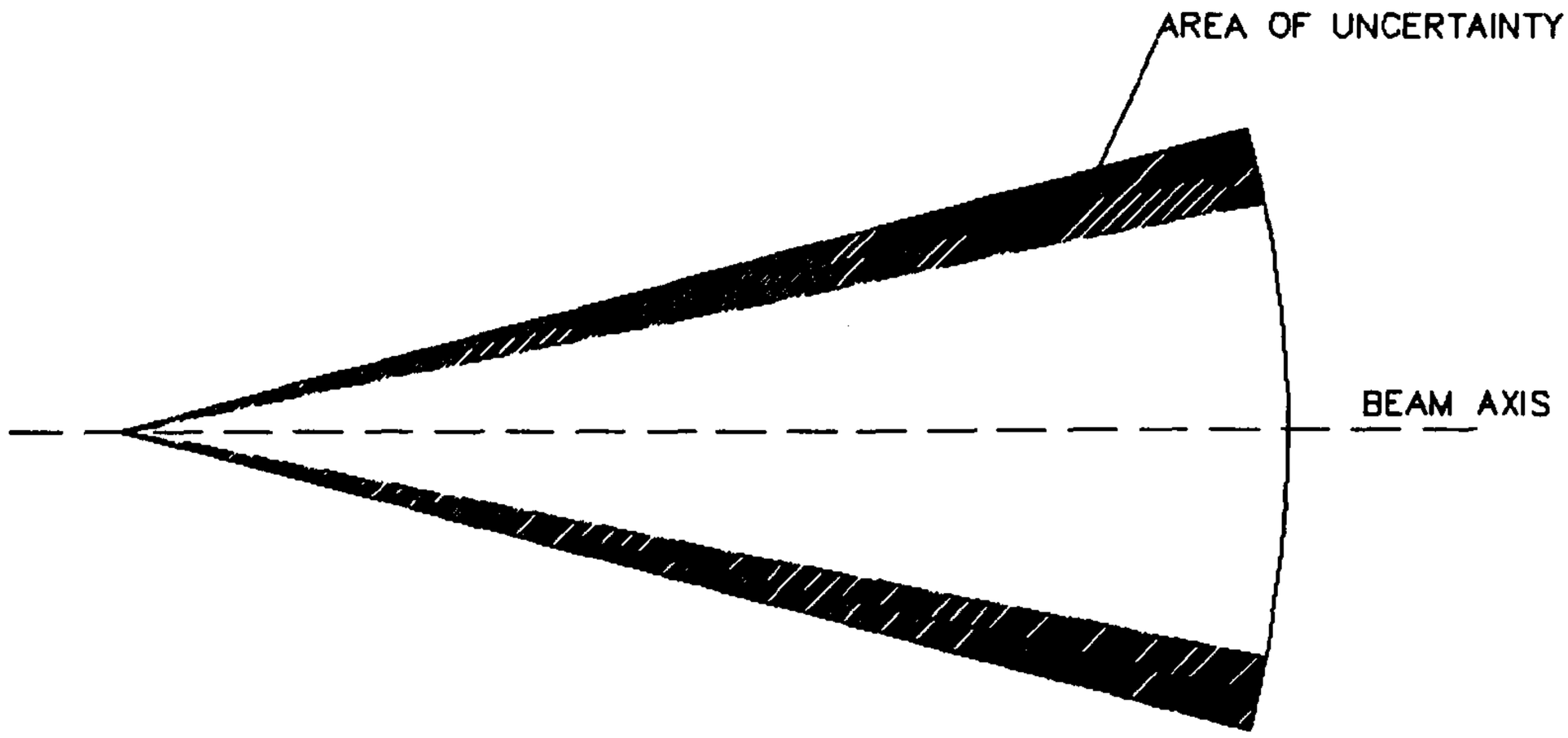

Figure 38: Diagram showing area of uncertainty within beam.

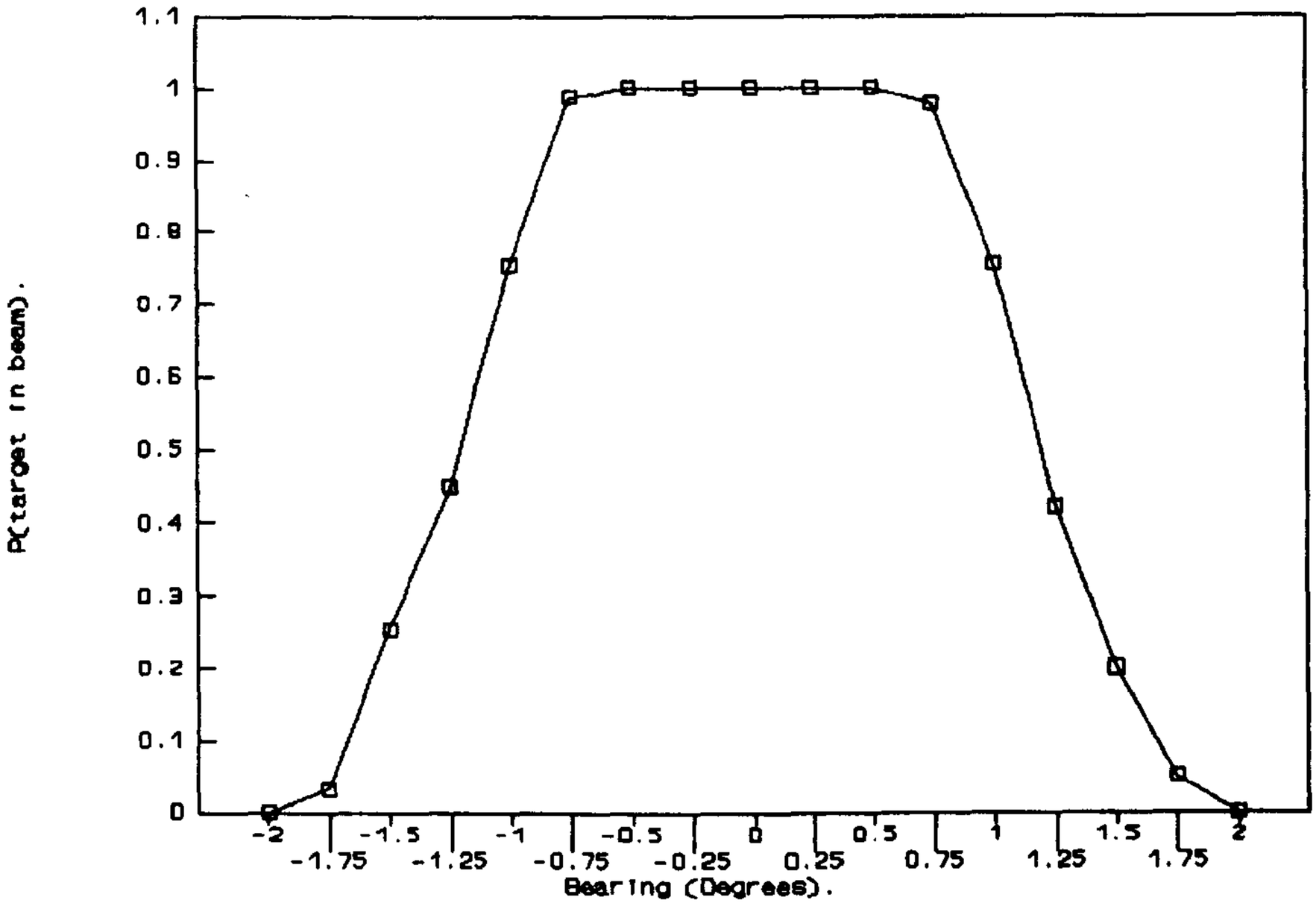

Figure 39: Plot showing probability of target falling 'in beam'.

9.7.1 Beam stability measurement

To quantify the width of the region of instability a series of measurements where taken at 0.25° increments across the axis of several beams. The results where then plotted as a series of graphs showing the probability of the target being

placed in the beam against bearing relative to the beam axis. A total of 8000 readings where taken and the results are shown in Figure 39.

9.7.2 Beam stability results

The results obtained for beam stability were as expected, with a 50% probability of being in the wrong beam at ±1.25° off the centre of the beam (the beam boundary). This was averaged out over many readings but it is apparent from the bearing accuracy measurements that errors do occur and so any real system would need to take a number of readings, and analyze them statistically, to guarantee accuracy.

9.8 Summary

It can be seen from sections 9.4 and 9.5 that the theoretical values for all the errors likely to be present are less than the resolution. This is only true in still air; in turbulent air the error due to random variations in the speed of sound is 0.16%. The effect of this can only be eliminated by using a number of temperature sensors or by shielding the workspace. If the expected resolution of the system is degraded then the error can of course be ignored.

9.9 References.

1. E. O. Doebelin, "Measurement Systems -Applications and Design", McGraw Hill, 1990.

2. Loughborough Sound Images Ltd, Private communication.

3. "The LeCroy Model 9400 Digital Oscilloscope Operators Manual", LeCroy, Switzerland, December 1986.

CHAPTER 10

IMAGING SYSTEM PERFORMANCE

10.1 Introduction.

Chapter 10 gives a detailed analysis of the operation of the system as an imaging system. The difference between this and the analysis presented in the previous chapter is that the system will be examined for its ability to locate multiple targets relative to each other, whereas in the previous chapter the emphasis was on the system's ability to locate a single target accurately. The chapter begins in section 10.2 with a discussion of the resolution of the imaging system. Section 10.3 gives a presentation of the results obtained in imaging experiments. Section 10.4 deals with the relative timings of the different beam forming systems whilst section 10.5 describes the ambiguities that may be present in an image and their causes. The chapter is summarised in section 10.6.

10.2 Resolution.

The resolution described in this section should not be confused with that encountered in measurement applications. Here the resolution of the system is the smallest distance between two objects that allows them to be resolved as separate objects rather than a single object. Whether or not the targets can be distinguished is determined by how well separated the signals from each target are

in the receiving array signals. The longitudinal resolution of the system is covered in section 10.2.1 and the angular resolution is covered in section 10.2.2.

10.2.1 Longitudinal resolution

If two targets are well separated in angle then the longitudinal resolution is the same as the range resolution for a single target. This was shown in chapter 5 to be determined by the transmitter pulse width and is ~1.7mm. If two or more targets are at the same bearing then the range resolution may be much greater than this due to shadowing effects.

10.2.2 Angular resolution

The resolving power of this system depends on the relative ranges of the targets; if they are well separated in range, the system can resolve them even if they have the same angular position. If however they have the same range, the path length difference between the received signals is due solely to the angular displacement. When this distance becomes sufficiently small the two received envelopes will overlap and the two targets will appear as one. This can occur at one or more elements on the array. The Rayleigh criterion is commonly used to determine whether or not two objects are resolved in an imaging system. This has already been derived in chapter 4 (equation 14) where it was shown that for two objects to be resolved the angular separation (θ_r) should be

$$\theta_r = \sin^{-1}\left(\frac{\lambda}{d}\right) \tag{1}$$

where

λ = wavelength.

d = array width.

From the same process used to derive equation 4.14; the angular resolution of an envelope beam former is

$$\theta_r = 2\sin^{-1}\left(\frac{n\tau_{3dB}C}{d}\right) \quad (2)$$

where

n_{3dB} = distance between the 3dB points of the received pulse in A/D samples.

τ = sampling interval.

C = speed of sound in air.

From equation 1, for an array with d equal to 120mm, θ_r is 1.64°. For the envelope beam former the width of the envelopes produced by the system is ~90μs; this corresponds to a 22kHz bandwidth which is approximately the system bandwidth. The measured envelope width at the 3dB points was ~50μs, this gives a calculated angular resolution (θ_r) of 16.5°. It should be noted that the values of θ_r obtained here are for the far field condition but these are good approximations for the near field.

Figure 1 shows the array signals for two targets at 300mm range and with a 70mm separation; this gives an angular separation of 13.5°. It can be seen that the two targets are not resolvable. The same data is also shown, after beam forming, as a beamplot in Figure 2. If the targets are now separated further to give a separation of 90mm (angular separation 17.5°) then the two targets can be

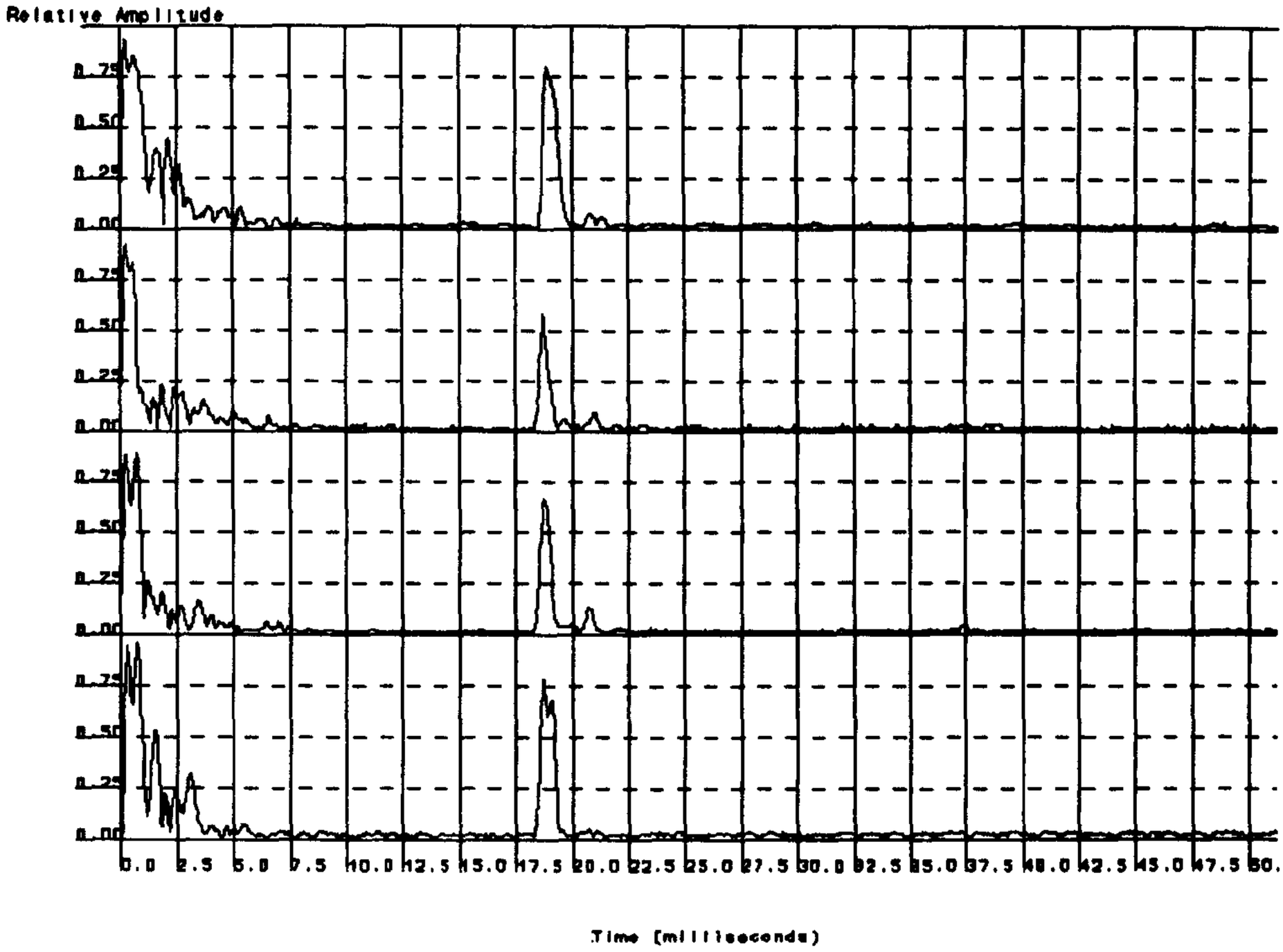

Figure 1: Array returns for two targets at equal range, 70mm separation.

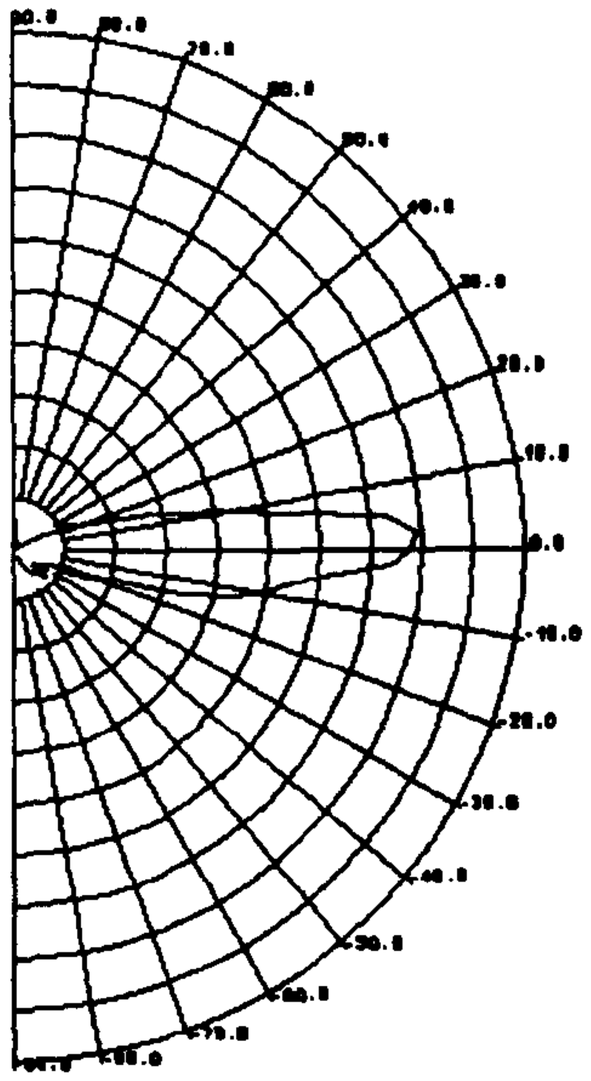

Figure 2: Beamplot for two targets.

Figure 3: Array output for two targets at equal range, 100mm separation.

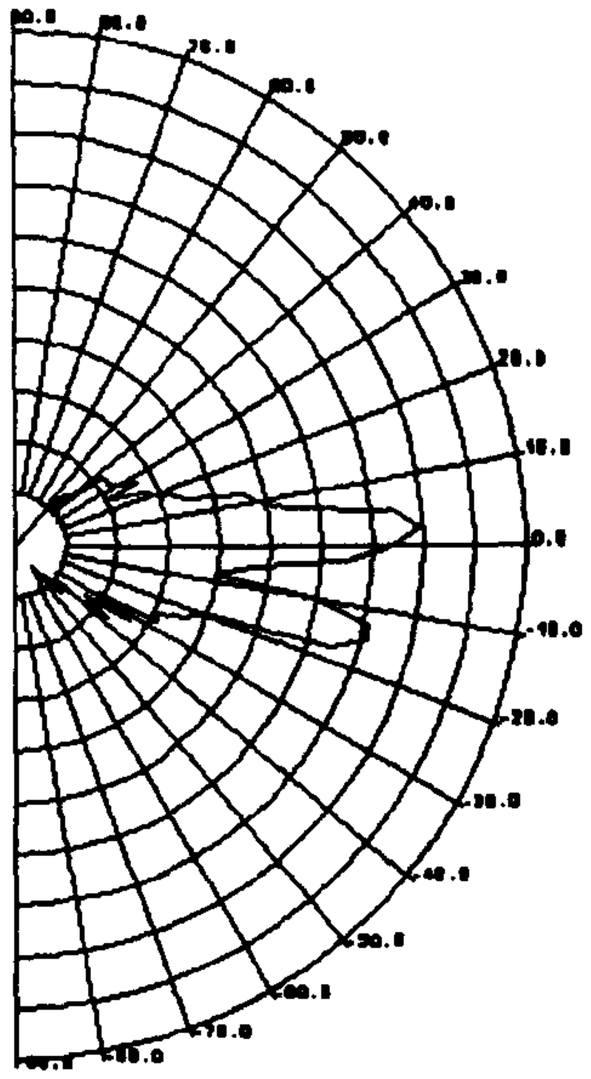

Figure 4: Beamplot for two equidistant targets.

clearly resolved. The resulting array returns are shown in Figure 3 the resulting beamplot for the beam formed data is shown in Figure 4. The resolution is slightly poorer than predicted but the amplitude of the received envelope may vary by ±10% between transmissions so the measured resolution is well within the expected range. It is important to remember that this is the minimum angular separation between targets at which they can both be resolved. This is different to the angular resolution discussed in chapter 4 section 4.2 which is the minimum angular increment through which the beam may be steered, this is 1.25° in theory.

10.3 Representation of the image.

The raw output of all the beam formers, can be presented in a number of different ways. The results are initially shown as a series of "grid plots", the x direction represents range, the y direction represents bearing and the z direction represents amplitude. The grids produced are 500 x 47 points which represents an angle of view of ±58.5° and a range of 850mm. The plots were generated by specially written software as there was no software readily available, for the IBM PC, which could handle the very large quantities of data produced. These plots are presented as an illustration of the function of the beam former. These outputs are normally subjected to further processing by the system to produce range and bearing information. This includes some form of thresholding to extract targets form the other signals, ie noise, present in the beam former output. The beam former output may also be represented as a grey scale amplitude plot. The outputs of each of the beam forming systems described in chapter 7 are presented in the

following sections.

10.3.1 4 Element array results.

The 4 element array used to obtain these results had an element spacing of 40mm or approximately 11λ. Results are presented for unfocused, focused and interpolation beam formers in sections 10.3.1.1, 10.3.1.2 and 10.3.1.3 respectively.

10.3.1.1 Unfocused digital beam former.

Figure 5 shows the output of an unfocused digital beam former for a single target placed central to the array. The peak output of the beam former represents the position of the target. Without focusing the position indicated by the beam former is very inaccurate for targets in the near field.

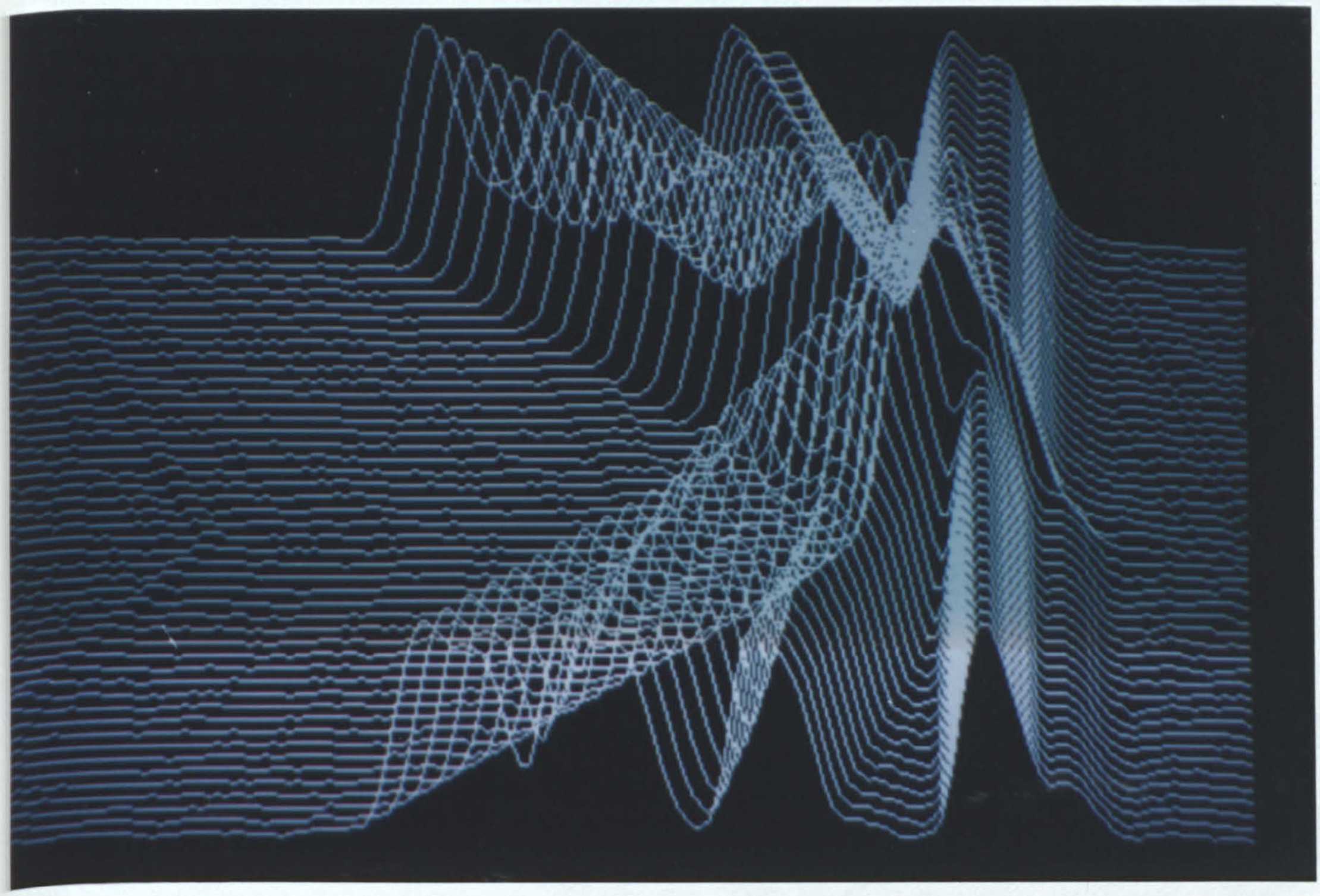

Figure 5: Grid plot for single target at range 350mm and bearing 0° (Unfocused).

10.3.1.2 Focused digital beam former.

With the array used in this section the near field region extends to 4.2m (see chapter 3) an so due to the maximum system range being 1.5m all targets are in the near field. This means that focused beam forming must be used (see chapter 4). Figure 6 shows the same target as shown in Figure 5 but with focused beam forming. Figure 7 shows the output of the beam former for a 30mm cube. The corners of the cube are shown highlighted. The two plots are also shown as grey scale images in Figure 8 and Figure 9.

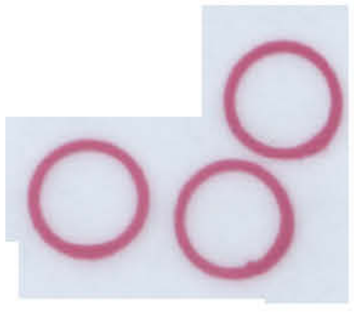

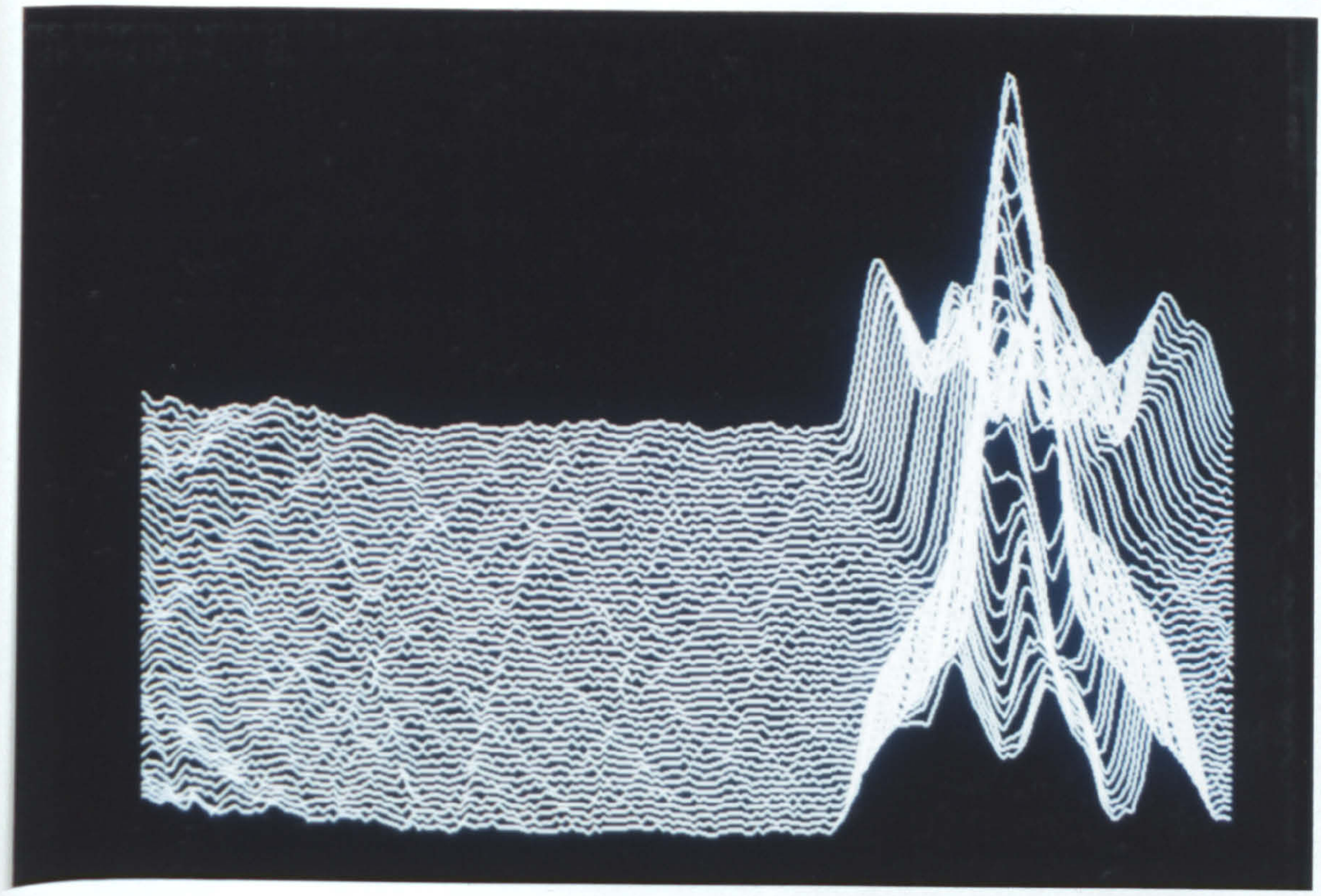

Figure 6: Grid plot for single target at range 350mm and bearing 0° (Focused).

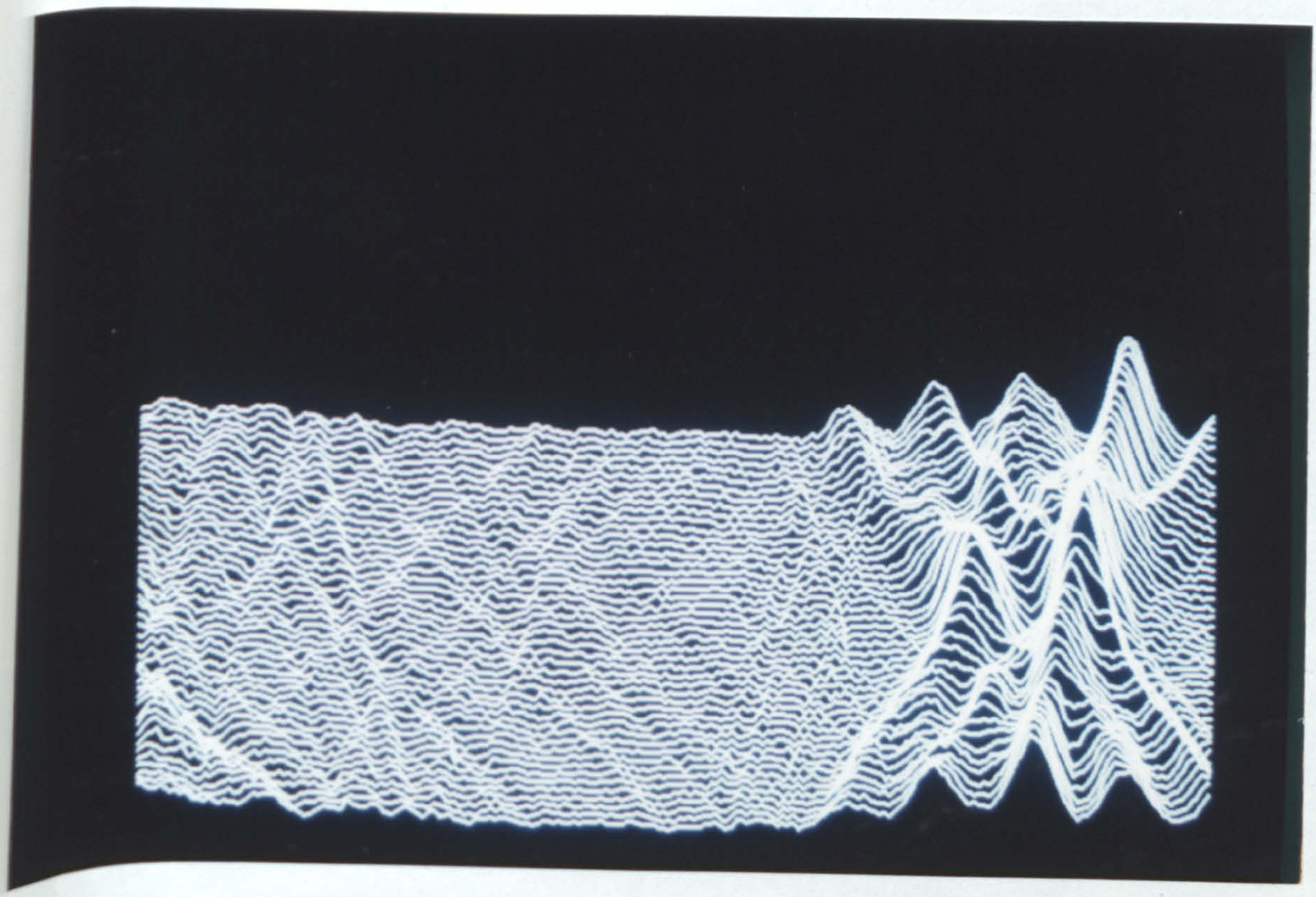

Figure 7: Grid plot for 30mm cube at range 350mm and bearing 0° (Focused).

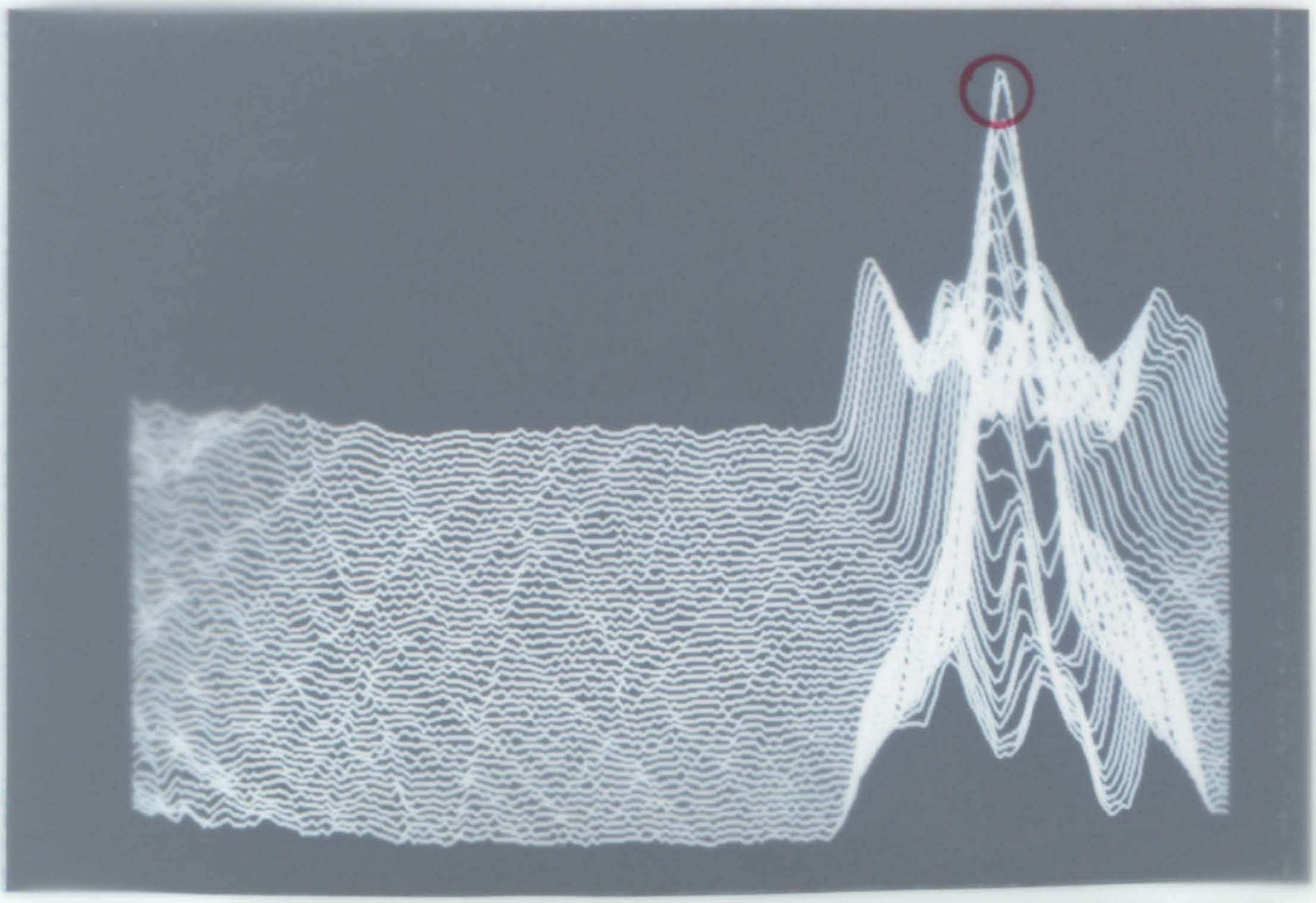

Figure 6: Grid plot for single target at range 350mm and bearing 0° (Focused).

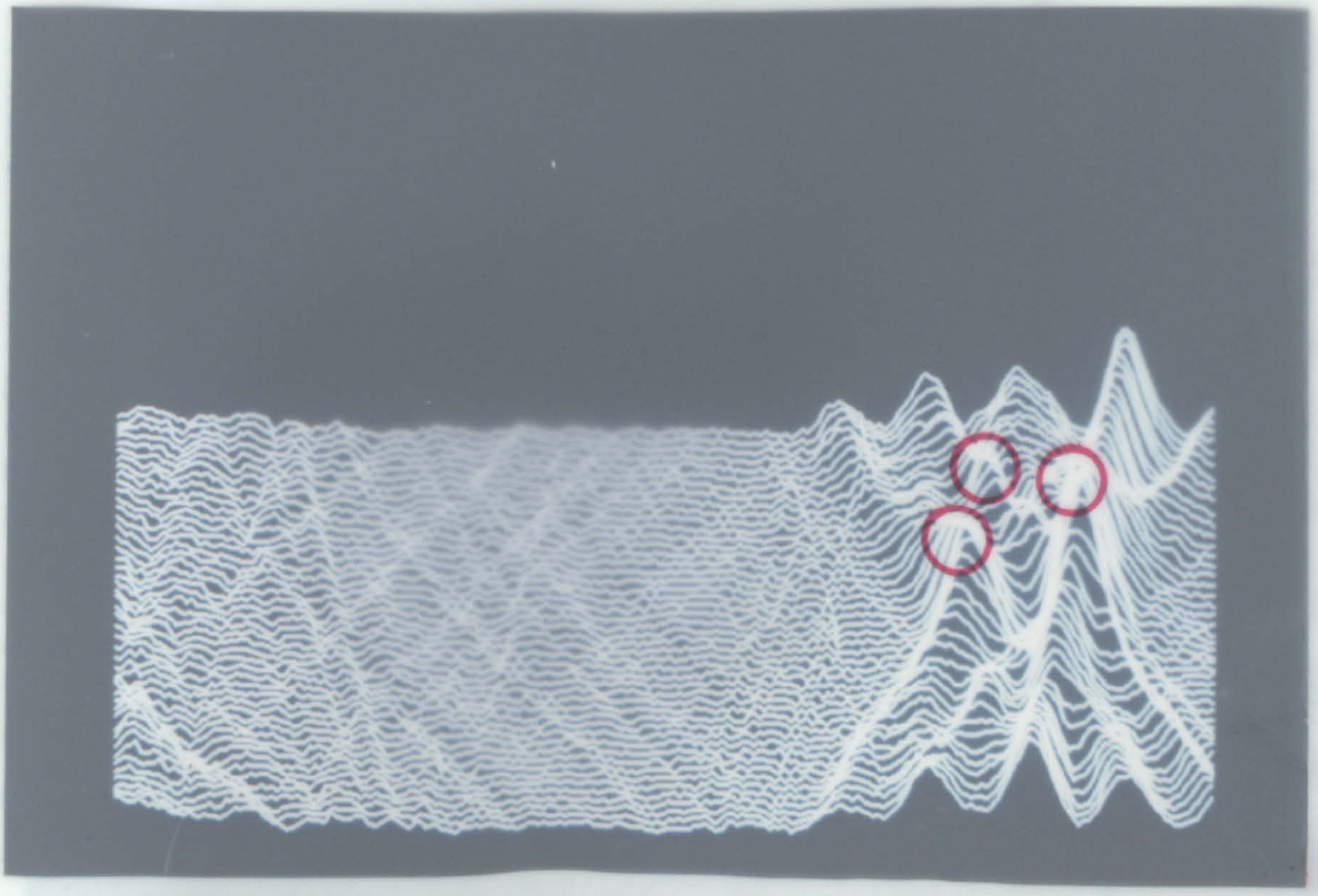

Figure 7: Grid plot for 30mm cube at range 350mm and bearing 0° (Focused).

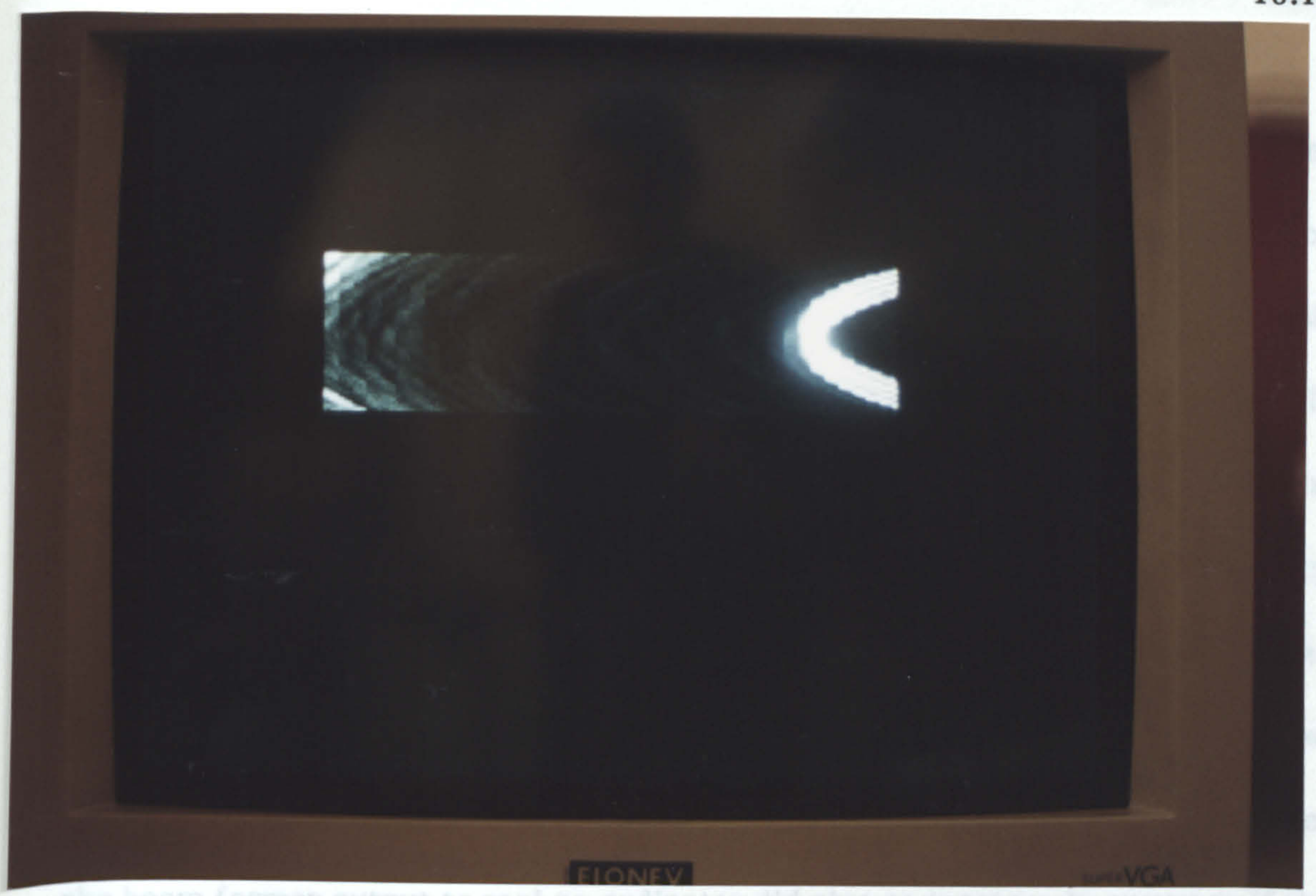

Figure 8: Grey scale image for a single target at range 350mm and bearing 0° (Focused).

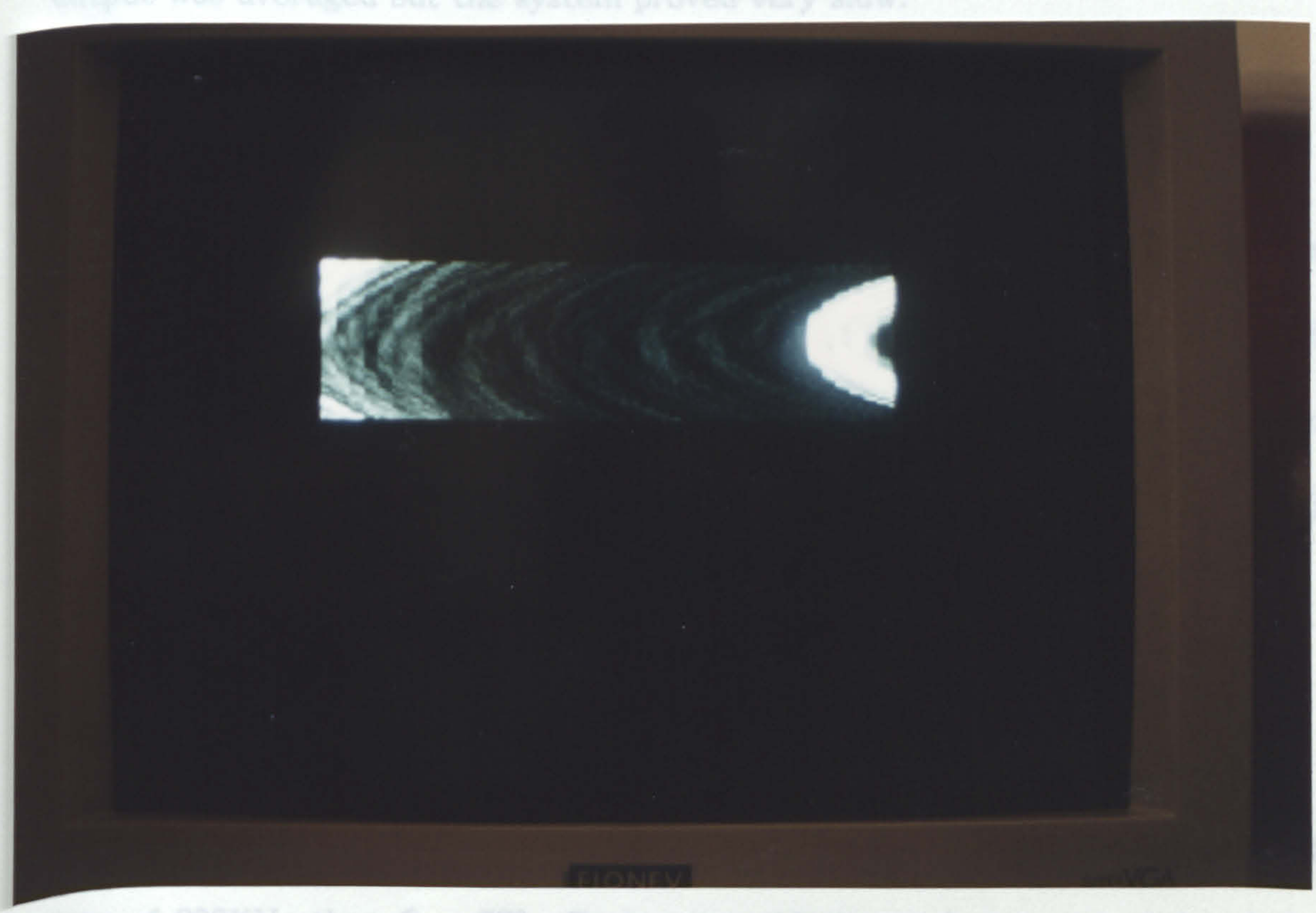

Figure 9: Grey scale image for a 30mm cube at range 350mm and bearing 0° (Focused).

10.3.1.3 Interpolated beam forming.

This section describes the results obtained with the interpolation beam former described in chapter 7. The system has been set to split the beams produced by the standard envelope beam former in the area where a target is detected. This is can be done either manually or automatically. The output is shown in Figure 10. The window in the top right hand corner of the display shows the output of the interpolation beam former. This system increased the maximum possible accuracy of the system to 0.75°. The resulting output proved to be very susceptible to jitter. The jitter was primarily caused by noise, firstly the peaks of the envelopes appear relatively flat at the higher sampling rates (see chapter 8). Conversion of the beam former output to real co-ordinates did give an increase in accuracy if the output was averaged but the system proved very slow.

10.3.2 16 element $\lambda/2$ array.

This section presents the results obtained with a 16 element $\lambda/2$ array. From Rayleigh's criterion the theoretical maximum angular resolution, θ_r, of a 16 element array with a $\lambda/2$ element separation operating at 100KHz is 80° for an envelope beam former. From chapter 4 the minimum angle between beams (θ_b) for a digital beam former is given by

$$\theta_b = \tan^{-1}\left(\frac{(n-1)\tau C}{d}\right) \qquad (3)$$

If the beam former were to be used with the envelopes sampled at the existing rate of 200KHz then θ_b = 25°. To improve this interpolation was used and the sampling rate increased to 1MHz giving θ_b = 5.3°. A photograph of the output of

this beam former is shown in Figure 11, the system was not developed further due to the high computational effort imposed by the interpolation algorithm and the poor resolution obtained in comparison with the less computationally intensive method described in section 10.3.1.2..

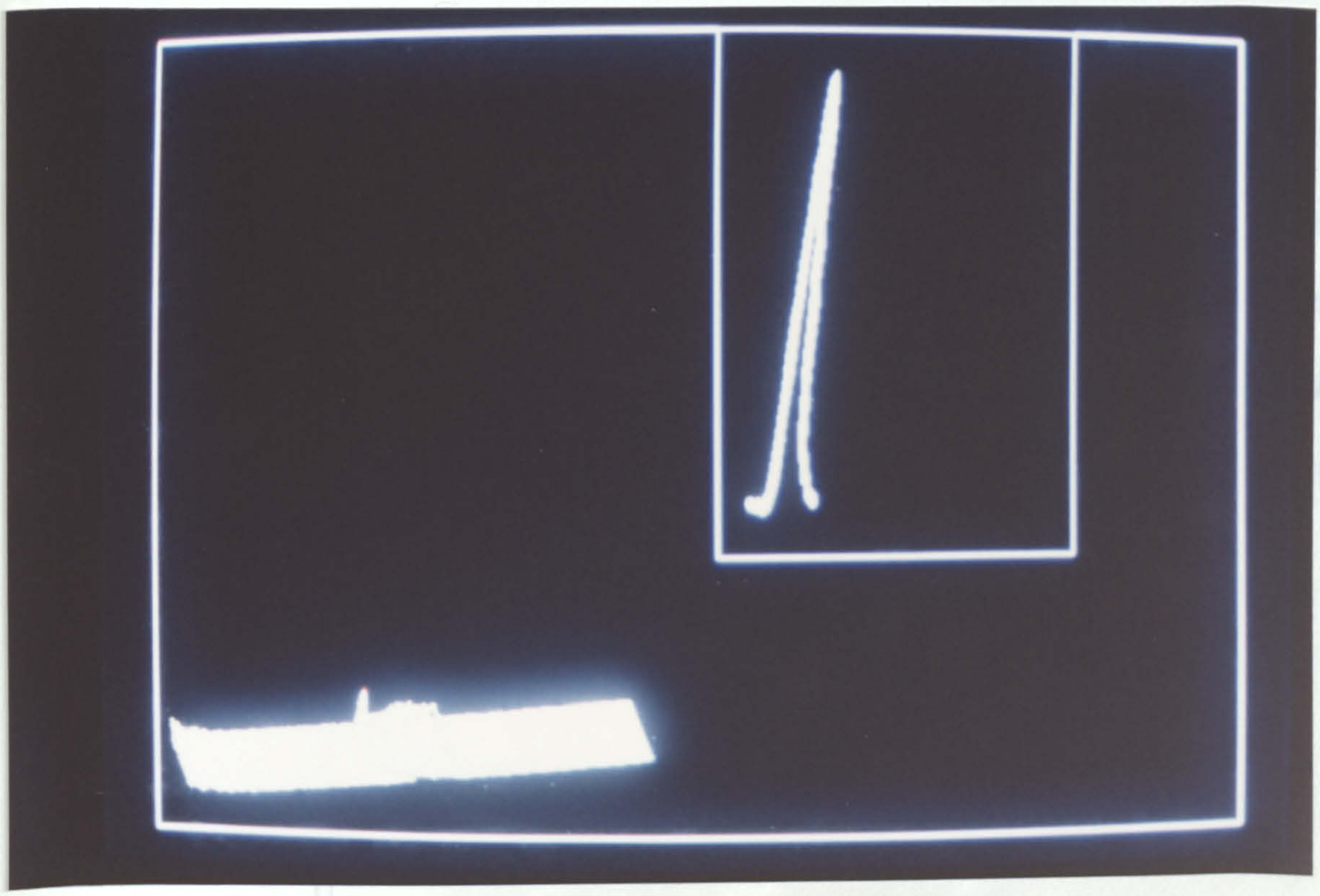

Figure 10: Output of interpolated beam former.

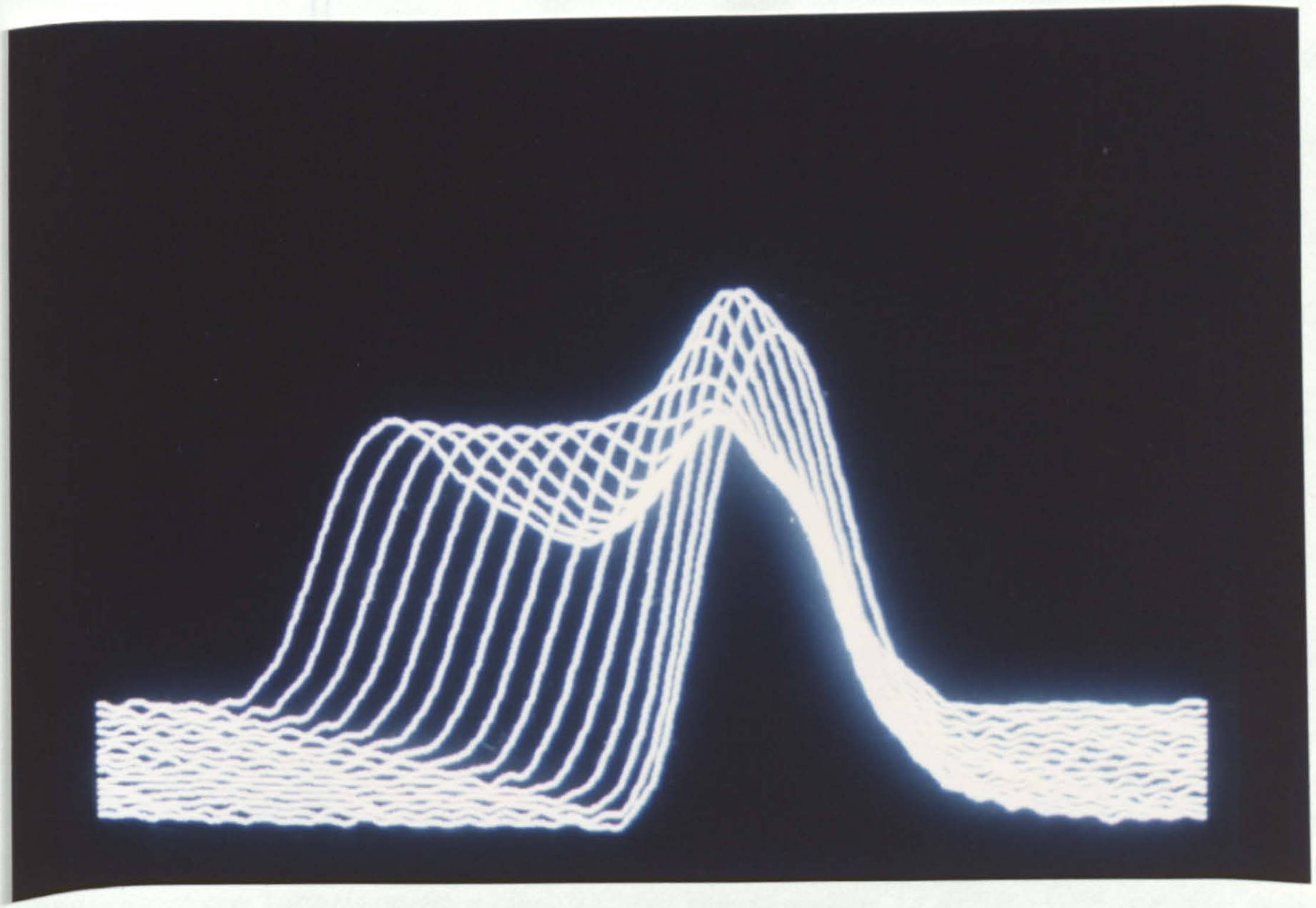

Figure 11: Output of 16 element $\lambda/2$ beam former.

10.3.3 Direct method.

The direct method relies on the ability of the system software to deduce the presence of possible targets form the array signals. It is therefore the effectiveness of the target extraction process that governs the effectiveness of an imaging system. The initial software used to produce images by this methods was relatively crude and only allowed very simple target arrangements to be imaged.

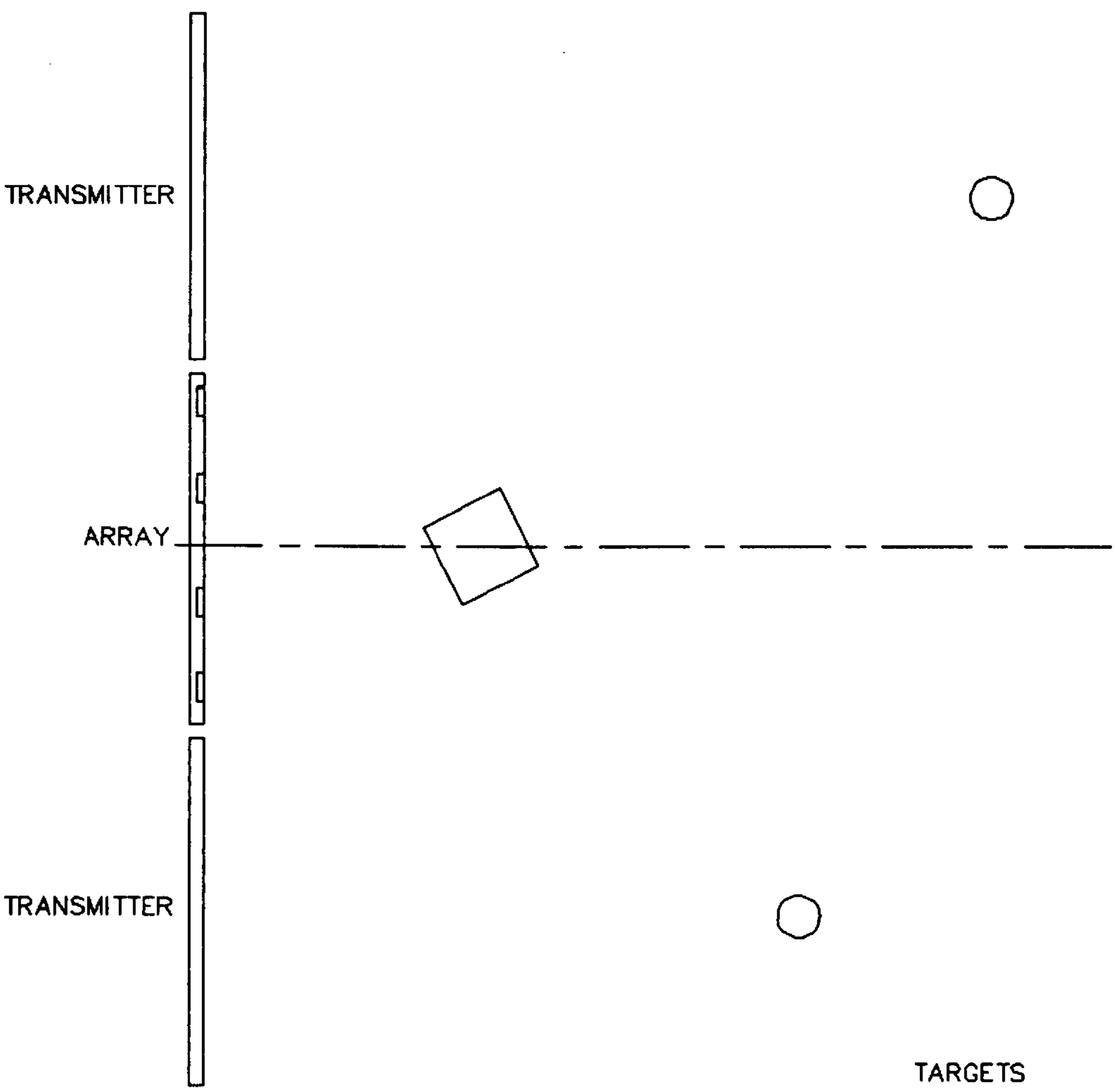

Figure 12: Target layout used to test the direct method.

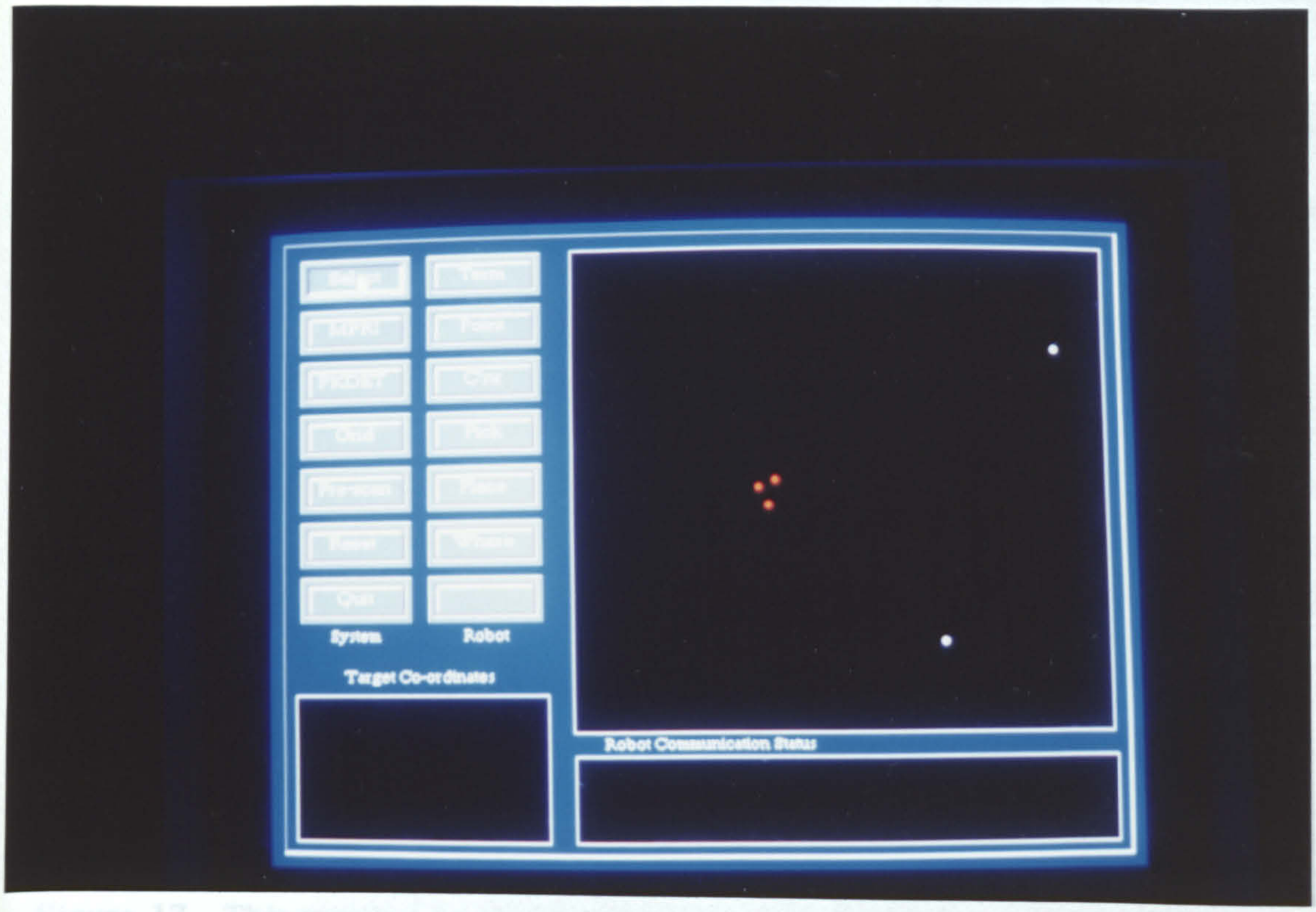

Figure 13: Photograph showing output of direct method.

The output of the system with the target layout shown in Figure 12 is presented as a photograph in Figure 13. The three corners of the cube and the two cylinders can be clearly seen on the display. The display is generated by detecting the targets developed by the direct method, thresholding them, and then marking their relative positions on the display.

10.3.4 Dual Method.

This is a combination of a focused digital beam former and the direct method. The data is first of all pre-scanned using a focused digital beam former to locate the presence of all targets. The array data is then reprocessed, using the approximate locations provided by the pre-scanner, to locate the targets more accurately using the direct, method called in this case the precision beam forming stage. This dual system gives both the robustness of the traditional beam former

and the accuracy of the direct method and overcomes many of the problems associated with the direct method when a complex environment is being scanned (see chapter 7). The penalty is slightly increased processing time but this can be overcome by degrading the accuracy of the digital beam former since the accuracy is provided by the direct method. The results of using this system are shown in Figure 14 to Figure 17. It can be seen in Figure 16 that most of the targets present have not been detected and several are shown in the wrong place. In Figure 17 all the targets can be seen clearly. The output of the digital beam former is shown in Figure 15, although all the targets can be seen it should be noted that the positional information is only accurate to 2.5° compared to 0.8° in Figure 17. This method is applied practically in chapter 11.

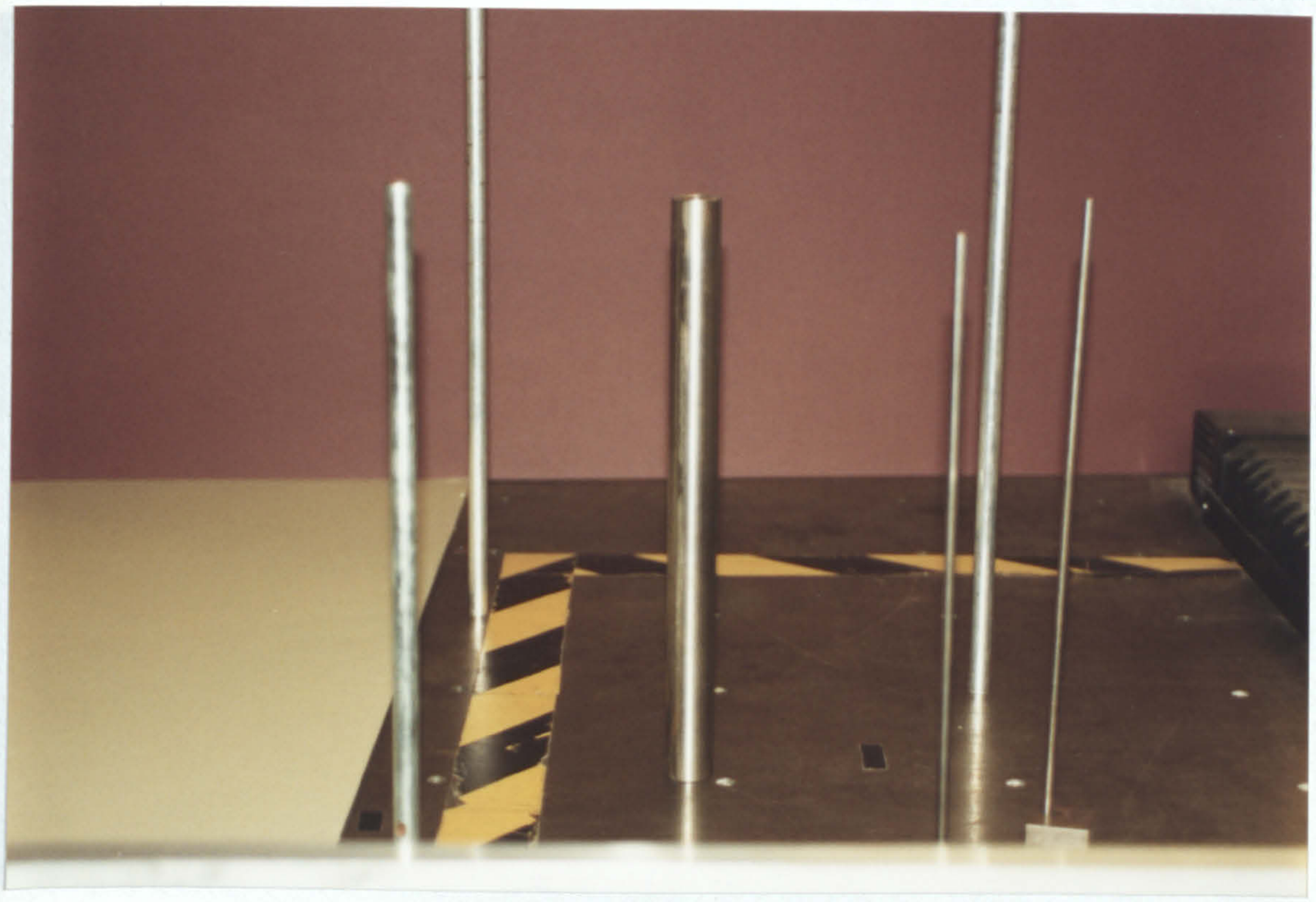

Figure 14: Photograph showing target arrangement used to test the dual method.

Figure 15: Output of digital beam former (pre-scanner) for scene shown in Figure 14.

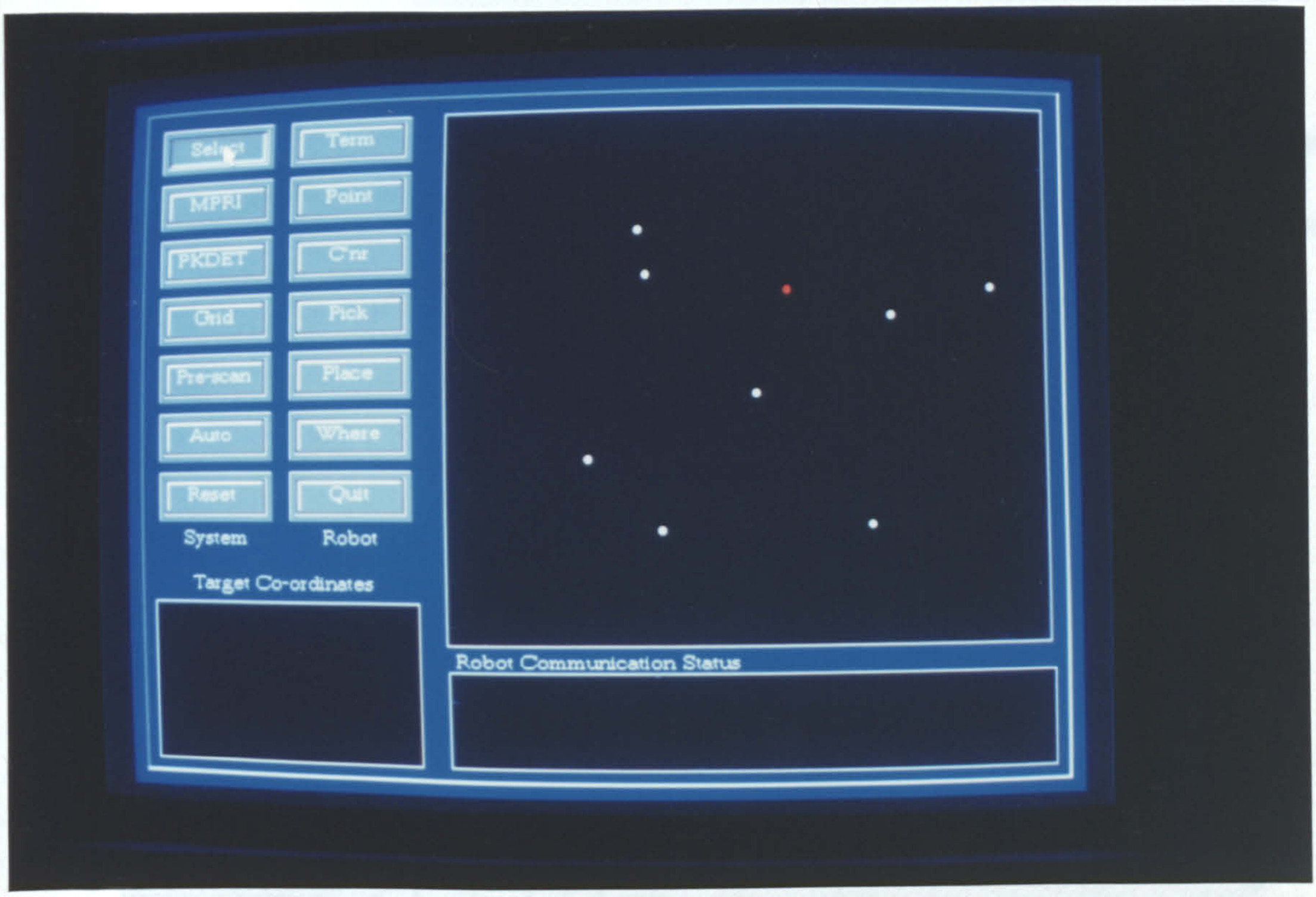

Figure 16: Output of direct method for scene shown in Figure 14.

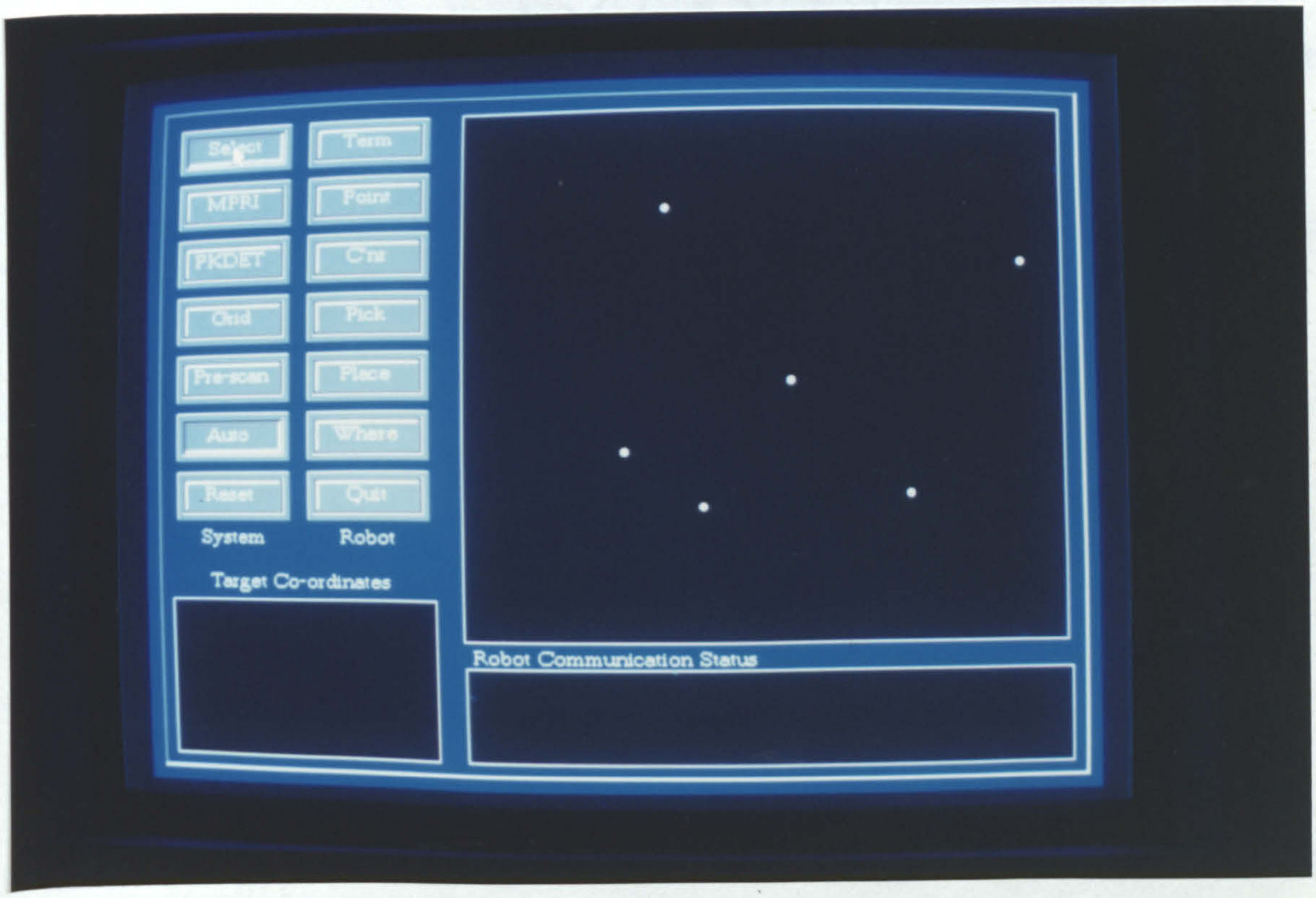

Figure 17: Output of Dual method for the target layout shown in Figure 14.

10.4 Timing.

This section gives the relative timings of the different beam forming software used with the ultrasonic location system. The timing for the digital beam formers used to generate the results presented in section 10.3 are shown in Table I.

Table I: Digital beam former timings.

Beam forming method.	time (ms)
4 Element with pre-calculated offsets	47.4
4 Element without pre-calculated offsets	3400
4 Element Interpolated Beam former	4500
16 Element interpolated beam former	5000
Dual method (dependant on number of targets)	3800

The significance of using precalculated offsets has already been discussed in chapter 7.

The timings for the direct method used to generate the results presented in section 10.3.3 are shown in Table II.

Table II: Direct method timings.

Beam forming method.	time (ms)
Direct method (without MPRF)	8.7
Direct method (with MPRF)	26.2

The significance of using a multiple PRF (MPRF) system already been discussed in chapter 8.

10.5 Ambiguities.

Ambiguities or false targets may be generated, by the beam forming process, when there are N array elements and ≥ N-1 targets present in the array field of view[1]. To illustrate this, consider two targets placed at equal range and equi-distant from the centre of the array - see Figure 18.

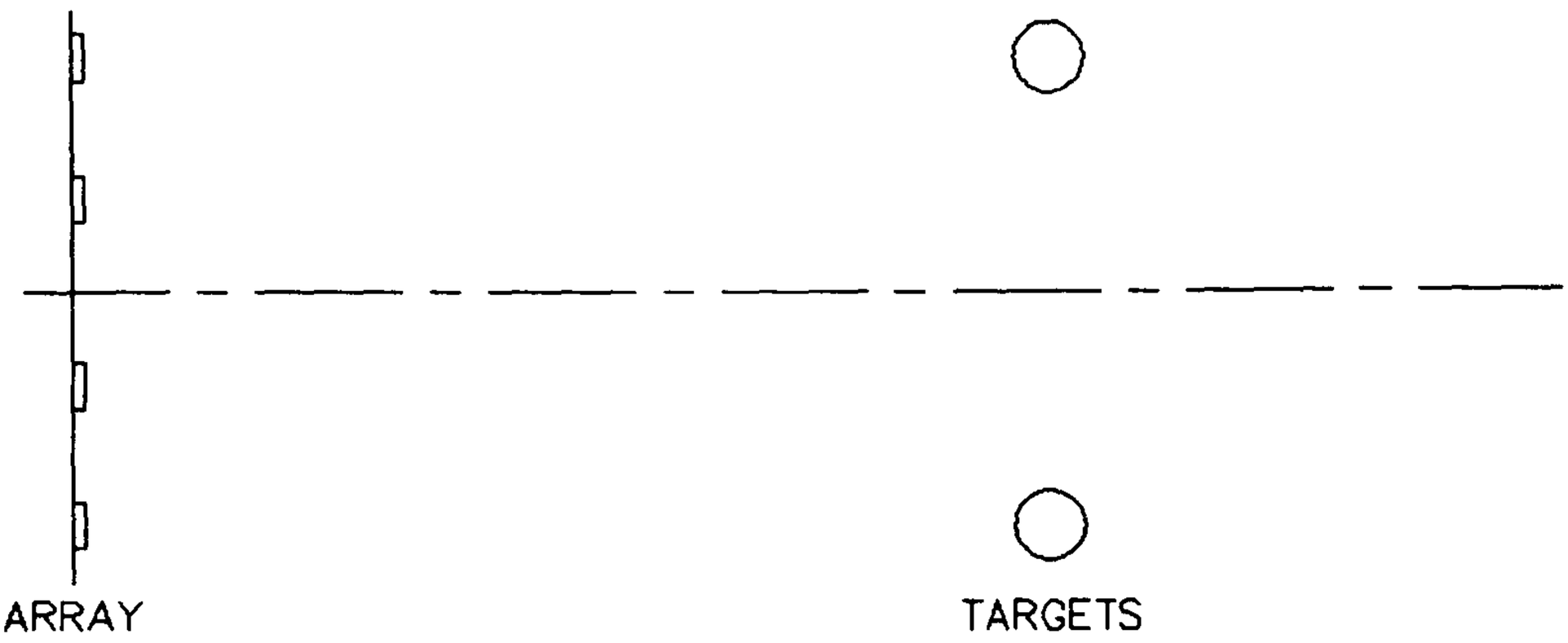

Figure 18: Targets likely to cause ambiguities with a two element array.

The output obtained from the two inner elements of the array are shown in Figure 19.

Since the array returns cannot be distinguished from the returns obtained with the layout shown in Figure 20 an ambiguity would be produced if a beam former where applied to the received data. A simple time domain beam former would indicate that there were 4 targets present. If a third element is used, the ambiguity will no longer occur and the two targets can be resolved correctly. Two false targets will still be generated in the same position as those shown in Figure 20 but the amplitude will be lower than the real targets. The reduction in amplitude is due to the false targets only being formed from the summation of two channels whilst the real targets are the result of the summation of three channels. Target returns

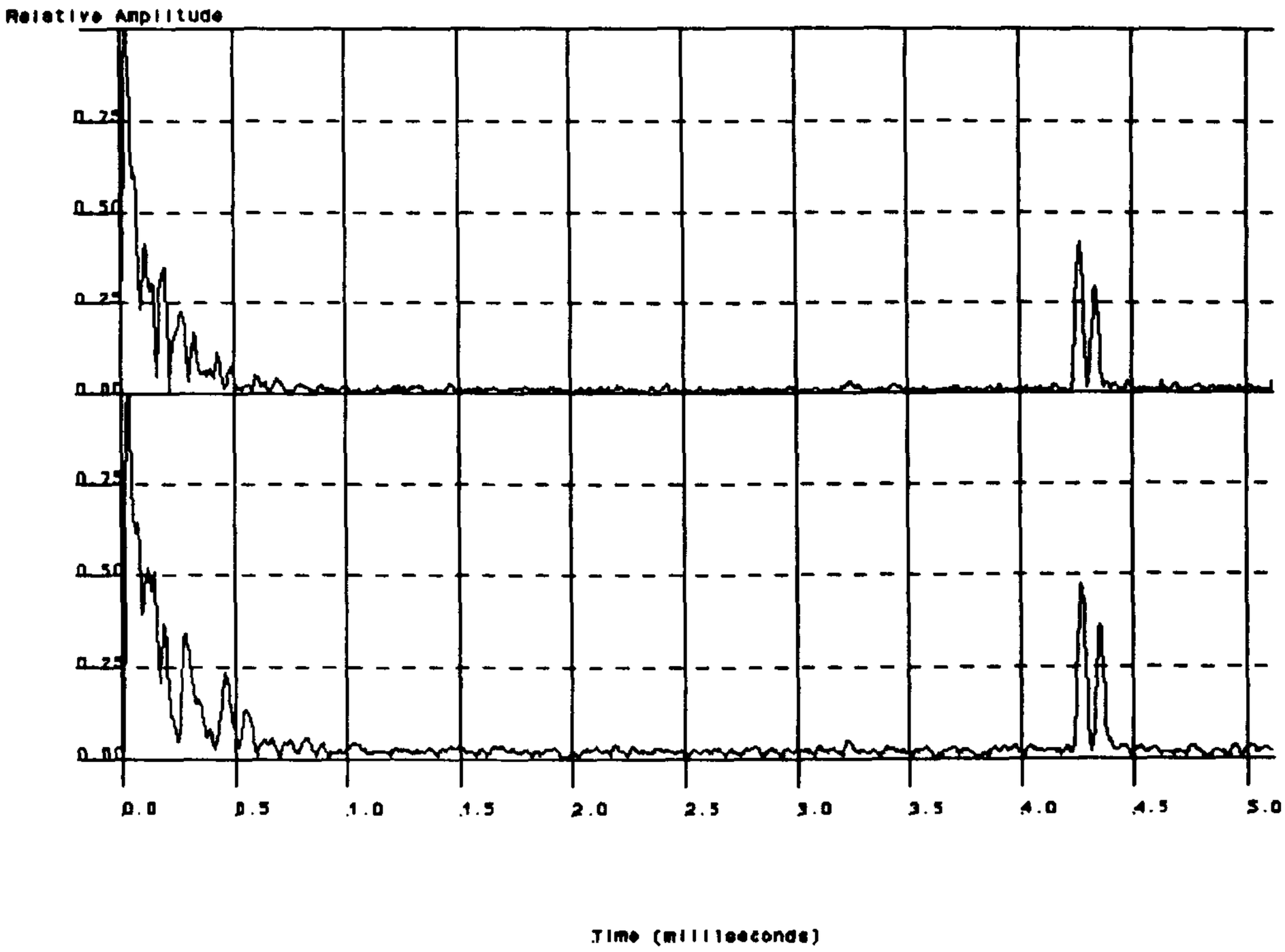

Figure 19: Output of two element array for ambiguous target.

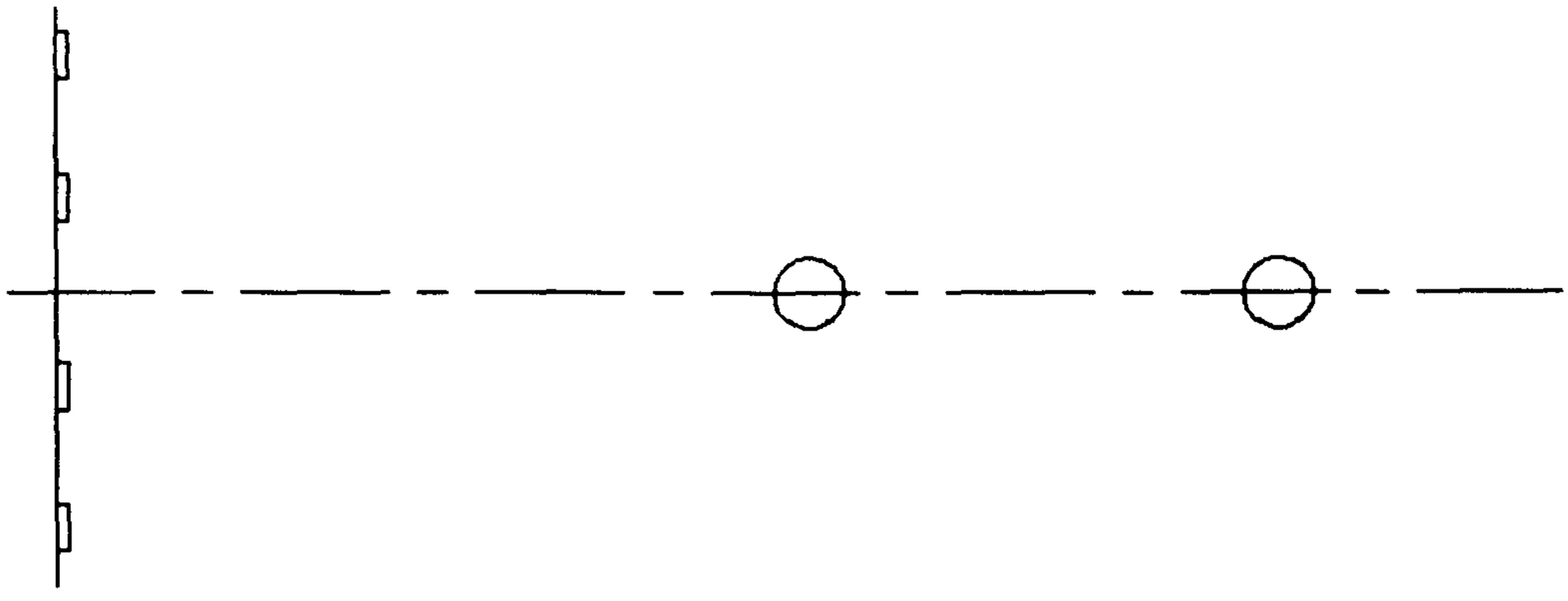

Figure 20: Alternative target layout to produce returns shown in Figure 19.

for the two target layouts shown in Figure 18 and Figure 20 are shown in Figure 21 and Figure 22 respectively.

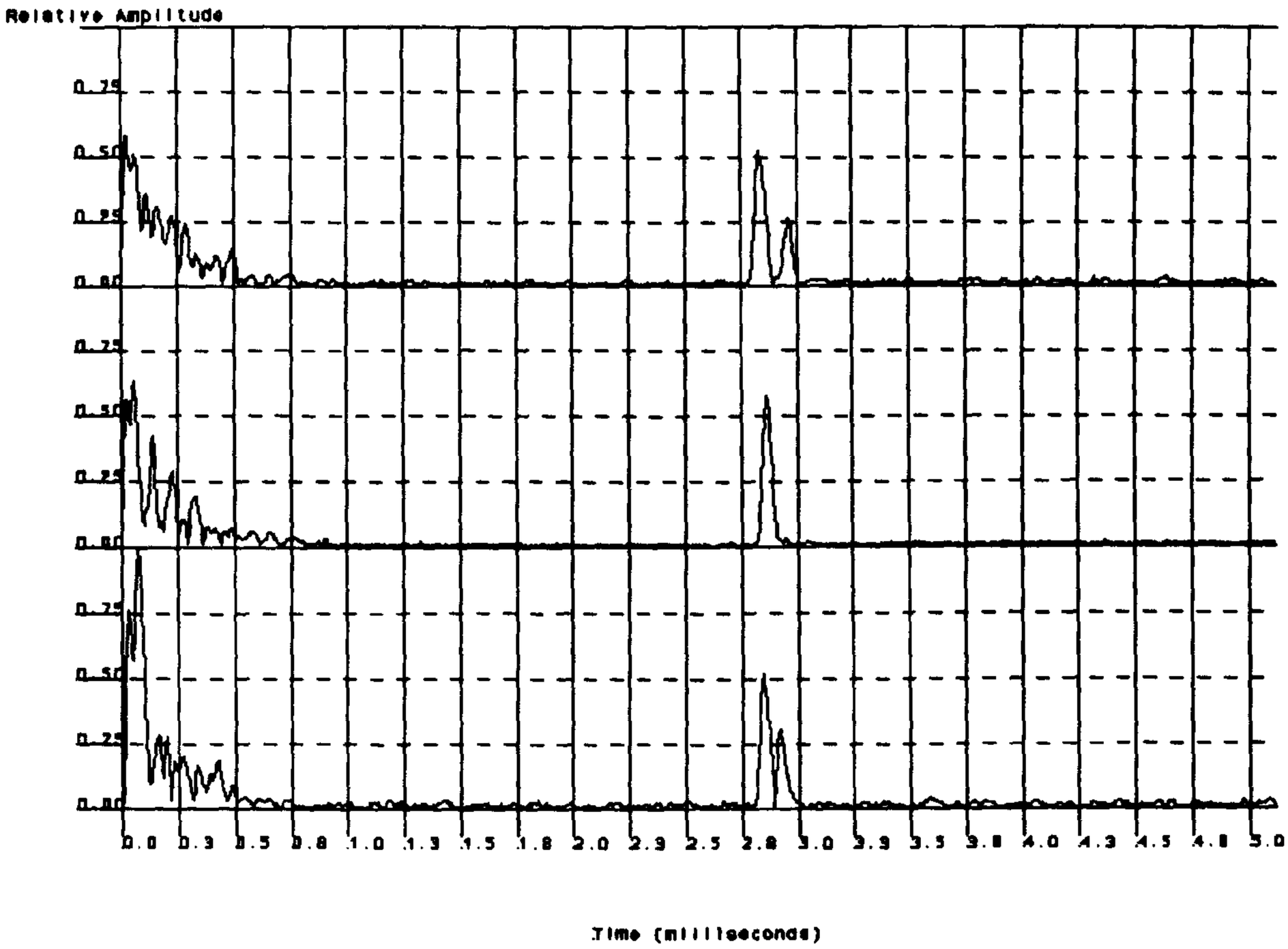

Figure 21: Returns for target layout shown in Figure 18.

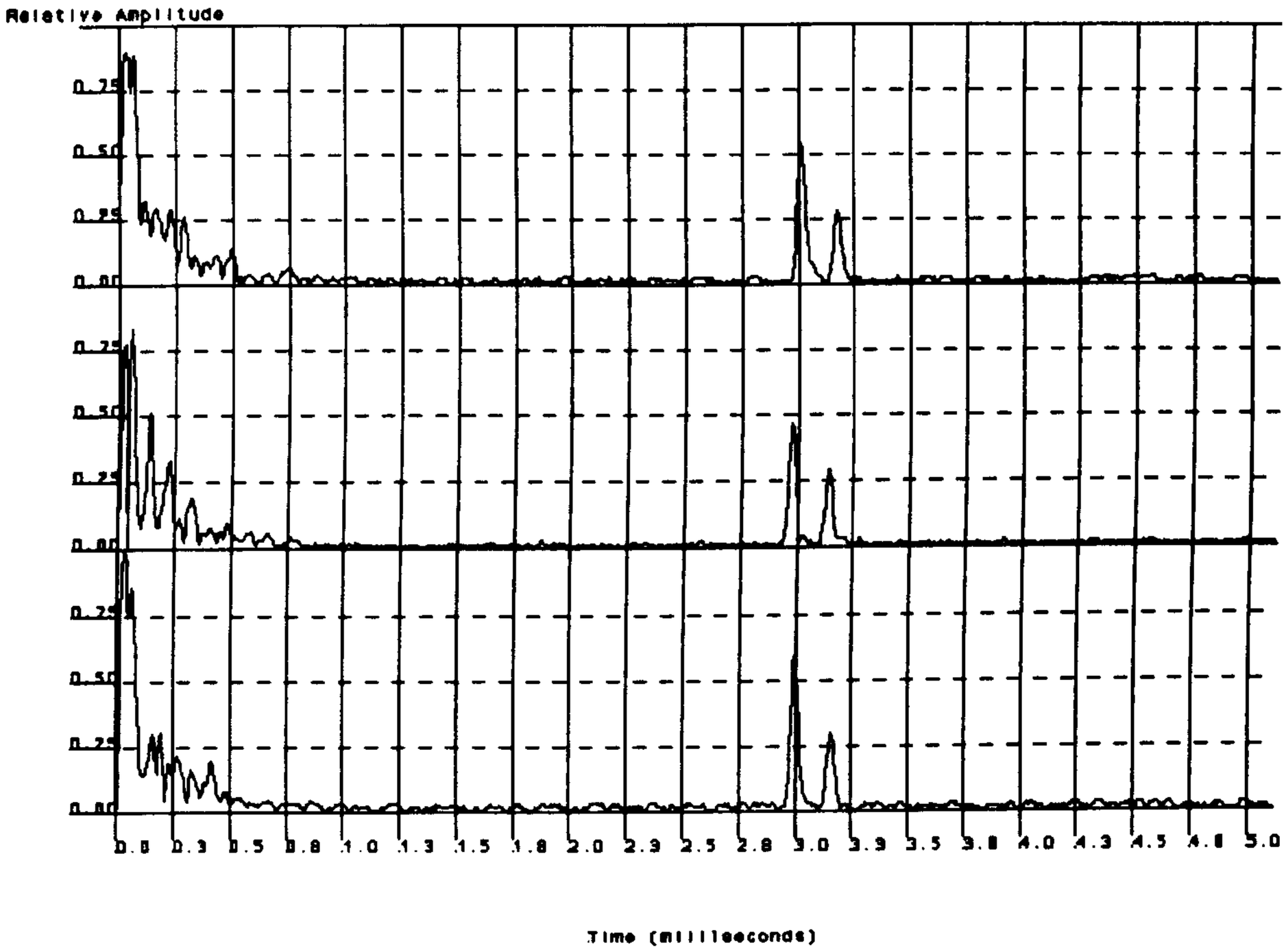

Figure 22: Array returns for three element array with targets shown in Figure 20.

10.6 Summary.

Overall the use of the system for imaging was limited by the lack of elements in the array. Good results where obtained with very simple objects such as cubes but the presence of ambiguities and limited angular resolution prevented the imaging of more complex objects. It is worth noting that medical ultrasound imagers use arrays with a minimum of 64 elements[2]. The system could be improved by increasing the number of elements but for high quality imaging a higher frequency is needed. The use of a higher frequency limits the effective range of the system. From the results presented in this and the previous chapter it is apparent that an ultrasonic system is ideal for the extraction of feature positions from a scene but is not suitable for detailed imaging. This is best accomplished by a vision system.

The development of a hybrid ultrasonic/vision system is discussed in chapter 12.

10.7 References.

1. I. Ziskind and M. Wax, "Maximum Likelihood Localization of Multiple Sources by Alternating Projection", IEEE Transactions on acoustics speech and signal processing, Vol. 36, No. 10, October 1988, pp1553-1560.

2. M. O'Donnell, "Efficient Parallel Receive Beam Forming for Phased Array Imaging using Phase Rotation", Proceedings IEEE Ultrasonics symposium, 1990, pp1495-1498.

CHAPTER 11

APPLICATION OF AN ULTRASONIC LOCATION SYSTEM TO A REAL-TIME ROBOT GUIDANCE TASK

11.1 Introduction

Chapter 11 covers the application of the ultrasonic location system to the guidance of a fixed robot performing a pick and place operation. The application is described in detail in section 11.2. Section 11.3 provides a description of the hardware used in the application. Section 11.4 describes a simple application capable of locating and retrieving a single target within the workspace. In section 11.5 a more complex system is described which embodies all the processing systems developed in this research work and is capable of operating in a multi target environment. The results obtained are described in section 11.6 and the chapter is summarised in section 11.7.

11.2 Application outline

This section discusses the application of the system to the control of a robot and a possible implementation of such a system. The purpose of the application is to simulate a hypothetical process in which a robot must be able to locate different objects within its workspace. The objets to be identified are to be confined to square and cylindrical types and the system needs to be able to locate the objects

with sufficient accuracy for the robot to pick them up. To pick up rectangular objects the system must be capable of calculating their orientation. It is also envisaged that there may be obstacles within the robot workspace the positions of which must also be mapped. The system must therefore be able to identify and locate multiple targets, within the constraints described in chapter 10. The robot chosen was a Unimation Puma 560 running under VAL 1. This robot was chosen as it was readily available to the author and is relatively easy to program. However, compared with more modern robots it is technically unsophisticated. There is no option available for remote control to allow the robot to be integrated into a more sophisticated system. The only means of establishing direct control of the Puma is to use the terminal interface[1]. All controlling systems must therefore appear to the robot as a VT52 or VT30 terminal and all the normal communication protocols must be observed. Whilst this may appear rather a cumbersome approach it proved more than adequate for the experiments performed here.

To simplify development, a system capable of dealing with single isolated objects only was developed first. To support the multiple object system, a number of advanced features were added to the single target system, these have been described in chapter 10. The final system was designed to be capable of the following operations:

1: Locate and map all the visible targets in a robot workspace.

2: Identify real targets and reject false targets within a noisy and cluttered environment.

3: Extract the size and orientation of simple objects.

4: Provide target data to a Puma robot to allow it to perform a pick and place operation in a cluttered environment.

11.3 Hardware

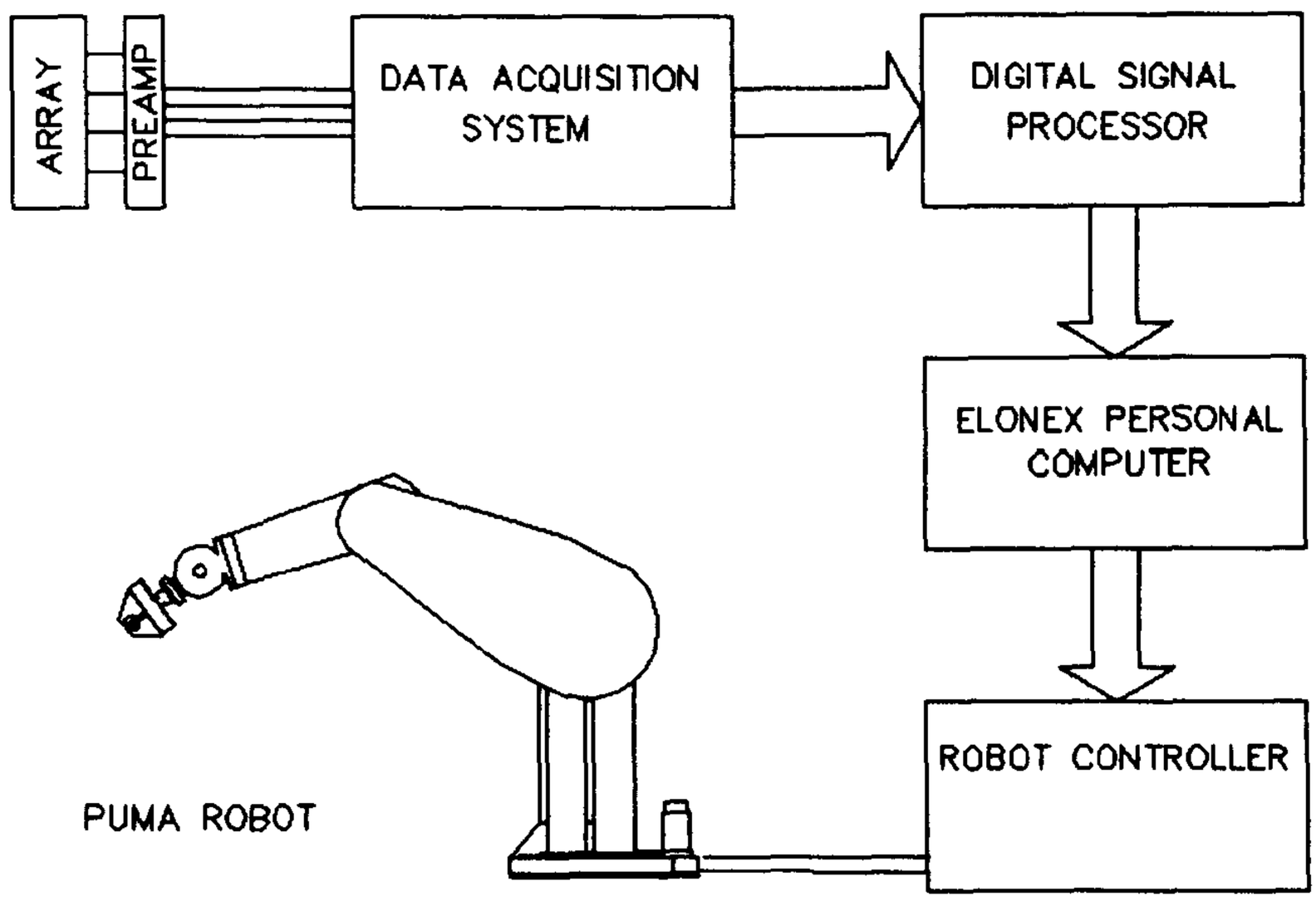

Figure 1: Block diagram of system used for robot control.

A block diagram of the system is shown in Figure 1. The hardware of the data acquisition system is identical to that described in chapter 6. The communications between the robot and the system PC are provided using an RS232 serial link between the PUMA terminal input and one of the PC serial ports. The serial port is interfaced to both the applications described in this chapter by a 'Virtual Terminal' interface which makes the ultrasonic system software appear as if it was a VT52 terminal. The 'Virtual Terminal' software provides a full bi-directional interface between the PC and the robot controller including error checking, timed out communications, error trapping and a translation table for special characters.

The resulting module allowed the interface to be invisible to the rest of the software, transferring or receiving strings from the robot controller. The software was designed to operate in two modes 'terminal mode' and 'control mode'. In terminal mode the PC can be used as a standard terminal to allow calibration and general housekeeping to be carried out. In control mode lines of VAL 1 program can be passed to the controller for execution or the controller can be interrogated to provide information on the current status of the robot.

The experimental setup used in both systems described in this chapter is shown in Figure 2.

11.4 Single target system

The object location software is based around that already described in chapter 9. It uses digital beam forming with focusing and aperture correction. Temperature compensation is provided by manual entry of the ambient temperature at system startup. The coefficient file corresponding to that temperature must be the file specified for down load to the DSP if pre-calculated offsets are to be used (see chapter 7).

The system is controlled by a simple keyboard driven interface where the operator presses a key when he wishes the robot to pick up an object. In principle the system could work automatically, picking up a target as soon as it enters the workspace, but this was not tried as the robot guards would have had to be removed with the resulting health and safety problems.

The PC program is capable of running simple VAL 1 programs by passing

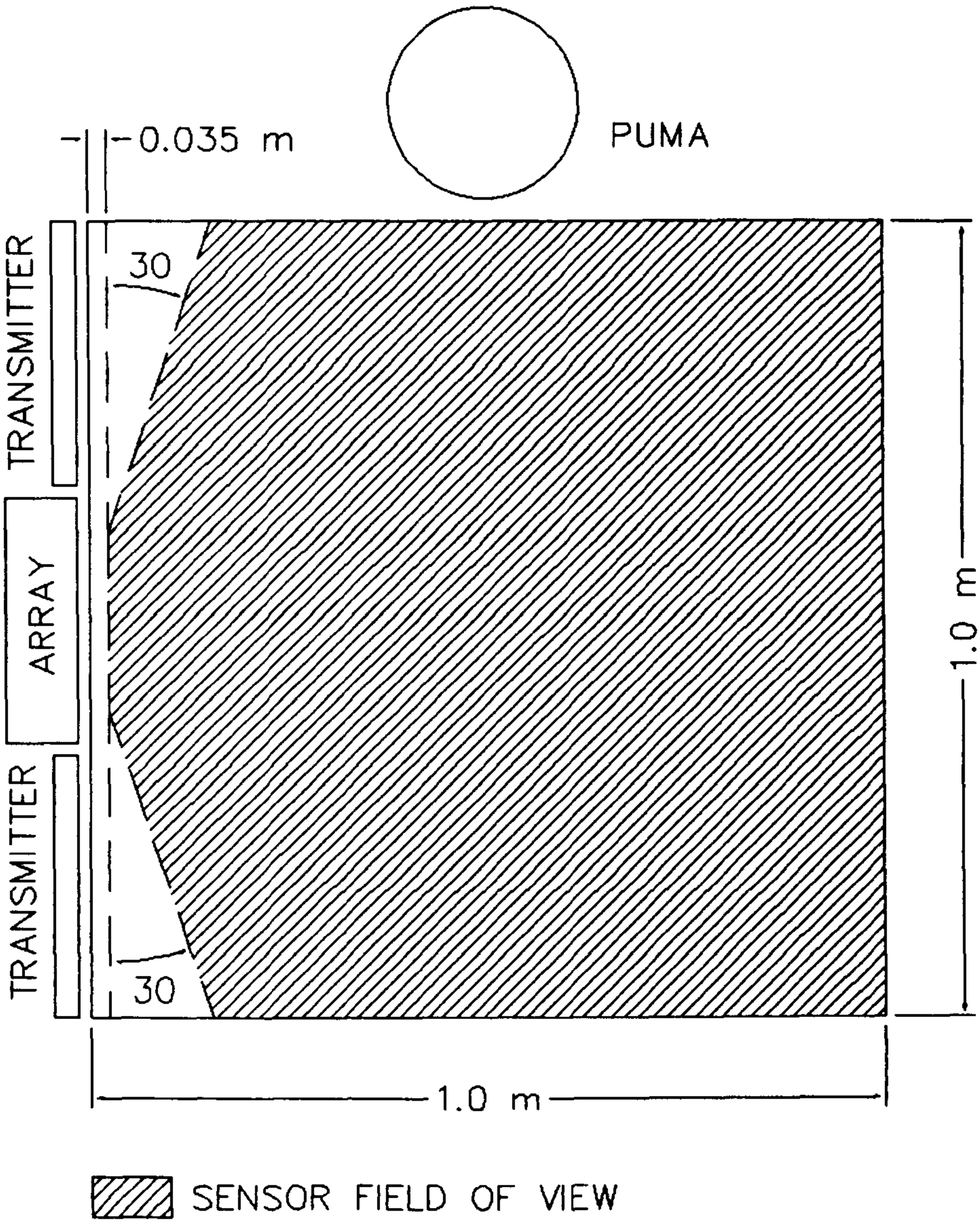

Figure 2: Experimental setup for robot guidance experiments.

them a line at a time to the controller. During operation the VAL 1 program lines are scanned for two special control characters, "^x" and "^y", which when encountered cause a real target position to be obtained from the ultrasonic location system and the target x,y co_ordinates inserted in the command. The program used simply instructed the robot to move its gripper to the position produced by the ultrasonic system and retrieve the object.

11.5 Multiple target system

The multiple target detection system is a large application consisting of over 4000 lines of C language and 500 lines of assembly language. It is not intended to give a detailed description of the code written but an overview of the major parts of the software is presented in this section. The software can be split into two sections, that which runs on the DSP card and that which runs on the PC. The basic structure of the two sections is shown in Figure 4 and Figure 5. The design and implementation of each of the modules within these sections will be described briefly.

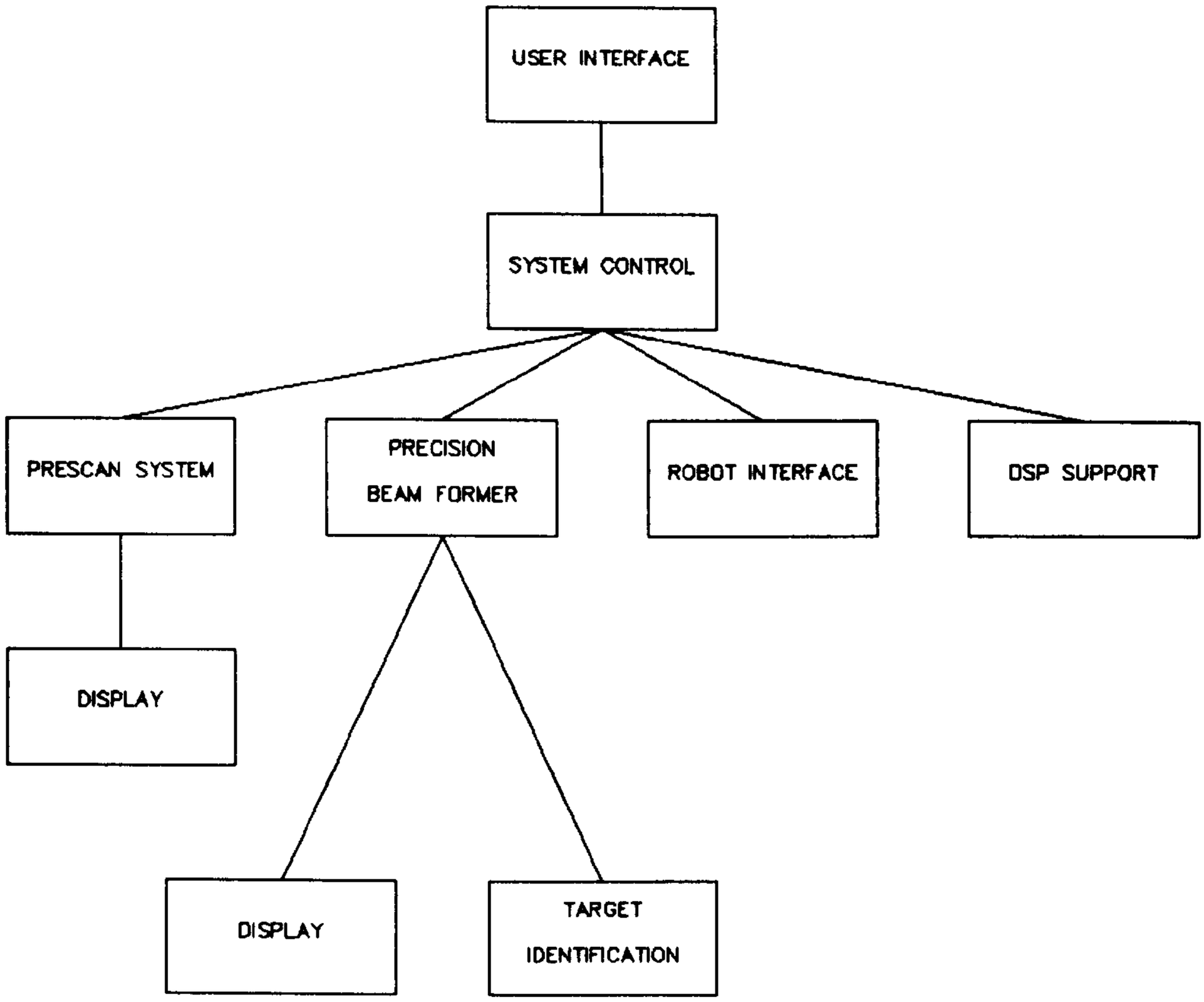

Figure 3: PC software overview.

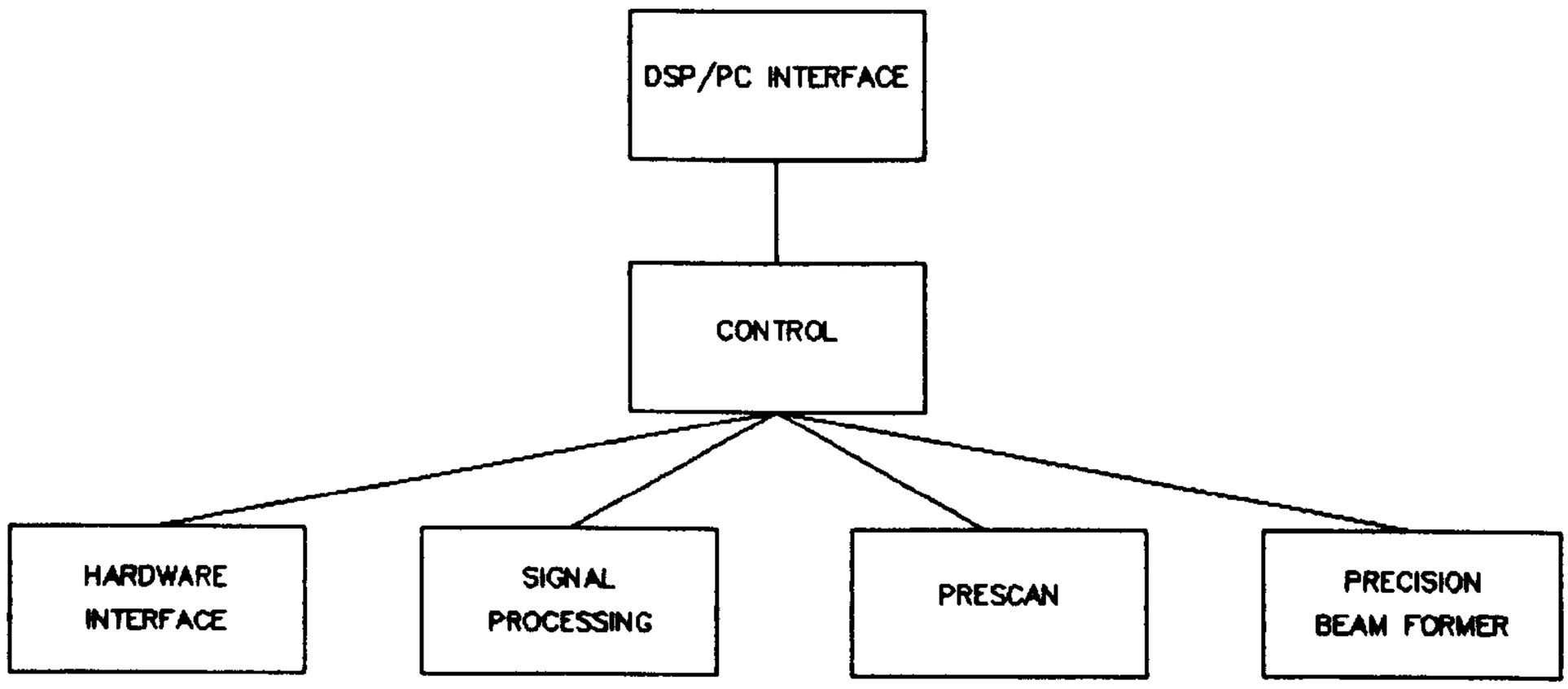

Figure 4: DSP software overview.

11.5.1 User interface.

The user interface is built around two different screen displays each containing several different windows. The graphics and all the text handling functions were written by the author and were made as simple as possible to conserve memory and simplify the development of the system.

11.5.2 System control.

The system control module decodes the inputs from the user interface and controls the operation of all other modules. This module is also responsible for all configuration and initialisation at start up and maintenance of the target data base.

11.5.2.1 Target database.

Once a target has been detected and validated by the software described in sections 11.5.3 and 11.5.4 the acquired target parameters are stored in a structure. This structure is then placed in a target data base for further processing and evaluation. The data base is constructed in the form of a linked list and a new member is dynamically generated each time a target is found. Each target placed in the data base is given what has been called a certainty value. This is a measure of how long the target has been present and provides a method of eliminating targets caused by random noise spikes. Before a target is entered the data base is first scanned to see if the target already exists ie. it has not moved since the last scan of the workspace. If the target is already present then the certainty is

incremented up to a maximum value of 2. After all targets have been entered and checked any targets which have not been updated have their certainty levels reduced by 1 and if the result is -1 then the target is discarded from the data base. The system only acts on targets with a certainty value of 2.

The structure contains several fields that contain the x,y co-ordinates of the target, the amplitude of the beam former output and the certainty. The structure contains a unique number which acts as an identifying tag for each target present in the workspace and a field that contains a 1 if the target has been classified as a corner and 0 otherwise. The last two entries give the addresses of the next and last target present in the data base.

11.5.3 Prescan system.

The prescanner, described in chapter 10, enables a coarse map of the position of all targets present within the workspace to be generated. In this development system operation is controlled by a series of mouse buttons located at the side of a display window. The raw output of the prescanner is displayed in real time within a display window.

11.5.4 Precision beam former.

In This development system, the operation of the precision beam forming system (see chapter 10) is controlled by a series of mouse buttons located at the side of a display window. The fully processed output of the system is displayed in real time within a display window. This module also contains the target detection algorithms.

11.5.4.1 Corner detection algorithm.

The corner detection algorithm scans the target database and looks for the presence of corners. The detection algorithm works on the principle that in any position a corner target will produce a smaller return echo than a curved or flat surface visible in the same position. This is due to the different reflection process involved, these processes are described in detail in chapter 3. The amplitudes of the returns produced by a target moved through the sensor field of view, at ranges of 250mm and 500mm, are shown in Figure 6 and Figure 7. It can be seen that large variations in return echo intensity can occur within the field of view. These variations occur for several reasons, firstly the receiving elements are not isotropic, secondly the array is operating in the near field, which causes amplitude fluctuations to occur across the transmitter aperture (see chapter 3). Finally here is a significant relationship between range and amplitude due to atmospheric absorbtion (see chapter 3). It can also be seen in Figure 6 and Figure 7 that there are two dead zones present at the junction between the array and the separate transmitters. The amplitude data collected was used to construct a series of empirical rules relating range bearing and amplitude for different target type. The system display differentiates target types by displaying corner targets in red and non-corner targets in white. A photograph of a typical display for a rectangle and a cylinder is shown in Figure 8.

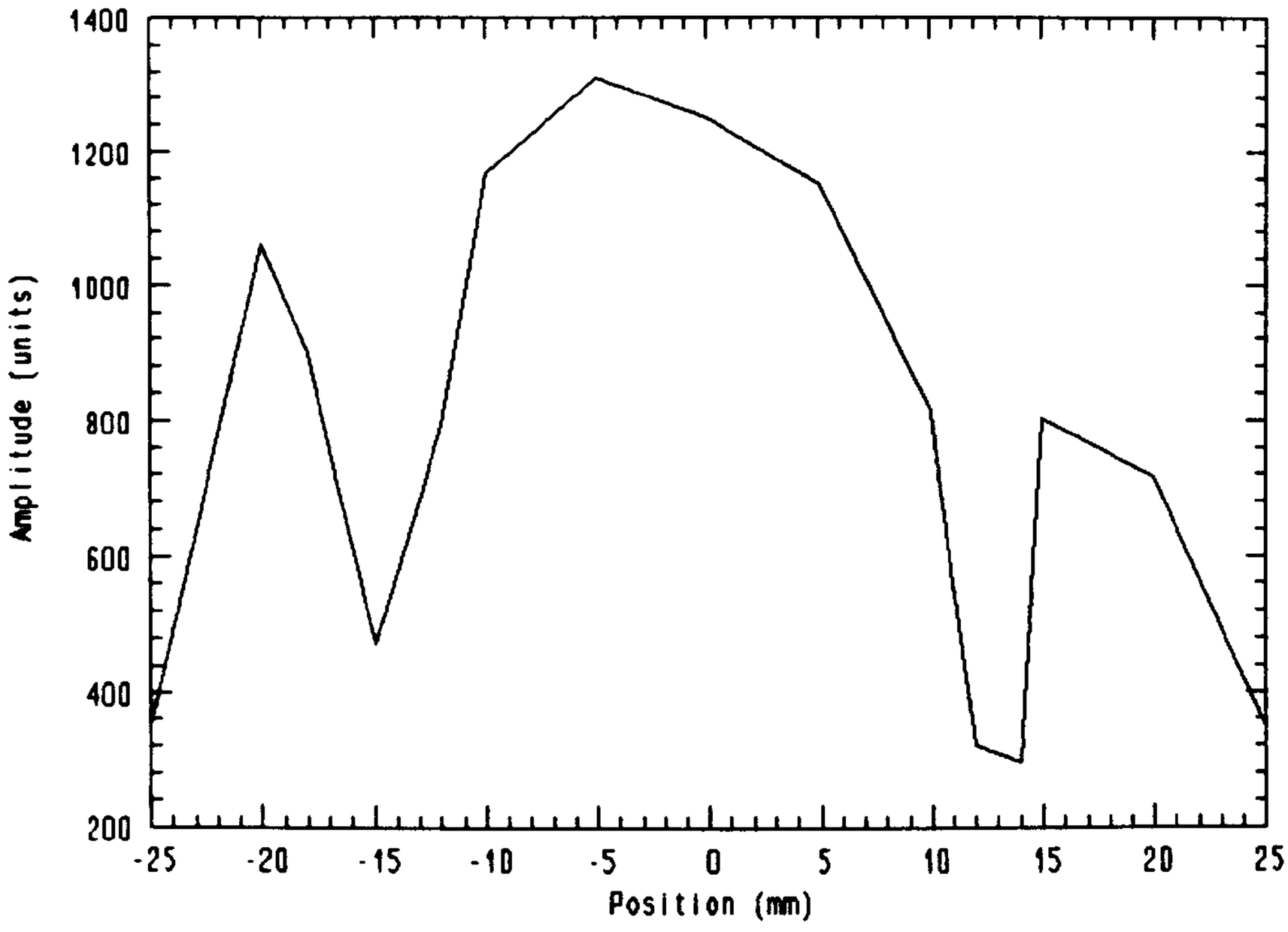

Figure 5: Amplitude plot for 500mm range.

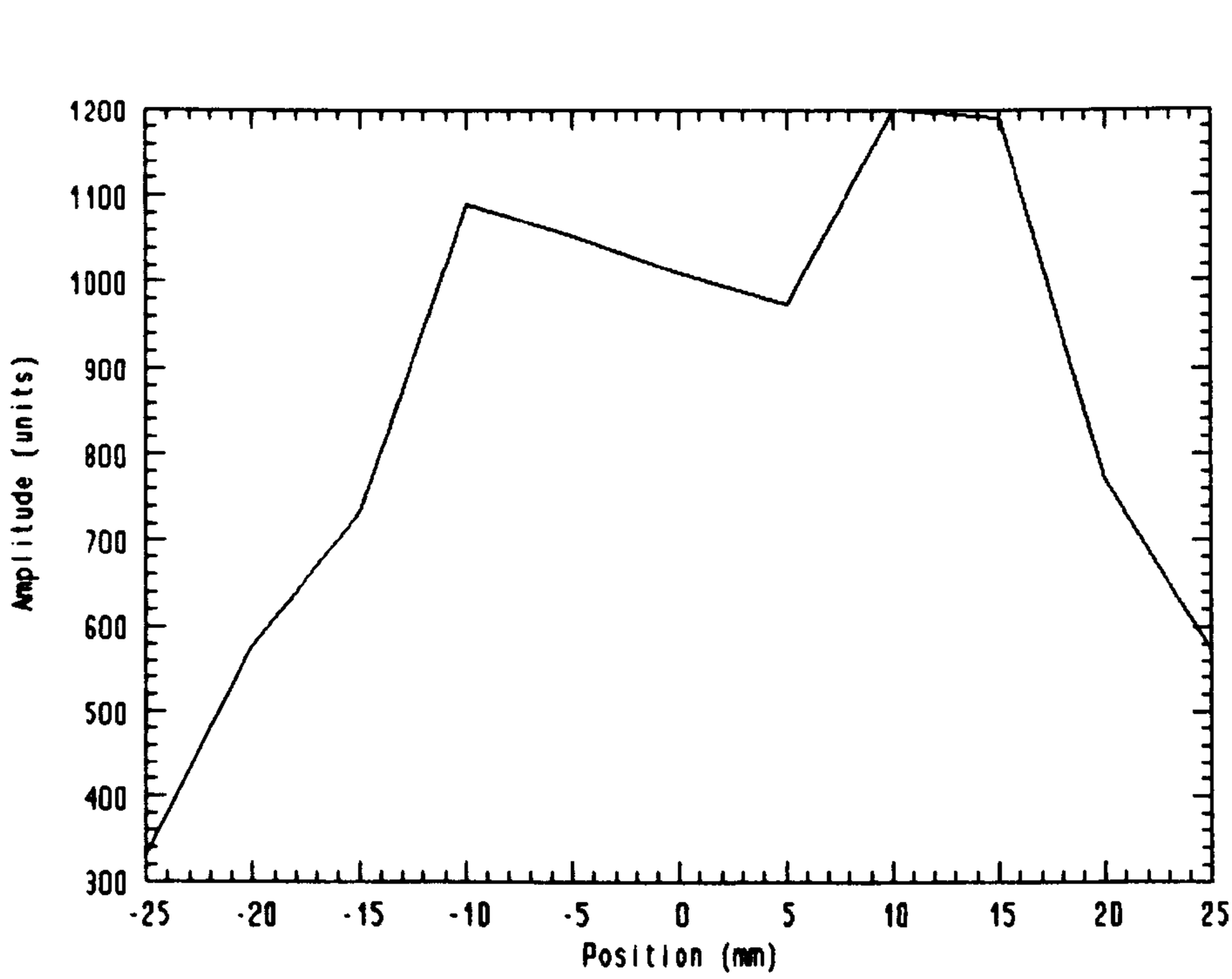

Figure 6: Amplitude plot for 250mm range.

11.5.4.2 Rectangle detection and measurement algorithm.

The rectangle detection algorithm is an extension of the corner detection algorithm described in section 11.5.4.1. This algorithm scans the data base looking for targets that have been labelled as corners and attempts to make associations between the corners detected. It operates using the following rules:

Look for the closest corner present in the database.

Look for the next closest corner present in the data base.

Is it within ±30mm of the first corner(z is the maximum size of rectangular object expected).

Look for the next closest corner present in the data base.

Is it within ±30mm of the first corner(z is the maximum size of rectangular object expected).

Repeat for all un-associated corners

This is a relatively crude system but it works well for the location of a single rectangular object present in the workspace. Once three corners have been located it is then a simple matter to calculate the length and orientation of the visible faces. These are then drawn on the screen and the generated data is stored in a structure. A photograph showing a typical display for the same rectangle and two cylinders is shown in Figure 8 is shown in Figure 9 after the rectangular object detection algorithm has been run.

The prescanner can be switched off when the system is operating in a simple environment. This gives a significant increase in processing speed but a

multiple PRF system must be used to remove second time around echoes.

11.5.5 Robot interface

The robot interface controls all communication between the robot and the PC. The module provides bi-directional communication and error handling facilities. A window is also provided on the user display which, when selected, can be used as terminal to provide direct communications between the PC keyboard and the robot controller.

11.5.6 DSP support

The DSP support module provides all the DSP housekeeping functions required. It is also responsible for the bi-directional transfer of commands, flags and data between PC and DSP.

11.5.7 Hardware interface.

The hardware interface software, which controls the data acquisition system, is described in appendix A.

11.5.8 Signal processing.

The following signal processing options have been implemented and may be selected by use of the control screens described in section 11.5.1.

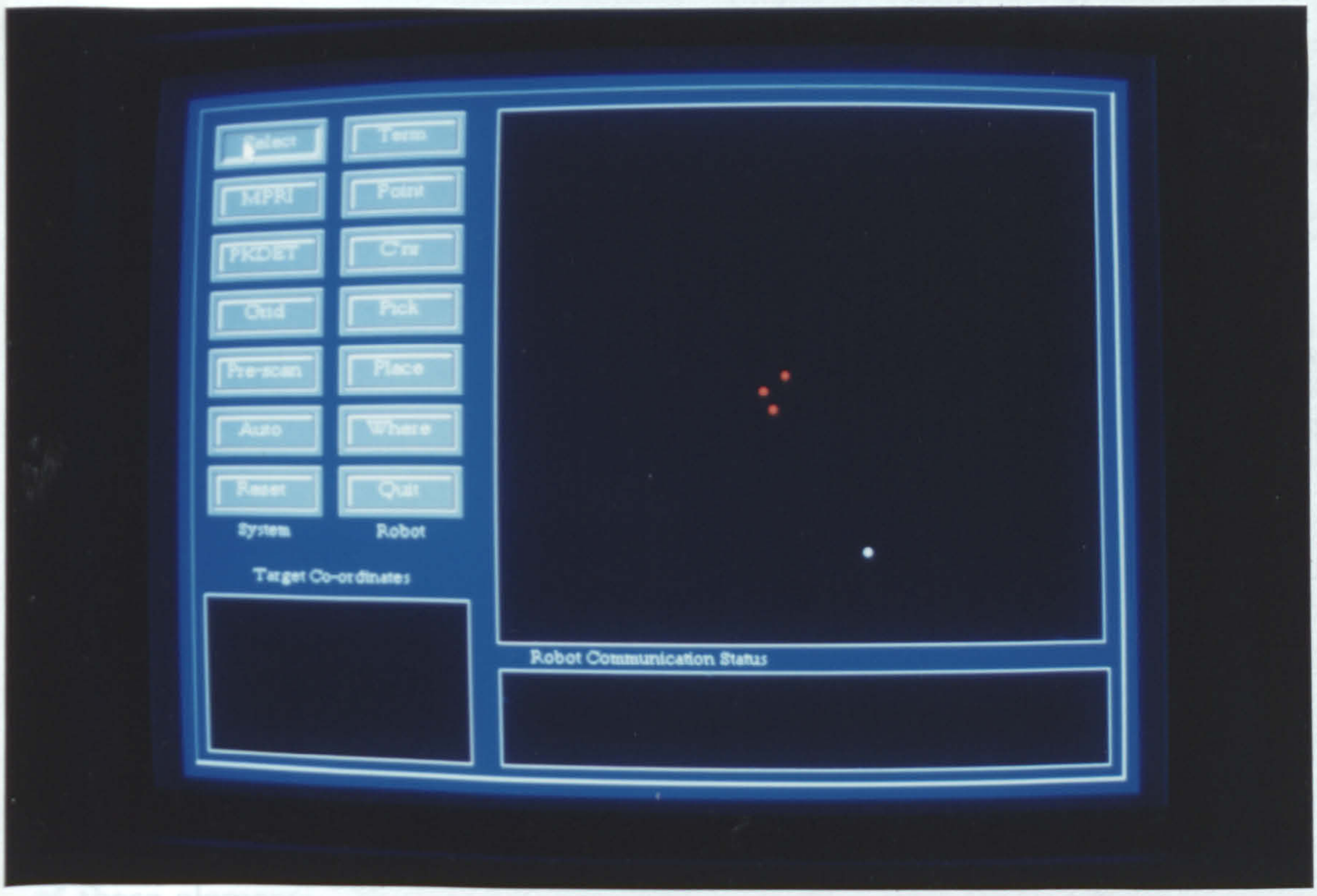

Figure 7: Photograph of typical display with corner detector operating.

Figure 8: Photograph showing typical display with rectangular object detector operating.

11.5.8.1: Multiple PRF

Due to the rapid firing rates used when operating with the direct target location method a multiple PRF system has been included to allow the removal of second time around echoes.

11.5.8.2: Adaptive threshold

With a cluttered environment it is possible that some points of reflection present on a target may not be visible to all elements on the array. This can cause problems since in the second detection system only the two outer array elements are used. It must therefore be ensured that the target is present in the outputs of these elements. To achieve this, before the data is beam formed, it is passed through an adaptive threshold (see chapter 8) and the target return is converted

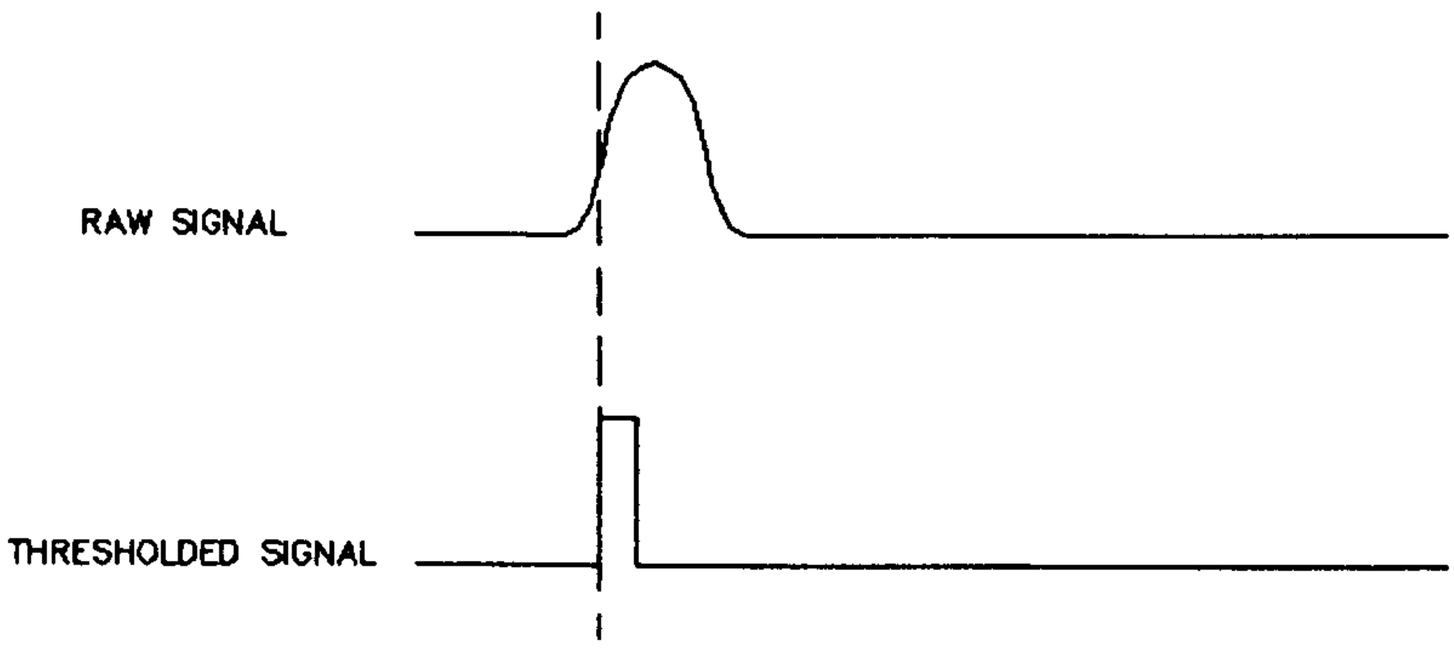

Figure 9: Effect of threshold on received envelope.

in to a rectangular pulse 4 samples wide and with a fixed amplitude see Figure 10. This removes the distinction between target types and gives all targets the same amplitude. It is thus possible to check, by measuring the amplitude of a possible target after beam forming, that it is present in all the array outputs. The data could of course be scanned before beam forming but this would introduce the

problems encountered with the direct method in chapter 9. A facility is also included to allow the use of a fixed threshold, the level of which can be set manually from the user interface.

11.5.9 Prescan and precision beam former.

The modules are based on the algorithms already described in chapter 7 and so will not be discussed further.

11.6 Experimental results.

The system was tested with a target placed in a number of different positions within the robot workspace. The robot proved capable of picking up a target any where within its workspace[2]. Problems may occur if the target falls in the area of uncertainty between beams (see chapter 9). The impact of this uncertainty is however dependent on the size of the target and the size of the robot gripper. The system was not fully tested with the cube targets because the robot gripper available was not large enough.

11.7 Summary

The system described in this section has proved the capability of an ultrasonic system as a method of object location in robot work cell.

11.8 References

1. Puma 560 Operating Manual, Unimation Inc, 1980.

2. P. F. Webb, I. Gibson, C. Wykes, "Robot Guidance using Ultrasonic arrays", Accepted for Publication Journal of Robotic Systems, 1993.

CHAPTER 12

CONCLUSIONS AND FURTHER DEVELOPMENTS

12.1 Introduction.

Chapter 12 provides a summary of the work completed and suggestions for further work. Section 12.2 assesses how well the objectives set in chapter 1 have been met. The new work that has been completed in fulfilment of these objectives is described in section 12.3. Section 12.4 describes some improvements that could be made to improve the efficiency of the hardware and software. Section 12.5 describes some of the possible ways in which this research may be extended in the future.

12.2 Fulfilment of objectives.

All the objectives set in chapter 1 and chapter 5 have been fully realised. A real time object location system has been developed. This system has been proved capable of directing a fixed robot within an unknown and unstructured workspace[1]. The objectives and their realisation are summarised in Table I. It can be seen that all the specifications listed in chapter 5 have been met or exceeded. The environmental independence specification can be met since ultrasound is unaffected by dust and the presence of humidity can be calibrated for. The resistance to corrosive gases would depend on the metallisation used on

Table I: Achievement of specification.

Objective	Required	Achieved
System Range	Min 30mm Max 500mm	Min 35mm Max 1m
Systematic Range Errors	±10%	0.25%
Random Range Errors	±5%	0.01%
Range Resolution	25mm	1.7mm
Bearing error	±30%	0.6%
Speed (Using direct method)	20ms	12ms

the membrane; in very harsh environments gold could be used.

As result of the work, a number of new signal processing methods have been developed and existing ones improved. These are listed in section 12.3.

In support of this work a comprehensive literature review has been undertaken, a synopsis of which is presented in chapter 2.

12.3 Author's work.

The following achievements and work are described in this thesis:

1. A real time data acquisition system has been designed and built. This is described in chapters 5 and 6. The data acquisition system speed has been increased above that of existing systems[2] by the use of analogue processing.

2. A new approach to digital beam forming has been developed. This

method removes the normal $\lambda/2$ limitation for array elements. This has allowed a greater resolution to be achieved, for a given number of array elements, than with traditional beam forming methods. This is described in chapter 7. The new beam forming system has been fully tested in real time, in conjunction with the hardware developed. The sources and effects of both systematic and random errors have been evaluated analytically and empirically. The results of this analysis are presented in chapter 9.

3. The hardware and software developed have been used successfully to control a robot performing a pick and place operation. The results and a full description of this application are presented in chapter 11.

4. A fast triangulation method has been developed (see chapter 7) and used in conjunction with a digital beam former. This combination of methods has lead to an increase in accuracy but without some of the disadvantages experienced by other workers using a triangulation method[3]. This is described in chapter 11.

5. A technique, which uses a variable transmitter firing interval, has been applied to the system. This has been successfully used to remove second time around echoes introduced by high firing rates. This method has been particularly successful in helping to increase the robustness of ultrasonic ranging when used to look at objects in front of reflecting surfaces. The technique is fully described in chapter 8.

12.4 System improvements.

This section discusses ways in which the system can be improved both in terms of hardware and software.

12.4.1 Hardware Improvements

12.4.1.1 Dynamic range improvement.

The dynamic range of the system could be improved by the inclusion of a non-linear gain element within the input stages of the system. The most common device used for this purpose is the logarithmic amplifier which has, as the name implies, a logarithmic gain characteristic. The use of such an amplifier is common in radar systems and is capable of giving large dynamic responses[4].

12.4.1.2 Inphase and quadrature drive signal generation.

The use of signal generators to produce the inphase and quadrature mixer signals is impractical in a real system. A number of methods are available; the simplest would be to use a ROM lookup table driving a pair of A/D converters. A digitally programable amplifier would be required since in the current system the drive to the mixers is used to control the system gain.

12.4.1.3 Integration of the system.

Whilst the present system, with its long external bus, provides a useful

development environment, the speed of the system is limited by transmission line effects. In a practical system the data acquisition system would need to be integrated with the DSP in order to minimise the length of the bus. If this could be done then extra channels could be accommodated.

12.4.2 Software

The software could be improved and speeded up by writing more of the DSP code in assembly language. (Note that the system using pre-calculated offsets has already been optimised in assembly language). The direct method would also derive little benefit from optimisation since the overall processing time is already short, it is only about 2ms longer than the time of flight.

A major limitation of the system is the time spent in transferring the data between the DSP and the PC. If the link between the PC and DSP could be dispensed with, and the output of the system obtained directly from the DSP, then a considerable increase in operating speed could be obtained.

12.5 Further development.

This section looks at areas in which the system could be expanded.

12.5.1 Application to mobile robot guidance.

The system described in this thesis has to date only been used to guide a static robot but there is no reason why the principles should not be applied to mobile robot guidance. The sensor used in this work is limited in its application to mobile

robot navigation by the operating frequency. With a 100KHz transducer the useful range is limited, by absorption, to about 2m. A similar array operating at 50KHZ has been developed at Nottingham University which, with slight modification to the system hardware, would allow the system to be used for navigation[5]. This array has a useful operating range in excess of 15m.

12.5.2 Fusion with vision systems.

The use of vision systems is now becoming widespread in industrial monitoring and control systems. The systems currently in use can identify the orientation of objects and recognise surface features[6,7]. They can be used to rapidly identifying objects and detect the presence of defective components. The majority of vision systems look down on the objects in question and can provide no range information. Without knowledge of the distance between object and camera no information on object size can be extracted. The classic example is that a small ball close to the camera cannot be distinguished from a large ball a long way from the camera. Although there are many different ranging systems available, they are all complex and expensive[8,9]. They may require structured lighting which can be at odds with the lighting requirements of the vision system[10]. An ultrasonic system would be ideal for this purpose since accurate ranges can rapidly be obtained. A current research project at Nottingham university involves linking the ultrasonic system to a vision system.

12.6 References.

1. P. Webb and C. Wykes, "Ultrasonic Arrays for Robot Guidance", Submitted to Journal of robotic systems, 1993.

2. S. C. Pomeroy, "Ultrasonic Phased Arrays for Robotics Modelling and Experimental Implementation", Ph. D. Thesis, University of Nottingham, 1990.

3. H. Peremans, K. Audenaert, and J. M. Campenhout, "A High-Resolution Sensor Based on Tri_Aural Perception", IEEE Transactions on robotics and automation, Vol. 9, No. 1, February 1993, pp36-48.

4. M. I. Skolnick, "Introduction to Radar Systems", McGraw-Hill International, 1984.

5. W. S. H. Munro, "Ultrasonic Phased Arrays for Use in Imaging and Automatic Vehicle Guidance", PhD Thesis, Nottingham University, 1990.

6. H. Ekerol, and D. C. Hodgeson, "A Machine Vision System for High Speed Object Tracking Using a Moments Algorithm", Mechatronics, Vol. 2, No. 6, 1992, pp555-565.

7. H. Ekerol and D. C. Hodgeson, "Angular Position Control of Objects Using a Transputer Based Vision System and Fuzzy logic Techniques", Proceedings of the institute of mechanical engineers, Vol. 207, Part 1, 19993, pp47-55.

8. B. G. Batchelor and F. M. Waltz, "Machine Vision Systems Integration", SPIE optical engineering press, Washington, 1991.

9. P. Cielo, "Optical Techniques for Industrial Inspection", Academic press Inc., San Diego, 1988.

10. Jarvis R. A., "A Perspective on Range Finding Techniques for Computer Vision", IEEE Transactions on pattern analysis and machine intelligence, Vol. 5, No. 2, March 1983, pp122-139.

APPENDIX A

SYSTEM SOFTWARE DEVELOPMENT

A.1 Introduction

Appendix A provides an overview of the software written during the course of the research. Section A.2 describes the system software which is responsible for interface and housekeeping functions. Sections A.3 to A.8 deal with main applications software whilst section A.9 gives brief details of some of the miscellaneous software written in support of this research. All software is written in plain C language, TMS320C30 assembly language or SPOX. The SPOX applications interface[1] is an extension of the C language which supports vector and matrix data objects and also provides many signal processing functions not present in the standard C libraries. All the applications consist of software which runs on the PC and software which runs on the DSP. In all cases these are totally separate entities compiled using different compilers. They communicate by passing a series of flags and or data through ports on the PC bus.

A.2 System software

The system software described here runs on both the PC and the DSP and forms the building blocks around which the main system applications are formed. All the software modules are contained in four separate libraries to allow them to be

easily integrated into any program.

A.2.1 Hardware interface software

The hardware interface software is written entirely in TMS320C30 assembly language and consists of 150 lines in total. It is responsible for the control of all the data acquisition system parameters and the initial management of acquired data. The primary functions are:

Initialisation of all DSP bus control registers.

Control of data multiplexers.

Generation of transmitter waveform.

Servicing of data acquisition interrupt routine.

Normalisation and storage of acquired data.

The assembly language has been written so that it may be called as a 'C' language function using spox data objects. This allows the hardware to be invisible to the user since one only has to call a function which then returns four arrays of data. The arrays returned are spox vector data objects; this enables signal processing functions to be applied directly to the data.

A.2.2 Graphical Interface

The graphical interface is written in three parts; there is the user interface, display graphics and communication.

A.2.2.1 User interface

The user interface provides two alternative levels of control, a mouse and

keyboard driven pull down menu system or a pseudo control panel. The pull down menus have been used as the basis of the analytical software written and the pseudo control panel system is used to drive the direct hardware applications. Whilst there are several commercially available packages that can perform this function it was decided that for efficiency and ease of development it would be easier to write a simple interface from scratch. Many of the commercial systems such as Microsoft windows are complex to use, require large amounts of memory and have a high processing overhead.

A.2.2.2 Display graphics

The display graphics are based around a simple grid display system which uses standard algorithms to provide a 3 dimensional grid display of data. The grid may be rotated and scaled in any direction. Initially a commercial standalone package was use for this purpose but it proved to be relatively cumbersome and was limited in the size of grid it could accommodate. A further advantage of writing a system from scratch was that it could be integrated directly with the user interface software.

A.2.2.3 Communication

The communication software consists of all the file handling software necessary for system data management and RS232 serial port software. The serial communications software was taken from a 'Shareware' package written by Thomas Wagner of Ferrari Electronics GMBH and is not the work of the author.

There is a further module associated with this area which control data

transfer and handshaking between the PC and DSP board. These are based on the C language functions provided with the DSP board by Loughborough Sound Images. Basic file I/O functions are also included in this module.

A.3 Array monitoring software.

The array monitoring software is based on a pull down menu system which allows the output of the array to be displayed in near real time. The software is also written so that it can easily be used to test signal processing algorithms on real data. A photograph of a typical display screen is shown in Figure 1.

A.4 Diagnostic software.

The diagnostic system consist of a virtual control panel on the PC which enables all aspects of the hardware to be monitored and measured. This software was written to allow diagnostic evaluation and calibration of the data acquisition system. A photograph of the virtual control panel is shown in Figure 2.

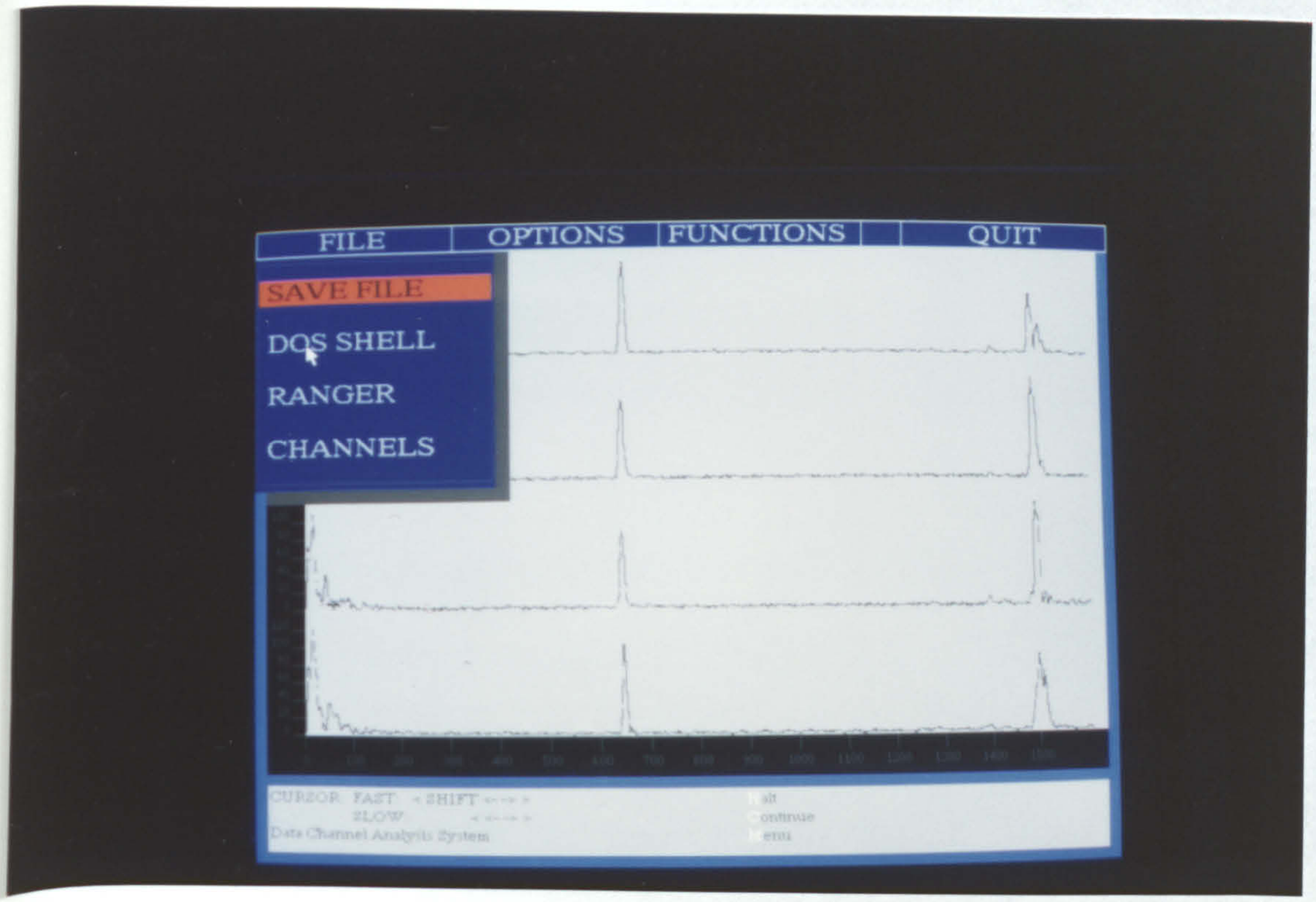

Figure 1: Typical screen display for array software.

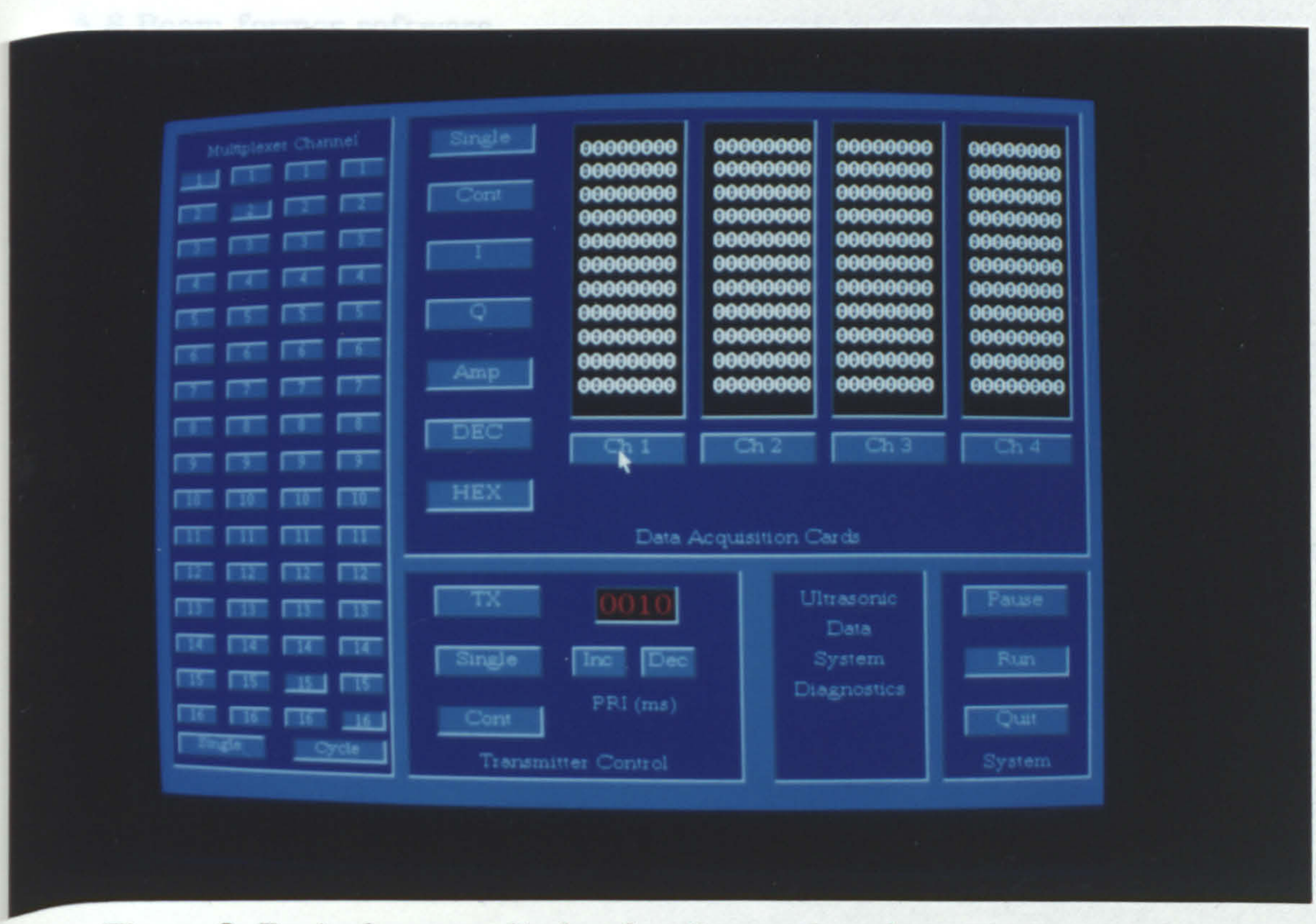

Figure 2: Typical screen display for diagnostic software.

A.5 Measurement software.

The measurement software again consists of a virtual control panel which controls a linear stage and the ultrasonic system. The ultrasonic system is used as a simple X, Y position measurement system which can be used in conjunction with a linear stage. This provides a means of precisely and repeatably measuring system accuracy. The stage is driven by the PC through an IEE488 interface, the system may be run either manually or automatically and allows large amounts of data to be acquired quickly. The measurement result are printed out on an epsom printer for later analysis. A photograph of the virtual control panel is shown in Figure 3.

A.6 Beam former software.

The beam former software is based on a series of pull down menus and provides all the necessary display and control facilities to provide a test bed for DSP beam forming algorithms. Most of the results presented in chapters 9 and 10 where generated using this software. A typical screen display is shown in a photograph in Figure 4.

A.7 Robot control software.

The robot control software is described and its performance analyzed in detail in chapter 11. It will not be dealt with in this section as it is the end product of most of the work described in this thesis.

Figure 3: Typical screen display for measurement software.

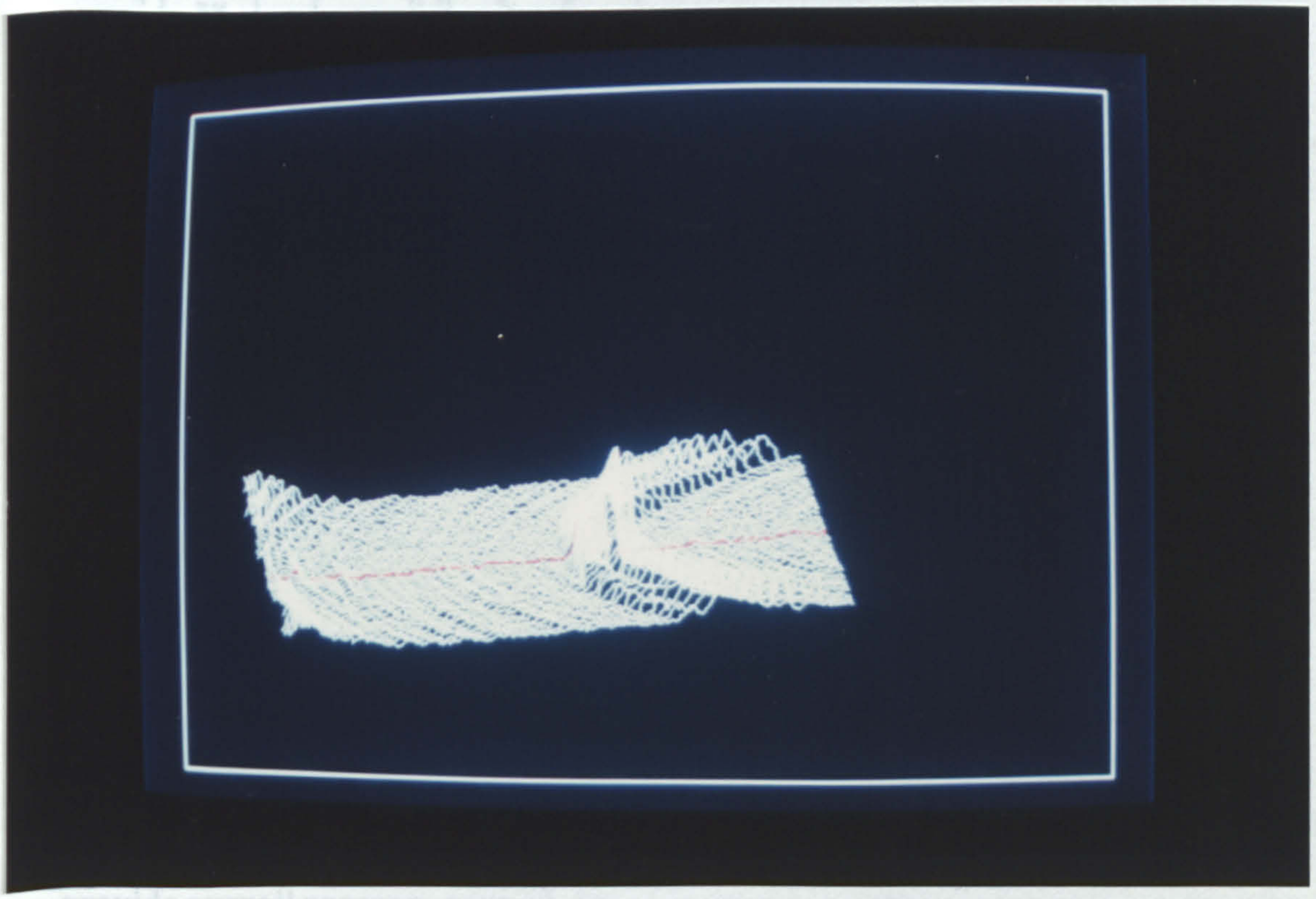

Figure 4: Typical screen display for beam former.

A.8 TLM Conversion Software.

The purpose of this software is to take data produced by the TLM modelling system[2] and convert it into a format suitable for beam forming.

The software consists of two separate modules TLMCNV.C and TLMPROC.C, the former runs on the DSP card whilst the latter runs concurrently on the PC. Both are written in C but TLMPROC uses signal processing functions from the spox extended library. A block diagram of the software is shown in Figure 5.

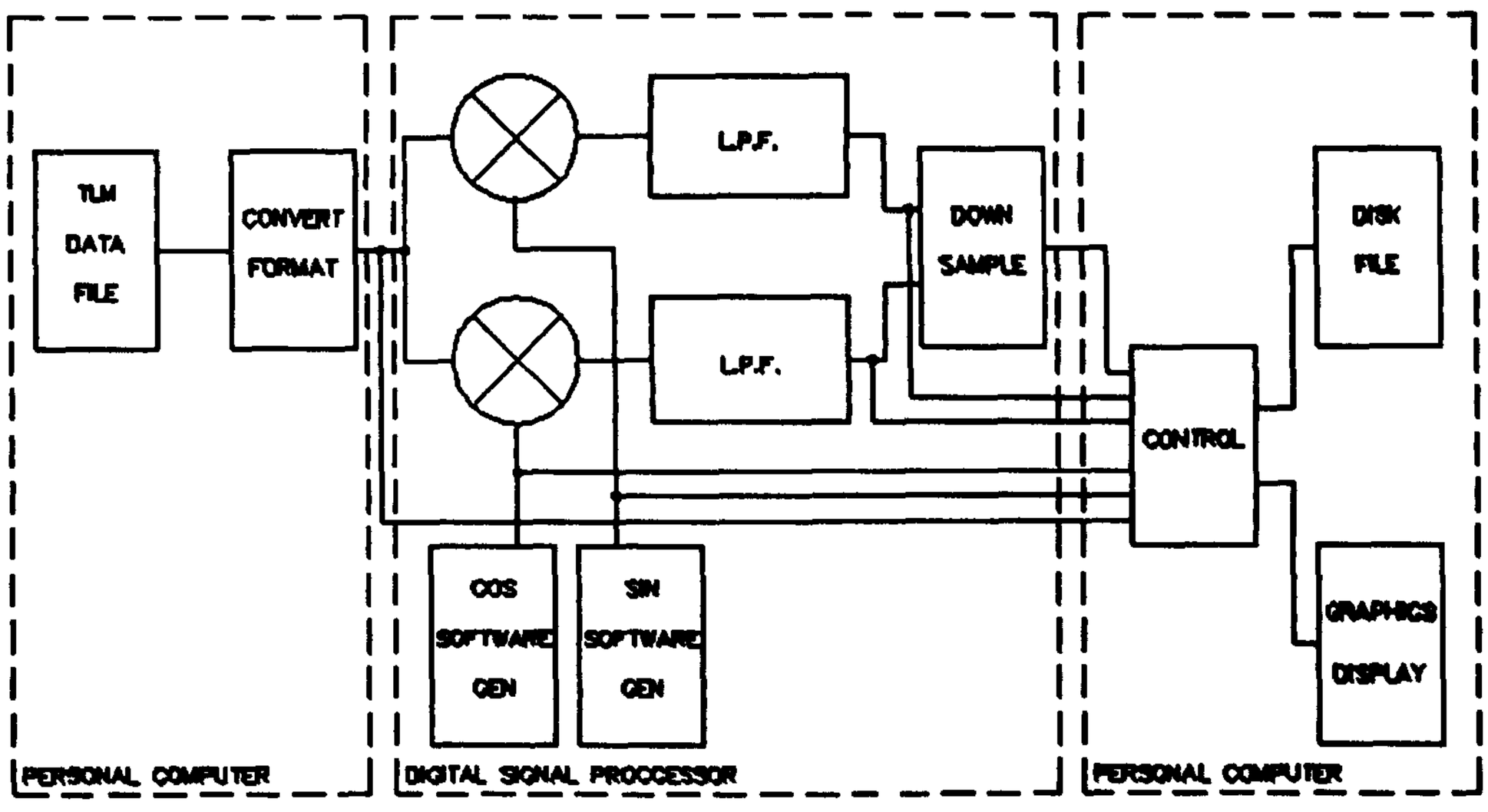

Figure 5: Functional block diagram of TLM data conversion software.

A.8.1 PC based software.

The PC based software uses functions from the system software library to provide overall program control, file management, DSP housekeeping and graphical display of data. The module also contains a function which strips the TLM data file of line numbers and commas before passing the data to the DSP card for

processing. At any stage during signal processing the data may be retrieved from the DSP card and either displayed on the PC monitor or stored in a disk file. Since the TLM modelling only produces dat for a window around the target a facility is included to allow files to be padded with dat so that the target appears in the same place within a file as it would for real data.

A.8.2 DSP based software.

The DSP based software effectively models the data acquisition hardware. It runs in two parts an initialisation routine generates and initialises all the spox data objects and puts the board into a state ready to receive data from the PC. The DSP is then placed in an infinite loop waiting for data from the PC. When data is present the second part of the software is started and the is data is processed. The processing software first copies the input data from the PC into two spox vectors these are then multiplied by sine and cosine vectors respectively (see Figure 6). The results are then filtered by an FIR implementation of a 6th order Butterworth filter, Figure 7 and Figure 8. The filter was designed using The Hypersignal workstation filter designer[3]. The design of the filter was chosen to mimic the hardware filters as closely as possible. After filtering the envelope amplitude vector is created, Figure 9, and down sampled from the TLM sampling rate, which is fixed by the mesh size and is therefore variable[2], to a frequency of 200KHz. The data is then returned to the PC for display or storage. The DSP card can only process one channel at a time and so the software processing must run four times to convert simulated data from a four element array. Once the process is complete the DSP returns to the loop and awaits further data.

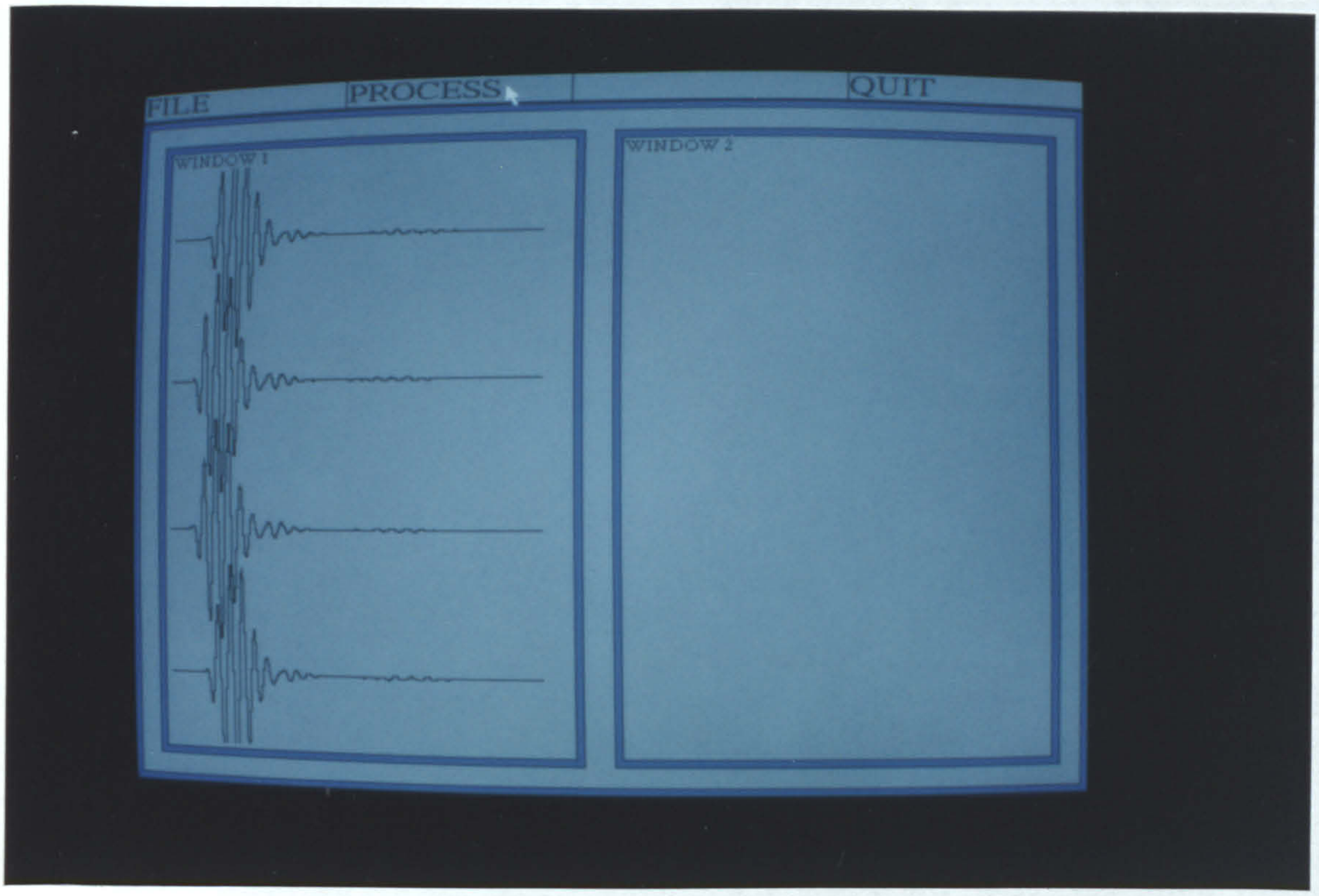

Figure 6: Input to DSP software mixer from stripped TLM data file.

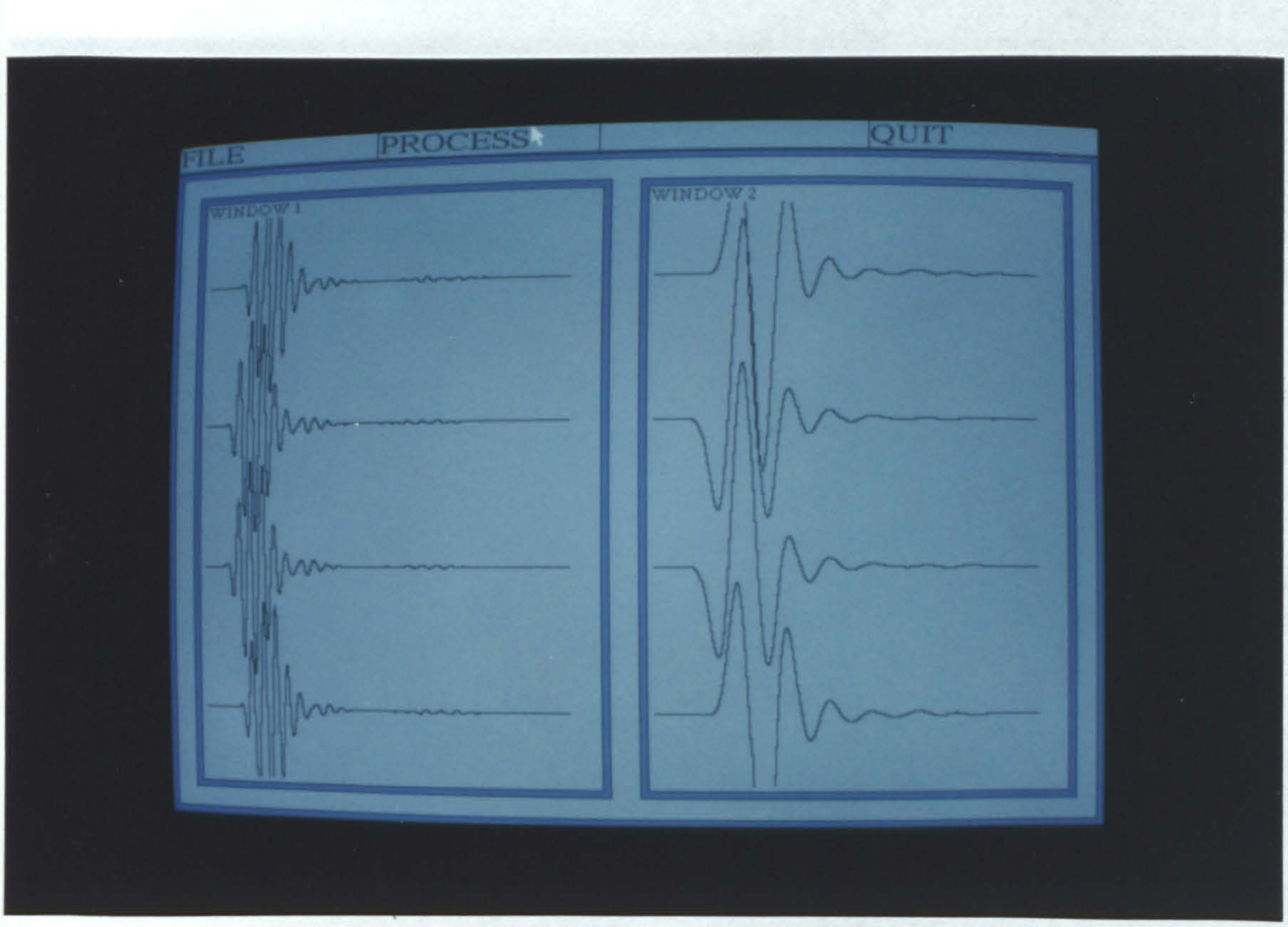

Figure 7 Signal after mixing with sine wave vector, (I channel).

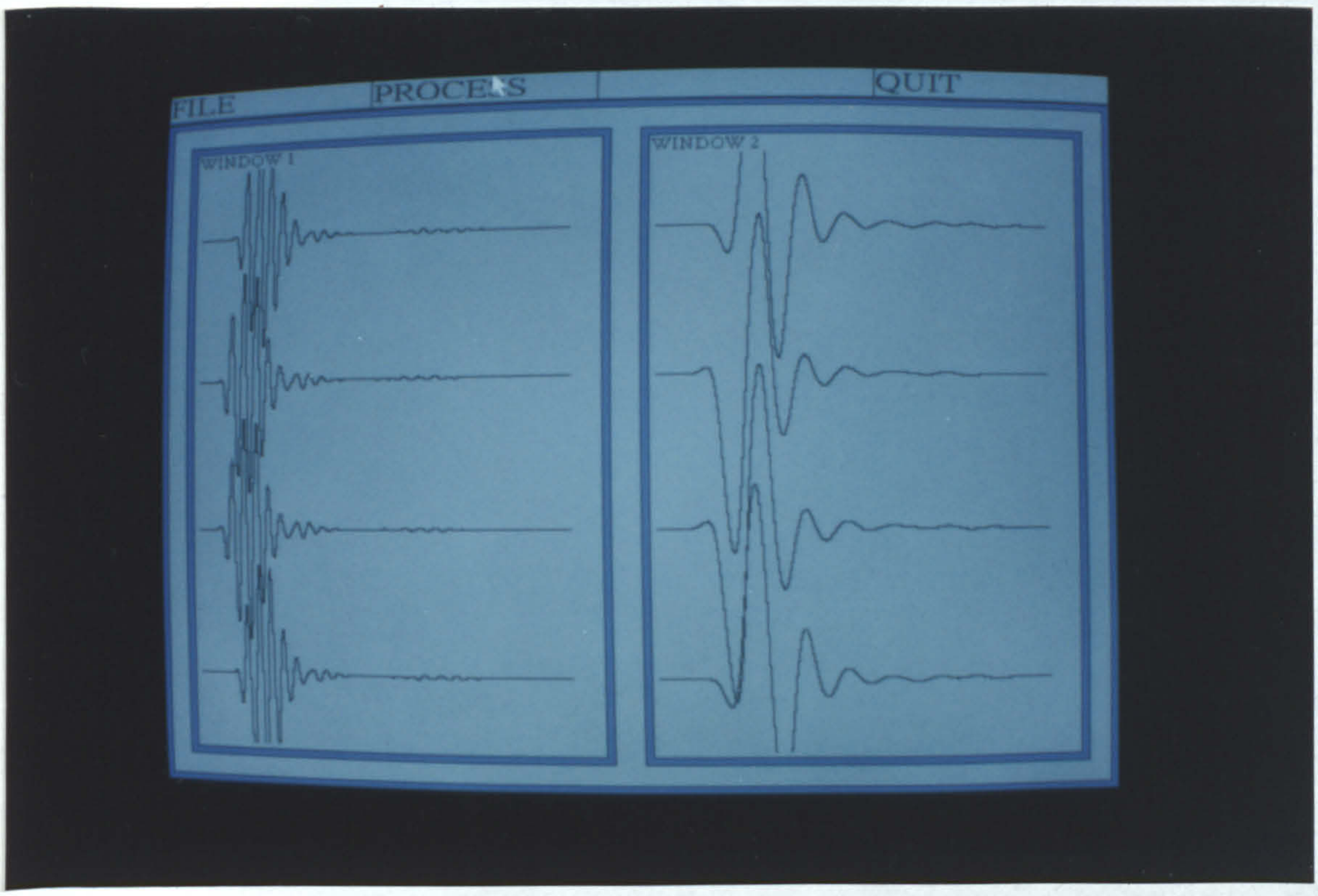

Figure 8 Signal after mixing with cosine vector, (Q channel).

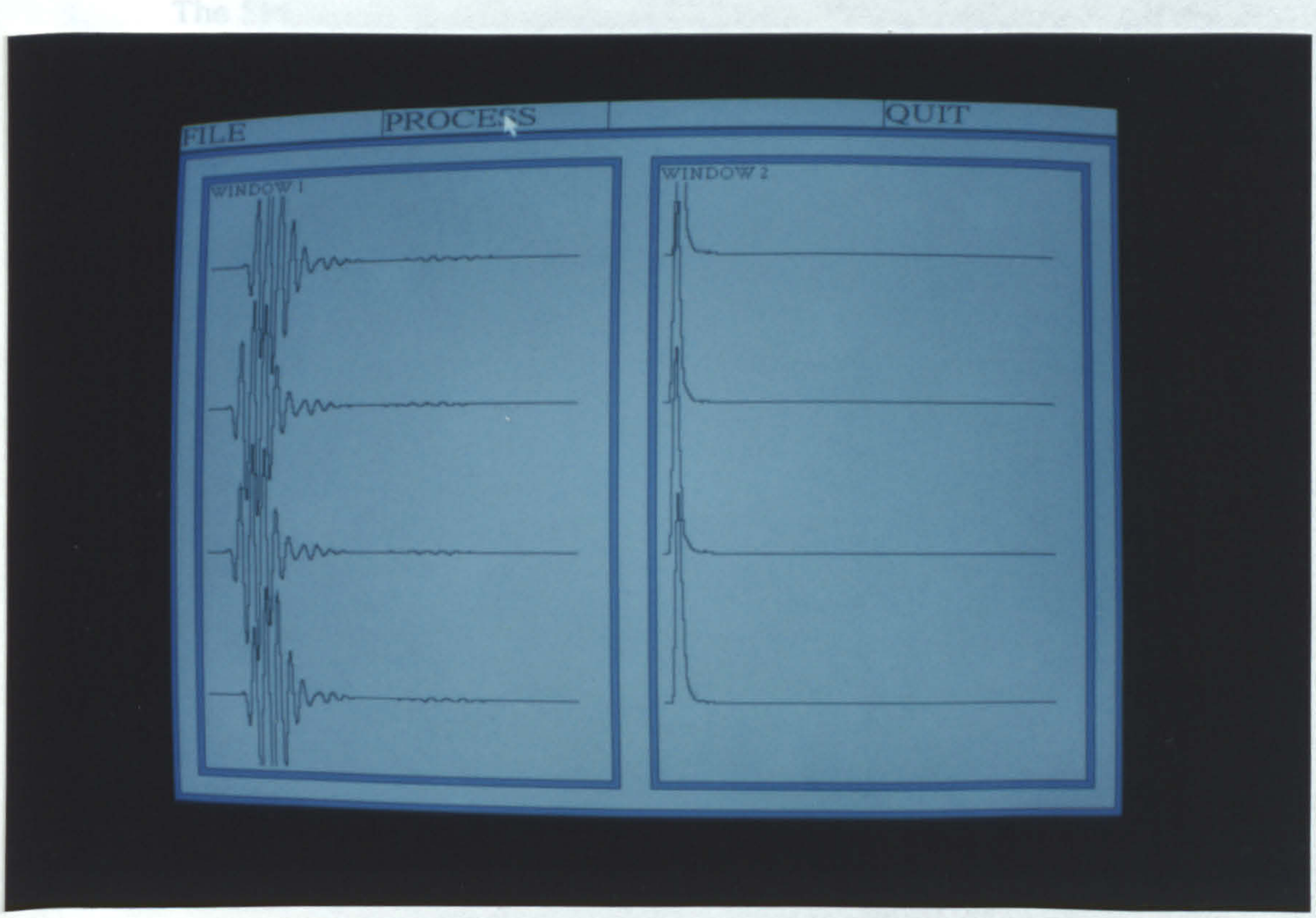

Figure 9: TLM envelope data four 4 channels before storage to file.

A.9 Other software.

Several other programs have been written in support of this work, these include:

Data file to HPGL conversion routines. These have been used to generate most of the results shown in this thesis.

Beamplot generation and plotting software.

Conversion of gridplot data files to HPGL files.

Since these are peripheral to the work described in this thesis they will not be described.

A.10 References.

1. The SPOX application programming manual, Spectron microsystems, 1991.

2. G. Zhang, "The Applications of Transmission Line (TLM) Method to the Modelling of Airborne Ultrasonics", Ph. D. Thesis, Nottingham University, 1993.

3. HYPER SIGNAL WORKSTATION. User manual, Hyperception Inc. February 1992.

APPENDIX B

BEAM FORMER ASSEMBLY LANGUAGE LISTINGS

Appendix B contains the assembly language listings for the DSP based beam forming algorithms. A detailed functional description of each program is also given.

B.1 Unfocused beam former code

The code can be divided into two sections a right hand beamform and a left hand beam form. Listings of these two sections are shown in figure 2 and figure 1 respectively. The software functions in the following way:

Left hand sweep: Lines 4-8 set the starting skews so that the extreme righthand beam is the first formed. The constant 'NUMLBEAMS' is the number of beams to form. Lines 13-16 load the starting addresses of the data vectors. Lines 18-21 add base offsets to the data vector starting addresses to allow the starting point for beam forming to be moved. These base offsets are set by the global variable '_offset'. Lines 23-24 set the starting address for storage in a data array. The previous starting address is held in AR2, the column length in R2 and the distance between columns in R3. This is allows the program to interface with spox data objects. Lines 27-37 set the skew for the next beam by decrementing the starting skews and adding them to the starting addresses of the data vectors. Lines 34-34 load the repeat counter

with the global variable _beamlength to set the length of beam to be formed. Lines 33-35 scan the data vectors and perform the summation to form the actual beam. Line 43 controls the loop counter which controls the number of beams to be formed.

Right hand sweep: The operation of the right hand beam former software 2 is very similar to that of the left hand except that the starting skews are set to zero and 22-29 consist of an increment compared with a decrement in lines 27-34 of figure 1. This causes the data vectors to be scanned in the opposite sense. The increment is a pre-increment compared with a post decrement. This prevents the central beam being duplicated.

```
;01;
;02;    ;left sweep;
;03;
;04;    LDI @NUMLBEAMS,R5          ;set starting skews;
;05;    LDI @NUMLBEAMS,R6
;06;    MPYI 2,R6
;07;    LDI @NUMLBEAMS,R7
;08;    MPYI 3,R7
;09;
;10;    LDI @NUMLBEAMS,AR1
;11;    SUBI 1,AR1
;12;
;13; Lb1 LDI @BUF0,AR4 ;load start addresses;
;14;    LDI @BUF1,AR5
;15;    LDI @BUF2,AR6
;16;    LDI @BUF3,AR7
;17;
;18;    ADDI @_offset,AR4          ;add offsets to adresses;
;19;    ADDI @_offset,AR5
;20;    ADDI @_offset,AR6
;21;    ADDI @_offset,AR7
;22;
;23;    LDI AR0,AR2          ;load next beam address;
;24;    ADDI R2,AR0
;25;    ADDI R3,AR0
;26;
;27;    ADDI R5,AR5          ;set skews;
;28;    SUBI 1,R5
;29;    ADDI R6,AR6
;30;    SUBI 2,R6
;31;    ADDI R7,AR7
;32;    SUBI 3,R7
;33;
;34;    LDI @_beamlength,RC
;35;   SUBI 1,RC
;36;
;37;    RPTB Lb2          ;form beams;
;38;    ADDF3 *AR4++(1),*AR5++(1),R0
;39;    ADDF *AR6++(1),R0
;40;    ADDF *AR7++(1),R0
;41; Lb2 STF R0,*AR2++(IR1)
;42; DBU AR1,Lb1
```

Figure 1 . Left hand beam former.

```
;*************************************************************;
;01;
;02;    ;right sweep;
;03;
;04;    LDI @NUMRBEAMS,AR1
;05;    SUBI 1,AR1
;06;
;07;
;08;Rb1 LDI @BUF0,AR7 ;load start addresses;
;09;    LDI @BUF1,AR6
;10;    LDI @BUF2,AR5
;11;    LDI @BUF3,AR4
;12;
;13;    ADDI @_offset,AR4        ;add offsets to adresses;
;14;    ADDI @_offset,AR5
;15;    ADDI @_offset,AR6
;16;    ADDI @_offset,AR7
;17;
;18;    LDI AR0,AR2              ;load next beam address;
;19;    ADDI R2,AR0
;20;    ADDI R3,AR0
;21;
;22;    ADDI 1,R5          ;set skews;
;23;    ADDI R5,AR5
;24;
;25;    ADDI 2,R6
;26;    ADDI R6,AR6
;27;
;28;    ADDI 3,R7
;29;    ADDI R7,AR7
;30;
;31;    LDI @_beamlength,RC
;32;    SUBI 1,RC
;33;
;34;    RPTB Rb2         ;form beams;
;35;
;36;    ADDF3 *AR4++(1),*AR5++(1),R0
;37;    ADDF *AR6++(1),R0
;38;    ADDF *AR7++(1),R0
;39;Rb2  STF R0,*AR2++(IR1)
;41;    DBU AR1,Rb1
;*************************************************************;
```

Figure 2 Right hand beam former.

B.2 Focused beam former code

The focused beam forming software figure 3 is very similar to that already described in section B.1 since all the offsets are pre calculated there is no separate left and right beam former. The focusing offsets are added to the data vector addresses in lines 36-39 and then subtracted ready for the next set of offsets, at lines 47-50. Within a focusing region, the length of which is set by the global variable '_region_width', the beam former behaves exactly as in the linear system.

```
;03;        LDI *-FP(11),AR2  ;set start address for beams;
;04;        SM_get4 AR2, SM_RINC|SM_RLEN|SM_CJMP|SM_LOC0 ,
;05;        IR1, R2 ,R3 ,AR0
;06;        STI AR0,@BASE   ;store matrix base address;
;07;        PUSH FP         ;free AR3;
;08;        LDI @_focus,AR0       ;get base address of;
;09;        STI AR0,@TFOCUS       ;focus offsets;
;10;
;11;        LDI @_num_beams,AR1
;12;        SUBI 1,AR1
;13;
;14; Lb1     LDI @BUF0,AR4       ;load start addresses;
;15;        LDI @BUF1,AR5
;16;        LDI @BUF2,AR6
;17;        LDI @BUF3,AR7
;18;
;19;        ADDI @_offset,AR4     ;add offsets to addresses;
;20;        ADDI @_offset,AR5
;21;        ADDI @_offset,AR6
;22;        ADDI @_offset,AR7
;23;
;24;        LDI @BASE,AR2         ;load next beam address;
;25;        LDI @BASE,AR0
;26;        ADDI R2,AR0
;27;        ADDI R3,AR0
;28;        STI AR0,@BASE
;29;
;30;        LDI @_beamlength,AR3
;31;        SUBI 1,AR3
;32; Lb3     LDI @_region_width,RC
;33;        SUBI 1,RC
;34;
;35;        LDI @TFOCUS,AR0
;36;        ADDI *AR0++(1),AR4
;37;        ADDI *AR0++(1),AR5
;38;        ADDI *AR0++(1),AR6
;39;        ADDI *AR0++(1),AR7
;40;
;41;        RPTB Lb2                    ;form beams;
;42;        ADDF3 *AR4++(1),*AR5++(1),R0
;43;        ADDF *AR6++(1),R0
;44;        ADDF *AR7++(1),R0
;45; Lb2     STF R0,*AR2++(IR1)
```

Figure 3 Focused beam former.

```
;46;
;47;        SUBI *-AR0(1),AR7
;48;        SUBI *-AR0(2),AR6
;49;        SUBI *-AR0(3),AR5
;50;        SUBI *-AR0(4),AR4
;51;        STI AR0,@TFOCUS
;52;        DBU AR3,Lb3
;53;        DBU AR1,Lb1
;54;        POP FP              ;restore frame pointer;
```

Figure 3a Focused beam former, (continued).

APPENDIX C

HARDWARE PERFORMANCE PARAMETERS.

C.1 Introduction.

This appendix gives the major operating parameters of the hardware. These include system timing in section C.2, system bandwidth in section C.3 and system signal to noise ratio in section C.4.

C.2 System timing

The ultimate limitation on system performance is the rate at which data may be acquired by the hardware. In a real time system the rate at which this data can be processed is also a limitation but initially the data acquisition rate only will be considered. From chapters 5 and 6 it is known that the theoretical maximum rate of data transfer is limited by the instruction time of the DSP. A single wait state is also required by the bus interface so theoretically 16 bits of data can be acquired in 120ns. This gives a maximum data acquisition rate of 133.3 Mbits/s. There are two reasons why this figure could not be achieved practically, firstly the timed interrupt used to control the A/D converters requires servicing and secondly the length of the bus connecting the data acquisition system to the DSP introduces transmission line effects. This means that effectively 8 instruction cycles are needed for each 16 bits of data retrieved. This reduces the maximum data acquisition rate to 33.3Mbits/sec.

Each D/A board acquires 16 bits of data every 5μs thus giving an acquisition

rate of 3.2Mbits/sec. This means that with the present hardware the maximum number of channels that may be used is 10. This number could be significantly increased if the A/D card w ere mounted next to the DSP card. This would reduce the transmission line effects present on the bus and thus remove the need for extra wait states.

C.3 System bandwidth.

The system analog bandwidth is limited primarily by the four filters present in the system. Two of these are 100kHz bandpass filters with 25kHz bandwidth located in the array preamplifiers and signal conditioning board, the D/A card contains two 25Khz lowpass filters. The system bandwidth was obtained by injecting a sinusoidal signal and measuring the input to the A/D converters using a oscilloscope. The resulting gain frequency curve is shown in Figure 1.

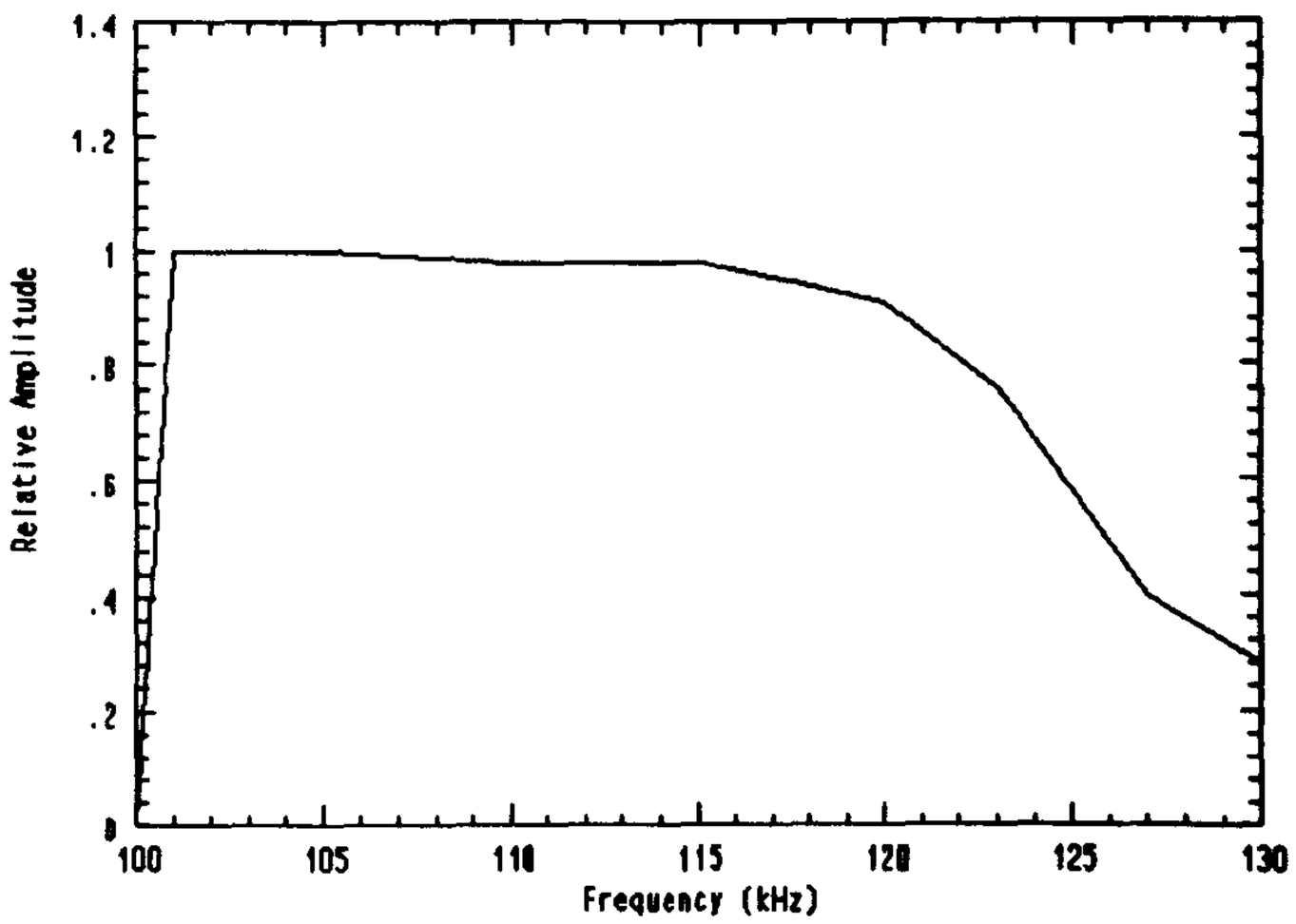

Figure 1: System gain frequency plot.

The system digital bandwidth is governed by two parameters the bus bandwidth of the

DSP and the sampling rate of the A/D cards. The issues relating to bus bandwidth have already been covered in section C.2 so only the sampling rate will be mentioned here.

The A/D convertors are clocked every 5μs giving a sampling rate of 200kHz. Therefore from Nyquist the maximum frequency that may be digitised is 100kHz. Since this is well above the bandwidth of the lowpass filters it will not be considered any further.

C.4 System signal to noise ratio.

The system SNR was measured for three different types of target placed at ranges of 0.5M, 1.0M and 1.5M. The results are shown Table I, Table II, Table II and Table III.

Table I: Signal to noise ratios for 25mm cylinder.

Target Range (mm)	Signal To Noise Ratio (dB)
500	35
1000	28
1500	23

Table II: Signal to noise ratios for a 5mm cylinder.

Target Range (mm)	Signal To Noise Ratio (dB)
500	32
1000	20
1500	14

Table III: Signal to noise ratio for corner.

Target Range (mm)	Signal To Noise Ratio (dB)
500	22
1000	8
1500	-

There is no figure given for the corner target at a range of 1500mm because the target could not be detected above the noise level.

APPENDIX D

SYSTEM NOISE TOLERANCE

D.1 Introduction.

This appendix gives the results of an experiment to discover how a noisy industrial environment may effect the operation of the ultrasonic location system.

D.2 Experimental method.

The noise source chosen was a Cincinnati Milacron robot performing an arc welding operation. To measure the noise output a Brüel and Kj¨r microphone No.4138 and a Brüel and Kj¨r Measuring Amplifier type 2608 were used. The microphone was placed approx 500cm from the welding torch and the output of the amplifier observed with a spectrum analyser.

D.3 Results.

The spectrum analyser revealed almost all of the noise produced was below the system operating frequency. This is in agreement with the work done by Estochen[1] on the use of ultrasonics to guide a welding robot.

D.4 References.

1. E. L. Estochen, "Application of Acoustic Sensors to Robotic Seam Tracking", IEEE Transactions on industrial electronics, Vol 31, 1984, pp219-224.

APPENDIX E

BEAM FORMER OFFSETS

E.1 Introduction

This appendix contains a listing of some of the offsets generated for a partially focused digital beam former with a region width of 5 samples.

The first 10 offsets generated for beams at 0°, 10°, 20° and 30° are shown in Figure 1 through to Figure 4 respectively. The offsets are listed such that each column represents the address offset applied to an individual channel; the values correspond to ranges between 75mm and 160mm. Figure 5 through to Figure 8 show the offsets generated for beams at 0°, 10°, 20° and 30° with ranges between 750mm and 835mm.

E.2 Offsets.

54	44	44	54
58	48	48	58
62	53	53	92
67	58	58	67
71	63	63	71
75	68	68	75
80	73	73	80
84	78	78	84
89	83	83	89
94	88	88	94

Figure 1: Beam former offsets for a 0° beam, short range.

60	45	37	42
64	59	42	45
68	54	46	58
73	58	51	52
77	63	55	56
81	68	60	60
85	72	65	64
90	77	69	68
94	82	74	72
99	86	79	77

Figure 2: Beam former offsets for a 10° beam, short range.

60	45	37	42
64	49	42	45
68	54	46	46
73	58	51	52
77	63	55	56
81	68	60	60
85	72	65	64
90	77	69	68
94	82	74	72
99	86	79	77

Figure 3: Beam former offsets for 20°beam, short range.

61	43	32	33
64	47	36	36
68	52	40	39
72	56	45	42
76	60	49	45
80	64	53	49
84	69	57	53
89	73	62	57
93	77	66	60
97	82	70	64

Figure 4: Beam former offsets for 30° beam, short range.

432	431	431	432
437	436	436	437
442	441	441	442
447	446	446	447
452	451	451	452
457	456	456	457
462	461	461	462
467	466	466	467
472	471	471	472
477	476	476	477

Figure 5: Beam former offsets for 0° beam, long range.

431	426	422	419
436	431	427	424
441	436	432	429
446	441	437	434
451	446	442	439
456	451	447	444
461	456	452	449
466	461	457	454
471	466	462	459
476	470	466	464

Figure 6: Beam former offsets for 10° beam, long range.

418	409	401	394
422	413	406	399
427	418	410	404
432	423	415	408
436	428	420	413
441	432	424	418
446	437	429	422
450	442	434	427
455	446	439	432
460	451	443	436

Figure 7: Beam former offsets for 20° beam, long range.

391	379	368	357
396	383	372	361
400	388	376	366
404	392	381	377
409	396	385	374
413	401	389	379
417	405	394	383
422	409	398	387
426	414	402	392
430	418	407	396

Figure 8: Beam former offsets for 30° beam, long range.

E.3 Discussion.

For the short range offsets it is worth noting that although the offsets have been generated for a region width of 5 samples the actual separation is not 5 samples in all cases. This is due to the nonlinearity of the focusing process. This can result (as shown in chapter 9) in measurement errors occurring. The long range offsets are much more linear and in most cases the separation between offsets is 5, this is because the beam former is operating closer to the far field.

The inaccuracy which results from the use of partial focusing must be traded off against the speed/memory advantages which result. An ideal solution would be to have a non-linear focusing region size which increases as the far field is approached. This would however considerably increase the complexity of the software.